HELMUT SCHMIDT
UNIVERSITÄT
Universität der Bundeswehr Hamburg

Euler–Lagrange Simulationen von turbulenten, blasenbeladenen Strömungen unter Berücksichtigung von Koaleszenz und Aufbrechen

Von der Fakultät für Maschinenbau
der Helmut-Schmidt-Universität/Universität der Bundeswehr Hamburg
zur Erlangung des akademischen Grades eines Doktor-Ingenieurs
genehmigte

DISSERTATION
vorgelegt von

Felix Hoppe

aus München

Hamburg, 2020

Erstgutachter
Univ.-Prof. Dr.-Ing. habil. Michael Breuer

Zweitgutachter
Prof. Michael Fairweather

Tag der mündlichen Prüfung
24.01.2020

Euler–Lagrange Simulations of Turbulent Bubble-Laden Flows Including Coalescence and Breakup

Doctoral Thesis

approved by the

Department of Mechanical Engineering

of the

Helmut-Schmidt-University
University of the German Federal Armed Forces

for obtaining the academic degree of

Doktor Ingenieur (Dr.-Ing.)

presented by

Felix Hoppe

from Munich

Hamburg, 2020

Kurzfassung

Diese Dissertation befasst sich mit der numerischen Berechnung von turbulenten, blasenbeladenen Strömungen unter Berücksichtigung wichtiger Phänomene wie Koaleszenz und Aufbrechen. Zu diesem Zweck wird der LES-basierte Euler-Lagrange Code $\mathcal{LESOCC}$ auf die Berechnung von Blasenbewegungen ausgeweitet. Die Schwerpunkte dieser Arbeit sind **(i)** die Modellierung des Einflusses der von LES nicht aufgelösten Skalen auf die disperse Phase, **(ii)** die Beschreibung von Koaleszenzvorgängen und **(iii)** die deterministische Vorhersage von turbulenzinduziertem Aufbrechen der Blasen.

Die nicht aufgelösten Skalen werden mit Hilfe des stochastischen Ansatzes von Pozorski und Apte (2009) modelliert, welcher durch die Berücksichtigung einer beliebigen Orientierung der Blasenbewegung verbessert wird. Zusätzlich wird eine stabile Lösungsmethode hergeleitet. Aufgrund des kleinen Betrags der durch das erweiterte Langevin-Modell abgeschätzten, nicht aufgelösten Geschwindigkeiten ist der Einfluss des Modells auf Blasen in einer Kanalströmung bei niedriger Reynolds-Zahl (Re) gering. Die Wirkung ist für feste Partikel in einem Kanal bei höheren Re-Zahlen stärker ausgeprägt. Beispielsweise wird ein höherer Volumenanteil der Partikel in der Nähe der Wände festgestellt, was signifikante Auswirkungen auf die Agglomeration und die Deposition der Partikel hat.

Bezüglich Koaleszenz wird das Model von Jeelani und Hartland (1991) durch die Berücksichtigung eines physikalisch realistischeren Abflussmechanismus und eines variablen Koeffizienten der virtuellen Masse weiter verfeinert. Die praktische Einsetzbarkeit des Modells wird durch die Verwendung einer Regressionsfunktion, die einmal am Anfang der Simulation bestimmt wird, erhöht. Das erweiterte Modell liefert eine gute Übereinstimmung der Simulationsergebnisse mit experimentellen Daten der Koaleszenz von sauberen und kontaminierten Einzelblasen mit einer freien Oberfläche. Simulationen einer Blasensäule, welche eine große Anzahl sauberer oder kontaminierter Blasen unterschiedlicher Größen enthält, zeigen deutliche Unterschiede zwischen den Entwicklungen der Größenverteilung der Blasen. Dies kann auf die unterschiedliche Fähigkeit der Blasen zurückgeführt werden, durch einen selbstverstärkenden Rückkopplungsmechanismus Turbulenz zu erzeugen.

Das Aufbrechen der Blasen wird beschrieben, indem das Modell von Hagesaether et al. (2002) in den Euler-Lagrange-Ansatz überführt wird. Dies umfasst die deterministische Bestimmung der Größe, der Trennungsachse und der dazugehörigen Trennungsgeschwindigkeiten der Tochterblasen. Zusätzlich wird eine Wartezeit eingeführt, während der die Tochterblasen nicht weiter aufbrechen können. Diese Größen werden basierend auf physikalischen Argumenten hergeleitet. Der Vergleich von Simulationsergebnissen mit experimentellen Daten des Blasenaufbrechens in einer turbulenten Düsenströmung zeigt, dass das Modell das Aufbrechen der Blasen zuverlässig vorhersagen kann. Weitere Untersuchungen ergeben in diesem Fall einen marginalen Einfluss der Koaleszenz, wohingegen die Oberflächenspannung eine wichtige Rolle für die Größenverteilung spielt.

Zusammengefasst haben die im Zuge dieser Dissertation durchgeführten Arbeiten zu einer zuverlässigen und gleichzeitig effizienten Simulationsmethode für turbulente Strömungen mit einer hoher Blasenbeladung geführt.

Abstract

This thesis is concerned with the numerical prediction of turbulent bubble-laden flows including important phenomena such as bubble coalescence and breakup. For this purpose, the LES-based Euler–Lagrange framework $\mathcal{LESOCC}$ is extended towards the tracking of bubbles. The major topics of this thesis are **(i)** the modeling of the unresolved scales of LES seen by the dispersed phase, **(ii)** the numerical description of bubble coalescence and **(iii)** the deterministic prediction of turbulence-induced bubble breakup.

The subgrid scales are modeled based on the stochastic approach by Pozorski and Apte (2009), which is further improved by considering arbitrary orientations of the particle motion. Furthermore, an unconditionally stable solution method is derived. Due to the small magnitude of the subgrid-scale velocities estimated by the extended Langevin model, the overall influence of the model is small for bubbles dispersed in a channel flow at a low Reynolds number (Re). For solid particles in a channel flow at a larger Re, the impact is more pronounced, e.g., an enhanced particle volume fraction is obtained in the vicinity of walls with significant implications on the agglomeration and the deposition of particles.

Regarding coalescence, the model by Jeelani and Hartland (1991) is further improved by considering a physically more realistic drainage mechanism and a variable added-mass coefficient for the bubbles. The extended model is made applicable to flows containing a large number of bubbles by the use of a regression function estimated once at the beginning of the simulation. Good agreement of the simulation results with experimental data of single clean or contaminated bubbles coalescing with a free surface is achieved demonstrating that the extended model yields reliable predictions of coalescence. Applying the coalescence model to simulations of a bubble column containing a large number of clean and contaminated bubbles of two different sizes reveals significant differences between the evolutions of the bubble size distributions, which can be attributed to the ability of the bubbles to induce turbulence in the fluid by a self-exciting feedback loop.

Lastly, bubble breakup is described by transferring the approach of Hagesaether et al. (2002) to the Euler–Lagrange framework. This involves the deterministic prediction of the size, the separation axis and the associated separation velocities of the daughter bubbles. Additionally, an idle time during which the daughter bubbles cannot break up is introduced. All quantities are derived purely based on physical arguments. Based on a comparison of the simulation results of bubble breakup in a turbulent jet flow with experimental data, the model is found to reliably predict breakup processes. Further investigations reveal a marginal influence of bubble coalescence in the present case, while the surface tension of the bubbles plays an important role for the size distributions.

In summary, the developments in the present thesis have led to a reliable and yet efficient simulation methodology for bubble-laden turbulent flows with high volume loading.

Danksagung

Diese Arbeit entstand während meiner Tätigkeit als wissenschaftlicher Angestellter an der Professur für Strömungsmechanik der Helmut-Schmidt Universität / Universität der Bundeswehr Hamburg. Mein Dank gilt Allen, die mich während dieser Zeit unterstützt und motiviert haben und ohne die diese Arbeit nicht möglich gewesen wäre.

Im Besonderen möchte ich Herrn Prof. Michael Breuer danken, der mir diese Arbeit erst ermöglicht hat. Seine fachliche Unterstützung bei der Entwicklung der hier präsentierten Modelle war ein entscheidender Beitrag zu dieser Arbeit.

Des weiteren möchte ich Herrn Prof. Michael Fairweather für die Übernahme des Zweitgutachtens danken.

Ein großes Dankeschön gilt auch allen Kollegen, die ich während meiner Zeit an der Professur für Strömungsmechanik kennenlernen durfte. Insbesondere möchte ich mich bei Guillaume De Nayer, Jens Nikolas Wood, Stephan Vollack (geb. Schmidt), Ali Khalifa und Naser Almohammed für anregende aber vor allem auch witzige Gespräche.

Meiner Freundin Marilyn Heger möchte ich für ihre große Unterstützung danken und dafür, dass sie mich auch in schwierigen Zeiten ertragen hat. Dank gilt auch ihrer ganzen Familie, die es möglich gemacht, dass ich mich hier im Norden heimisch fühle.
Zu guter Letzt möchte ich meinen Eltern danken, die mich mein ganzes Leben lang immer unterstützt und gefördert haben.

Hamburg, Februar 2020 Felix Hoppe

Contents

1 Introduction

Multiphase flows are among the most common types of flows encountered in both natural processes and industrial applications. Numerical predictions of these complex flow phenomena play an increasing role in engineering as well as natural sciences thanks to the enhancing computational capabilities of computers and the cost-efficiency of computational fluid dynamics (CFD) compared to experimental investigations. The scope of the present thesis is to advance the numerical methodologies available for describing a specific portion of multiphase flows, i.e., turbulent flows laden with small dispersed bubbles.

Since gas-liquid flows can have a variety of forms, the first chapter starts with a classification of these flows in Section 1.1. Subsequently, the motivation behind the present thesis is presented in Section 1.2. Section 1.3 summarizes the main objectives of the thesis. Lastly, the outline of the remaining thesis is sketched in Section 1.4.

1.1 Classification of Gas-Liquid Flows

According to Prosperetti and Tryggvason (2007) multiphase flows are defined as systems in which two or more different phases are simultaneously present. Among the large number of flows satisfying this definition, gas-liquid flows are the most complex ones, since the evolution of the interface between the two phases is involved. Hence, for describing these flows it is not only necessary to account for the forces on the individual phases, but also the interfacial interaction between the phases has to be considered. The form of the interface, and therefore of the multiphase flow topology, can strongly vary. It is known that several groups of patterns exist, which are more or less the same in all gas-liquid flows (Kelessidis and Dukler, 1989) allowing to classify gas-liquid flows. In order to do this, experimental investigations have been performed in various geometries, e.g., vertical (Fernandes et al., 1983; Hewitt and Roberts, 1969; Taitel et al., 1980) and horizontal (Hashizume, 1983; Taitel and Dukler, 1976) pipe flows or flows through annuli (Kelessidis and Dukler, 1989; Zahid et al., 2018).

In Fig. 1.1 typical gas-liquid flow types are depicted using the example of the simultaneous upwards flow of gas and liquid in a vertical pipe. According to Cheng et al. (2008) the observable patterns are:

1. Bubble flow occurs for gas flow rates which are small compared to the liquid flow rate (Cheng et al., 2008). The gas phase is homogeneously distributed in the continuous liquid phase in form of small, discrete bubbles, which are dragged upwards by the liquid (Kelessidis and Dukler, 1989; Taitel et al., 1980). Consequently, this flow type fulfills the definition of a disperse flow (Brennen, 2005).

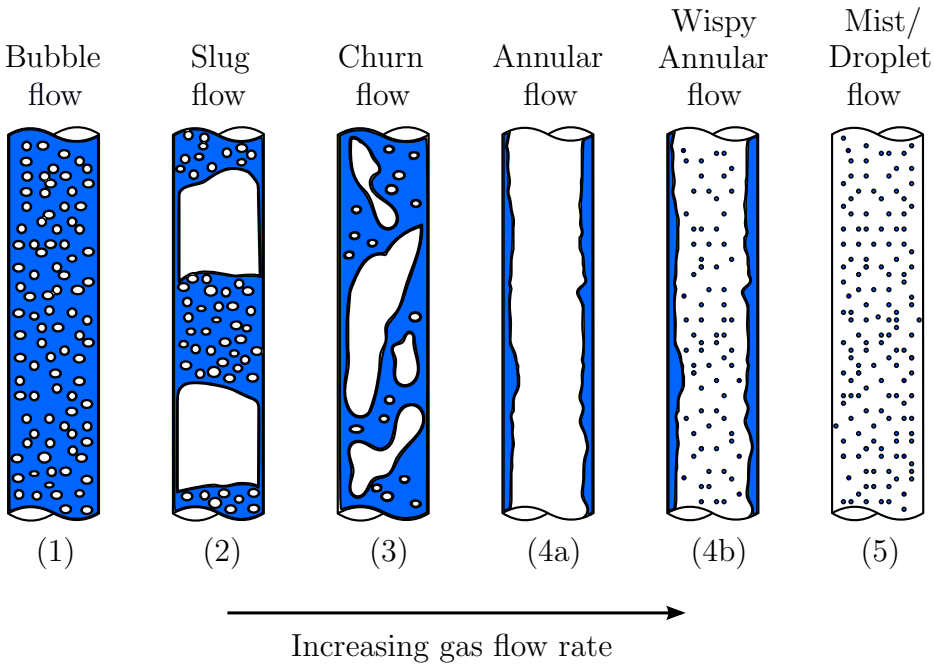

Fig. 1.1. Schematic of the typical flow patterns encountered in vertically upward gas-liquid flows for increasing gas flow rate. Based on Cheng et al. (2008).

2. Slug flow arises due to an increased gas flow rate compared to the bubble flow regime leading to the coalescence of the disperse bubbles (Cheng et al., 2008). Large, bullet-shaped Taylor bubbles are formed, which span over the complete diameter of the tube (except from a small liquid film between the bubbles and the pipe wall). The large bubbles have a length of one to two pipe diameters. Between the Taylor bubbles slugs of continuous liquid containing disperse bubbles moves upwards (Taitel et al., 1980). Consequently, slug flow is a separated flow (Brennen, 2005).

3. A further increase of the flow rates leads to churn flow (Cheng et al., 2008). This flow regime is similar to the slug flow, but is characterized by a more chaotic and disordered topology (Kelessidis and Dukler, 1989; Taitel et al., 1980). The shape of the large gas bubbles is strongly distorted and the continuous slugs of liquid are destroyed by small to medium sized gas bubbles.

4. If the gas flow rate is further increased, annular flow appears. This flow pattern, which is denoted by type (4a) in Fig. 1.1 is characterized by a continuous gas phase that flows upwards in the center of the pipe, while the liquid phase moves upwards in the annular space between the gas and the pipe walls in the form of a wavy liquid film (Kelessidis and Dukler, 1989; Taitel et al., 1980). A second form of annular flow is defined by some authors (see, e.g., Cheng et al., 2008) as wispy-annular flow (type (4b) in Fig. 1.1), where liquid is teared from the annular liquid flow leading to droplets of liquid carried by the gas in the center of the pipe (Kelessidis and Dukler, 1989; Taitel et al., 1980).

5. Lastly, at very high gas flow rates, all the liquid is sheared from the wall and is carried by the gas phase in form of droplets (Cheng et al., 2008). Consequently, the flow is turned into a disperse flow again, i.e., a droplet-laden flow is obtained, which is sometimes also denoted by the term mist flow.

Due to the large variety of flow patterns shown in Fig. 1.1 and the complex flow phenomena arising in all cases, it becomes apparent that the numerical simulation of gas-liquid flows is a difficult task. The focus of the present thesis is on the simulation of gas-liquid flows of type (1), i.e., turbulent flows laden with disperse bubbles. Here, major aspects of this work are the accurate prediction of the bubble movement and the capturing of physical mechanisms such as coalescence and breakup. The framework of Euler–Lagrange prediction in combination with large-eddy simulations of the fluid is chosen for these tasks. The motivation behind the present thesis is given in the next section.

1.2 General Overview and Motivation

Bubble flows are frequently encountered in many engineering applications and natural phenomena. For example, gas bubbles occur in oil-drilling wells (Wang and Sun, 2009; Zahid et al., 2018) or deepwater gas plumes created by accidents during deep sea drilling (Bandara and Yapa, 2011). Other applications are encountered in the treatment of wastewater (Chang and Judd, 2002; Gresch et al., 2011; Rosso et al., 2008), the estimation of heat transfer characteristics in power plants (Krepper and Rzehak, 2011; Sato et al., 1981a,b; Situ et al., 2005; Ünal, 1976) or processing and refinement of metals (Oeters et al., 1988; Sheng and Irons, 1995; Zhang et al., 2007). Two additional examples – bubbles in the ocean and bubble columns – are discussed in more detail in the following in order to demonstrate the importance of gas bubbles.

Bubbles produced by the breaking of wind-generated waves in the ocean play an important role for the gas transfer between the air and the ocean as well as for the reflection of light by the sea. The breaking of waves leads to the entrainment of air into the sea water in form of dispersed bubbles (Deike et al., 2017). The size of these bubbles strongly varies from bubbles with diameters of $\mathcal{O}(10 \text{ to } 100\,\mu\text{m})$ (Medwin and Breitz, 1989) up to diameters of $\mathcal{O}(4\,\text{mm})$ (Anguelova and Huq, 2012). The smallest bubbles are generated by the breakup of larger bubbles due to the strong turbulence close to the surface of the ocean. This is of importance for the dispersion of the bubbles, since large bubbles quickly rise upwards to the surface due to the buoyancy force. In contrast, small bubbles follow the turbulent fluid motion more directly and, thus, can be dragged downwards into depths of more than $\mathcal{O}(10\,\text{m})$ (Anguelova and Huq, 2012; Melville, 1996) leading to an increased dispersion of the bubbles.

The presence of these bubbles plays an important role for the bubble-mediated gas transfer in the sea (Liang et al., 2011, 2013), e.g., it was shown by Vagle et al. (2010) that bubbles lead to an increased transfer of nitrogen and oxygen to the water. Since all living beings require oxygen, this is of special importance to all sea life. Additionally, the bubble-mediated absorption of gases plays a role for the carbon dioxide take-up of

the oceans (Woolf, 1993), which is known to be a major factor in the global CO_2 balance (Tans et al., 1990). According to Liang et al. (2011, 2013) two mechanisms play a role for bubble-mediated gas transfer. On the one hand, the dispersed bubbles increase the contact area between the gas and the liquid phase. On the other hand, small bubbles, which are found in greater depths, can be dissolved into the sea water due to the high hydrostatic pressure and their own surface tension. The second mechanism is still in effect even if the water is already close to supersaturation, i.e., a state where the liquid can not dissolve any more gas. Consequently, the turbulence-induced breakup of gas bubbles into smaller fragments plays an important role in the gas transfer into the oceans.

Aside from the gas transfer, gas bubbles residing in the upper layers of the sea close to the surface also change the optical properties of the water in form of an increased albedo, which is a measure for the reflection of solar radiation by a body. Since the refraction index of the gas bubbles is significantly smaller than that of the surrounding water and the bubbles are large compared with the wavelengths of light, gas bubbles scatter light very efficiently (Terrill et al., 2001). It was estimated by Terrill et al. (2001) and Zhang et al. (1998) that the backscattering of light by small gas bubbles close to the sea surface can be the dominating effect in the reflection of solar radiation. This was later experimentally validated by Zhang et al. (2002) who found that up to 40 % of the backscattering is due to the bubbles. Consequently, by increasing the albedo of the sea water the disperse bubble are able to reduce the solar energy absorption of the ocean. This feature of bubbles even leads to the suggestion by Seitz (2011) to inject bubbles into bodies of water in order to combat global warming.

Bubble flows are also encountered in industrial applications in form of gas-liquid reactors, which can have a variety of forms (Carrà and Morbidelli, 1987; Shah et al., 1982). One type of those reactors is the bubble column reactor, which are towers with a height of at least two to three diameters. The gas is supplied at the bottom of the tower by gas spargers (an array of gas nozzles) and then rises through a liquid (Carrà and Morbidelli, 1987; Kantarci et al., 2005). Bubble columns are used in a vast number of industrial applications (see, e.g., Shah et al., 1982, for an overview). Important examples of chemical processes include oxidation (Morbidelli et al., 1986), chlorination (Wachi and Morikawa, 1987) and hydrogenation (Winterbottom et al., 2003). Bubble columns are also used for wastewater treatment (Rosso et al., 2008), e.g., by using ozonation to remove dyes (Konsowa, 2003), ammonia (Yang et al., 1999) or pharmaceuticals (Huber et al., 2005) from the water. Lastly, the application as bioreactors is mentioned here, i.e., bubble columns are commonly used in biochemical and biotechnological applications like the growth of algae (Singh and Sharma, 2012) or production of citric acid (Sassi et al., 1991; Tisnadjaja et al., 1996) and penicillin (Koenig et al., 1981).

Due to the large variety of applications in industry, bubble columns have been the subject of both experimental and numerical studies with focus on both the liquid as well as the gas phase. Since biological cell cultures were shown to be susceptible to high shear rates by Grima et al. (1997) and Mirón et al. (2003), the flow structures emerging from the rising bubbles are important for the use of bubble columns in biotechnological applications. The flow in air-sparged bubble columns was for example investigated by Degaleesan et al. (2001) in cylindrical bubble columns with three different diameters (0.14,

0.19 and 0.44 m) and varying liquid heights (1.0 to 1.8 m). Similar investigations were performed by Hlawitschka et al. (2017) in a column with a diameter of 0.14 m and a height of 0.73 m and Deen et al. (2001) who used a square cross-sectioned bubble column with side lengths of 0.15 m and a height of 0.45 m. Gas was released at the bottom of the columns through gas spargers leading to dispersed bubbles rising upwards due to the buoyancy force in the form of a meandering bubble plume (Deen et al., 2001). Thereby, the rising bubbles induce an upwards directed turbulent fluid velocity in the center of the column, which is accompanied by a downward directed flow close to the walls. It was shown by Degaleesan et al. (2001) that the turbulent kinetic energy of the fluid is dominated by the velocity fluctuations in the axial direction, which are generated by the rising bubbles.

The interfacial area between the gas and the liquid phase is the relevant quantity for most chemical processes. Wilkinson and van Dierendonck (1990) studied the effect of the pressure of the system and the gas density on the gas hold-up and the bubble size in pressurized bubble columns. A bubble column with a diameter of 0.026 m and a height of 0.7 m was used. It was found that both an increasing pressure and gas density lead to an increasing gas hold-up, but a decreasing bubble size. This was explained by the observation that both an increased pressure and gas density lead to an increased rate of bubble breakup. Consequently, a larger number of smaller bubbles is observed in the bubble column. It was shown in a subsequent study by Wilkinson et al. (1994) that the presence of a larger number of smaller bubbles leads to a substantially increased mass transfer rate between the gas and the liquid phases, which can be explained by the increased surface area of the bubbles. Furthermore, it was found by Wilkinson et al. (1994) that the addition of electrolytes to the liquid leads to a further increased gas hold-up and, therefore, to an increased mass transfer. This was explained by the fact that the electrolyte solution inhibits the coalescence of the bubbles (Zieminski and Whittemore, 1971). Hence, the smaller bubbles generated by breakup processes do not coalesce easily again but remain small. Similar results have been reported by Letzel et al. (1999).

Another experimental study on the evolution of the bubble sizes in a bubble column was performed by Lau et al. (2013). They used a pseudo-2D column, i.e., the rectangular base area had a width of 0.2 m but only a depth of 0.03 m. The height of the column was 1 m. Again a strong influence of coalescence processes on the bubble size distribution was found depending on the distance to the sparger region. Due to coalescence, the size of the bubbles increases at larger heights of the column. However, the fluid turbulence induced by the bubbles leads to the occurrence of breakup processes. Consequently, a balance between coalescence and breakup is reached (Lau et al., 2013).

Despite their importance for industry, experiments on bubble columns are mostly performed in relatively small laboratory scales (see, e.g., Deen et al., 2001; Degaleesan et al., 2001; Hlawitschka et al., 2017; Letzel et al., 1999; Wilkinson et al., 1994; Wilkinson and van Dierendonck, 1990). However, industrially operated bubble columns are typically much larger, e.g., reactors with diameters of 6 to 8 meters and heights of up to 30 meters exist (Krishna et al., 2001). For this reason, most large-scale bubble column reactors are designed based on scale-up criteria. Those empirical relations connect important features that are relevant for the operation of the bubble column like the gas hold-up or the mass

transfer rate to the general properties of the bubble column such as the size of the column or the densities and viscosities of the liquids used. Scale-up criteria are usually obtained by performing (laboratory scale) experiments with varying column geometries and flow characteristics. Afterwards a correlation between the desired quantity and the column properties is proposed, where a set of coefficients describe the dependency on those variables. By fitting the relation to the measured results, the coefficients can be determined. Some typical examples of scale-up criteria are the ones by Deckwer and Schumpe (1993), Krishna et al. (2001) and Wilkinson et al. (1992). A list of criteria can be found in the review by Shaikh and Al-Dahhan (2013).

Alternatively, numerical predictions of gas-liquid flows can be used to estimate the critical quantities beforehand or to study the complex phenomena. Due to the increasing calculation capabilities of modern computers, the prediction of multiphase flows by computational means became more and more popular in the last decades. Different methodologies exist with varying complexity and computational costs. All approaches have in common that they have to reliably predict the liquid carrier phase as well as the disperse gas phase. From the examples listed above, it can be deduced that an accurate prediction of the dispersed gas phase requires a correct tracking of the bubbles through the fluid, a treatment of bubble-bubble interactions in form of coalescence and an estimation of the breakup of bubbles due to fluid forces induced by turbulence. In principle, three different approaches exist for the computation of gas-liquid flows, i.e., fully-resolved, Euler–Euler and Euler–Lagrange simulations.

As the name implies, the framework of fully-resolved simulations requires to resolve all scales of both the fluid as well as the gas phase including the evolution of the deformable gas-liquid interface. Direct numerical simulations (DNS) are used to compute the complete fluid field from the smallest up to the largest scales of turbulence. The tracking of the bubbles and their deformable surfaces can be done by several techniques. For example, the level-set method devised by Osher and Sethian (1988) is available, where the motion of an interface is computed by the evolution of a smooth function that represents the interface as the set of points at which the function is zero. Additional information on the level-set method and some of its applications can be found in reviews by Gibou et al. (2018), Mitchell (2008) and Osher and Fedkiw (2001). A similar alternative used to track deformable interfaces is the volume-of-fluid method by Hirt and Nichols (1981). In this method a fraction function that describes the fractional volume of each fluid in each computational cell is defined. Computational cells containing an interface between the two phases can be identified by the values of the fraction function, i.e., if they are between zero and one. For more details the interested reader is referred to the literature, e.g., by Albert et al. (2012), Pilliod and Puckett (2004), Prosperetti and Tryggvason (2007) and Scardovelli and Zaleski (1999). Lastly, the immersed boundary method is mentioned here, which is based on the approach by Peskin (1972, 1977, 2002) to simulate the fluid-structure interaction of blood flow around heart valves. The idea behind this method is to describe the interface and its deformation by a number of discrete, interconnected points, which interact with the surrounding fluid by the forces acting on them (Peskin, 2002). Again, for further information see additional literature, e.g., by Kempe and Fröhlich (2012), Peskin (2002), Schwarz et al. (2016) and Uhlmann (2005).

Since fully-resolved simulations require to determine all turbulent scales of the fluid up to the smallest ones in addition to the complex tracking of the interface between the liquid and the gas phase, these approaches provide the most detailed description of gas-liquid flows. However, this level of detail has the drawback that the computational costs of fully-resolved simulations are very high limiting the applicability of these methods to low-Reynolds number flows containing only few bubbles. For example, in the simulations by Dabiri et al. (2013), Lu et al. (2005) and Lu and Tryggvason (2006, 2007, 2008, 2013) the volume-of-fluid method is coupled with a direct numerical simulation to track a small number of bubbles ($\mathcal{O}(10-100)$) through a low-Re turbulent channel flow ($\mathrm{Re} \leq \mathcal{O}(3000)$ based on the half-width of the channel and the bulk velocity of the fluid).

An alternative to fully-resolved simulations are Euler–Euler predictions of turbulent gas-liquid flows. This ansatz assumes that the dispersed gas phase can be modeled as a second continuum penetrating the fluid phase (Anderson and Jackson, 1967). Consequently, both phases are individually described by the conservation equations of mass and momentum for a continuous fluid with different values for the fluid properties such as density and viscosity. This means that information on individual bubbles is not available, but only the volume fraction or number densities of the bubbles are available. The interaction between the two phases is described by modeled interface force terms. The conservation equations of the Euler–Euler approach are mostly solved in the framework of the Reynolds-averaged Navier–Stokes (RANS) equations (see, e.g., Chen et al., 2005; Deju et al., 2013; Shi and Rzehak, 2018) or in the context of large-eddy simulations (LES) (see, e.g., Gupta and Roy, 2013; Liu and Li, 2018; Ma et al., 2015). The coupling of the Euler–Euler framework with direct numerical simulations was investigated by Kaufmann et al. (2008). Simulations in the framework of the Euler–Euler approach are the most frequently used predictions in the literature, see, e.g., the works by Colombo and Fairweather (2016), Gruber et al. (2015), Olmos et al. (2001), Patel et al. (2006) and Solsvik and Jakobsen (2014).

One of the largest difficulties for the Euler–Euler ansatz is the description of coalescence and breakup processes. Since the bubbles are not tracked individually through the flow field and only the number densities are known at a certain position, collisions between two bubbles leading to coalescence or the exertion of large fluid stresses leading to breakup are not resolved. Hence, those processes are modeled by corresponding rates like the famous ones by Prince and Blanch (1990) or Luo and Svendsen (1996), which appear in population balance equations describing the evolution of the bubble number density (see, e.g., Liao and Lucas, 2009, 2010; Liao et al., 2015, for reviews on coalescence and breakup rates). Due to the lack of more detailed information, the derivation of those relations requires to make simplifications and assumptions on the conditions of the flow and the bubbles. For example, the coalescence model by Prince and Blanch (1990) requires to estimate the collision frequency of the bubbles according to the kinetic theory of gases. The same theory is used by Luo and Svendsen (1996) to predict the impact frequency of turbulent eddies on the bubble surface, which leads to the deformation and breakup of the bubbles.

Lastly, the framework of Euler–Lagrange predictions is mentioned here. In this approach the liquid phase is still treated as a continuum in the Eulerian frame of reference, which can be determined by direct numerical simulations, by the Reynolds-averaged Navier–

Stokes approach or by large-eddy simulations (Sommerfeld et al., 2008). Direct numerical simulations are the most accurate option, but also the most costly one restricting the flow to relatively small Reynolds numbers. Giusti et al. (2005) and Molin et al. (2012) used DNS in their Euler–Lagrange predictions of disperse bubble-laden flow in a channel. The Reynolds-averaging approach was applied for example by Farrell (2003) and Gao et al. (2012). Simulations based on the RANS method usually require much lower computational effort, but have the major drawback that only the average fluid field is determined demanding the modeling of the velocity fluctuations. A compromise between DNS and RANS predictions is provided by the framework of large-eddy simulations, which is characterized by resolving the important large, energy-carrying structures of the flow, while modeling the smallest, subgrid-scale velocity (SGS) fluctuations. That makes the simulation of highly turbulent, large Reynolds-number flows in a cost-efficient, yet accurate way possible. However, note that large-eddy simulations of flows laden with bubbles, droplets or particles also require the estimation of the subgrid scales acting on the dispersed phase, since these unresolved scales have a non-negligible effect, see Section 2.1.

In the Euler–Lagrange methodology the dispersed phase is treated in a Lagrangian frame of reference, i.e., the gas bubbles are tracked individually through the flow field by calculating the forces acting on the bubbles. Since the deformation of the gas-liquid interface is not resolved in full detail, the Euler–Lagrange approach requires less computational effort than fully resolved simulations. Yet, the motion of each individual bubble is accounted for making the treatment of phenomena that pose to be difficult for the Euler–Euler ansatz possible. For example, the occurrence of collisions in the dispersed phase can be readily determined by collision-detection algorithms (Alletto and Breuer, 2012; Breuer and Alletto, 2012). Since collisions are the pre-requisite for the coalescence of bubbles, the occurrence of coalescence can be determined more precisely compared to Euler–Euler predictions, which have to rely on empirical collision rates (see, e.g., Coulaloglou and Tavlarides, 1977; Prince and Blanch, 1990). The estimation of such rates is based on simplifications decreasing the accuracy of the multiphase flow prediction. A similar argumentation is valid for the breakup of bubbles due to the interaction with the turbulent structures of the flow.

1.3 Objectives of the Thesis

The scope of this thesis is the simulation of a large number of dispersed bubbles distributed in turbulent flows at large Reynolds numbers. It was argued above that a proper estimation of the disperse gas phase is ideally based on detailed information on the bubbles. Consequently, the Euler–Lagrange approach in the framework of large-eddy simulations is chosen in this thesis, since it resolves the most important structures of the flow and allows to follow the individual bubbles through the flow field in a cost-efficient manner. In the present thesis the in-house CFD code $\mathcal{LESOCC}$ (Large-Eddy Simulation On Curvilinear Coordinates) by Breuer (1998a,b, 2000, 2002) is used, which can efficiently track a huge number of bubbles, particles or droplets and incorporates mechanisms to realistically predict effects like inter-particle collisions and collisions of the particulate phase with

smooth or rough walls, agglomeration and breakup of solid particles and coalescence of droplets. See the work by Alletto and Breuer (2012, 2013a,b, 2015), Almohammed and Breuer (2016a,b, 2019), Breuer and Alletto (2011, 2012), Breuer et al. (2012), Breuer and Almohammed (2015) and Breuer and Khalifa (2019a,b) for more information.

The accurate prediction of turbulent, bubble-laden flows in the framework of Euler–Lagrange predictions combined with the large-eddy simulation ansatz requires to incorporate the following three mechanisms:

1. The modeling of the subgrid-scale velocity fluctuations acting on the bubbles.
2. The coalescence of colliding bubbles.
3. The breakup of bubbles due to turbulent velocity fluctuations.

Consequently, those three topics will be a major focus of this thesis. Firstly, for all topics suitable modeling approaches have to be identified based on an assessment of their advantages and drawbacks allowing to select appropriate models adequately describing the subgrid-scale fluctuations, the coalescence of bubbles and the turbulence-induced breakup of bubbles. Existing drawbacks of the chosen models are identified and tried to overcome by incorporating several improvements. Afterwards, the models are implemented into the existing Euler–Lagrange framework and validated based on appropriate test cases.

In the case of the subgrid scales of the fluid velocities seen by the bubbles, the model by Pozorski and Apte (2009) is chosen as a starting point, since it includes the description of several important physical effects. However, several enhancements regarding the applicability to arbitrary movement directions of the bubbles and the numerical solution process are proposed in the context of this thesis. Since many important features of the coalescence process of bubbles, which are often neglected by other approaches, are considered by the model of Jeelani and Hartland (1991), it is applied here. Some improvements in the modeling of the coalescence process are introduced. The main focus of the implementation of the model by Jeelani and Hartland (1991) is to reduce the high computational effort in the context of coalescence of contaminated bubbles, which was one of the major drawbacks of the model. Lastly, since the approach of Hagesaether et al. (2002) provides a physically reasonable estimation of the breakup process of bubbles, it is used in this thesis. The main challenge for the prediction of breakup processes in the framework of Euler–Lagrange predictions is the treatment of the daughter bubbles and their size after the breakup. Up to now, only very simplistic approaches exist in the literature. Consequently, the post-breakup treatment including the separation axis, the separation velocities of the daughter bubbles and the breakup time is the emphasis of the present work.

1.4 Outline of the Thesis

Firstly, in Chapter 2 an overview on existing modeling concepts of the subgrid-scale fluctuations, the bubble coalescence and the bubble breakup is given. In Chapter 3 the framework of large-eddy simulations is introduced giving a brief overview on this

approach. Next, in Chapter 4 the Lagrangian tracking of bubbles is explained including details on the force balance and boundary conditions. Chapter 5 concentrates on the interaction mechanisms including the bubble-fluid interaction (two-way coupling) and the bubble-bubble collisions (four-way coupling). In the next three chapters the modeling approaches of the subgrid-scale fluctuations for the particulate phase (Chapter 6), the bubble coalescence (Chapter 7) and the bubble breakup (Chapter 8) are presented. The numerical methodology used in the present thesis to determine the turbulent, bubble-laden flows is provided in Chapter 9. In Chapter 11 the results of the application of the simulation framework are shown. Finally, in Chapter 12 conclusions are drawn and an outlook on further possibilities and challenges of the present framework is given.

2 Literature Overview

The subgrid-scale fluctuations, the coalescence of bubbles and the turbulence-induced breakup of bubbles can be modeled with varying degrees of complexity by a large number of different approaches. The objective of this section is to provide a brief overview of important models found in the literature. The basic assumptions made for their derivation are sketched together with the associated advantages and drawbacks of the models. Note that the literature overview given in Sections 2.1 to 2.3 has been previously published in a similar manner in Breuer and Hoppe (2017) and Hoppe and Breuer (2018, 2020)

2.1 Subgrid-Scale Fluctuations

An accurate estimation of the forces on the individual bubble requires the knowledge of the exact fluid velocity at the position of the bubble (Minier et al., 2014). However, this situation is only given by direct numerical simulations, which resolve all scales of the fluid. Predictions in the framework of RANS or LES have to estimate the fluctuations depending on the respective approach. Since only time-averaged fluid velocities are calculated by RANS simulations, the complete velocity fluctuations at the bubble position have to be modeled (see, e.g., Minier et al., 2004, 2014; Minier and Peirano, 2001). Note that this is another drawback of the Reynolds-averaging approach in the framework of Euler–Lagrange predictions. In large-eddy simulations the velocity fluctuations of the small subgrid scales are removed by a filtering operation. In order to account for the influence of these unresolved scales on the momentum balance of the fluid phase, a variety of subgrid-scale models is available (see, e.g., Section 3.2). However, the effect of the subgrid-scale velocity fluctuations on the motion of the dispersed phase was mostly neglected in the earlier days of Euler–Lagrange studies based on LES (see, e.g., Apte et al., 2003; Wang and Squires, 1996). That was justified by the small values of the unresolved scales compared with the resolved ones. However, several authors noted that this assumption is not always correct and that depending on the properties of the dispersed phase the subgrid scales may have an influence on the dispersed phase.

Among the first authors reporting such an influence were Armenio et al. (1999), who demonstrated that neglecting the unresolved scales in the equations of motion of the dispersed phase affects the dispersion of the particulate phase. Another example is the erroneous capturing of turbophoresis due to ignoring the subgrid scales (Kuerten and Vreman, 2005). The turbophoresis effect is a transport mechanism of the dispersed phase caused by the inhomogeneity of the turbulent fluctuations in wall-bounded flows (Reeks, 1983; Young and Leeming, 1997). Furthermore, Marchioli et al. (2008) compared the results of a-priori and a-posteriori large-eddy simulations of a turbulent channel flow

with a reference DNS. The filtering in both cases results in significant differences of the distribution and the velocity statistics of the particulate phase compared with the results of the DNS.

Consequently, in the Euler–Lagrange framework the unresolved scales of large-eddy simulations need to be considered in the equation of motion of the dispersed phase. Note that the above mentioned studies mostly investigated the influence of the subgrid scales on solid particles. However, droplets and bubbles are affected by the unresolved scales as well. Hence, the modeling approaches presented in the following can be applied to solid particles, liquid droplets and gas bubbles. While the focus of this thesis is on bubbles, in the following the dispersed phase is nevertheless denominated as particles.

Subgrid-scale models for the velocity fluctuations of the fluid seen by the dispersed phase can be divided into several groups. Two of the most common approaches are the approximate deconvolution method and the stochastic models applying a Langevin equation, which rely on different ideas to estimate the subgrid-scale fluctuations.

2.1.1 Approximate Deconvolution Models

The first type of models are approximate deconvolution models (ADM), which are based on the idea to reverse the filtering process characterizing large-eddy simulations. From a mathematical point of view the filtering process is a mathematical operation, which can be inverted by applying the inverse of the operation to the filtered velocity field. In LES the mathematical operation performed to obtain the filtered velocity field is a convolution of the exact fluid velocity with a filter function (Breuer, 2002; Piomelli and Chasnov, 1996; Sagaut, 2006). Inverting the filtering operation was first proposed to model the influence of the subgrid scales on the continuous phase (see, e.g., Domaradzki and Loh, 1999; Geurts, 1997; Kuerten et al., 1999; Loh and Domaradzki, 1999; Stolz and Adams, 1999; Stolz et al., 2001). Later, the idea was extended to describe the subgrid-scale velocity fluctuations of the fluid seen by the dispersed phase (see, e.g., Kuerten, 2006; Kuerten and Vreman, 2005; Shotorban and Mashayek, 2005). The subgrid-scale fluctuations are obtained by a convolution of the filtered fluid field with the inverse filter function. The inverse of the filter function is usually approximated based on an idea by Stolz and Adams (1999) and Stolz et al. (2001), who proposed to represent the inverse filter by a truncated series expansion of the filter function. Thus, the subgrid scales are estimated based on a sum of velocity fields, which are filtered with an increasing filter width (Kuerten, 2006; Shotorban and Mashayek, 2005).

Shotorban and Mashayek (2005) demonstrated that the use of the approximate deconvolution method in a large-eddy simulation of turbulence in a box leads to a better agreement of the particle properties with a reference DNS, i.e., the estimation of the turbulent kinetic energy, the probability density function of the number density and the diffusivity of the particles was improved. However, Shotorban and Mashayek (2005) also pointed out that several discrepancies between the DNS and the LES results remained. Since ADM can only retrieve scales which are of the order of the grid size (Shotorban and Mashayek, 2005), the deviations to DNS are supposedly caused by the subgrid scales not captured by the deconvolution model. Additional difficulties arising in the context of

applying ADM have been specified in the study by Okong'o and Bellan (2000). Firstly, it was mentioned that the filtering in LES is usually done in an implicit way. Hence, the definition of an explicit inverse of the filter function is challenging. Secondly, it was noted that there exists no unique relation between the filtered and the non-filtered velocity field, i.e., the same filtered velocity can be obtained from the filtering of different realizations of the exact velocity field. Lastly, since the velocity field has to be filtered several times in ADM, the potentially high computational costs pose a difficulty (see, e.g., Kuerten, 2006; Shotorban and Mashayek, 2005). Additionally, Kuerten (2006) showed that the application of ADM requires to interpolate the full (filtered component plus the subgrid-scale component restored by ADM) fluid velocities to the positions of the particles by an interpolation scheme that is at least of fourth order. According to Kuerten (2006) a second-order accurate interpolation acts as an additional filtering operation, which cancels out the positive effect of the ADM. Consequently, since a fourth-order accurate interpolation requires more numerical effort compared to a second-order accurate variant, the computational costs associated with the ADM are further increased.

2.1.2 Stochastic Models

The second type of models are stochastic models, in which the unresolved scales are modeled by solving a stochastic differential equation (SDE), also known as Langevin equation. Langevin equations are typically composed of two terms (Gardiner, 2003; Kloeden and Platen, 1995): a drift term driving the corresponding random variable towards a certain average solution and a stochastic diffusion term adding randomness to the process. The use of stochastic differential equations in the context of Euler–Lagrange predictions originates from the estimation of the fluid field by the Reynolds-averaging approach, which makes it necessary to model the complete turbulent fluctuations of the fluid velocity for an adequate prediction of the motion of the dispersed phase (Minier et al., 2004, 2014; Minier and Peirano, 2001). Later, the Langevin approach was transferred to the framework of large-eddy simulations in order to estimate the subgrid-scale velocity fluctuations (see, e.g., Berrouk et al., 2007, 2008; Fede et al., 2006; Pozorski and Apte, 2009).

Stochastic subgrid-scale models can be classified into different groups. For example, Langevin models can be distinguished by the form of the fluid velocity estimated. The SDE can either provide the complete fluid velocity seen by the particulate phase (see, e.g., Berrouk et al., 2007, 2008; Minier et al., 2014) or only the unresolved subgrid-scale fluctuations (see, e.g., Fede et al., 2006; Pozorski and Apte, 2009). Note that according to Fede et al. (2006) one formulation can be transformed into the other. Another way to categorize stochastic models is by the type of the Langevin equation. On the one hand, there exist generalized Langevin equations. Here, the unresolved scales are modeled by stochastic diffusion processes, where effects like the inhomogeneity of turbulence are described by modifications to the drift and diffusion terms (Minier et al., 2014). This approach was used by Minier et al. (2004, 2014) in the context of RANS and by Berrouk et al. (2007, 2008) and Fede et al. (2006) in the framework of LES. On the other hand, normalized Langevin equations can be used to determine the required components of the

fluid velocities seen by the dispersed phase, i.e., either the full fluid velocity or the subgrid-scale fluctuations. Here, the inhomogeneity of turbulence is described by normalizing the components of the fluid velocities predicted by the model by certain characteristic velocities. According to Minier et al. (2014) the characteristic velocities can be estimated by the standard deviation of the fluctuations of the corresponding velocity component. Taniére and Arcen (2014) applied this ansatz in the framework of RANS, while Pozorski and Apte (2009) used it in the framework of LES.

One example of a generalized Langevin model is the one by Fede et al. (2006), who transferred the model by Pope (1994) for the fluid fluctuations in a RANS prediction to the framework of LES. The basic assumption of the model by Fede et al. (2006) is that the turbulence is homogeneous and isotropic. This leads to simple expressions for the drift and diffusion terms. Hence, the drift term solely contains the temporal decay of the subgrid-scale velocity fluctuations. The diffusion term estimates the intensity of the random process by the subgrid-scale dissipation. Additional terms are added to the Langevin equation in order to prevent so-called spurious drifts (Minier et al., 2014). These drifts cause the non-physical accumulation of the dispersed phase in regions of low velocity fluctuations (Taniére and Arcen, 2014).

Another stochastic model for the framework of LES is provided by Pozorski and Apte (2009), who also assumed homogeneous isotropic turbulence. Compared to the model by Fede et al. (2006), the drift and diffusion terms are extended by Pozorski and Apte (2009) to account for the crossing-trajectory and the continuity effects described by Csanady (1963). The crossing-trajectory effect originates from the fact that particles can leave a certain eddy and enter a new one driven by external forces. This leads to a reduction of the time scales over which the fluid velocities at the particle position are correlated. The continuity effect is related to the crossing-trajectory effect. It occurs when a particle leaves an eddy in the direction perpendicular to the mean relative velocity. According to Csanady (1963) the fluid fluctuations in the new eddy are not correlated to the fluctuations of the previous eddy. Hence, the time scales of the correlations seen by the particles are further shortened. Consequently, both effects influence the temporal decay of the subgrid-scale fluctuations and, thus, should ideally be considered in the subgrid-scale models. However, terms preventing spurious drifts are neglected by Pozorski and Apte (2009). While this can be interpreted as a drawback of this approach, it also leads to a simpler Langevin equation with a lower computational effort for the solution process.

Lastly, the model of Berrouk et al. (2007, 2008) is mentioned, which is based on the models by Minier et al. (2004, 2014) and Minier and Peirano (2001) originally devised for RANS predictions. In contrast to the previous two models, the full fluid velocity seen by the particles is modeled in the approach of Berrouk et al. (2007). The model accounts for both the crossing-trajectory and the continuity effects and includes terms preventing spurious drifts. However, it was annotated by Minier et al. (2014) that one term containing the relative velocity of the particles is missing in the formulation of Berrouk et al. (2007, 2008) for a complete description of the spurious drift effect. Additionally, the diffusion term is more complex here compared with Fede et al. (2006) and Pozorski and Apte (2009). The underlying idea is to include effects of anisotropic, statistically non-stationary turbulence in the modeling of the particle diffusion. Consequently, a significantly more

complex Langevin equation is obtained, which requires more computational effort for its solution.

Additionally, it has to be noted that many subgrid-scale models (e.g., the previously mentioned models by Berrouk et al., 2007, 2008; Fede et al., 2006; Pozorski and Apte, 2009) for the fluid velocity at the position of the particle are formulated under the assumption that the particle motion is aligned with one of the major axes of the Eulerian flow, which is incorrect for arbitrary orientations of the particle motion (Minier et al., 2004, 2014). Another difficulty arises in the context of the solution of the stochastic differential equation. Some of the available solution methods require to fulfill rather severe constraints on the time-step sizes, which can limit the applicability to arbitrary flow configurations.

These issues are approached in Chapter 6, where the presently used subgrid-scale model is presented. Starting from the approach by Pozorski and Apte (2009), which is chosen since it can account for several important effects, while keeping the associated numerical effort low, their approach is extended towards arbitrary orientations of the particle motion. Furthermore, the extended model is formulated in a way that is not constrained by the time-step size. Note that the derivation of the present subgrid-scale model has been previously published in Breuer and Hoppe (2017).

2.2 Bubble Coalescence

Coalescence processes in gas-liquid flows are mostly described by models that can be divided into three categories (Liao and Lucas, 2010): energy-based, critical velocity and film drainage models. Note that it is frequently assumed that the coalescence of gas bubbles and liquid droplets is equivalent (Chesters, 1991; Liao and Lucas, 2010). Consequently, many coalescence models are applied for the description of both bubble and droplet coalescence despite their largely different properties.

2.2.1 Energy-Based Models

Energy-based models (see, e.g., the very prominent one by Sovová, 1981) were mostly devised for the coalescence of droplets. The idea behind this approach is to determine the outcome of a collision based on a comparison of the kinetic energy of the relative motion of the collision partners and their respective surface energy. If the kinetic energy exceeds the surface energies, the collision partners coalesce (Sovová, 1981). Consequently, a high approach velocity associated with a high kinetic energy is favorable for the occurrence of coalescence. However, several authors (see, e.g., Doubliez, 1991; Kirkpatrick and Lockett, 1974; Kosior et al., 2014; Zawala et al., 2007, 2013; Zawala and Malysa, 2011) found experimental evidence that the opposite is true for the case of bubbles. Those authors investigated the impact of a single bubble rising in a quiescent liquid with a free surface. All of them reported that higher impact velocities increase the chance of a rebound from the surface. The experiments by Lehr et al. (2002) described in more detail in the next section support these results. Hence, energy-based models seem to incorrectly capture the dependency of the bubble coalescence on the collision velocity. It has to be remembered

that energy-based models mostly consider the coalescence of droplets. Consequently, one possible explanation for the above described discrepancy is that the coalescence of bubbles and droplets is subject to different physical mechanisms originating from their largely different properties. Hence, the common assumption that the coalescence of bubbles and droplets can be treated by the same models may be inappropriate.

2.2.2 Critical Velocity Models

Critical velocity models (e.g., Lehr et al., 2002) are also based on a velocity threshold. However, here coalescence takes place, if the relative collision velocity is below a certain critical value. In the model by Lehr et al. (2002) the value of the critical velocity is determined experimentally based on high-speed recordings of the coalescence of bubbles dispersed in a downward channel flow of distilled water. The velocity of the liquid flow was adjusted such that the bubbles remained at roughly the same vertical position. This allowed Lehr et al. (2002) to analyze the dependency of the collision outcome on the size of the collision partners and their relative collision velocity. It was found that coalescence occurs at collision velocities below a critical value of $u_{\mathrm{crit}} = 0.08\,\mathrm{m/s}$ independently of the bubble diameter. Hence, this result also contradicts the energy-based models. It has to be noted that the estimation of the critical velocity by Lehr et al. (2002) is based on experimental observations with a limited range of bubble diameters (3×10^{-3} to $8\times10^{-3}\,\mathrm{m}$) and collision velocities (0.02 to 0.26 m/s). Additionally, only the coalescence of bubbles dispersed in clean water is considered. However, it is known that the coalescence of contaminated bubbles is largely different from the coalescence of clean ones (Chesters, 1991; Hartland et al., 1989; Jeelani and Hartland, 1991). Consequently, the application of the model by Lehr et al. (2002) to arbitrary turbulent bubble-laden flows is not appropriate.

2.2.3 Film Drainage Models

The largest group of coalescence models is made up by the so-called film drainage models. A large amount of literature is available for this approach, see, e.g., Liao and Lucas (2010) for an overview. Due to strong simplifications made during the derivation of these models, most of them are restricted to very specific cases. The reason behind these simplifications is the complex physics involved in the coalescence of bubbles.

All film drainage models picture the coalescence by a three-step process (Chesters, 1991):

1. Bubbles collide with a certain relative collision velocity trapping a small amount of liquid between them due to the deformation of the bubble surfaces.

2. The liquid trapped in the gap between the bubbles is forced out by a pressure gradient. Due to the drainage of the liquid, the thickness of the film decreases[1].

3. If the film thickness reaches a critical minimum during a certain period of time, the film separating the bubbles ruptures instantaneously leading to the coalescence of

[1] This is the reason behind the name *film drainage* models.

the bubbles. If the critical thickness is not reached, the deformed bubbles restore their original (spherical) form and separate from each other, i.e., a rebound occurs.

Consequently, coalescence is usually modeled by comparing the two characteristic time scales of the coalescence process, i.e., the time t_c the bubbles are in contact with each other during the collision and the time t_d during which the film thickness is reduced to the critical value allowing coalescence (see, e.g. Chesters, 1991). Note that it is alternatively possible to compare the final value h_f of the film thickness reached by the drainage process during the contact time with a critical film thickness h_{crit}, where the liquid film ruptures. Both approaches are equivalent and one approach can be readily transferred to the other. However, in the literature on bubble coalescence the comparison of the time scales is the more prominent ansatz.

One obvious drawback of nearly all coalescence models available in the literature is that the contact time cannot be estimated based on the coalescence model itself, but a separate model needs to be applied. Thus, additional assumptions and simplifications are introduced to the description of the coalescence process. For example, Sommerfeld et al. (2003) estimated the contact time by the time it takes a bubble with a constant relative collision velocity to travel a certain fraction of the radius of the corresponding collision partner. This fraction was arbitrarily chosen to be 0.5 by Sommerfeld et al. (2003), without any physical motivation behind it. An additional drawback of this approach is that the deceleration of the bubble during the collision is not taken into account. A similar model for the contact time was devised by Chesters (1991). Here, the fraction of the radius is estimated by the conservation of energy balancing the kinetic energy of the bubbles and the surface energy. Lastly, Kamp et al. (2001) refined the model by Chesters (1991) incorporating the deceleration of the bubbles into the energy balance. Thus, an expression for the bubble velocity during the collision process was obtained, which could be used to estimate the contact time including the effect of the deceleration.

Film drainage models are typically divided into approaches describing the coalescence of clean or surfactant-contaminated bubbles (see, e.g., Chesters, 1991; Liao and Lucas, 2010), although some models exist that can treat both types of bubbles, see the later parts of this section. According to Chesters (1991) the surface of clean bubbles is fully mobile, while the surface of contaminated bubbles is fully immobile, see also Section 4.1.1.1 for more details. Consequently, the absence (clean bubbles) or presence (contaminated bubbles) of surfactants affects the type of the boundary condition at the bubble surfaces, i.e., slip or no-slip boundary conditions hold. This results in a different outflow mechanism for the bubbles. The drainage of the liquid trapped between clean bubbles is completely controlled by inertia (Hartland, 1967; Jeffreys and Davis, 1971), while the outflow between contaminated bubbles is mostly dominated by viscous effects (Kirkpatrick and Lockett, 1974). Note that Hartland et al. (1989) demonstrated that the assumption of fully viscous-controlled drainage in the case of contaminated bubbles is incorrect. In reality the outflow is initially controlled by inertia followed by viscous forces after a certain period of time.

The models by Hartland (1967) and Jeffreys and Davis (1971) consider the coalescence of contaminated bubbles with a fully immobile surface. Thus, the drainage of the liquid trapped between the colliding bubbles is controlled by viscosity and the outflow is laminar. The major drawback of both models is that the size of the area the bubbles are in contact

with each other has a not-specified constant value. Consequently, the application of the models by Hartland (1967) and Jeffreys and Davis (1971) requires to set the contact surface to an arbitrary value. This is problematic, since the contact surface is known to vary during the collision (Chesters, 1991; Jeelani and Hartland, 1991; Kamp et al., 2001), i.e., it first increases during the approach and then decreases during the separation of the colliding bubbles.

Later, Sagert and Quinn (1976) extended the models by Hartland (1967) and Jeffreys and Davis (1971) by including the effect of the van-der-Waals force on the drainage process. Additionally, a temporal variation of the contact surface following a power law is proposed. It is further suggested by Sagert and Quinn (1976) to determine the exponents of the power law based on high-speed recordings of coalescence processes. However, the actual form of the power law was not given by Sagert and Quinn (1976). Additionally, the evolution of the contact surface is known to depend on the properties of the flow and the bubbles participating in the collision making the application of the model by Sagert and Quinn (1976) to general bubble-laden flows questionable.

Kirkpatrick and Lockett (1974) proposed a model that is analogous to the models by Hartland (1967) and Jeffreys and Davis (1971) but for the coalescence of clean bubbles. Hence, the drainage is controlled by inertia allowing to describe the outflow by the Bernoulli equation. The major drawback of the models by Hartland (1967) and Jeffreys and Davis (1971) is retained in this approach, i.e., the unknown contact surface still has to be set to an arbitrary value.

One of the most prominent coalescence models (applied, e.g., by Darmana et al., 2006; Jain et al., 2014; Lau et al., 2014; Sommerfeld et al., 2003; Sungkorn et al., 2012) is the one by Prince and Blanch (1990). Due to several simplifications (e.g., neglecting viscosity effects and assuming a time-independent outflow), a drainage equation describing the coalescence of clean bubbles is obtained from the approach by Oolman and Blanch (1986). Note that the resulting drainage equation is identical to the one previously obtained by Kirkpatrick and Lockett (1974). Prince and Blanch (1990) proposed to estimate the unknown diameter of the contact surface by a fraction of the bubble diameter. Yet, a specific value of the fraction is not provided by Prince and Blanch (1990). Consequently, the fraction is set to unity making the contact surface equal to the projected area of the bubble. This probably overestimates the size of the contact surface.

Chesters (1975) devised a more complex coalescence model, which is among the very few that is suitable for the treatment of clean and contaminated bubbles. The approach by Chesters (1975) is based on the integration of the complete momentum equation describing the outflow of the liquid in the radial direction. Consequently, both inertia as well as viscous effects are incorporated in this model allowing to consider the coalescence of clean and contaminated bubbles. Additionally, the transition from a flat to a spherical shape at the edge of the contact surface is included in the modeling, which affects the pressure gradient in the radial direction. However, the size of the contact surface is still assumed to be an arbitrarily chosen constant. Another drawback of the approach by Chesters (1975) is that the resulting second-order differential equation cannot be solved analytically. Hence, only the extreme cases dominated either by inertia or by viscosity are considered yielding drainage equations for the respective cases. Note that Doubliez (1991) proposed

a drainage model based on the approach by Chesters (1975). Several simplifications are introduced by Doubliez (1991) leading to a model that is analytically solvable. However, the drawback of a constant contact surface remains. Additionally, only the case of clean bubbles is considered by Doubliez (1991).

Lastly, the model by Jeelani and Hartland (1991) is mentioned here, which is based on the force balance of the bubbles during the collision process. Different forces acting on the colliding bubbles are considered depending on the boundary condition at the bubble surface. Hence, it is possible to consider both clean and contaminated bubbles. Since the approach of Jeelani and Hartland (1991) incorporates a temporally evolving size of the contact surface, one of the major drawbacks of other coalescence models described above is eliminated. Furthermore, this variation of the contact surface allows to simultaneously estimate the contact time of the colliding bubbles. Thus, it is not necessary to rely on a second model for the contact time. In the approach by Jeelani and Hartland (1991) the drainage of the liquid trapped between clean bubbles is solely controlled by inertia. For contaminated bubbles the outflow transforms from inertia to viscous-controlled after a certain time interval, which was shown by Hartland et al. (1989) to represent the physically correct behavior. Note that this transition time can unfortunately not be determined analytically requiring the application of a numerical root-finding algorithm. In summary, the model by Jeelani and Hartland (1991) incorporates important positive features neglected by most other coalescence models. However, the applicability of the model is limited due to the high computational effort associated with it. Especially the estimation of the transition time interval by a numerical method is a time-consuming process, if a large number of contaminated bubbles is dispersed in the flow.

Hence, the objective of the present thesis is to improve the applicability of the model by Jeelani and Hartland (1991). As described in Chapter 7 and earlier in the work by Hoppe and Breuer (2018), utilizing a suitable and cost-efficient numerical methodology allows to circumvent the necessity to numerically determine the transition time for each collision process. It renders the coalescence model feasible for flows with a large number of bubbles.

2.3 Bubble Breakup

The modeling of the breakup of bubbles is usually categorized based on the physical mechanism responsible for the breakup. According to the reviews by Liao and Lucas (2009) and Solsvik et al. (2013) the following mechanisms exist: surface instabilities, viscous shear stresses due to velocity gradients and stresses due to turbulent fluctuations.

2.3.1 Surface Instabilities

Breakup due to surface instabilities is mainly caused by the Rayleigh–Taylor or the Kelvin–Helmholtz instabilities (Liao and Lucas, 2009; Solsvik et al., 2013). The Rayleigh–Taylor instability arises at the interface of two fluids that differ in their densities. If the less dense fluid pushes the denser one (e.g., when gas bubbles accelerate the fluid surrounding them),

the pushing leads to the formation of spikes of denser fluid penetrating the less dense fluid (Sharp, 1984). A sufficiently strong penetration can cause the rupture of the lighter phase. The Kelvin–Helmholtz instability is the result of a difference in the tangential velocity component across the interface between the two fluids. Tripathi et al. (2015) performed fully-resolved simulations of an initially spherical bubble rising in a quiescent liquid. It was demonstrated that the difference in the tangential velocity causes a deformation of the bubble into a toroidal shape, which ultimately leads to the breakup of the bubble. A second form of breakup related to the Kelvin–Helmholtz instability is the erosive breakup observed for bubbles with the shape of a spherical cap. Here, small daughter bubbles are sheared off from the edge of the deformed bubble (Tripathi et al., 2015). Note that this form of breakup is sometimes listed as a separate mechanism (e.g., in the review by Liao and Lucas, 2009). It has to be mentioned that breakup due to surface instabilities occurs mostly for large, non-spherical bubbles. In the case of small bubbles, surface instabilities typically play no role, since the high surface tension of small bubbles prevents their deformation due to instabilities.

2.3.2 Viscous Shear Stresses

Breakup due to viscous shear stresses originates from the existence of a velocity gradient in the mean flow around the bubbles (Liao and Lucas, 2009). The different fluid velocities at the opposing sides of the bubble lead to the exertion of different stresses at those ends. Consequently, the bubble is distorted from its spherical shape. First, an ellipsoidal bubble shape is obtained, which is then further transformed into a so-called sigmoidal form with thin, pointed tips (Müller-Fischer et al., 2008; Wei et al., 2012). Based on experiments of air bubbles dispersed in a shear flow of silicone oil, Müller-Fischer et al. (2008) demonstrated that small daughter bubbles are ruptured from the pointed tips of the parent bubble. According to these experiments the breakup due to shear stresses can be described by the dimensionless capillary number Ca, which represents the ratio of viscous forces to surface tension forces (Müller-Fischer et al., 2008). If the capillary number exceeds a certain critical value, the erosive breakup occurs. In the experiments by Müller-Fischer et al. (2008) the critical value was found to lie between 30 and 45. Based on two-dimensional Lattice Boltzmann simulations, Wei et al. (2012) estimated the critical capillary number to be roughly 35. However, Wei et al. (2012) predicted that the breakup yields mostly equally-sized daughter bubbles, thus, contradicting the experimental results by Müller-Fischer et al. (2008). Similar to the breakup due to surface instabilities, the breakup due to shear stresses mainly occurs for large bubbles. Small bubbles usually resist the deformation due to viscous shear stresses, since the velocity gradients on the length scale of the bubbles are usually not large enough to overcome the effect of the high surface tension.

2.3.3 Turbulent Velocity Fluctuations

The last breakup mechanism is the breakup due to turbulent velocity fluctuations. The turbulence-induced breakup can be further divided into the breakup due to turbulence in

the viscous and the inertial subrange based on the size of the bubbles. If the bubbles have a size comparable to the viscous subrange of turbulence, they are subjected to the shear stresses of this range. However, according to Hinze (1955) except for low Reynolds numbers the length scales of the viscous subrange are typically very small. Hence, the bubbles are usually larger than the length scales of the viscous subrange and, thus, not affected by the corresponding shear stresses. Consequently, the turbulent fluctuations in the inertial subrange are commonly assumed to be responsible for the bubble breakup. However, note that in several more recent studies (see, e.g., Castellano et al., 2019; Karimi and Andersson, 2019; Solsvik and Jakobsen, 2016a,b) it is proposed to consider the complete spectrum of turbulence for breakup, since fluid particles (droplets or bubbles) largely vary in size.

The physical mechanism responsible for turbulence-induced breakup are the pressure fluctuations associated with the turbulent velocity fluctuations of the fluid flow surrounding the bubbles (Hinze, 1955). These pressure fluctuations lead to a deformation of the bubbles, which are not able to restore their originally spherical shape and break up into smaller fragments, if the deformation is sufficiently strong. The actual deformation of the bubbles is a highly complex process making the prediction of breakup very challenging. The deformation process due to turbulent fluctuations has been investigated both experimentally and numerically, for example by Andersson and Andersson (2006a,b), Qian et al. (2006) and Risso and Fabre (1998). It was observed that the impact of a turbulent eddy on the surface of a bubble deforms the initially spherical bubble to dumbbell-like shape, i.e., the deformed bubble consists of two, usually not equally-sized non-spherical volumes of gas connected by a small neck. According to Andersson and Andersson (2006a) this initial deformation can be followed up by three different outcomes.

Firstly, it is possible that the bubble restores its original spherical shape, i.e., no breakup occurs. Since the volumes of gas making up the ends of the dumbbell-like bubble are usually not of the same size, the surface tension and the different radii of the two ends cause an internal pressure gradient inside the deformed bubble. Hence, a rapid flow from the smaller end through the neck to the larger end of the bubble exists restoring the spherical shape of the bubble. The second possibility is the pinch off of a small daughter bubble during the redistribution of the gas inside the bubble. Due to the backflow, the pressure in the neck is reduced compared with the pressure in the surrounding fluid. Hence, the neck is shrinking making it possible that the neck collapses before the spherical shape of the bubble is fully restored. The resulting daughter bubble typically contains only a small fraction of the gas volume of the parent bubble. The third possible outcome is the direct breakup of the dumbbell-like bubble without any previously occurring backflow. This requires a large enough energy of the turbulent eddy deforming the parent bubble to split the bubble during the deformation process (Andersson and Andersson, 2006a). It has to be remarked that according to Andersson and Andersson (2006a,b), Hesketh et al. (1991a,b), Martínez-Bazán et al. (1999a), Risso and Fabre (1998), Stewart (1995) and Walter and Blanch (1986) bubble breakup due to turbulent fluctuations is typically binary, i.e., two daughter bubbles are formed by the breakup. However, Risso and Fabre (1998), Solsvik and Jakobsen (2015) and Wilkinson et al. (1993) also reported the rare occurrence of breakup into up to ten fragments in their experiments.

Note that in addition to the previously described breakup mechanisms, Risso and Fabre (1998) experimentally observed that bubble breakup can occur due to a resonance mechanism. An eddy hitting a bubble with insufficient turbulent kinetic energy to cause breakup can excite an oscillation of the bubble surface. Subsequent excitations of the oscillating bubble by such eddies can lead to an amplification of the deformation of the bubble. Consequently, the breakup occurs due to the resonance of turbulent eddies and bubble oscillations.

Due to the complex physics involved in the deformation process and the subsequent breakup, the modeling of breakup requires the introduction of several simplifications and assumptions. Firstly, most models (see, e.g., Hagesaether et al., 2002; Lehr et al., 2002; Luo and Svendsen, 1996; Martínez-Bazán et al., 1999a,b; Tsouris and Tavlarides, 1994) apply the aforementioned argument by Hinze (1955) that only velocity fluctuations in the inertial subrange of turbulence contribute to the deformation and, thus, to the breakup. Additionally, it is also assumed that the turbulence is locally isotropic allowing to estimate the fluctuations by a simple relation, see, e.g., the ones by Batchelor (1953) and Hinze (1955). A third common assumption is that only turbulent structures with a size up to the bubble diameter contribute to the breakup. Larger structures only transport the bubbles but do not deform them (Coulaloglou and Tavlarides, 1977), while smaller structures cause small-scaled deformations of the bubble surface but do not contribute to the breakup process (Andersson and Andersson, 2006a). Furthermore, the resonance mechanism by Risso and Fabre (1998) is usually neglected accounting only for the direct breakup of bubbles due to sufficiently strong turbulence. Lastly, only binary breakup is considered.

Typically, breakup models are formulated in form of the dimensionless Weber number We, which relates either the turbulent kinetic energy to the surface energy or analogously the turbulent inertial forces to the surface forces. If the Weber number exceeds a certain critical value $\mathrm{We}_{\mathrm{crit}}$, breakup occurs. In the bubble breakup model by Prince and Blanch (1990) the critical Weber number was a fixed value of $\mathrm{We}_{\mathrm{crit}} = 2.3$, i.e., the turbulent kinetic energy of the fluid fluctuations with a size equal to the bubble diameter has to be larger than a certain fraction of the surface energy of the corresponding bubble. The estimation of the critical Weber number was based on a parameter fit to the experimental results by Bhavaraju et al. (1978), who observed the maximum stable bubble size in a gas-sparged bubble column. Hence, the application of the criterion by Prince and Blanch (1990) is probably not valid for arbitrary turbulent flows. Another difficulty of the approach by Prince and Blanch (1990) is that the sizes of the daughter bubbles has to be estimated based on an arbitrary size distribution.

Tsouris and Tavlarides (1994) proposed that the energy required for breakup is related to the increase of the surface energy due to breakup. The physical mechanism behind this argument is that the total surface of the two daughter bubbles is always larger than the surface of the parent bubble. Hence, the related surface energy of the daughter bubbles is larger as well. The increase of the total surface energy due to breakup is estimated by Tsouris and Tavlarides (1994) based on the mean value of the increase in surface energy resulting from equally-sized breakup and the increase corresponding to unequally-sized breakup into one small and one larger daughter bubble. Note that Tsouris and Tavlarides

(1994) did not motivate this choice in their work. Especially the choice of the daughter bubble sizes in the case of unequally-sized breakup is arbitrary making the application of the model questionable. Again the problem of the estimation of the actual size of the daughter bubbles after breakup remains.

Later, Luo and Svendsen (1996) advanced the approach by Tsouris and Tavlarides (1994) by proposing that the turbulent kinetic energy of the fluctuations has to be equal or larger than the difference in surface energy of the bubbles prior and after breakup. Aside from the improved physical argumentation, the model by Luo and Svendsen (1996) has the major advantage that it also provides the size of the daughter bubbles by relating the turbulent kinetic energy of the bubble-deforming eddies to the diameters of the daughter bubbles. In the work by Luo and Svendsen (1996) it is assumed that the size estimated from the breakup criterion is the upper boundary of the diameter of the smaller daughter bubble. Then the actual size of the smaller daughter bubble is randomly estimated according to a bubble size distribution which is related to the breakup rate of the model. However, it can be shown that the criterion by Luo and Svendsen (1996) can be fulfilled for arbitrary small Weber numbers (Hagesaether et al., 2002). This is caused by the fact that the increase in surface energy tends to zero, if the size of the smaller daughter bubble tends to zero, since then the parent bubble and the larger daughter bubble have nearly the same size. This is usually not a problem in the framework of population balance equations used in Euler–Euler predictions, but makes this ansatz unfeasible for methods relying on the Euler–Lagrange approach where each bubble is tracked individually.

In the model by Martínez-Bazán et al. (1999a,b) breakup occurs, if the turbulent stresses of the velocity fluctuations leading to a deformation of a bubble exceed the surface restoring pressure counteracting the deformation. The turbulent stresses are estimated based on the turbulent kinetic energy of the fluid fluctuations, while the surface restoring pressure is connected to the surface energy of the parent bubble. Since only the diameter of the parent bubble appears in the breakup criterion, the size of the daughters is again estimated based on a random distribution related to the breakup rate of the model. Martínez-Bazán et al. (1999a,b) performed experiments of bubble breakup in a turbulent jet flow and found a good agreement of the model with their experimental results. One problem related to this model is the prediction of breakup even if the turbulent kinetic energy only slightly exceeds the surface stresses required to deform the bubble but not necessarily to break it. Hence, breakup occurs in cases where the associated deformation is rather small. This contradicts the results of experiments by Risso and Fabre (1998) and numerical studies by Qian et al. (2006) on bubble breakup, who stated that a significant minimum deformation of the bubble surface is required for breakup to occur. For example, Risso and Fabre (1998) demonstrated that the surface of the parent bubble increase by at least 50% compared with the surface of the spherical shape prior to breakup. Nevertheless, the model by Martínez-Bazán et al. (1999a,b) has been applied in the Euler–Lagrange predictions by Jain et al. (2014) and Lau et al. (2014). Additionally, it has to be remarked that the aforementioned drawback has been addressed by Martínez-Bazán et al. (2010). Further improvements of the model by Martínez-Bazán et al. (1999a,b, 2010) have been proposed by Solsvik et al. (2017).

A similar approach was chosen by Lehr et al. (2002), who assumed that the turbulent stresses of the fluid deform the bubble into a cylindrical shape. The bubble breaks up at some point of the tube when a necking occurs which contracts. According to Lehr et al. (2002) the surface restoring pressure counteracting the necking is determined by the pressure inside the cylindrical bubble given by the Young–Laplace equation. Consequently, the breakup occurs if the turbulent stresses associated with the deformation process exceed this surface restoring pressure. The model by Lehr et al. (2002) has the advantage that the size of the daughter bubbles can be estimated based on the breakup criterion. However, one drawback of the model is the unphysical assumption of a deformation of the parent bubble into a cylindrical shape. As shown by Risso and Fabre (1998) this assumption by Lehr et al. (2002) does not reflect the real bubble deformation.

Lastly, another breakup criterion was devised by Hagesaether et al. (2002). This model is based on the assumption that the energy density of the turbulent velocity fluctuations deforming the bubble has to be higher or equal to the surface energy of the daughter bubbles. This corresponds to the argument that the deforming turbulent stresses are larger than the surface restoring pressures of the daughter bubbles. Since the restoring pressure acts against the contraction of the neck and, thus, against the breakup of the parent bubble, the assumption by Hagesaether et al. (2002) makes sense from a physical point of view (Andersson and Andersson, 2006a,b; Qian et al., 2006; Risso and Fabre, 1998). Additionally, it is possible to estimate the size of the daughter bubbles based on the breakup criterion making the approach favorable.

Note that in addition to the above criterion Hagesaether et al. (2002) proposed that the criterion by Luo and Svendsen (1996) has to be fulfilled at the same time combining two breakup criteria into one model. Additionally, according to Hagesaether et al. (2002) all turbulent fluctuations up to the size of the parent bubble have to be accounted for the breakup process. This is achieved by integrating over all turbulent scales up to the size of the parent bubble. The idea is that in the case of small-scale turbulent fluctuations the criterion by Hagesaether et al. (2002) yields a lower boundary for the size of the smaller daughter bubble, while the criterion by Luo and Svendsen (1996) provides the upper boundary. The actual size of the daughter bubbles is then randomly chosen between the lower and upper boundary values based on a size distribution that is connected to the breakup criterion. However, the assumption that all turbulent scales up to the size of the parent bubble contribute to breakup contradicts experimental observations by Andersson and Andersson (2006a). If only turbulent velocity fluctuations with a length scale equal to the size of the parent bubble are accounted for, a Weber number fulfilling the criterion by Hagesaether et al. (2002) automatically satisfies the criterion by Luo and Svendsen (1996). Hence, all daughter bubble sizes larger than the lower boundary given by the criterion of Hagesaether et al. (2002) up to equally-sized breakup are possible. In other words, the criterion of Luo and Svendsen (1996) does not play a role in the typically assumed case that only turbulent fluctuations of a scale similar to the size of the parent bubble contribute to breakup. The same reasoning is valid for the model by Wang et al. (2003), who combined the breakup criteria of Luo and Svendsen (1996) and Lehr et al. (2002). Note that for the sake of brevity only a small part of the models available in the literature

is listed here. The interested reader can find a more detailed summary in the extensive review by Solsvik et al. (2013).

Aside from the breakup criterion itself, another critical point of the modeling of the bubble breakup in the Euler–Lagrange framework is the treatment of the daughter bubbles after breakup. Firstly, the diameters of the daughter bubbles have to be estimated. Since only some breakup models (e.g., the ones by Hagesaether et al., 2002; Lehr et al., 2002; Luo and Svendsen, 1996) allow to estimate the sizes directly based on the respective models, often additional models have to be used (see, e.g., Lau et al., 2013). Secondly, the tracking of the individual bubbles requires an axis along which the daughter bubbles separate from each other. Additionally, a corresponding velocity at which they separate has to be estimated. To the best of the author's knowledge, no models exist for both quantities. For example, Jain et al. (2014) and Lau et al. (2014) simply separated the daughter bubbles along an arbitrarily oriented direction. The velocities of the daughter bubbles are set equal to the velocity of the parent bubble, i.e., the separation velocity is assumed to be zero. Lastly, the occurrence of repeated breakups of the same bubble at several successive time steps is a difficulty arising in Euler–Lagrange predictions. This is possible when a large bubble is broken up by strong turbulent fluctuations leading to one small and one large daughter bubble. Under certain circumstances, the larger daughter bubble can fulfill the breakup criterion again in the subsequent time step. Hence, the bubble is further split into two daughter bubbles, where the larger one is only slightly smaller than the previous large daughter bubble. This erosion process is repeated until the breakup criterion cannot be fulfilled anymore leading to a possibly large swarm of small daughter bubbles. Since in such a case the breakup rate is directly proportional to the numerical time-step size applied, the associated breakup rate is unphysically large. Especially in LES, where the time-step sizes are usually quite small, such an artificial erosion may take place very fast.

Except from the estimation of the daughter bubble size, most of the aforementioned difficulties have not been addressed in the literature yet or only in a very simplistic way. The reason for this is that breakup phenomena are mostly treated in the framework of population balance equations in Euler–Euler predictions. Since the dispersed phase is considered by a number density in this approach, the separation axis and velocity of the daughter bubbles is not required. Similarly, the repeated breakup does not pose a difficulty due to the treatment of breakup in form of a breakup rate.

Thus, one major focus of Chapter 8 is the transfer of an adequate breakup criterion to the Euler–Lagrange framework by proposing suitable post-breakup conditions for the daughter bubbles. In Table 2.1 the previously discussed turbulence-induced breakup models are summarized. The critical Weber numbers $\mathrm{We}_{\mathrm{crit}}$ required for breakup are listed together with some comments about advantages and disadvantages of the respective models. It is apparent from Table 2.1 that the model of Hagesaether et al. (2002) has two advantageous properties which the other models cannot necessarily provide. Firstly, the model relies on a reasonable physical mechanism agreeing with experimental and numerical investigations of the deformation and breakup procedure (Andersson and Andersson, 2006a,b; Qian et al., 2006; Risso and Fabre, 1998). Secondly, in the approach of Hagesaether et al. (2002) the size of the daughter bubbles can be deterministically estimated based on the breakup

Tab. 2.1. Overview of well-known breakup models and their critical Weber numbers $\mathrm{We}_{\mathrm{crit}}$, which have to be exceeded for breakup to occur. Additionally, comments about their advantages and disadvantages are made. Note that $d_{\mathrm{b,p}}$ denotes the size of the parent bubble, while $d_{\mathrm{b,s}}$ and $d_{\mathrm{b},\ell}$ are the diameters of the smaller and the larger daughter bubble, respectively. The terms $d_{\mathrm{b,max}}$ and $d_{\mathrm{b,min}}$ represent the arbitrarily chosen diameters generated in the case of unequally-sized breakup in the model by Tsouris and Tavlarides (1994). Table taken from Hoppe and Breuer (2020).

Model	$\mathrm{We}_{\mathrm{crit}}$	Comments
Prince and Blanch (1990)	2.3	Based on specific experiment, hence, not generally valid. No daughter bubble size estimation possible.
Tsouris and Tavlarides (1994)	$6\left[\left(d_{\mathrm{b,max}}^2+d_{\mathrm{b,min}}^2\right)/d_{\mathrm{b,p}}^2-2+2^{\frac{1}{3}}\right]$	Values of $d_{\mathrm{b,max}}$ and $d_{\mathrm{b,min}}$ not specified. No daughter bubble size estimation possible.
Luo and Svendsen (1996)	$12\left[\left(d_{\mathrm{b,s}}^2+d_{\mathrm{b},\ell}^2\right)/d_{\mathrm{b,p}}^2-1\right]$	Daughter size obtainable. Breakup estimated for arbitrary small We (critical for E–L predictions).
Martínez-Bazán et al. (1999a,b)	12	Physical mechanism reasonable, although breakup is estimated for slightly deformed bubbles. No daughter bubble size estimation possible.
Lehr et al. (2002)	$4\,d_{\mathrm{b,p}}/d_{\mathrm{b,s}}$	Daughter size obtainable. Assumption of cylindrical shape not realistic.
Hagesaether et al. (2002)	$12\,d_{\mathrm{b,p}}/d_{\mathrm{b,s}}$	Daughter size obtainable. Physical mechanism reasonable.

criterion, which is not the case for other models like the ones by Martínez-Bazán et al. (1999a,b), Prince and Blanch (1990) and Tsouris and Tavlarides (1994). Based on these considerations the approach by Hagesaether et al. (2002) is chosen in the present thesis as the starting point for the modeling of bubble breakup. As argued above, its application to the Euler–Lagrange framework requires the additional estimation of the separation axis, the separation velocity and the breakup time, which is described in Chapter 8. This work has been published in Hoppe and Breuer (2020).

3 Large-Eddy Simulation Framework

The purpose of this chapter is to provide the theoretical background of large-eddy simulations by describing the corresponding governing equations of the Eulerian fluid phase. Since the numerical simulation of fluids is a vast topic, only a brief overview is given here. For more details on CFD in general and LES in special the reader is referred to the literature, e.g., by Breuer (1998a,b, 2000, 2002), Garnier et al. (2009), Piomelli and Chasnov (1996) and Sagaut (2006).

This chapter starts in Section 3.1 with the derivation of the governing equations of the continuous phase in the framework of LES. The modeling of the subgrid scales not resolved by the large-eddy approach is described in Section 3.2. Lastly, boundary conditions of the continuous phase are given in Section 3.3.

3.1 Governing Equations of the Continuous Phase

The present thesis is concerned with the flow of incompressible Newtonian fluids. Additionally, it is assumed that neither the continuous phase nor the dispersed one is affected by temperature effects. Consequently, the fluid phase is described by the incompressible Navier–Stokes equations without an energy equation, which are given in their dimensionless form by:

$$\frac{\partial u_j}{\partial x_j} = 0, \tag{3.1}$$

$$\frac{\partial u_i}{\partial t} + \frac{\partial (u_i\, u_j)}{\partial x_j} = -\frac{\partial p}{\partial x_i} - \frac{1}{\mathrm{Re}} \frac{\partial \tau_{ij}^{\mathrm{mol}}}{\partial x_j} + f_i, \tag{3.2}$$

$$\text{where} \quad \tau_{ij}^{\mathrm{mol}} = -2\,\mu_{\mathrm{f}}\, S_{ij} \quad \text{with} \quad S_{ij} = \frac{1}{2}\left(\frac{\partial u_i}{\partial x_j} + \frac{\partial u_j}{\partial x_i}\right). \tag{3.3}$$

Equations (3.1) and (3.2) describe the conservation of mass and momentum of the fluid, respectively. Equation (3.3) defines the viscous stress tensor τ_{ij}^{mol}, where the dynamic viscosity $\mu_{\mathrm{f}} = 1$ due to the dimensionless formulation. The variables x_i denote the three spatial directions in a Cartesian frame of reference, while u_i are the components of the velocity in the corresponding directions. Further terms in Eqs. (3.1) to (3.3) are the time t, the pressure p and a momentum source term f_i due to external body forces acting on the fluid. Since the fluid is assumed to be incompressible, the fluid density is $\rho_{\mathrm{f}} = 1$ and,

thus, not present in Eqs. (3.1) and (3.2). The Reynolds number Re characterizes the flow regime and is typically defined by a reference length ℓ'_{ref} and velocity u'_{ref}:

$$\mathrm{Re} = \frac{\rho'_{\mathrm{f}}\, u'_{\mathrm{ref}}\, \ell'_{\mathrm{ref}}}{\mu'_{\mathrm{f}}} = \frac{u'_{\mathrm{ref}}\, \ell'_{\mathrm{ref}}}{\nu'_{\mathrm{f}}}, \tag{3.4}$$

where the prime denotes a dimensional variable. In Eq. (3.4) ρ'_{f} is the density of the fluid and $\nu'_{\mathrm{f}} = \mu'_{\mathrm{f}}/\rho'_{\mathrm{f}}$ is its kinematic viscosity.

The idea behind the large-eddy simulation approach is to remove the small-scale structures of the flow by applying a spatial filter function to the Navier–Stokes equations (Breuer, 2002). Consequently, only the large, energy-carrying structures of the flow are resolved by a LES. The effect of the small-scale structures on the flow has to be accounted for by so-called subgrid-scale models. Different filter functions are available in the literature, e.g., the top-hat, the cut-off and the Gauß filter (see, e.g., Breuer, 2002; Piomelli and Chasnov, 1996). Applying a filter function to the Navier–Stokes equations yields the filtered Navier–Stokes equations:

$$\frac{\partial \overline{u}_j}{\partial x_j} = 0, \tag{3.5}$$

$$\frac{\partial \overline{u}_i}{\partial t} + \frac{\partial (\overline{u_i\, u_j})}{\partial x_j} = -\frac{\partial \overline{p}}{\partial x_i} - \frac{1}{\mathrm{Re}} \frac{\partial \overline{\tau}^{\mathrm{mol}}_{ij}}{\partial x_j} + \overline{f}_i, \tag{3.6}$$

In Eqs. (3.5) and (3.6) the overline denotes a filtered quantity. The typical form (see, e.g., Breuer, 2002; Piomelli and Chasnov, 1996) of the filtered Navier–Stokes equations is obtained by defining the so-called subgrid-scale stress tensor:

$$\tau^{\mathrm{SGS}}_{ij} = \overline{u_i\, u_j} - \overline{u}_i\, \overline{u}_j. \tag{3.7}$$

By inserting Eq. (3.7) into Eq. (3.6) the final form of the governing equations of the fluid in the large-eddy simulation framework is obtained:

$$\frac{\partial \overline{u}_j}{\partial x_j} = 0, \tag{3.8}$$

$$\frac{\partial \overline{u}_i}{\partial t} + \frac{\partial (\overline{u}_i\, \overline{u}_j)}{\partial x_j} = -\frac{\partial \overline{p}}{\partial x_i} - \frac{1}{\mathrm{Re}} \frac{\partial \overline{\tau}^{\mathrm{mol}}_{ij}}{\partial x_j} - \frac{\partial \tau^{\mathrm{SGS}}_{ij}}{\partial x_j} + \overline{f}_i, \tag{3.9}$$

$$\text{where} \quad \overline{\tau}^{\mathrm{mol}}_{ij} = -2\,\mu_{\mathrm{f}}\, \overline{S}_{ij} \quad \text{with} \quad \overline{S}_{ij} = \frac{1}{2}\left(\frac{\partial \overline{u}_i}{\partial x_j} + \frac{\partial \overline{u}_j}{\partial x_i} \right). \tag{3.10}$$

The subgrid-scale stress tensor τ^{SGS}_{ij} describes the influence of the small unresolved scales on the large resolved scales. It is obtained by filtering the non-linear convective momentum fluxes in the Navier–Stokes equations, i.e., the second term on the left side of Eq. (3.2). The subgrid-scale stress tensor can be further decomposed into (Breuer, 2002):

$$\tau^{\mathrm{SGS}}_{ij} = \overline{u_i\, u_j} - \overline{u}_i\, \overline{u}_j = \underbrace{\overline{\overline{u}_i\, \overline{u}_j} - \overline{u}_i\, \overline{u}_j}_{\mathcal{L}_{ij}} + \underbrace{\overline{\overline{u}_i\, u'_j} + \overline{u'_i\, \overline{u}_j}}_{\mathcal{C}_{ij}} + \underbrace{\overline{u'_i\, u'_j}}_{\mathcal{R}_{ij}}. \tag{3.11}$$

The second step in Eq. (3.11) is obtained by noting that the full fluid velocity u_i is comprised of the filtered velocity $\overline{u}_i$ and the subgrid-scale part u_i'. The terms $\mathcal{L}_{ij}$, $\mathcal{C}_{ij}$ and $\mathcal{R}_{ij}$ denote the so-called Leonard, cross-term and subgrid-scale Reynolds stress tensors. According to Breuer (2002) the Leonard term describes the interaction between the large-scale structures of the flow, while the cross-term represents the interaction between the large and the subgrid scales. Lastly, the subgrid-scale Reynolds stress term characterizes the interaction between the unresolved scales of the flow. For more details on the physical meaning of the three terms and their modeling the reader is referred to more in-depth literature, e.g., by Breuer (2002), Garnier et al. (2009) and Piomelli and Chasnov (1996).

Note that in this thesis the filtering is implicit, i.e., no filter function is explicitly applied to the governing equations. Implicit filtering means that the governing equations are formally filtered by the discretization procedure which is equivalent to the application of a top-hat filter with a filter width Δ_i that is equal to the grid spacing h_i (Breuer, 2002). According to Breuer (2002) the major advantages of the implicit filtering are that the approach is readily applicable to curvilinear grids and that the explicit filtering step is avoided, which can lead to difficulties for non-uniform grids. Furthermore, implicit filtering requires a typically eight times lower number of grid points compared with an explicitly filtered LES for the same resolution of the flow structures.

Since the subgrid-scale stress tensor contains unknown quantities, τ_{ij}^{SGS} has to be modeled in order to close Eqs. (3.8) and (3.9). This is typically done by splitting the subgrid-scale stress tensor into an isotropic part $\tau_{ij}^{\mathrm{SGS,i}}$ and an anisotropic, traceless part $\tau_{ij}^{\mathrm{SGS,a}}$ leading to:

$$\tau_{ij}^{\mathrm{SGS}} = \tau_{ij}^{\mathrm{SGS,i}} + \tau_{ij}^{\mathrm{SGS,a}} = \frac{1}{3}\,\delta_{ij}\,\tau_{kk}^{\mathrm{SGS}} + \tau_{ij}^{\mathrm{SGS,a}}, \tag{3.12}$$

The anisotropic part of the subgrid-scale stress tensor has to be modeled. Typical models are explained in Section 3.2. The modeling is often done by eddy-viscosity models which relate the subgrid-scale stress tensor to the traceless deformation tensor $\overline{S}_{ij}$ defined in Eq. (3.10). Hence, the above decomposition of τ_{ij}^{SGS} into an isotropic and an anisotropic part is necessary for reasons of consistency between the stress and the deformation tensor. The isotropic part is usually added to the resolved pressure providing a new pressure variable:

$$\overline{P} = \overline{p} + \frac{1}{3}\,\tau_{kk}^{\mathrm{SGS}}. \tag{3.13}$$

3.2 Subgrid-Scale Modeling

Modeling of the subgrid-scale stress tensor can be done in various ways, see again the works by Breuer (2002), Piomelli and Chasnov (1996) and Sagaut (2006) for more information. Here, two of the most common approaches applied in the present thesis are presented.

3.2.1 Smagorinsky Model

One of the most famous and widely-used subgrid-scale models is the one by Smagorinsky (1963), which belongs to the aforementioned eddy-viscosity models. Based on an assump-

tion by Boussinesq (1878) the anisotropic part of the subgrid-scale stress tensor $\tau_{ij}^{\mathrm{SGS,a}}$ is connected with the filtered strain-rate tensor $\overline{S}_{ij}$ according to:

$$\tau_{ij}^{\mathrm{SGS,a}} = -2\,\mu_{\mathrm{T}}\,\overline{S}_{ij}. \tag{3.14}$$

The proportionality factor μ_{T} appearing in Eq. (3.14) is the turbulent eddy viscosity, which depends on the structure of the turbulence, i.e., it can vary in space and in time. One can show by dimensional analysis (see, e.g., Breuer, 2002) that μ_{T} can be defined by:

$$\mu_{\mathrm{T}} = l^2 \left|\overline{S}_{ij}\right| \quad \text{with} \quad \left|\overline{S}_{ij}\right| = \left(2\,\overline{S}_{ij}\,\overline{S}_{ij}\right)^{\frac{1}{2}}, \tag{3.15}$$

where l is a characteristic length scale. Since in a LES the largest non-resolved scales are of the order of the filter width Δ, the characteristic length can be given by:

$$l = C_{\mathrm{S}}\,\Delta = C_{\mathrm{S}}\,(\Delta V)^{\frac{1}{3}}, \tag{3.16}$$

where C_{S} is the Smagorinsky constant. Its value typically ranges between $0.065 < C_{\mathrm{S}} \leq 0.1$ (Breuer, 2002). In Eq. (3.16) the filter width is approximated by the cubic root of the volume $\Delta V = \Delta x\,\Delta y\,\Delta z$ of the computational cell. This is necessary since the grids applied in a LES are usually not uniform in all three directions. Note that the form of this approximation is arbitrary, i.e., other formulations of the filter width are possible as well (Breuer, 2002).

One drawback of the model by Smagorinsky (1963) occurs in wall-bounded flows, where different flow regimes are present. Since at the walls the fluid fluctuations have to vanish, the subgrid-scale stress has to vanish as well. However, Eq. (3.14) can not ensure such a behavior as $\overline{S}_{ij}$ is typically non-zero near the walls. Hence, the damping function of van Driest (1956) is taken into account in the estimation of the characteristic length scale in wall-bounded flows:

$$\begin{aligned} &l = C_{\mathrm{S}}\,\Delta\,f_{\mathrm{wd}} \\ &\text{with} \quad f_{\mathrm{wd}} = \left[1 - \exp\left(-\frac{y^+}{A^+}\right)^3\right]^{\frac{1}{2}}, \quad y^+ = \frac{u_\tau\,y}{\nu_{\mathrm{f}}} \quad \text{and} \quad A^+ = 25. \end{aligned} \tag{3.17}$$

In Eq. (3.17) ν_{f} is the kinematic viscosity of the fluid, while $u_\tau = \sqrt{\tau_{\mathrm{w}}/\rho_{\mathrm{f}}}$ defines the friction velocity. Note that τ_{w} denotes the wall shear stress.

Additionally, the model by Smagorinsky (1963) has difficulties with the correct estimation of the subgrid-scale stress tensor in transitional flows (Breuer, 2002). Furthermore, it is incapable of accounting for the backscatter effect (Leslie and Quarini, 1979), i.e., the energy transfer from the small scales to the large ones. Despite these drawbacks, the model by Smagorinsky (1963) is very popular, which is related to its simplicity and the stabilizing effect it has on the numerical procedure of a LES (Breuer, 2002).

3.2.2 Dynamic Model by Germano

A more advanced subgrid-scale model is the one by Germano et al. (1991), which is based on the idea to dynamically adjust the parameters of a chosen basis model by evaluating the smallest resolved scales of the flow at every point in space. While in principle any subgrid-scale model can be chosen as the basis, the one by Smagorinsky (1963) is used in the present work. This means that the Smagorinsky '*constant*' C_S is dynamically adjusted and does not have a pre-defined value.

The starting point of the model by Germano et al. (1991) is to filter the governing equations of LES (Eqs. (3.5) and (3.6)) a second time with a so-called test filter of wider filter width $\widetilde{\Delta} > \Delta$. Consequently, the doubly filtered momentum equation reads:

$$\frac{\partial \widetilde{\overline{u}}_i}{\partial t} + \frac{\partial (\widetilde{\overline{u_i}\,\overline{u_j}})}{\partial x_j} = -\frac{\partial \widetilde{\overline{p}}}{\partial x_i} - \frac{1}{\mathrm{Re}} \frac{\partial \widetilde{\overline{\tau}}_{ij}^{\mathrm{mol}}}{\partial x_j}, \tag{3.18}$$

where the tilde denotes doubly filtered quantities. Note that in Eq. (3.18) the term $\overline{f}_i$ describing external forces is dropped for the sake of simplicity. Analogously to definition (3.7) in Section 3.1 a new stress tensor T_{ij}^{SGS} can be defined by:

$$T_{ij}^{\mathrm{SGS}} = \widetilde{\overline{u_i}\,\overline{u_j}} - \widetilde{\overline{u}}_i\,\widetilde{\overline{u}}_j, \tag{3.19}$$

which corresponds to the subgrid-stress obtained by the second filtering with the test filter. Equation (3.19) allows to write the doubly filtered momentum equation (3.18) in the form (Breuer, 2002):

$$\frac{\partial \widetilde{\overline{u}}_i}{\partial t} + \frac{\partial (\widetilde{\overline{u}}_i\,\widetilde{\overline{u}}_j)}{\partial x_j} = -\frac{\partial \widetilde{\overline{p}}}{\partial x_i} - \frac{1}{\mathrm{Re}} \frac{\partial \widetilde{\overline{\tau}}_{ij}^{\mathrm{mol}}}{\partial x_j} - \frac{\partial T_{ij}^{\mathrm{SGS}}}{\partial x_j}. \tag{3.20}$$

Similar to Eq. (3.11), T_{ij}^{SGS} can be further decomposed yielding the resolved turbulent stress tensor L_{ij} defined by:

$$L_{ij} = \widetilde{\overline{u}_i\,\overline{u}_j} - \widetilde{\overline{u}}_i\,\widetilde{\overline{u}}_j, \tag{3.21}$$

which represents the contribution of the scales lying between the original filter width Δ and the test filter width $\widetilde{\Delta}$ related to T_{ij}^{SGS}. According to the Germano identity (Germano et al., 1991) the stress tensor T_{ij}^{SGS} based on the test filter and the original one τ_{ij}^{SGS} are related by:

$$L_{ij} = \underbrace{\left(\widetilde{\overline{u_i}\,\overline{u_j}} - \widetilde{\overline{u}}_i\,\widetilde{\overline{u}}_j\right)}_{T_{ij}^{\mathrm{SGS}}} - \underbrace{\left(\widetilde{\overline{u_i}\,\overline{u_j}} - \widetilde{\overline{u}_i}\,\widetilde{\overline{u}_j}\right)}_{\widetilde{\tau}_{ij}^{\mathrm{SGS}}}. \tag{3.22}$$

Since L_{ij} only contains resolved quantities and can thus be calculated directly, Eq. (3.22) can be used to dynamically determine the Smagorinsky constant C_S. By combining Eq. (3.14) and (3.16) and inserting into Eq. (3.22) one obtains:

$$L_{ij}^{\mathrm{a}} = L_{ij} - \frac{1}{3}\,\delta_{ij}\,L_{kk} = \underbrace{\left(-2\left(C_\mathrm{S}\,\widetilde{\Delta}\right)^2 |\widetilde{\overline{S}}_{ij}|\widetilde{\overline{S}}_{ij}\right)}_{T_{ij}^{\mathrm{SGS,a}}} - \underbrace{\widetilde{\left(-2\left(C_\mathrm{S}\,\Delta\right)^2 |\overline{S}_{ij}|\overline{S}_{ij}\right)}}_{\widetilde{\tau}_{ij}^{\mathrm{SGS,a}}}. \tag{3.23}$$

In Eq. (3.23) L_{ij}^{a} denotes the anisotropic, traceless part of L_{ij}. According to Germano et al. (1991) the term $C_{\mathrm{S}}\,\Delta$ can be factored out despite appearing within the filtering operation by the test filter in the second term on the r.h.s. of Eq. (3.23). Thus, Eq. (3.23) can be written as:

$$L_{ij}^{\mathrm{a}} = -2\,(C_{\mathrm{S}}\,\Delta)^2 \left[\frac{\widetilde{\Delta}^2}{\Delta^2}\,|\widetilde{\overline{S}}_{ij}|\,\widetilde{\overline{S}}_{ij} - \widetilde{|\overline{S}_{ij}|\,\overline{S}_{ij}}\right] = -2\,(C_{\mathrm{S}}\,\Delta)^2\,M_{ij}. \tag{3.24}$$

Since L_{ij}^{a} and M_{ij} are symmetric and traceless tensors, Eq. (3.24) is comprised of five independent components for one unknown quantity making the set of equations overdetermined. Different methods to overcome this problem are available in the literature (see, e.g., Breuer, 2002). In the present thesis the least-squares approach by Lilly (1992) is used. The residual Q of Eq. (3.24) is defined by:

$$\begin{aligned} Q &= \left(L_{ij}^{\mathrm{a}} + 2\,(C_{\mathrm{S}}\,\Delta)^2\,M_{ij}\right)^2 \\ &= L_{ij}^{\mathrm{a}}\,L_{ij}^{\mathrm{a}} + 4\,(C_{\mathrm{S}}\,\Delta)^2\,L_{ij}^{\mathrm{a}}\,M_{ij} + 4\,(C_{\mathrm{S}}\,\Delta)^4\,M_{ij}\,M_{ij}. \end{aligned} \tag{3.25}$$

The optimal value of $(C_{\mathrm{S}}\,\Delta)^2$ is the one that minimizes the residual Q. Taking the derivative of Q with respect to $(C_{\mathrm{S}}\,\Delta)^2$ and setting $\partial(Q)/\partial\,(C_{\mathrm{S}}\,\Delta)^2 = 0$ yields:

$$(C_{\mathrm{S}}\,\Delta)^2 = -\frac{1}{2}\,\frac{L_{ij}^{\mathrm{a}}\,M_{ij}}{M_{mn}\,M_{mn}}, \tag{3.26}$$

which can be used to dynamically determine the Smagorinsky '*constant*' C_{S} from the solution of the LES.

According to Breuer (2002) the dynamic model yields highly instationary values of C_{S} that can vary largely throughout the flow domain. Consequently, by using Eq. (3.26) the estimated eddy viscosity μ_{T} can have very large as well as negative values, which both leads to a destabilization of the numerical solution procedure. In order to counteract this problem, different approaches can be used (see, e.g., Breuer, 2002, for more details). Firstly, it is possible to prevent or at least to restrict the occurrence of eddy viscosities with negative values. This is done by limiting the values the total viscosity μ_{total} can reach:

$$\mu_{\mathrm{total}} = \mu_{\mathrm{T}} + \frac{1}{\mathrm{Re}} = \begin{cases} \max\left(\mu_{\mathrm{total}},\ 0\right), \\ \max\left(\mu_{\mathrm{total}},\ \frac{1}{\mathrm{Re}}\right). \end{cases} \tag{3.27}$$

In Eq. (3.27) the first option restricts the total viscosity to positive values, while the eddy viscosity may still become negative. The second option prevents negative values of μ_{T} itself. A second option reducing numerical instabilities is the averaging of the enumerator and the denominator of Eq. (3.26). Especially in flows containing homogeneous directions (e.g., the streamwise and spanwise directions of a channel flow), the averaging in those homogeneous directions is a viable option. Lastly, in the case of inhomogeneous flows a

low-pass filter can be used to remove high-frequency oscillations of $C_\mathrm{S}\,\Delta$. The filter used in this thesis is of the form:

$$(C_\mathrm{S}\,\Delta)^2_{\mathrm{f},n+1} = (1-\epsilon)\,(C_\mathrm{S}\,\Delta)^2_{n+1} + \epsilon\,(C_\mathrm{S}\,\Delta)^2_{n}, \tag{3.28}$$

with the indices n and $n+1$ denoting the last and the present time step and the subscript f indicating the filtered value of $C_\mathrm{S}\,\Delta$. According to Breuer (2002) a filter parameter ϵ of $\mathcal{O}(10^{-3})$ is sufficient to remove all high-frequency oscillations.

To conclude this section, some additional remarks on the dynamic model by Germano et al. (1991) are given. As already mentioned, the main advantage of the dynamic model is that the Smagorinsky constant can now be determined based on the local flow structure and does not have to be pre-defined. The only adjustable parameter of the model is the width $\widetilde{\Delta}$ of the test filter, where $\widetilde{\Delta}/\Delta = 2$ has been found to be optimal (Breuer, 2002). Hence, this ratio is adopted in the present thesis as well. Lastly, an additional advantage is that in contrast to the model by Smagorinsky (1963) no special treatment of the near-wall regions is required, i.e., $(C_\mathrm{S}\,\Delta)^2$ automatically vanishes at the wall due to L^a_{ij} approaching zero.

3.3 Boundary Conditions

Since the Navier–Stokes equations are elliptical in space, the solution of Eqs. (3.8) to (3.10) requires the definition of appropriate conditions at the boundaries of the computational domain. In this section only the boundary conditions used in the framework of this thesis are covered. For a more detailed overview the reader is referred to the literature, e.g., by Breuer (2002).

3.3.1 Wall Boundary Conditions

In turbulent flows bounded by solid walls the no-slip condition holds at the walls, i.e., the fluid adheres to the wall. Consequently, the tangential velocity components of the fluid have to be equal to the velocity of the wall. If the wall is impermeable and not moving in the wall-normal direction, which is always assumed in this thesis, the normal component of the fluid velocity is zero. Hence, the boundary condition for the fluid velocity at the walls is:

$$\overline{u}_i\big|_{\boldsymbol{x}_\mathrm{w}} = u_{\mathrm{w},i}, \tag{3.29}$$

where $u_{\mathrm{w},i}$ is the velocity of the wall at the position $\boldsymbol{x}_\mathrm{w} = (x_\mathrm{w}, y_\mathrm{w}, z_\mathrm{w})$ of the wall. The boundary condition defined by Eq. (3.29) is also known as no-slip condition. It belongs to the class of Dirichlet boundary conditions (Schäfer, 2006).

The implication of using Eq. (3.29) in a LES has been discussed in detail, for example by Baggett et al. (1997), Breuer (2002) and Piomelli and Chasnov (1996). In short, the no-slip boundary condition requires that the fluid in the vicinity of the wall is well resolved by a fine-enough grid, i.e., $\gtrsim 5$ grid points are needed in the viscous sublayer (Breuer, 2002). These restrictions reduce the applicability of wall-resolved LES to moderate Reynolds

numbers. Since the present thesis is solely concerned with such flows, enforcing Eq. (3.29) at the walls is still possible. In the case of high-Re flows the use of wall models, which try to approximate the flow structures in the near-wall region, is an option. Among the most prominent wall models are the ones by Piomelli et al. (1989), Schumann (1975) and Werner and Wengle (1993), which are described in more details in the works by Breuer (2002), Breuer et al. (2006b), Piomelli (2008) and Piomelli and Balaras (2002).

3.3.2 Free Surface Conditions

Since flows bounded by a free surface require the determination of the location of the moving boundary, the simulation of such flows is highly challenging and, thus, beyond the scope of this thesis. Here, several simplifications will be used. Firstly, it is assumed that the form of the free surfaces remains unchanged throughout the simulation. Furthermore, the surface is restricted to be of planar form yielding curvature effects negligible. Lastly, the influences of the surface tension and of the viscosity are neglected as well. Under these assumptions it can be shown (Breuer, 2002) that the kinematic and dynamic boundary conditions at a free surface reduce to a symmetry boundary condition:

$$\overline{u}_{\mathrm{n}} = 0 \tag{3.30}$$

$$\frac{\partial \overline{u}_{\mathrm{t}_{1/2}}}{\partial n} = 0. \tag{3.31}$$

In Eqs. (3.30) and (3.31) u_{n} and $\partial/\partial n$ denote the fluid velocity and the gradient in the direction normal to the free surface. The components $u_{\mathrm{t}_{1/2}}$ are the fluid velocities in the two directions tangential to the surface. In other words, Eqs. (3.30) and (3.31) prevent that the fluid flows through the free surface boundary, while it may freely flow along the surface.

3.3.3 Inflow Conditions

Since solving the governing equations is done inside a finite computational domain, which usually only comprises the area of interest (for example, the region shortly downstream of a jet nozzle or in the vicinity of a hemisphere), the size of the domain has to be restricted. Consequently, an artificial cut through the flow domain is made leading to the problem of defining appropriate inflow conditions at the generated boundaries. Again different options are available (see, e.g., Breuer, 2002). One possibility is to generate suitable inflow conditions by a complementary simulation using the simpler periodic boundary conditions described in Section 3.3.5. For example, the inflow conditions of a jet flow can be determined by the auxiliary simulation of a pipe flow. A second option is the use of a synthetic turbulence inflow generator (STIG). In general, several options are available in the literature to artificially generate inflow conditions. In the lab of *PfS* a digital filter based inflow generator, which was devised by Klein et al. (2003) and later extended by Schmidt and Breuer (2015), is often applied.

In the present thesis a simpler option is chosen, i.e., inflow conditions are obtained by prescribing a mean velocity profile at the boundary:

$$\overline{u}_i\left(x_i,\, t\right) = \langle u_i\left(x_i\right)\rangle, \tag{3.32}$$

where x_i are the coordinates of the boundary and $\langle\centerdot\rangle$ denotes an average. The use of such an inflow condition is valid in cases where turbulent velocity fluctuations are of minor importance for the flow development. Otherwise, the simulated flow field downstream of the inflow boundary is estimated incorrectly. One example, where the application of Eq. (3.32) is prominent and yields good results, is the simulation of a jet flow (see, e.g., Bogey and Bailly, 2006, 2010; Gohil et al., 2011, 2014). Note that the velocities defined by Eq. (3.32) can be superimposed by artificial velocity fluctuations in order to accelerate the development of turbulence. However, the definition of realistic fluctuations is often difficult. Consequently, this is not done in the present thesis.

3.3.4 Outflow Conditions

Since the fluid field is usually unknown at the outflow boundary, the fluid has to be approximated in a physically meaningful way. Here, the problem arises that the outflow boundary can affect the flow in the computational domain by disturbances that travel upstream. Hence, the outflow boundary should be always located far enough downstream of the region of interest. Furthermore, reasonable outflow boundary conditions have to be used. According to Breuer (2002) the convective boundary condition is appropriate for LES:

$$\frac{\partial \overline{u}_i}{\partial t} + u_{\mathrm{conv}} \left.\frac{\partial \overline{u}_i}{\partial \chi}\right|_{\mathrm{outflow}} = 0. \tag{3.33}$$

In Eq. (3.33) $\partial/\partial\chi$ denotes the gradient in the direction of the convective velocity u_{conv}, which has to be chosen based on the problem. One way to estimate u_{conv} is based on the conservation of mass, i.e., the mass flow based on u_{conv} and the area of the outflow boundary should be equal to the mass flow at the inflow boundary. In the present thesis an outflow boundary is used for the simulation of a jet flow. Here, the convective velocity is based on the average centerline velocity of the free jet flow at a distance from the nozzle corresponding to the location of the outflow boundary.

3.3.5 Periodic Boundary Conditions

A special type of boundary conditions are the periodic boundary conditions, which are applicable in flows with homogeneous directions, i.e., directions in which the statistically averaged fluid properties do not vary. Prominent examples of homogeneous directions are the streamwise and spanwise directions of a channel flow. The idea behind periodic boundary conditions is to set the fluid properties at two corresponding boundaries equal to each other:

$$\overline{u}_i\left(x_i,\, t\right) = \overline{u}_i\left(x_i + L_i,\, t\right). \tag{3.34}$$

In Eq. (3.34) L_i is a vector comprised of the extensions of the computational domain in the homogeneous directions. The application of Eq. (3.34) requires that the two-point correlations of the turbulent fluctuations tend to zero within $L_i/2$ (Kim et al., 1987; Piomelli and Chasnov, 1996).

Since in pipe or channel flows the pressure has to decrease in streamwise direction, the pressure can not simply be assumed to be periodic. One way to solve this issue is to split the pressure gradient into an averaged part and a fluctuating one. The fluctuating part can be assumed to be periodic. The average pressure gradient can be treated in two ways. It is either set to a fixed value, which especially in LES leads to a temporally varying mass flow (Breuer, 2002). A second option is to estimate the average pressure gradient by a time-dependent forcing term f_i, where the index i denotes the spatial direction in which the corresponding pressure gradient acts. Based on an idea by Benocci and Pinelli (1990) the discrete forcing term f_i^{n+1} of the present time step is given by:

$$f_i^{n+1} = f_i^n + \frac{\alpha}{\Delta t}\left(u_{\text{mean}}^0 + u_{\text{mean}}^n - 2\,u_{\text{mean}}^{n+1}\right), \tag{3.35}$$

where $\alpha = 0.3$ is an under-relaxation factor and Δt is the size of the time step. The forcing term of the previous time step is denoted by f_i^n, while u_{mean}^{n+1} and u_{mean}^n are the mean velocities of the present and the last time step. Finally, u_{mean}^0 denotes the mean velocity aimed for. Hence, Eq. (3.35) describes a simple control mechanism, which regulates the mass flow by varying the pressure gradient.

4 Lagrangian Particle Tracking

This chapter explains the Lagrangian tracking of the dispersed phase through the liquid flow field. As already mentioned in Section 1.2 the bubbles are tracked individually through the continuous flow by a point-particle approach, i.e., the bubbles are not fully resolved by the numerical scheme. Consequently, analytical expressions of the forces acting on the bubbles are required, which are presented in Section 4.1 including the corresponding basic assumptions made for their derivation. Section 4.2 describes how bubbles are treated upon reaching a boundary of the computational domain. Note that in this chapter only the governing equations of motion of the individual bubble are described. Effects like the interaction of the bubbles with the fluid or with each other are explained separately in Chapter 5.

4.1 Governing Equations of the Dispersed Phase

The present thesis relies on a Lagrangian approach to determine the evolution of the dispersed phase. Since this thesis is mainly concerned with bubbles, in the following only the term bubble is used. However, in general most of the considerations below are also valid for droplets or solid particles. Note that in the two latter cases several simplifications can be made in the description of the dispersed phase (see, e.g., Alletto and Breuer, 2012; Almohammed and Breuer, 2019), which are not appropriate for bubbles.

The motion of any body is determined by solving its equation of motion, which is given by Newton's second law. Accordingly, the change of translational momentum of a single bubble is equal to the sum of all forces $\boldsymbol{F}_{\mathrm{b},i}$ acting on it:

$$m_{\mathrm{b}} \frac{\mathrm{d}\boldsymbol{u}_{\mathrm{b}}}{\mathrm{d}t} = \sum_i \boldsymbol{F}_{\mathrm{b},i} \,. \tag{4.1}$$

In Eq. (4.1) the vector $\boldsymbol{u}_{\mathrm{b}}$ represents the translational velocity of the bubble, while m_{b} denotes its mass. Eq. (4.1) provides a relation for the velocity of each individual bubble from which the positions $\boldsymbol{x}_{\mathrm{b}}$ of the bubbles can be determined by:

$$\frac{\mathrm{d}\boldsymbol{x}_{\mathrm{b}}}{\mathrm{d}t} = \boldsymbol{u}_{\mathrm{b}} \,. \tag{4.2}$$

Hence, predicting the motion of the dispersed phase requires the knowledge of the sum of forces, which is provided in Section 4.1.1. Note that the mass m_b of a spherical bubble and the mass m_f of the fluid displaced by it are given by the well-known formulas:

$$m_\mathrm{b} = \rho_\mathrm{b} V_\mathrm{b} = \rho_\mathrm{b} \frac{\pi}{6} d_\mathrm{b}^3 \,, \tag{4.3}$$

$$m_\mathrm{f} = \rho_\mathrm{f} V_\mathrm{b} = \rho_\mathrm{f} \frac{\pi}{6} d_\mathrm{b}^3 \,, \tag{4.4}$$

where ρ_b and ρ_f are the densities of the bubble and the fluid. Equation (4.4) is required in several forces, see, e.g., Sections 4.1.1.2 to 4.1.1.5.

In contrast to solid particles where the rotational motion plays an important role due to the Magnus lift force (see, e.g., Alletto and Breuer, 2012, 2013b), the rotation of bubbles can be neglected. The physical reason behind this is the vanishing moment of inertia $I_\mathrm{b} = 0.1\, m_\mathrm{b}\, d_\mathrm{b}^2$ given by the small mass m_b of the gas bubbles. Due to the small moment of inertia the bubbles immediately adapt to changes of the rotation of the surrounding fluid. Hence, virtually no relative rotation between the bubbles and the fluid exists, which is the driving factor of the Magnus lift.

4.1.1 Force Balance

In principle, the forces can be divided into external forces and forces caused by the fluid surrounding the bubbles. While the first type of forces are due to external mechanisms (e.g., gravitational forces or the Lorentz force in the case of electrically charged particles inside an electro-magnetic field), the fluid forces are caused by fluid stresses acting on the surfaces of the bubbles (Gatignol, 1983; Maxey and Riley, 1983). Hence, the evaluation of the latter requires a detailed knowledge of the fluid velocities and the associated stresses on the surface of the bubble. As already argued in the introduction (Section 1.2), fully-resolved simulations are only possible for relatively small Reynolds numbers and a small number of bubbles.

However, the fluid forces on the bubbles can be determined analytically if the assumption of the point-particle approach holds. According to Balachandar and Eaton (2010) the point-particle approach holds for bubble sizes much smaller than the smallest resolved scales in a LES. Hence, the bubble diameter has to be smaller than the grid spacing, i.e., $d_\mathrm{b} \ll h_i$. Under this condition the ambient flow surrounding the bubble remains nearly uniform on the order of $\mathcal{O}(d_\mathrm{b})$ and it can be assumed that the disturbances caused by the presence of the bubbles decay within a length scale smaller than the grid spacing. Then, in the limit of Stokes flow around a single, spherical entity of the dispersed phase ($\mathrm{Re}_\mathrm{b} \ll 1$) Gatignol (1983) and Maxey and Riley (1983) have derived an expression for the forces $\boldsymbol{F}_{\mathrm{b},i}$. Note that both Gatignol (1983) and Maxey and Riley (1983) considered irrotational flow. Hence, the lift force caused by rotations was not present in their expressions. However, the lift can be readily added to the sum of forces (Balachandar and Eaton, 2010; Magnaudet and Eames, 2000) yielding the expression of the forces on a spherical bubble used in this thesis:

$$\sum_i \boldsymbol{F}_{\mathrm{b},i} = \boldsymbol{F}_\mathrm{D} + \boldsymbol{F}_\mathrm{G} + \boldsymbol{F}_\mathrm{B} + \boldsymbol{F}_\mathrm{L} + \boldsymbol{F}_\mathrm{AM} + \boldsymbol{F}_\mathrm{PG} \,. \tag{4.5}$$

In Eq. (4.5) the appearing forces are the drag force $\boldsymbol{F}_\mathrm{D}$, the gravity force $\boldsymbol{F}_\mathrm{G}$, the buoyancy force $\boldsymbol{F}_\mathrm{B}$, the lift force $\boldsymbol{F}_\mathrm{L}$, the added-mass force $\boldsymbol{F}_\mathrm{AM}$ and the pressure gradient force $\boldsymbol{F}_\mathrm{PG}$, which are explained in more detail in Sections 4.1.1.1 to 4.1.1.5. The Basset history force $\boldsymbol{F}_\mathrm{BH}$ also appearing in the relations by Gatignol (1983) and Maxey and Riley (1983) is commonly neglected in Euler–Lagrange predictions due to the huge computational effort associated with it, although this may not be entirely justified for the case of bubbles (see Section 4.1.1.6 for a more detailed discussion). Additionally, the effect of the Brownian motion on the bubbles is assumed to be small.

Two further remarks have to be made on the basic assumptions of the point-particle approach used to derive Eq. (4.5). Firstly, the rather harsh restriction to Stokes flow around the bubbles can be extended towards flow problems with $\mathrm{Re}_\mathrm{b} > 1$ by the use of empirical relations for the forces, see Sections 4.1.1.1 and 4.1.1.3. Secondly, the assumption of the bubbles being small compared with the grid spacing can be problematic. One example where the size of the bubbles may become critically large are wall-bounded flows. As already mentioned in Section 3.3.1 a wall-resolved LES requires fine grid resolutions in the vicinity of the walls. Thus, the ratio of bubble diameter to grid spacing can become large. It was shown by Horwitz and Mani (2016) that in this case the relations used to estimate the drag coefficient become inaccurate making the prediction of the bubble movement erroneous.

4.1.1.1 Drag Force

The drag force is caused by the friction the surrounding fluid exerts on the bubble and the pressure difference between the front and the backside produced by the flow around a sphere (Maxey and Riley, 1983). The drag is determined based on the well-known formula:

$$\boldsymbol{F}_\mathrm{D} = C_\mathrm{D}\,\frac{\rho_\mathrm{f}}{2}\,A_\mathrm{b}\,|\boldsymbol{u}_\mathrm{f} - \boldsymbol{u}_\mathrm{b}|\,(\boldsymbol{u}_\mathrm{f} - \boldsymbol{u}_\mathrm{b})\,. \tag{4.6}$$

with the bubble velocity $\boldsymbol{u}_\mathrm{b}$ and its diameter d_b. The terms ρ_b and $\boldsymbol{u}_\mathrm{f}$ denote the density of the fluid and its velocity at the position of the center of the bubble. $A_\mathrm{b} = \pi\, d_\mathrm{b}^2/4$ is the projected area of the bubble. Hence, the drag force acts against the direction of the relative velocity $\boldsymbol{u}_\mathrm{rel} = \boldsymbol{u}_\mathrm{f} - \boldsymbol{u}_\mathrm{b}$, which is also often called the slip velocity.

The term C_D denotes the drag coefficient, which is known to depend on two distinctive effects, i.e., the boundary condition at the bubble surface and the shape of the bubble (Clift et al., 1978; Tomiyama et al., 1998). The boundary condition holding at the bubble surface can vary based on the level of contamination of the fluid with surfactants. In the case of bubbles dispersed in pure fluids, which are not contaminated by small surfactants, the boundary condition is a free-slip one. According to Dijkhuizen et al. (2010) and Tomiyama et al. (1998) the physical reason behind this is that the fluid flow over the surface of the bubbles induces an internal circulation of the gas inside the bubbles, i.e., the bubble surface is mobile. However, if the fluid contains surfactants, these impurities will adhere to the surface of the bubbles (Dijkhuizen et al., 2010; Tomiyama et al., 1998). Thus, a solid, immobile interface as observed for solid particles is mimicked by the accumulating contaminants. In order to account for the two distinctive boundary conditions possible

for bubbles, the formulation of the drag coefficient $C_{\mathrm{D,Re}}$ has to distinguish between clean and contaminated bubbles:

$$C_{\mathrm{D,Re}} = \begin{cases} C_{\mathrm{D,clean}} & \text{for clean bubbles,} \\ C_{\mathrm{D,cont.}} & \text{for contaminated bubbles.} \end{cases} \tag{4.7}$$

Different relations are used to estimate the drag coefficients of clean and contaminated bubbles, $C_{\mathrm{D,clean}}$ and $C_{\mathrm{D,cont.}}$, respectively.

In the present thesis the drag coefficient proposed by Mei and Klausner (1992) is used for clean, spherical bubbles:

$$C_{\mathrm{D,clean}} = \frac{16}{\mathrm{Re_b}}\,\alpha' \quad \text{with} \quad \alpha' = 1 + 2\left[1 + \frac{16}{\mathrm{Re_b}} + \frac{3.315}{\sqrt{\mathrm{Re_b}}}\right]^{-1}. \tag{4.8}$$

In both Eqs. (4.8) and (4.12) the bubble Reynolds number $\mathrm{Re_b}$ is defined by:

$$\mathrm{Re_b} = \frac{|\boldsymbol{u}_\mathrm{f} - \boldsymbol{u}_\mathrm{b}|\, d_\mathrm{b}}{\nu_\mathrm{f}}. \tag{4.9}$$

According to Mei and Klausner (1992) the correction factor α' extends the validity of the drag coefficient $C_{\mathrm{D,clean}}$ towards bubble Reynolds numbers of up to $\mathrm{Re_b} \leq 1000$. Note that Eq. (4.8) approaches the asymptotic behavior for small and large bubble Reynolds numbers given by Golovin and Ivanov (1971) and Moore (1963), respectively. On the one hand, for small bubble Reynolds numbers Eq. (4.8) tends to the relation by Golovin and Ivanov (1971):

$$C_{\mathrm{D,clean}}^{\mathrm{small}} = \frac{16}{\mathrm{Re_b}} + 2, \tag{4.10}$$

obtained by the analytical solution of the drag force acting on a clean, spherical bubble owing to the steady flow of a viscous fluid. Golovin and Ivanov (1971) demonstrated that Eq. (4.10) agrees well with experimental results up to $\mathrm{Re_b} \leq 5$. On the other hand, Eq. (4.8) follows the expression by Moore (1963) for large Reynolds numbers:

$$C_{\mathrm{D,clean}}^{\mathrm{large}} = \frac{48}{\mathrm{Re_b}}\left(1 - \frac{2.21}{\mathrm{Re_b^{\frac{1}{2}}}}\right). \tag{4.11}$$

Equation (4.11) is analytically derived for a steady flow of a liquid of small viscosity around a clean bubble and was shown to agree well with experimental results for $\mathrm{Re_b} \geq 50$.

In the case of surfactant-contaminated, spherical bubbles the drag coefficient for Stokes flow around a rigid sphere is applicable (Aybers and Tapucu, 1969; Tomiyama et al., 1998). Hence, the relation:

$$C_{\mathrm{D,cont.}} = \frac{24}{\mathrm{Re_b}}\,\alpha \quad \text{with} \quad \alpha = 1 + 0.15\,\mathrm{Re}_b^{0.687} \tag{4.12}$$

is used. The coefficient α is given by Schiller and Naumann (1933) and extends the validity of Eq. (4.12) towards larger bubble Reynolds numbers up to $\mathrm{Re_b} \leq 800$. Note that in typical flow problems contaminated bubbles are far more commonly encountered than clean ones, which only occur in liquids that have been carefully purified (Aybers and Tapucu, 1969; Dijkhuizen et al., 2010; Duineveld, 1995).

The second effect influencing the drag coefficient is that bubbles do not necessarily preserve their spherical form. Especially, a too large bubble size or a too small surface tension lead to a distortion from a sphere. For example, according to the bubble shape regimes shown by Clift et al. (1978) air bubbles in water remain spherical for $d_\mathrm{b} \lesssim 1.3\,\mathrm{mm}$. In the present thesis the effect of small deviations from the spherical form is described by a model by Dijkhuizen et al. (2010), who proposed the relation:

$$C_{\mathrm{D,Eo}} = \frac{4\,\mathrm{Eo}}{\mathrm{Eo} + 9.5} \tag{4.13}$$

based on a DNS of a flow around a slightly non-spherical bubble. In Eq. (4.13) the variable Eo denotes the Eötvös number, which relates the gravity force to the surface tension force and is defined by (Clift et al., 1978):

$$\mathrm{Eo} = \frac{g\,(\rho_\mathrm{f} - \rho_\mathrm{b})\,d_\mathrm{b}^2}{\sigma} \tag{4.14}$$

with the gravitational acceleration g and the surface tension σ of the bubbles.

Following an idea by Dijkhuizen et al. (2010) the effects of the boundary condition and the bubble shape are accounted for by combining the drag coefficients $C_{\mathrm{D,Re}}$ and $C_{\mathrm{D,Eo}}$ according to:

$$C_\mathrm{D} = \left(C_{\mathrm{D,Re}}^2 + C_{\mathrm{D,Eo}}^2\right)^{\frac{1}{2}}, \tag{4.15}$$

yielding the total drag coefficient C_D applied in Eq. (4.6).

4.1.1.2 Gravity and Buoyancy Force

The gravity force $\boldsymbol{F}_\mathrm{G}$ originates from the fact that bubbles like all bodies with a certain mass are affected by the gravitational field of the earth. Hence, the gravity force acts in the direction of the gravitational acceleration $\boldsymbol{g}$ and is proportional to the mass m_b of the bubbles. The buoyancy force $\boldsymbol{F}_\mathrm{B}$ is closely related to the gravity force. It is known that the gravitational acceleration leads to an increasing pressure in the direction of $\boldsymbol{g}$ in the fluid. Consequently, a pressure difference between the top and the bottom of a bubble arises, which according to the principle of Archimedes leads to a force proportional to the mass m_f of the displaced fluid, which is directed opposite to the direction of $\boldsymbol{g}$. Due to their similar form, the two forces can be readily combined resulting in the expression:

$$\boldsymbol{F}_\mathrm{G+B} = \boldsymbol{F}_\mathrm{G} + \boldsymbol{F}_\mathrm{B} = m_\mathrm{b}\,\boldsymbol{g} - m_\mathrm{f}\,\boldsymbol{g} = m_\mathrm{b}\left(1 - \frac{\rho_\mathrm{f}}{\rho_\mathrm{b}}\right)\boldsymbol{g}. \tag{4.16}$$

In contrast to solid particles, the buoyancy force dominates by far in Eq. (4.16) due to $\rho_\mathrm{f}/\rho_\mathrm{b} \gg 1$. Thus, the gravity force could in principle be neglected in Eq. (4.5). Since the combined treatment by Eq. (4.16) is computationally cheap, gravity is retained nevertheless.

4.1.1.3 Lift Force

If the bubbles are suspended in a shear flow, the different velocity distributions on the opposing halves of the bubble surfaces yield different pressures and stresses on both sides. Hence, the bubble exhibits a lift force $\boldsymbol{F}_\mathrm{L}$ normal to the relative velocity $\boldsymbol{u}_\mathrm{f} - \boldsymbol{u}_\mathrm{b}$ of the bubble and the vorticity $\boldsymbol{\omega}_\mathrm{f}$ of the fluid. In the present thesis the formulation of the lift force is given by Auton (1987) and Auton et al. (1988):

$$\boldsymbol{F}_\mathrm{L} = C_\mathrm{L}\, m_\mathrm{f}\, (\boldsymbol{u}_\mathrm{f} - \boldsymbol{u}_\mathrm{b}) \times \boldsymbol{\omega}_\mathrm{f}, \tag{4.17}$$

where the vorticity vector is given by the rotation of the fluid velocity, i.e., $\boldsymbol{\omega}_\mathrm{f} = \mathrm{rot}\, \boldsymbol{u}_\mathrm{f} = \nabla \times \boldsymbol{u}_\mathrm{f}$. Various models for the lift coefficient C_L exist in the literature, e.g., the ones by Auton et al. (1988), Kurose and Komori (1999) and Tomiyama et al. (2002). In the present thesis the expression by Legendre and Magnaudet (1998) is used, since it is valid for a wide range of bubble Reynolds numbers up to $\mathrm{Re}_\mathrm{b} \leq 500$. Additionally, this approach can describe both clean and contaminated bubbles. Based on fully-resolved simulations of a linear shear flow around spherical bubbles, Legendre and Magnaudet (1998) obtained two different lift coefficients $C_\mathrm{L,high}$ and $C_\mathrm{L,low}$ by considering the cases of large ($\mathrm{Re}_\mathrm{b} > 5$) and low bubble Reynolds numbers ($\mathrm{Re}_\mathrm{b} \leq 1$). The numerically determined lift coefficients are:

$$C_\mathrm{L,high} = \frac{1}{2} \times \frac{1 + 16\,\mathrm{Re}_\mathrm{b}^{-1}}{1 + 29\,\mathrm{Re}_\mathrm{b}^{-1}} \qquad \text{for} \quad 5 < \mathrm{Re}_\mathrm{b} \leq 500, \tag{4.18}$$

$$C_\mathrm{L,low} = C_\mathrm{L,b}\, (\mathrm{Re}_\mathrm{b}\, \mathrm{Sr})^{-\frac{1}{2}}\, J' \qquad \text{for} \quad \mathrm{Re}_\mathrm{b} \leq 1. \tag{4.19}$$

According to Legendre and Magnaudet (1998) the constant pre-factor $C_\mathrm{L,b}$ appearing in Eq. (4.19) varies based on the boundary condition holding at the bubble surface, i.e., based on the cleanliness or contamination of the surface:

$$C_\mathrm{L,b} = \begin{cases} \dfrac{6}{\pi^2} & \text{for clean bubbles,} \\[2ex] \dfrac{27}{2\,\pi^2} & \text{for contaminated bubbles.} \end{cases} \tag{4.20}$$

The variable Sr denotes the dimensionless shear rate over the size of the bubbles, which is defined by the ratio of the absolute values of the vorticity and the relative velocity:

$$\mathrm{Sr} = \frac{|\nabla \times \boldsymbol{u}_\mathrm{f}|}{|\boldsymbol{u}_\mathrm{f} - \boldsymbol{u}_\mathrm{b}|}\, d_\mathrm{b}. \tag{4.21}$$

The empirical relation J' is defined by Legendre and Magnaudet (1998) based on the corresponding formulation in the model by McLaughlin (1991). Consequently, J' reads:

$$J' = \frac{2.255}{\left(1 + 0.2\,\frac{\mathrm{Re_b}}{\mathrm{Sr}}\right)^{\frac{3}{2}}}. \tag{4.22}$$

In order to achieve the correct asymptotic behavior for both small and large Reynolds numbers, the lift coefficients given by Eqs. (4.18) and (4.19) are combined in a similar manner as the drag coefficients $C_{\mathrm{D,Re}}$ and $C_{\mathrm{D,Eo}}$ in Eq. (4.15). Hence, the lift coefficient applied in Eq. (4.17) is formed according to:

$$C_{\mathrm{L}} = \left(C_{\mathrm{L,high}}^2 + C_{\mathrm{L,low}}^2\right)^{\frac{1}{2}}. \tag{4.23}$$

4.1.1.4 Added-Mass Force

Any body moving through a fluid with an unsteady relative velocity has to accelerate or decelerate the fluid surrounding it depending on whether it is moving faster or slower than the fluid. The additional work required for the acceleration or deceleration has to be done by the body in order to change the kinetic energy of the fluid (Brennen, 1982, 2005; Crowe et al., 1998). Thus, the body exhibits an additional force proportional to the changes of the bubble velocity and the changes of the fluid velocity at the position of the bubble. The resulting added-mass force $\boldsymbol{F}_{\mathrm{AM}}$ acting on the bubbles is typically given by (Magnaudet and Eames, 2000; Maxey and Riley, 1983):

$$\boldsymbol{F}_{\mathrm{AM}} = C_{\mathrm{m}}\, m_{\mathrm{f}} \left(\frac{\mathrm{D}\boldsymbol{u}_{\mathrm{f}}}{\mathrm{D}t} - \frac{\mathrm{d}\boldsymbol{u}_{\mathrm{b}}}{\mathrm{d}t}\right). \tag{4.24}$$

It is known that the added-mass coefficient C_{m} varies depending on the shape of the body, see, e.g., the works by Brennen (1982, 2005) and Morel (2015). Since the present thesis is concerned with (nearly) spherical bubbles, the added-mass coefficient is set to that of a sphere (Brennen, 1982, 2005):

$$C_{\mathrm{m}} = \frac{1}{2}. \tag{4.25}$$

Deviations from the spherical shape are assumed to be small in all cases considered within this thesis allowing to neglect the influence of non-spherical bubbles on C_{m}. In Eq. (4.24) the term $\mathrm{d}\boldsymbol{u}_{\mathrm{b}}/\mathrm{d}t$ denotes the acceleration of the bubble, while $\mathrm{D}\boldsymbol{u}_{\mathrm{f}}/\mathrm{D}t$ are the total changes to the fluid velocity at the bubble position. According to Magnaudet and Eames (2000) and Maxey and Riley (1983) the total changes of the fluid velocity are given by:

$$\frac{\mathrm{D}\boldsymbol{u}_{\mathrm{f}}}{\mathrm{D}t} = \frac{\partial \boldsymbol{u}_{\mathrm{f}}}{\partial t} + \left(\boldsymbol{u}_{\mathrm{f}} \cdot \nabla\right) \boldsymbol{u}_{\mathrm{f}}. \tag{4.26}$$

The first term in Eq. (4.26) describes the local changes, whereas the second denotes the convective changes.

4.1.1.5 Pressure-Gradient Force

If aside from the pressure increase caused by the gravitational acceleration (Section 4.1.1.2) an additional pressure gradient exists in the fluid, a so-called pressure gradient force $\boldsymbol{F}_{\mathrm{PG}}$ is exerted on the bubbles. Similar to the case of the gravity force the pressure gradient leads to a higher pressure at one side of the bubble resulting in a force directed opposite to the direction of the gradient. According to Magnaudet and Eames (2000) and Maxey and Riley (1983) the pressure gradient force is defined by:

$$\boldsymbol{F}_{\mathrm{PG}} = m_{\mathrm{f}} \frac{\mathrm{D}\boldsymbol{u}_{\mathrm{f}}}{\mathrm{D}t}, \tag{4.27}$$

assuming a constant pressure gradient over the diameter of the bubble. Note that the pressure gradient force is not related to the drag force, which describes effects of the pressure and the viscosity of the (uniform) flow around the bubble. Due to the similar form of Eqs. (4.24) and (4.27), the added-mass and the pressure gradient force are usually combined similar to the gravity and buoyancy force in Section 4.1.1.2, i.e., $\boldsymbol{F}_{\mathrm{AM+PG}} = \boldsymbol{F}_{\mathrm{AM}} + \boldsymbol{F}_{\mathrm{PG}}$.

4.1.1.6 Basset-History Force

As already mentioned in Section 4.1.1, relation (4.5) should contain the Basset history force $\boldsymbol{F}_{\mathrm{BH}}$ (Gatignol, 1983; Maxey and Riley, 1983), which is named after Basset (1888). According to Crowe et al. (1998) the Basset history force stems from a retarded development of the fluid boundary layer around the surface of an unsteadily moving bubble. Hence, $\boldsymbol{F}_{\mathrm{BH}}$ is proportional to the past accelerations of the bubble and the fluid. The Basset history force is commonly defined by the expression (Maxey and Riley, 1983; Mei, 1994; Mei and Adrian, 1992):

$$\boldsymbol{F}_{\mathrm{BH}} = 6\,\rho_{\mathrm{f}}\,A_{\mathrm{b}} \left(\frac{\nu_{\mathrm{f}}}{\pi}\right)^{\frac{1}{2}} \int_0^t K(t,\,\tau) \left(\frac{\mathrm{d}\boldsymbol{u}_{\mathrm{f}}}{\mathrm{d}\tau} - \frac{\mathrm{d}\boldsymbol{u}_{\mathrm{b}}}{\mathrm{d}\tau}\right) \mathrm{d}\tau, \tag{4.28}$$

where the term $\mathrm{d}\boldsymbol{u}_{\mathrm{f}}/\mathrm{d}\tau$ denotes the temporal variation of the fluid velocity along the *bubble trajectory* (Maxey and Riley, 1983; van Hinsberg et al., 2011). Hence, the derivative $\mathrm{d}\boldsymbol{u}_{\mathrm{f}}/\mathrm{d}\tau$ is determined by the difference between the fluid velocities at the bubble positions at two successive instants in time. This point is emphasized in order to prevent confusion with Eq. (4.26) describing the total changes of the fluid velocity. In Eq. (4.28) the lower limit ($\tau = 0$) of the integral stands for the time at which the bubble was released into the fluid, while the upper limit t represents the present point in time. $K(t,\,\tau)$ is the Basset history kernel, which depends on the difference $\Delta\tau = t - \tau$. The typical kernel function used by most models of the Basset history force is given by the expression (Gatignol, 1983; Maxey and Riley, 1983):

$$K(t,\,\tau) = (t-\tau)^{-\frac{1}{2}}\,. \tag{4.29}$$

It can be seen from Eq. (4.29) that the kernel function slowly decreases with an increasing $\Delta\tau$. Hence, changes to the relative velocity of the bubble and the fluid that occurred

further back in time do not contribute as much to the Basset history force as more recent ones. However, all changes to the relative velocity have to be accounted for, making the integral over all time steps up to the present mandatory in order to express the aforementioned retarded development of the boundary layer. It has to be noted here that the form of the Basset kernel given by Eq. (4.29) is based on an analytical derivation (see, e.g., Gatignol, 1983; Landau and Lifshitz, 1966; Maxey and Riley, 1983), which requires the assumption of a no-slip condition at the surface of the particle and a vanishing particle Reynolds number. This yields some difficulties when Eq. (4.29) is used for (clean) bubbles with a finite bubble Reynolds number (see below).

The enormous computational effort associated with Eq. (4.28) is the main reason why the Basset history force is neglected in nearly all studies on disperse multiphase flows. Since the present instant in time appears in the Basset kernel, $\boldsymbol{F}_{\mathrm{BH}}$ can not be calculated from a previously obtained value, i.e., Eq. (4.28) can not be transformed into an updating formula. Hence, it is necessary to compute the complete integral of Eq. (4.28) for all three Cartesian velocity components of each bubble individually at each time step. To make things worse, this requires the storage of all changes of the relative velocities of all bubbles from their insertion into the flow until the present. If the physical problem considered consists of a large number of bubbles, both the computational effort as well as the required storage capacities become intractable. Note that in cases, where the density of the dispersed phase is much larger than the fluid density ($\rho_{\mathrm{p}}/\rho_{\mathrm{f}} \gg 1$, which is typically true for solid particles dispersed in gas flows), it is usually justified to neglect the Basset history force. However, when $\rho_{\mathrm{p}}/\rho_{\mathrm{f}} \approx 1$ or $\rho_{\mathrm{p}}/\rho_{\mathrm{f}} \ll 1$ this might not be the case (see, e.g., Armenio and Fiorotto, 2001; Daitche, 2015; Olivieri et al., 2014), i.e., the Basset history force could potentially affect the dispersion of the bubbles.

Several modeling approaches with reduced computational requirements have been proposed in the literature, see, e.g., the models by Bombardelli et al. (2008), Daitche (2015), Dorgan and Loth (2007), Elghannay and Tafti (2016), Michaelides (1992) and van Hinsberg et al. (2011). However, most of these models suffer from drawbacks in form of a not substantial reduction of the computational effort or an inaccurate estimation of the Basset history force. One prominent example is the so-called window model proposed by Dorgan and Loth (2007). The idea behind their approach is to evaluate the integral in Eq. (4.28) only within a certain time window t_{win} preceding the present instant in time, while all influences on the Basset history force that occurred before are neglected. This idea is justified by the fact that the decreasing kernel function suppresses the effect of changes of the relative velocities that took place a long time before the present. Since the history kernel $K(t, \tau)$ in Eq. (4.29) decreases very slowly (order $\mathcal{O}(\Delta\tau^{-1/2})$), the size of the time window has to be very large in order to achieve a good approximation of $\boldsymbol{F}_{\mathrm{BH}}$ (van Hinsberg et al., 2011). Otherwise the estimated Basset history force is inaccurate. More refined approaches like the one by van Hinsberg et al. (2011) are able to somewhat reduce the computational and storage requirements, while providing a more precise estimation. The idea behind the approach by van Hinsberg et al. (2011) is to extend the window model by approximating the parts of the Basset kernel neglected by Dorgan and Loth (2007) using a sum of exponential functions. The major advantage of the approximation of this so-called tail of the Basset kernel by exponential functions is

that the resulting expression of the Basset force can be written in form of an updating formula (van Hinsberg et al., 2011). However, the costs associated with the estimation of the Basset history force still remain high compared with all other forces. Additionally, the stability of the numerical solution scheme may be reduced due to approximations introduced by the modeling approaches. Hence, a smaller time step size of the simulation is required to prevent an unstable solution procedure (van Hinsberg et al., 2011).

The model of van Hinsberg et al. (2011) has been implemented into the present Euler–Lagrange framework within the master thesis of Douteau (2016). The window part of the Basset history force consisted of the changes to the relative velocity only at the last time step. Note that van Hinsberg et al. (2011) proposed to use the last five time steps. The tail of the Basset history force was estimated by a sum of ten exponential functions as suggested by van Hinsberg et al. (2011). Note that aside from these variables the temporal changes of the relative velocity of the second-to-last time step has to be stored as well (van Hinsberg et al., 2011). Consequently, in the implementation done by Douteau (2016) $N_{\mathrm{var}} = 12$ variables have to be stored for each of the three spatial components of the Basset history force and each bubble, i.e., a total of 36 variables per bubble. Hence, despite the fact that the refined approach of van Hinsberg et al. (2011) is applied to model the Basset history force, the numerical effort remains very large. The effect of the Basset history force on the motion of the individual bubbles was investigated in several academic test cases like a bubble suspended into fluid of linearly increasing velocity or a sudden reversal of the bubble velocity. It was found that the bubbles followed the fluid flow more closely due to the Basset history force (Douteau, 2016), i.e., the bubbles behaved more like fluid particles. This observation agrees with the results of Daitche (2015). However, the arising difficulty of an unstable numerical solution scheme in the case of a too large time-step size was also observed, i.e., the dimensionless time step has to be set to $\Delta t = 10^{-5}$ or smaller. This is a major disadvantage considering that the time-step size in a LES is typically of the order of $\mathcal{O}(10^{-3})$.

Lastly, it has to be again remarked that the kernel $K(t, \tau)$ of the Basset history force given by Eq. (4.29) has been derived for the case of a *solid* particle (no-slip condition at the surface) at a *vanishing* ($\mathrm{Re_p} \to 0$) particle Reynolds number (Maxey and Riley, 1983; Mei, 1994; Mei and Adrian, 1992). Consequently, for the case of a non-vanishing particle or bubble Reynolds number Eq. (4.29) yields an inadequate representation of the kernel function. Additionally, as argued in Section 4.1.1.1, a no-slip condition is only present at the surface of contaminated bubbles. Hence, for clean bubbles the correct form of the Basset kernel will also deviate from Eq. (4.29). Both issues have been investigated by several authors (see, e.g., Mei, 1993; Mei and Adrian, 1992; Mei et al., 1994; Yang and Leal, 1991). Mei (1993) and Mei and Adrian (1992) determined the Basset history force acting on a rigid sphere dispersed in an unsteady flow containing small oscillations in the free-stream velocity u_{fs} based on a DNS. The Reynolds numbers $\mathrm{Re_p}$ based on the radius r_{p} of the sphere, the velocity u_{fs} and the kinematic viscosity ν_{f} of the fluid was varied between 0.05 and 50, i.e., the case of a non-vanishing $\mathrm{Re_p}$ was analyzed. It was found that for all Reynolds numbers the history kernel initially decays following Eq. (4.29), i.e., with an order of magnitude of $\mathcal{O}(\Delta\tau^{-1/2})$). However, for all Reynolds numbers further increasing differences $\Delta\tau$ lead to a much faster decay of the history kernel with

an order of magnitude according to $\mathcal{O}(\Delta\tau^{-2})$. The exact point of the transition depends on the Reynolds number. For small $\mathrm{Re_p}$ the transition occurred at dimensionless times of $\Delta\tau' = \Delta\tau\, u_{\mathrm{fs}}/r_{\mathrm{p}} = \mathcal{O}(10)$, while at larger $\mathrm{Re_p}$ the transition was quicker ($\Delta\tau' = \mathcal{O}(1)$). The faster decay of $K(t,\,\tau)$ at large $\Delta\tau$ means that changes of the relative acceleration that occurred a long time in the past affect the present far less compared to the kernel given by Eq. (4.29). Consequently, the actual effect of the Basset history force should be less pronounced than what is estimated by Eq. (4.29). However, note that only the Basset kernel is affected by these effects. The general form of the Basset history force as given by Eq. (4.28) is still valid.

The uncertainty regarding the form of the Basset history force becomes even larger in the case of non-rigid particles with a free-slip boundary condition at their surface, i.e., liquid droplets or clean bubbles. It was analytically shown by Yang and Leal (1991) that in the limit of $\mathrm{Re_b} \to 0$ the kernel function of the Basset history force acting on a clean bubble is fundamentally different to the one given by Eq. (4.29). While the kernel found by Yang and Leal (1991) retains a decay of the order $\mathcal{O}(\Delta\tau)^{-1/2}$ for large differences $\Delta\tau$ to the present point in time, it approaches a finite value for $\Delta\tau \to 0$, i.e., $K_{\mathrm{clean}}(t,\,\tau)$ does not tend to infinity as proposed by Eq. (4.29) for vanishing $\Delta\tau$. Additionally, it was found by Yang and Leal (1991) that in the case of clean bubbles the kernel function is generally smaller than the one for rigid spheres. Later, Mei et al. (1994) extended the analysis of Yang and Leal (1991) to Reynolds numbers larger than zero. Again a temporal decay of the order $\mathcal{O}(\Delta\tau^{-2})$ was found for large $\Delta\tau$. Consequently, combining the results of the studies by Mei et al. (1994) and Yang and Leal (1991) in the case of clean bubbles the history kernel is always smaller than the one proposed by Mei (1993) and Mei and Adrian (1992) for rigid spheres. This implies that the Basset history force on clean bubbles is smaller than it would be expected from the usual kernel (Eq. (4.29)).

Despite these findings by Mei (1993), Mei and Adrian (1992), Mei et al. (1994) and Yang and Leal (1991) to the best of the author's knowledge all presently available models of the Basset history force are based on the kernel function given by Eq. (4.29). Consequently, models like the ones by Dorgan and Loth (2007) and van Hinsberg et al. (2011) would overestimate the influence of the Basset history force on both contaminated and clean bubbles. Yet, even if the models would be adapted to rely on the kernel functions by Mei (1993), Mei and Adrian (1992) and Mei et al. (1994) the required effort would still remain large, since the decay is initially slow ($\mathcal{O}(\Delta\tau)^{-1/2}$) for dimensionless times of up to $\mathcal{O}(1-10)$. In Euler–Lagrange approaches using LES, where the dimensionless time step size is usually of the order of magnitude $\mathcal{O}(10^{-3})$ this would still lead to an unfeasibly large effort.

In summary, large uncertainties regarding the actual form of the kernel $K(t,\,\tau)$ of the Basset history force exist and computational effort associated with its calculation remains unfeasibly high, despite the efforts made to model the Basset history force. Therefore, the Basset history force will be neglected throughout this thesis, although the findings of Daitche (2015) and Douteau (2016) indicate that the motion of the individual bubbles is affected by the Basset history force. This approach is supported by the studies by Giusti et al. (2005) and Molin et al. (2012) who showed among other things that the Basset history force does not play a major role for the averaged properties of bubbles in

a turbulent channel flow. Nevertheless, it has to be remembered that there might be an influence of the Basset history force.

4.1.2 Resulting Equation of Motion

The equation of motion used in this thesis is obtained by combining Eqs. (4.1) and (4.5), where the forces are given by Eqs. (4.6), (4.16), (4.17), (4.24) and (4.27). Dividing the resulting expression by the mass m_b of the bubbles yields an expression for the acceleration of the bubbles:

$$\frac{\mathrm{d}\boldsymbol{u}_\mathrm{b}}{\mathrm{d}t} = \boldsymbol{f}_\mathrm{D} + \boldsymbol{f}_\mathrm{G+B} + \boldsymbol{f}_\mathrm{L} + \boldsymbol{f}_\mathrm{AM+PG}, \tag{4.30}$$

where the ratios $\boldsymbol{f}_\mathrm{D}$, $\boldsymbol{f}_\mathrm{G+B}$, $\boldsymbol{f}_\mathrm{L}$ and $\boldsymbol{f}_\mathrm{AM+PG}$ of the forces to the bubble mass are defined by:

$$\boldsymbol{f}_\mathrm{D} = C_\mathrm{D}\,\frac{3}{4}\,\frac{1}{d_\mathrm{b}}\,\frac{\rho_\mathrm{f}}{\rho_\mathrm{b}}\,|\boldsymbol{u}_\mathrm{f}-\boldsymbol{u}_\mathrm{b}|\,(\boldsymbol{u}_\mathrm{f}-\boldsymbol{u}_\mathrm{b})\,, \tag{4.31a}$$

$$\boldsymbol{f}_\mathrm{G+B} = \left(1-\frac{\rho_\mathrm{f}}{\rho_\mathrm{b}}\right)\boldsymbol{g}, \tag{4.31b}$$

$$\boldsymbol{f}_\mathrm{L} = C_\mathrm{L}\,\frac{\rho_\mathrm{f}}{\rho_\mathrm{b}}\,(\boldsymbol{u}_\mathrm{f}-\boldsymbol{u}_\mathrm{b})\times\boldsymbol{\omega}_\mathrm{f}, \tag{4.31c}$$

$$\boldsymbol{f}_\mathrm{AM+PG} = (1+C_\mathrm{m})\,\frac{\rho_\mathrm{f}}{\rho_\mathrm{b}}\frac{\mathrm{D}\boldsymbol{u}_\mathrm{f}}{\mathrm{D}t} - C_\mathrm{m}\,\frac{\rho_\mathrm{f}}{\rho_\mathrm{b}}\,\frac{\mathrm{d}\boldsymbol{u}_\mathrm{b}}{\mathrm{d}t}. \tag{4.31d}$$

In Eq. (4.31) the gravity and buoyancy forces as well as the added-mass and the pressure gradient forces are combined in Eqs. (4.31b) and (4.31d). Note that the second term on the r.h.s. of Eq. (4.31d) contains the acceleration of the bubble. This term can be added to the l.h.s. of Eq. (4.30) yielding the expression:

$$\underbrace{\left(1+C_\mathrm{m}\,\frac{\rho_\mathrm{f}}{\rho_\mathrm{b}}\right)}_{f_\mathrm{m}}\frac{\mathrm{d}\boldsymbol{u}_\mathrm{b}}{\mathrm{d}t} = \boldsymbol{f}_\mathrm{D} + \boldsymbol{f}_\mathrm{G+B} + \boldsymbol{f}_\mathrm{L} + \boldsymbol{f}^\mathrm{mod}_\mathrm{AM+PG}, \tag{4.32}$$

where $\boldsymbol{f}^\mathrm{mod}_\mathrm{AM+PG}$ is readily given by the first term on the r.h.s. of Eq. (4.31d).

Finally, it remains to formulate Eq. (4.30) in its dimensionless form. This can be readily achieved by introducing the following dimensionless variables denoted by a prime: the velocities $\boldsymbol{u}'_\mathrm{b} = \boldsymbol{u}_\mathrm{b}/u_\mathrm{ref}$ and $\boldsymbol{u}'_\mathrm{f} = \boldsymbol{u}_\mathrm{f}/u_\mathrm{ref}$ of the bubble and the fluid at the position of the bubble center, the bubble diameter $d'_\mathrm{b} = d_\mathrm{b}/\ell_\mathrm{ref}$, the bubble density $\rho'_\mathrm{b} = \rho_\mathrm{b}/\rho_\mathrm{f}$, the time $t' = t\,u_\mathrm{ref}/\ell_\mathrm{ref}$, the rotation of the fluid $\boldsymbol{\omega}'_\mathrm{f} = \boldsymbol{\omega}_\mathrm{f}\,\ell_\mathrm{ref}/u_\mathrm{ref}$ and the gravitational acceleration $\boldsymbol{g}' = \boldsymbol{g}\,\ell_\mathrm{ref}/u^2_\mathrm{ref}$. Inserting these dimensionless variables into Eqs. (4.30) and (4.31) and dividing by $u^2_\mathrm{ref}/\ell_\mathrm{ref}$ yields the governing equation of the dispersed phase in the dimensionless form:

$$\frac{\mathrm{d}\boldsymbol{u}'_\mathrm{b}}{\mathrm{d}t'} = \frac{1}{f'_\mathrm{m}}\left(\boldsymbol{f}'_\mathrm{D} + \boldsymbol{f}'_\mathrm{G+B} + \boldsymbol{f}'_\mathrm{L} + \boldsymbol{f}'^\mathrm{mod}_\mathrm{AM+PG}\right), \tag{4.33}$$

with

$$\boldsymbol{f}'_{\mathrm{D}} = C_{\mathrm{D}} \frac{3}{4} \frac{|\boldsymbol{u}'_{\mathrm{f}} - \boldsymbol{u}'_{\mathrm{b}}|}{d'_{\mathrm{b}}\, \rho'_{\mathrm{b}}} \left(\boldsymbol{u}'_{\mathrm{f}} - \boldsymbol{u}'_{\mathrm{b}}\right), \tag{4.34a}$$

$$\boldsymbol{f}'_{\mathrm{G+B}} = \left(1 - \frac{1}{\rho'_{\mathrm{b}}}\right) \boldsymbol{g}', \tag{4.34b}$$

$$\boldsymbol{f}'_{\mathrm{L}} = C_{\mathrm{L}} \frac{1}{\rho'_{\mathrm{b}}} \left(\boldsymbol{u}'_{\mathrm{f}} - \boldsymbol{u}'_{\mathrm{b}}\right) \times \boldsymbol{\omega}'_{\mathrm{f}}, \tag{4.34c}$$

$$\boldsymbol{f}'^{\,\mathrm{mod}}_{\mathrm{AM+PG}} = (1 + C_{\mathrm{m}}) \frac{1}{\rho'_{\mathrm{b}}} \frac{\mathrm{D}\boldsymbol{u}'_{\mathrm{f}}}{\mathrm{D}t'}, \tag{4.34d}$$

$$\text{and} \quad f'_{\mathrm{m}} = 1 + C_{\mathrm{m}} \frac{1}{\rho'_{\mathrm{b}}}. \tag{4.34e}$$

4.2 Boundary Conditions for the Dispersed Phase

The description of the dispersed phase requires the definition of appropriate boundary conditions as it was done in Section 3.3 for the fluid domain. Hence, in this section the procedures followed when a bubble reaches one of the various types of boundaries are explained.

4.2.1 Free Surface Boundary

Firstly, it is assumed that bubbles impacting on a free surface of the fluid immediately coalesce with the surface. Hence, the bubbles are removed from the computational domain. Note that it has been observed in experiments (e.g., by Kosior et al., 2014; Zawala et al., 2007, 2013; Zawala and Malysa, 2011) that bubbles bounce back from a free surface. This phenomenon is neglected here for the sake of simplicity. Additionally, it is obvious that free surfaces are normal to the gravitational acceleration driving the bubbles towards the boundary. Consequently, even if bubbles bounce back from the free-surface boundary, the buoyancy force leads to a repeated approach until the bubbles finally coalesce.

4.2.2 Outflow Boundary

Similarly, the bubbles are also removed from the computational domain if they pass through an outflow boundary carried by the fluid flow. This approach is reasonable, since the fluid flow carrying the bubbles is assumed to leave the domain at the outflow boundary. A back flow which would drive the bubbles back into the computational domain is presently not included.

4.2.3 Periodic Boundary

Lastly, in the case of periodic boundary conditions the bubbles leaving the domain at one boundary are re-inserted at the corresponding opposite boundary. The physical properties of the bubble remain unchanged, only the positions are adjusted. In particular, this means that the bubble re-enters the computational domain with the same velocity it possesses before it leaves the domain.

4.2.4 Bubble-Wall Collisions

The collisions of bubbles with walls bounding the computational domain is described within the framework of an inelastic hard-sphere model (Crowe et al., 1998). The wall-collision model implemented in the in-house code $\mathcal{LESOCC}$ was first derived for the treatment of wall collisions of solid particles. Since the modeling approach relies on a hard-sphere model, the deformation of the particles during the impact is neglected. The friction between the particles and the wall is governed by Coulomb's law of friction. Hence, the particles can slide or roll over the wall during the collision depending on the tangential and normal restitution coefficients $e_{\mathrm{t,w}}$ and $e_{\mathrm{n,w}}$ and the static and kinetic friction coefficients $\mu_{\mathrm{st,w}}$ and $\mu_{\mathrm{kin,w}}$ (Breuer et al., 2012). Furthermore, the model is suitable to describe the particle impact on both smooth and rough walls (Breuer et al., 2012). Later, the particle-wall collision model was extended by Almohammed and Breuer (2016b) to account for adhesive forces acting on the particles during the collision. A more detailed derivation of the wall-collision modeling can be found in the works by Almohammed and Breuer (2016b) and Breuer et al. (2012). Therein and in further studies, e.g., by Alletto and Breuer (2013b, 2015), the effect of the collisions on the fluid and the dispersed phase was investigated. For the case of bubbles the same modeling approach is used. However, the treatment is strongly simplified due to several assumptions:

- The deformation of the bubbles during the collision process can still be neglected allowing a description by the hard-sphere model. This is justified if the time scale of the collision is smaller than the time step size used in the simulation. It has to be noted that this assumption may not be fulfilled for bubble-wall collisions, since bubbles can be largely deformed during the collision. Nevertheless, the hard-sphere collision model is applied in the present thesis for the sake of simplicity. This choice is partly motivated by the fact that strong bubble deformations are mostly observed for the impact of vertically upwards rising bubbles with horizontal walls (see, e.g., Tsao and Koch, 1997; Zawala et al., 2007; Zawala and Dabros, 2013; Zenit and Legendre, 2009, and the discussion at the end of this section). However, this setup is rather uncommon, e.g., in the present thesis only cases where bubbles move mostly parallel to a wall are considered. In such a configuration the bubble deformation during a wall collision is much smaller.

- In contrast to solid particles, where friction plays a major role, these forces are neglected for the case of bubbles. This is meaningful since the friction between gases and solids is small. A direct consequence of this assumption is that bubbles

only slide over the wall during the collision but do not stick to it. Hence, a rolling collision is not possible.

- The influence of the roughness of the walls is not considered in the present thesis. This is motivated by the fact that the roughness of solid walls is assumed to appear at low spatial wave lengths of the surface and with amplitudes of the order of $\mathcal{O}(1-10\,\mu\text{m})$ (Breuer et al., 2012). However, bubbles are usually much larger with diameters that are at least of the order $\mathcal{O}(100\,\mu\text{m})$. It was demonstrated by Breuer et al. (2012) that the collision of solid particles much larger than the amplitude of the wall roughness is unaffected by the roughness. Hence, in the case of bubbles any wall can be treated as a smooth wall.

Based on these assumptions the wall-collision process of the bubbles is reduced to a frictionless, inelastic collision on a smooth wall. Since sticking collisions are excluded in the present framework, the governing equation of the wall collision is given by the conservation of translational momentum:

$$m_\mathrm{b}\left(\boldsymbol{u}_\mathrm{b}^{+}-\boldsymbol{u}_\mathrm{b}^{-}\right)=\hat{\boldsymbol{f}}^\mathrm{bw}, \tag{4.35}$$

where $\boldsymbol{u}_\mathrm{b}^{-}$ and $\boldsymbol{u}_\mathrm{b}^{+}$ denote the bubble velocity prior and posterior to the wall impact and $\hat{\boldsymbol{f}}^\mathrm{bw}$ is the total impulse vector. The superscript 'bw' indicates that a bubble-wall collision is considered. Since friction is neglected, the impulse vector contains solely a wall-normal component $\hat{\boldsymbol{f}}_\mathrm{n}^\mathrm{bw}$, which is given by the integral over all forces acting on the bubble during the collision in the wall-normal direction $\boldsymbol{n}$. Hence, the impulse vector can be written as:

$$\hat{\boldsymbol{f}}^\mathrm{bw}=\hat{f}_\mathrm{n}^\mathrm{bw}\,\boldsymbol{n}=\int\hat{\boldsymbol{F}}_\mathrm{n}^\mathrm{bw}\,\mathrm{d}t. \tag{4.36}$$

The magnitude $\hat{f}_\mathrm{n}^\mathrm{bw}$ of the normal impulse vector can be obtained by setting Eqs. (4.35) and (4.36) equal to each other and multiplying by $\boldsymbol{n}$. Thus, $\hat{f}_\mathrm{n}^\mathrm{bw}$ is given by:

$$\hat{f}_\mathrm{n}^\mathrm{bw}=\hat{\boldsymbol{f}}^\mathrm{bw}\cdot\boldsymbol{n}=m_\mathrm{b}\left(\boldsymbol{u}_\mathrm{b}^{+}-\boldsymbol{u}_\mathrm{b}^{-}\right)\cdot\boldsymbol{n}. \tag{4.37}$$

The unknown bubble velocity after the wall collision can be specified by using the definition of a normal restitution coefficient $e_\mathrm{n,w}$. Such a coefficient is commonly defined based on the magnitudes of the wall-normal velocities $u_\mathrm{b,n}^{-}$ and $u_\mathrm{b,n}^{+}$ prior and posterior to the wall impact (Breuer et al., 2012; Crowe et al., 1998):

$$e_\mathrm{n,w}=-\frac{u_\mathrm{b,n}^{+}}{u_\mathrm{b,n}^{-}}=-\frac{\boldsymbol{u}_\mathrm{b}^{+}\cdot\boldsymbol{n}}{\boldsymbol{u}_\mathrm{b}^{-}\cdot\boldsymbol{n}}\quad\text{with}\quad 0<e_\mathrm{n,w}\leq 1. \tag{4.38}$$

Solving Eq. (4.38) for the post-collision velocity and inserting into Eq. (4.37) yields the magnitude of the wall-normal impulse vector:

$$\hat{f}_\mathrm{n}^\mathrm{bw}=-m_\mathrm{b}\left(1+e_\mathrm{n,w}\right)\left[\boldsymbol{u}_\mathrm{b}^{-}\cdot\boldsymbol{n}\right]. \tag{4.39}$$

Consequently, the bubble velocity after a wall collision is given by:

$$\boldsymbol{u}_\mathrm{b}^+ = \boldsymbol{u}_\mathrm{b}^- + \frac{1}{m_\mathrm{b}}\,\hat{\boldsymbol{f}}^\mathrm{bw} = \boldsymbol{u}_\mathrm{b}^- - (1+e_\mathrm{n,w})\left[\boldsymbol{u}_\mathrm{b}^- \cdot \boldsymbol{n}\right]\boldsymbol{n}. \tag{4.40}$$

The normal restitution coefficient $e_\mathrm{n,w}$ has to be specified prior to the simulation. In the literature only a few studies on the interaction of bubbles with solid walls exist, see, e.g., the works by Tsao and Koch (1997), Zawala et al. (2007), Zawala and Dabros (2013) and Zenit and Legendre (2009). In all those studies the collision of a bubble rising in a quiescent liquid with a horizontal wall was considered. Note that among those studies only Zenit and Legendre (2009) explicitly investigated the normal restitution coefficient proposing a relation for $e_\mathrm{n,w}$ based on the Stokes number $\mathrm{St} = 2\,(\rho_\mathrm{b} + C_\mathrm{m}\,\rho_\mathrm{f})\,d_\mathrm{b}\,u_\mathrm{b,n}^-/9\,\mu_\mathrm{f}$. It was found that the normal restitution coefficient decreases with decreasing Stokes number, i.e., the post-collision velocity becomes smaller until the situation occurs that the bubbles do not rebound from the walls. However, the impact on a horizontal wall is rather untypical. In the present thesis only cases are considered in which the bubbles move mostly parallel to the walls, e.g., bubbles rising upwards in a cylindrical bubble column or bubbles dispersed in a vertically downward channel flow. Hence, gravity points in a direction parallel to the walls and not in the wall-normal direction. Consequently, in most of the presently considered cases the wall-normal velocity $u_\mathrm{b,n}^-$ prior to the collision is small compared to the tangential component, whereas in the experimental studies by Tsao and Koch (1997), Zawala et al. (2007), Zawala and Dabros (2013) and Zenit and Legendre (2009) the buoyancy-driven wall-normal impact velocity is large.

Hence, the results of the above mentioned studies cannot be readily transferred to the present cases. Firstly, the range of wall-normal collision velocities obtained in the present cases are mostly not covered by the experiments. This is due to the fact that in the experiment the wall-normal velocity prior to the impact is given by the buoyancy-driven terminal rise velocity of the bubble, which cannot be freely adjusted. Hence, for small collision velocities the relation found by Zenit and Legendre (2009) is subject to experimental uncertainties. Additionally, in the experiment the bubbles are affected by gravity during the collision, since the buoyancy force acts in the wall-normal direction during the approach as well as the rebound of the bubble. Thus, the post collision velocity is influenced by gravity. In the presently considered cases of bubbles moving parallel to the walls gravity is directed parallel to the walls, i.e., no gravity or buoyancy force component affects the collision outcome.

Consequently, the normal restitution coefficient is set to $e_\mathrm{n,w} = 1$ in the present thesis for the sake of simplicity, except for the validation of the coalescence model, see Sections 10.3 and 11.3.1. Since sticking collisions are not taken into account, the static and kinetic friction coefficients are set to $\mu_\mathrm{st,w} = \mu_\mathrm{kin,w} = 0$. This corresponds to a fully elastic collision, i.e., the normal component of the bubble velocity prior to the wall impact is reversed while the tangential components remain unchanged:

$$\boldsymbol{u}_\mathrm{b}^+ = \boldsymbol{u}_\mathrm{b}^- - 2\left[\boldsymbol{u}_\mathrm{b}^- \cdot \boldsymbol{n}\right]\boldsymbol{n}. \tag{4.41}$$

Note that the same approach on modeling bubble-wall collisions was chosen by Darmana et al. (2006) in their Euler–Lagrange framework devised for tracking bubbles through turbulent liquid flows. This framework was later adapted by Jain et al. (2014) and Lau et al. (2014).

5 Interaction Mechanisms

The interaction between the different phases is an integral part of two-phase flow systems, since it governs the evolution of both phases. Elghobashi (1991, 1994) classified two-phase flows into different regimes of a flow map, in which different types of interactions play a role: one-way, two-way and four-way coupling (see Sections 5.1 to 5.3). Figure 5.1 depicts such a flow map based on the volume fraction Φ_b of the bubbles, which is defined as the ratio of the total volume $V_\mathrm{b,tot}$ of the bubbles to the total volume V_tot of the computational domain:

$$\Phi_\mathrm{b} = \frac{V_\mathrm{b,tot}}{V_\mathrm{tot}} = \frac{V_\mathrm{b,tot}}{V_\mathrm{b,tot} + V_\mathrm{f,tot}}. \tag{5.1}$$

In Eq. (5.1) V_tot is given by the sum of the total volumes $V_\mathrm{b,tot}$ of the bubbles and the fluid $V_\mathrm{f,tot}$, respectively. Hence, Eq. (5.1) describes which fraction of the computational domain is occupied by bubbles. Therefore, the volume fraction is an important parameter characterizing the influence the bubbles have on the fluid and on each other.

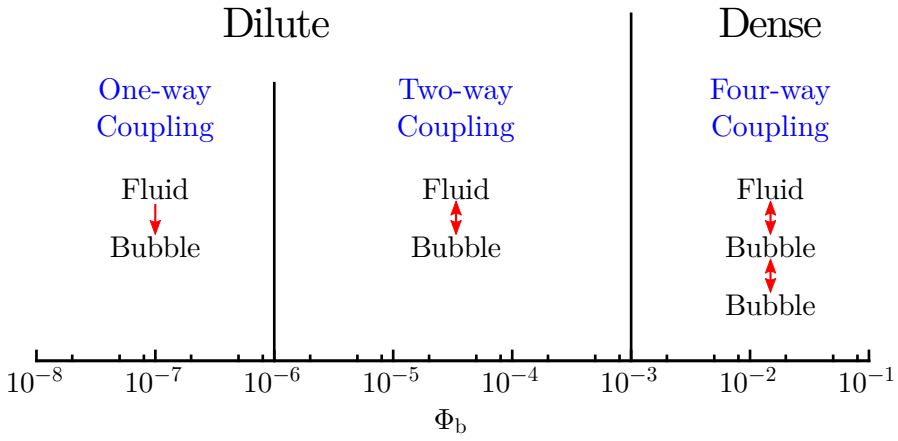

Fig. 5.1. Map of coupling regimes in two-phase flows based on Elghobashi (1991, 1994).

It can be seen in Fig. 5.1 that two-phase flows can be divided into dilute and dense systems based on the volume fraction, where the boundary between the two flow types is roughly at $\Phi_\mathrm{b} = 10^{-3}$ (Elghobashi, 1991, 1994). Note that this is not a sharp boundary, but the transition is smooth. Furthermore, it has to be taken into account that the bubble number density can strongly vary in space due to preferential concentration effects leading to locally high volume fractions (Balachandar and Eaton, 2010). The flow regimes can be further classified according to the type of interactions playing a role.

However, note that the original classification by Elghobashi (1991, 1994) is based on turbulent flows laden with *solid* particles and not bubbles. Despite the different properties

of particles and bubbles, the results of Elghobashi (1991, 1994) are frequently applied to distinguish the coupling regimes of bubbly flows (Balachandar and Eaton, 2010; Molin et al., 2012; Pang and Wei, 2014; Sommerfeld et al., 2008). This is supported by the numerical studies of Molin et al. (2012) and Pang and Wei (2014), who showed that for bubble-laden flows in the two-way coupling regime with volume fractions of the order of magnitude of $\mathcal{O}(10^{-4})$ the continuous phase is significantly affected by the presence of the bubbles, while bubble-bubble collisions do not play a major role. Additionally, it is plausible to assume that the transition from the two-way to the four-way coupling regime is comparable for both solid particles and gas bubbles, since the concentration of the respective entities is responsible for the likeliness of collisions. Consequently, in the present thesis the boundaries of the coupling regimes as given by Elghobashi (1991, 1994) are assumed to be valid for bubble-laden flows as well.

5.1 One-way Coupling

According to Elghobashi (1991, 1994) the effect of the dispersed phase on the fluid is negligibly small in highly dilute systems with volume fractions $\Phi_\mathrm{b} \lesssim 10^{-6}$. Furthermore, bubble-bubble collisions take place so scarcely that this interaction does not play a role either. Since only the fluid affects the bubble, this regime is referred to as one-way coupled. Hence, the bubble is transported by the fluid by exerting the forces described in Section 4.1, i.e., the bubble dispersion is solely given by the governing equation (4.34) of the bubble motion. A feedback effect of the bubble on the continuous phase is neglected. Additionally, the fluid velocity fluctuations exert turbulent stresses on the bubble surface. If these stresses are sufficiently strong, breakup can occur due to the associated bubble deformation. The modeling of turbulence-induced breakup is described in more detail in Chapter 8.

In order to correctly estimate the forces acting on the bubble given by Eq. (4.34), the full fluid velocity at the position of the bubble is required. Yet, the defining characteristic of the large-eddy simulation framework used in the present thesis is that the small, subgrid-scales of the flow are not resolved. Purely the filtered quantities are obtained. However, the full fluid velocity at the bubble position is given by:

$$\boldsymbol{u}_\mathrm{f} = \overline{\boldsymbol{u}}_\mathrm{f} + \boldsymbol{u}'_\mathrm{s}, \tag{5.2}$$

where $\overline{\boldsymbol{u}}_\mathrm{f}$ denotes the filtered fluid velocity at the bubble position, which is determined by expanding the corresponding value at the nearest cell center (see Section 9.3.1) by a second-order accurate Taylor series (Marchioli et al., 2007). The term $\boldsymbol{u}'_\mathrm{s}$ describes the unresolved subgrid-scale velocity at the position of the bubble. Hence, $\boldsymbol{u}'_\mathrm{s}$ is commonly denoted to be the subgrid-scale velocity *seen* by the bubble yielding the index s. As already mentioned in Section 2.1, an extended version (Breuer and Hoppe, 2017) of the subgrid-scale model by Pozorski and Apte (2009) is used for modeling the subgrid-scale velocities in the present thesis. The detailed derivation of this model is given in Chapter 6. Beside the subgrid-scale model no further measures are necessary for the one-way coupling.

5.2 Two-way Coupling

Increasing the volume fraction of the dispersed phase to values $10^{-6} \lesssim \Phi_\mathrm{b} \lesssim 10^{-3}$ leads to an increasing influence of the bubbles on the fluid. Hence, not only the bubbles are transported by the fluid, but the fluid is affected by the momentum of the bubbles. Therefore, this regime is described as two-way coupled (Elghobashi, 1991, 1994). Note that Φ_b is still too small for bubble-bubble interactions to play a significant role.

In order to account for the momentum exchange from the bubbles to the fluid, in the present Euler–Lagrange framework an additional source term is considered in the governing equations of the fluid phase, i.e., the term f_i in Eq. (3.9) describing the feedback of the bubble on the flow. For this purpose the particle-source-in-cell (PSI-CELL) method devised by Crowe et al. (1977) is applied. Hence, the momentum source is determined by the total fluid-dynamically related force exerted by all bubbles N_b located in a certain computational cell of the volume ΔV, i.e., f_i^PSIC is given by:

$$f_i^\mathrm{PSIC} = -\frac{1}{\Delta V} \sum_{k=1}^{N_\mathrm{b}} F_i^{(k)}. \tag{5.3}$$

In Eq. (5.3) the index i denotes the Cartesian coordinate, while the superscript (k) is the running index.

The force terms $F_i^{(k)}$ exerted by the individual bubbles present in the computational cell can be determined by considering the changes to the momentum balance of the fluid due to the presence of a bubble (see, e.g., Mazzitelli, 2003; Sridhar and Katz, 1999). According to Sridhar and Katz (1999) the forcing term caused by a single bubble is related to the shear stress gradients present in the fluid in the absence of a bubble, i.e., shear stress gradients due to external pressure gradients and gravitationally induced pressure gradients. If a bubble is present, these shear stresses on the bubble surface are balanced by the drag, lift and added-mass forces, i.e., the fluid-dynamically related forces. Consequently, the force exerted by the bubble on the fluid is given by (Sridhar and Katz, 1999):

$$F_i^{(k)} = F_{\mathrm{D},i}^{(k)} + F_{\mathrm{L},i}^{(k)} + F_{\mathrm{AM},i}^{(k)} = m_{\mathrm{b},k} \frac{\mathrm{d}u_{\mathrm{b},i}^{(k)}}{\mathrm{d}t} - F_{\mathrm{G+B},i}^{(k)} - F_{\mathrm{PG},i}^{(k)}. \tag{5.4}$$

In the second step of Eq. (5.4) relations (4.1) and (4.5) describing Newton's second law are inserted in order to obtain $F_i^{(k)}$ based on the acceleration of the bubbles. The forces appearing in Eq. (5.4) are calculated according to the formulas provided in Sections 4.1.1.1 to 4.1.1.5. Note that Eq. (5.4) reduces to the forcing term proposed by Crowe et al. (1977) for the case of solid particles or liquid droplets dispersed in gas flows ($\rho_\mathrm{p} \gg \rho_\mathrm{f}$), since in these cases the drag force is typically one order of magnitude larger than the lift and added-mass forces. A detailed derivation of Eq. (5.4) is omitted here for the sake of brevity referring the interested reader to the study by Sridhar and Katz (1999) instead.

Thus, the forcing term is estimated in an indirect manner based on Eq. (5.4). Since the acceleration of the bubble has already been determined using Eq. (4.33), this method avoids the re-calculation of the drag, lift and added-mass forces. The substantial derivative of the

fluid velocity required for the determination of the pressure gradient force is interpolated to the position of the bubble center based on a trilinear interpolation. Afterwards, the forcing term is distributed to the centers of the eight computational cells surrounding the bubble. The weighting coefficients are determined following a trilinear interpolation scheme. Accordingly, the weighting coefficient increases with decreasing distance between the bubble position and the center of the corresponding cell. The measure ensures a smooth distribution of the source term, which avoids convergence problems related to large isolated source terms.

5.3 Four-way Coupling

As seen from Fig. 5.1 further increasing the volume fraction to values $\Phi_\mathrm{b} \gtrsim 10^{-3}$ causes the interaction between the bubbles to play a more important role, i.e., bubble-bubble collisions occur significantly more often. Since collisions are the pre-requisite for the highly important coalescence mechanism of bubbles, an adequate description of collisions is essential for a correct prediction of bubbly two-phase flows at high volume loadings.

Similar to the bubble-wall collisions, inter-bubble collisions are accounted for by a hard-sphere collision model (Crowe et al., 1998). Hence, the same basic assumptions listed in Section 4.2.4 are applied for bubble-bubble collisions. Hence, the governing equation describing the collision process is the conservation of translational motion:

$$m_{\mathrm{b},1}\left(\boldsymbol{u}_{\mathrm{b},1}^{+}-\boldsymbol{u}_{\mathrm{b},1}^{-}\right)=-\hat{\boldsymbol{f}}^{\mathrm{bb}}, \tag{5.5a}$$

$$m_{\mathrm{b},2}\left(\boldsymbol{u}_{\mathrm{b},2}^{+}-\boldsymbol{u}_{\mathrm{b},2}^{-}\right)=\quad\hat{\boldsymbol{f}}^{\mathrm{bb}}, \tag{5.5b}$$

where the superscripts '-' and '+' again denote the bubble velocities prior and posterior to the collision. The superscript 'bb' indicates that a bubble-bubble collision is considered. The total impulse vector $\hat{\boldsymbol{f}}^{\mathrm{bb}}$ is given by the integral over the forces acting on the bubbles during the collision time. Since friction forces between the colliding bubbles are neglected, $\hat{\boldsymbol{f}}^{\mathrm{bb}}$ acts solely in the collision-normal direction $\boldsymbol{n}_\mathrm{c}$. Consequently, the impulse vector is given by:

$$\hat{\boldsymbol{f}}^{\mathrm{bb}}=\hat{f}_\mathrm{n}^{\mathrm{bb}}\,\boldsymbol{n}_\mathrm{c}=\int\hat{\boldsymbol{F}}_\mathrm{n}^{\mathrm{bb}}\,\mathrm{d}t, \tag{5.6}$$

where the collision-normal direction $\boldsymbol{n}_\mathrm{c}$ is defined by the direction pointing from the center $\boldsymbol{x}_{\mathrm{p},1}$ of one bubble to the center $\boldsymbol{x}_{\mathrm{p},2}$ of the other bubble:

$$\boldsymbol{n}_\mathrm{c}=\frac{\boldsymbol{x}_{\mathrm{p},2}-\boldsymbol{x}_{\mathrm{p},1}}{|\boldsymbol{x}_{\mathrm{p},2}-\boldsymbol{x}_{\mathrm{p},1}|}=2\,\frac{\boldsymbol{x}_{\mathrm{p},2}-\boldsymbol{x}_{\mathrm{p},1}}{d_{\mathrm{b},2}+d_{\mathrm{b},1}}\,. \tag{5.7}$$

Following a similar procedure as in Section 4.2.4, the magnitude of the total impulse vector can be expressed by the velocities of the bubbles participating in the collision. First, Eqs. (5.5a) and (5.5b) can be solved for the corresponding velocities by dividing with $m_{\mathrm{b},1}$

and $m_{\mathrm{b},2}$, respectively. Multiplying the resulting expressions with $\boldsymbol{n}_\mathrm{c}$ and solving for the magnitude of the total impulse vector yields:

$$\hat{f}_\mathrm{n}^\mathrm{bb} = \frac{m_{\mathrm{b},1}\, m_{\mathrm{b},2}}{m_{\mathrm{b},1} + m_{\mathrm{b},2}} \left[\left(\boldsymbol{u}_{\mathrm{b},2}^{+} - \boldsymbol{u}_{\mathrm{b},1}^{+} \right) - \left(\boldsymbol{u}_{\mathrm{b},2}^{-} - \boldsymbol{u}_{\mathrm{b},1}^{-} \right) \right] \cdot \boldsymbol{n}_\mathrm{c}. \tag{5.8}$$

The normal restitution coefficient of a bubble-bubble collision is defined in a similar manner as the one for a bubble-wall collision, i.e., $e_{\mathrm{n,b}}$ is given by:

$$e_{\mathrm{n,b}} = -\frac{\left(\boldsymbol{u}_{\mathrm{b},2}^{+} - \boldsymbol{u}_{\mathrm{b},1}^{+} \right) \cdot \boldsymbol{n}_\mathrm{c}}{\left(\boldsymbol{u}_{\mathrm{b},2}^{-} - \boldsymbol{u}_{\mathrm{b},1}^{-} \right) \cdot \boldsymbol{n}_\mathrm{c}} \quad \text{with} \quad 0 < e_{\mathrm{n,b}} \leq 1. \tag{5.9}$$

By inserting Eq. (5.9) into Eq. (5.8) one obtains the impulse vector solely depending on the bubble velocities prior to the collision:

$$\hat{f}_\mathrm{n}^\mathrm{bb} = -\frac{m_{\mathrm{b},1}\, m_{\mathrm{b},2}}{m_{\mathrm{b},1} + m_{\mathrm{b},2}} \left(1 + e_{\mathrm{n,b}}\right) \left(\boldsymbol{u}_{\mathrm{b},2}^{-} - \boldsymbol{u}_{\mathrm{b},1}^{-} \right) \cdot \boldsymbol{n}_\mathrm{c}. \tag{5.10}$$

Consequently, the velocities of the bubbles after the collision are given by combining Eqs. (5.5) and (5.10) and solving for the respective velocities:

$$\boldsymbol{u}_{\mathrm{b},1}^{+} = \boldsymbol{u}_{\mathrm{b},1}^{-} - \frac{1}{m_{\mathrm{b},1}} \hat{\boldsymbol{f}}^\mathrm{bw} = \boldsymbol{u}_{\mathrm{b},1}^{-} + \frac{m_{\mathrm{b},2}}{m_{\mathrm{b},1} + m_{\mathrm{b},2}} \left(1 + e_{\mathrm{n,b}}\right) \left[\left(\boldsymbol{u}_{\mathrm{b},2}^{-} - \boldsymbol{u}_{\mathrm{b},1}^{-} \right) \cdot \boldsymbol{n}_\mathrm{c} \right] \boldsymbol{n}_\mathrm{c}, \tag{5.11a}$$

$$\boldsymbol{u}_{\mathrm{b},2}^{+} = \boldsymbol{u}_{\mathrm{b},2}^{-} + \frac{1}{m_{\mathrm{b},2}} \hat{\boldsymbol{f}}^\mathrm{bw} = \boldsymbol{u}_{\mathrm{b},2}^{-} - \frac{m_{\mathrm{b},1}}{m_{\mathrm{b},1} + m_{\mathrm{b},2}} \left(1 + e_{\mathrm{n,b}}\right) \left[\left(\boldsymbol{u}_{\mathrm{b},2}^{-} - \boldsymbol{u}_{\mathrm{b},1}^{-} \right) \cdot \boldsymbol{n}_\mathrm{c} \right] \boldsymbol{n}_\mathrm{c}. \tag{5.11b}$$

As before, the normal restitution coefficient $e_{\mathrm{n,b}}$ has to be specified prior to the simulation similar to bubble-wall collisions (Section 4.2.4). However, to the best of the author's knowledge for the case of inter-bubble collisions no literature on the restitution coefficient is available. Hence, similar to bubble-wall collisions the normal restitution coefficient is set to $e_{\mathrm{n,b}} = 1$ in the present thesis as done by Darmana et al. (2006). According to Eq. (5.11) the bubbles experience a change in the normal velocity component during the collision, whereas the tangential component remains unchanged. Additionally, it is remarked here that the method for the detecting of a collision between two bubbles will be explained in Chapter 9, where the numerical methodology used in the present thesis is described. The possibility of coalescence of the colliding bubbles will be also discussed separately in Chapter 7.

6 Modeling of Subgrid-Scale Fluctuations for the Lagrangian Particle Tracking

It is known from a number of studies that the subgrid scales of LES affect the evolution of the dispersed phase (see, e.g., Armenio et al., 1999; Breuer and Almohammed, 2015; Breuer and Hoppe, 2017; Kuerten and Vreman, 2005; Marchioli et al., 2008; Pozorski and Apte, 2009). Consequently, in the equations of motion of the bubbles (Eqs. (4.1) and (4.2)) the full fluid velocity at the bubble position given by Eq. (5.2) is required, i.e., a modeled subgrid-scale velocity has to be added to the filtered fluid velocity provided by LES. As argued in the literature overview in Section 2.1, the description of the subgrid scales seen by the bubbles based on a stochastic model is among the most promising approaches. Stochastic differential equations (SDE) originate from the description of the random process of Brownian motion of a particle suspended in water by Langevin (1908) leading to the denotation of SDEs as *Langevin* equations. Later, among various other applications (see, e.g., Gardiner, 2003; Kloeden and Platen, 1995), Langevin equations were used in the Euler–Lagrange framework to model the unresolved subgrid scales of the fluid velocity acting on the dispersed phase (Berrouk et al., 2007, 2008; Fede et al., 2006; Minier et al., 2004, 2014; Minier and Peirano, 2001; Pozorski and Apte, 2009).

In this chapter the presently used subgrid-scale model is presented. First, in Section 6.1 a brief overview on the theoretical background of stochastic differential equations is given. In Section 6.2 the Langevin-based approach by Pozorski and Apte (2009) is presented. Afterwards, in Section 6.3 the drawbacks previously discussed in Section 2.1 of the model by Pozorski and Apte (2009) are removed by introducing several enhancements. This also involves a solution method introduced in Section 6.4 for the enhanced Langevin equation which does not impose a stability constraint. Note that most of these considerations have already been published in Breuer and Hoppe (2017, 2018).

6.1 Theoretical Background on Langevin Equations

The purpose of this brief introduction to stochastic differential equations is to help the reader to understand the concept of the stochastic modeling of the subgrid scales. Furthermore, the theoretical derivation of the mean and the variance of the Ornstein–Uhlenbeck process (Gardiner, 2003; Kloeden and Platen, 1995) described below is required for the solution method of the present subgrid-scale model explained in Section 6.4.

Stochastic differential equations describe the evolution of an arbitrary, time-dependent stochastic quantity X. According to Gardiner (2003) and Kloeden and Platen (1995) all Langevin equations can be written in the form:

$$\mathrm{d}X = A(X,\, t)\,\mathrm{d}t + B(X,\, t)\,\mathrm{d}W. \tag{6.1}$$

In Eq. (6.1) the term $A(X,\, t)$ denotes the drift term driving the stochastic variable towards a certain average solution in time, while $B(X,\, t)$ is the stochastic diffusion term which randomly perturbs X. Note that the actual form of the drift and diffusion term can vary giving rise to specific, well-known stochastic processes like the white-noise process or the Ornstein–Uhlenbeck process (Gardiner, 2003). The diffusion term in Eq. (6.1) depends on the increment $\mathrm{d}W$ of a Wiener process W, which is a time-dependent, stochastic process. According to Kloeden and Platen (1995) a Wiener process describes the evolution of a probabilistic system by a sequence of random variables, where W has to obey the following properties:

$$\text{Zero initial condition:} \qquad W_{t=0} = 0, \tag{6.2a}$$

$$\text{Gaussian distribution:} \qquad W_t - W_{t_0} = \mathcal{N}(0,\, t - t_0)\,, \tag{6.2b}$$

$$\text{Independence:} \qquad [W_{t_2} - W_{t_1}] \perp [W_{t_1} - W_{t_0}]\,. \tag{6.2c}$$

Equation (6.2a) means that a Wiener process has a zero initial condition, i.e., the random process starts with a value of zero. Equation (6.2b) defines that the increment $W_t - W_{t_0}$ of the Wiener process between the points t and t_0 in time follows a Gaussian distribution $\mathcal{N}$ with a vanishing mean and a variance equal to the difference $t - t_0$. Lastly, in Eq. (6.2c) the perpendicular symbol $\perp$ describes that all increments of the Wiener process are independent from each other, i.e., the Wiener process at a certain instant in time does not depend on previous realizations of W.

A special type of stochastic processes is the Ornstein–Uhlenbeck process (Gardiner, 2003; Kloeden and Platen, 1995), which is introduced here since the modeling of the subgrid scales by the approach of Pozorski and Apte (2009) corresponds to an Ornstein–Uhlenbeck process. The Ornstein–Uhlenbeck process is characterized by the following form of the Langevin equation (Gardiner, 2003; Kloeden and Platen, 1995):

$$\mathrm{d}X = -a\,X\mathrm{d}t + b\,\mathrm{d}W, \tag{6.3}$$

where both a and b are arbitrary positive constants defining how fast the stochastic process drifts towards its mean solution and how strong the randomness of the process is, respectively. Hence, the drift term $(-a\,X)$ of the SDE depends only on the stochastic variable X but not on the time, while the randomness of the process is given by a constant stochastic diffusion term b. The solution to the Ornstein–Uhlenbeck process can be

obtained by integration of Eq. (6.3), see, e.g., Gardiner (2003) for a detailed derivation. Hence, the solution to the stochastic process defined by Eq. (6.3) is given by:

$$X(t) = X(t_0)\,\mathrm{e}^{-a(t-t_0)} + \int_{t_0}^{t} \mathrm{e}^{-a(t-t')}\,b\,\mathrm{d}W'. \tag{6.4}$$

Note that the prime appearing in the second term of the r.h.s. of Eq. (6.4) indicates that the integral over the Wiener process $\mathrm{d}W'$ depends on the variable of integration t', where the prime is introduced to distinguish t' from the present instant in time t. Due to the stochastic nature of the Wiener process, this integral can not be solved analytically. The reason behind this is the fact that for each time step the integral yields a different, normally distributed value. However, it is possible to use Eq. (6.4) to estimate the mean value, which the Ornstein-Uhlenbeck process approaches in time and the corresponding variance (Gardiner, 2003; Kloeden and Platen, 1995). The mean value of the Ornstein-Uhlenbeck process can be readily determined by averaging Eq. (6.4) yielding:

$$\langle X(t)\rangle = \langle X(t_0)\rangle\,\mathrm{e}^{-a(t-t_0)}. \tag{6.5}$$

In order to obtain Eq. (6.5) it is utilized that the mean of a Wiener process is zero. Hence, on average the stochastic integral appearing in Eq. (6.4) vanishes as well. From Eq. (6.5) it is obvious that for $t \to \infty$ the Ornstein–Uhlenbeck process approaches a mean value of zero, which is reasonable since the Wiener process randomly disturbing the stochastic process has a vanishing mean as well. The variance of the Ornstein–Uhlenbeck process is given by the well-known relation:

$$\mathrm{Var}\,[X(t)] = \langle X^2(t)\rangle - \langle X(t)\rangle^2, \tag{6.6}$$

where $\langle X(t)\rangle$ and $\langle X^2(t)\rangle$ are commonly referred to as first and second moments of the random variable X. The first term on the r.h.s. of Eq. (6.6) is calculated by squaring Eq. (6.4) and then taking the average. Thus, $\langle X^2(t)\rangle$ is given by the relation:

$$\begin{aligned}\langle X^2(t)\rangle = \langle X^2(t_0)\rangle\,\mathrm{e}^{-2\,a(t-t_0)} &+ \underbrace{\left\langle 2\,X(t_0)\,\mathrm{e}^{-a(t-t_0)} \int_{t_0}^{t} \mathrm{e}^{-a(t-t')}\,b\,\mathrm{d}W' \right\rangle}_{=0} \\ &+ \left\langle \int_{t_0}^{t} \mathrm{e}^{-a(t-t')}\,b\,\mathrm{d}W' \int_{t_0}^{t} \mathrm{e}^{-a(t-t')}\,b\,\mathrm{d}W' \right\rangle.\end{aligned} \tag{6.7}$$

In the first line of Eq. (6.7) again the vanishing mean of the Wiener process is used to eliminate the second term on the right-hand side. The third term on the r.h.s. of Eq. (6.7) can be transformed to a simple integral in time by applying an identity of the Wiener

process given for example by Gardiner (2003). Consequently, $\langle X^2(t) \rangle$ can be determined according to:

$$\begin{aligned} \langle X^2(t) \rangle &= \langle X^2(t_0) \rangle \, \mathrm{e}^{-2\,a(t-t_0)} + \left\langle \int_{t_0}^{t} \mathrm{e}^{-2\,a(t-t')} \, b^2 \, \mathrm{d}t' \right\rangle \\ &= \langle X^2(t_0) \rangle \, \mathrm{e}^{-2\,a(t-t_0)} + \frac{b^2}{2\,a} \left[1 - \mathrm{e}^{-2\,a(t-t_0)} \right] . \end{aligned} \tag{6.8}$$

Consequently, the variance can be determined by inserting Eq. (6.8) and the square of Eq. (6.5) into Eq. (6.6). After some minor re-arrangements, the variance of an Ornstein–Uhlenbeck process is given by:

$$\mathrm{Var}\left[X(t) \right] = \mathrm{Var}\left[X(t_0) \right] \mathrm{e}^{-2\,a(t-t_0)} + \frac{b^2}{2\,a} \left[1 - \mathrm{e}^{-2\,a(t-t_0)} \right] . \tag{6.9}$$

Hence, the variance of an Ornstein–Uhlenbeck process approaches a constant value of $b^2/2\,a$ for $t \to \infty$.

6.2 Subgrid-Scale Model of Pozorski and Apte (2009)

As previously mentioned, the starting point of the subgrid-scale modeling in the present thesis is the normalized Langevin model by Pozorski and Apte (2009). Recapitulating Section 2.1, the basic assumptions made by Pozorski and Apte (2009) are that the fluid turbulence is homogeneous and isotropic and that the direction of the relative motion defined by the difference of the (filtered) fluid velocity and the particle velocity is aligned with one of the three major Cartesian axes of the flow. The meaning behind the latter assumption will be explained in more detail below. Additionally, it has to be remembered that the approach by Pozorski and Apte (2009) solely considers the subgrid-scale velocities, in contrast to other models existing in the literature modeling the full fluid velocity (see, e.g., Berrouk et al., 2007, 2008; Minier et al., 2014).

Using these simplifications, Pozorski and Apte (2009) proposed to describe the fluctuating subgrid-scale velocities $u_{\mathrm{s},i}^{\prime\mathrm{R}}$ by the following Langevin equation:

$$\mathrm{d}u_{\mathrm{s},i}^{\prime\mathrm{R}} = -\frac{u_{\mathrm{s},i}^{\prime\mathrm{R}}}{\tau_{\mathrm{L}}^{\prime}} \, \mathrm{d}t + \sqrt{\frac{2\,\sigma_{\mathrm{SGS}}^2}{\tau_{\mathrm{L}}^{\prime}}} \, \mathrm{d}W_i \, . \tag{6.10}$$

In Eq. (6.10) the terms $\tau_{\mathrm{L}}^{\prime}$ and σ_{SGS} refer to characteristic time scales and the characteristic velocity of the subgrid scales seen by the particle, respectively. The increments $\mathrm{d}W_i$ of a Wiener process are defined by Eq. (6.2) in the previous section, i.e., they obey a Gaussian distribution with zero mean and the variance equal to the increment of the time step. The superscript R denotes that the direction of the relative velocity of the particle to the fluid is aligned with one of the Cartesian axes of the Eulerian fluid flow. Additionally, the index s indicates that Eq. (6.10) models the subgrid-scale velocity of the fluid seen by the

particle, cf. Section 5.1. Comparing Eqs. (6.3) and (6.10) it immediately becomes obvious that the modeling of the subgrid scales by the approach of Pozorski and Apte (2009) is indeed equivalent to an Ornstein–Uhlenbeck process. The first term on the r.h.s. of Eq. (6.10) is the drift term of the stochastic process, while the second term represents the random diffusion term.

In the approach by Pozorski and Apte (2009) τ_L' appearing in Eq. (6.10) describes the characteristic time scales over which the subgrid-scale fluctuations seen by the particle are correlated. Since Pozorski and Apte (2009) assume that the direction of the relative velocity $\boldsymbol{u}_\mathrm{r}$ is aligned with one of the Cartesian axes of the flow, τ_L' has to be distinguished into the time scales $\tau_{\mathrm{L},\parallel}'$ of the fluctuations in the corresponding direction and $\tau_{\mathrm{L},\perp}'$ in the two remaining spatial directions. Consequently, the time scales $\tau_{\mathrm{L},\parallel}'$ and $\tau_{\mathrm{L},\perp}'$ are given by:

$$\tau_{\mathrm{L},\parallel}' = \frac{\tau_\mathrm{SGS}}{\sqrt{1+\beta^2\frac{|\boldsymbol{u}_\mathrm{r}|^2}{\sigma_\mathrm{SGS}^2}}}, \tag{6.11a}$$

$$\tau_{\mathrm{L},\perp}' = \frac{\tau_\mathrm{SGS}}{\sqrt{1+4\,\beta^2\frac{|\boldsymbol{u}_\mathrm{r}|^2}{\sigma_\mathrm{SGS}^2}}}\,. \tag{6.11b}$$

It is apparent from Eq. (6.11) that $\tau_{\mathrm{L},\parallel}'$ and $\tau_{\mathrm{L},\perp}'$ are connected to the time scales τ_SGS of the subgrid scales, i.e., the time scales during which the subgrid-scale fluctuations decay. Since the crossing-trajectory effect and the continuity effect are taken into account by Pozorski and Apte (2009), it is possible that a particle leaves the corresponding eddy before it decayed. Hence, the time scales $\tau_{\mathrm{L},\parallel}'$ and $\tau_{\mathrm{L},\perp}'$ of the subgrid-scale fluctuations seen by the particle are shorter than τ_SGS. Consequently, the characteristic time scales of the subgrid scales have to be multiplied by the factors of Csanady (1963) given by Eq. (6.11). Furthermore, this leads to the distinction of the time scales τ_L' into directions parallel and perpendicular to the direction of the relative velocity $\boldsymbol{u}_\mathrm{r}$. As already explained in Section 2.1.2 this distinction is necessary due to the following reason. Since a particle leaving an eddy in a direction perpendicular to the relative velocity exhibits subgrid-scale fluctuations which are less correlated to the original fluctuations, the time scales in these directions are shorter than the time scales in the direction parallel to the relative velocity. According to Csanady (1963), this property is reflected by the additional factor of four in Eq. (6.11b) in comparison to Eq. (6.11a).

The time scales of the subgrid-scale fluctuations can be estimated according to (Pozorski and Apte, 2009) by:

$$\tau_\mathrm{SGS} = C\,\frac{\Delta}{\sigma_\mathrm{SGS}}\,, \tag{6.12}$$

where Δ again denotes the filter width of the large-eddy simulation. According to Pozorski and Apte (2009) the model constant C is of the order of $\mathcal{O}(1)$ and, therefore, set to unity in the present thesis. The factor β appearing in Eq. (6.11) is a model constant defined as the ratio of the Lagrangian time scale to the Eulerian time scale (Pozorski and Apte, 2009). Different values of β exist throughout the literature. For example, Berrouk et al. (2007, 2008) and Cernick et al. (2015) use $\beta = 0.356$ as proposed by Wang and Stock

(1993), while Pozorski and Apte (2009) set $\beta = 1$. Here, the suggestion of Pozorski and Apte (2009) is followed. Lastly, it remains to specify the characteristic velocity of the subgrid-scale fluctuations. Pozorski and Apte (2009) proposed to estimate σ_{SGS} by the turbulent kinetic energy k_{SGS} of the subgrid scales:

$$\sigma_{\mathrm{SGS}} = \sqrt{\frac{2}{3}\, k_{\mathrm{SGS}}}\,. \tag{6.13}$$

Note that Pozorski and Apte (2009) did not explicitly specify how the turbulent kinetic energy k_{SGS} is determined. In the present thesis the approach by Bardina et al. (1980) is used, see Eq. (6.18) in the following section.

6.3 Enhanced Langevin Subgrid-Scale Model

The major drawback of the model by Pozorski and Apte (2009) is that Eq. (6.10) is formulated under the assumption that the direction of the relative velocity of the particles is aligned with one of the Cartesian axes of the Eulerian flow. Consequently, the component of the subgrid-scale velocities corresponding to this major axis is related to subgrid-scale fluctuations decaying with a time scale of $\tau'_{\mathrm{L},\parallel}$ given by Eq. (6.11a). The remaining two components of $u'_{\mathrm{s},i}$ depend on faster decaying subgrid-scale fluctuations, i.e., the time scales are given by $\tau'_{\mathrm{L},\perp}$ (Eq. (6.11b)). In the case that the direction of the relative velocity is not aligned with one of the Cartesian axes, the subgrid-scale fluctuations in the corresponding direction obviously decay within a time scale that is smaller than $\tau'_{\mathrm{L},\parallel}$ but larger than $\tau'_{\mathrm{L},\perp}$. Since an arbitrary orientation of the direction of the relative velocity is the general case, in practically relevant applications the drift and diffusion terms have to be matrices (Minier et al., 2004, 2014), which incorporate the different time scales with which the subgrid-scale fluctuations decay. Hence, it was proposed by Breuer and Hoppe (2017) to extend the original model of Pozorski and Apte (2009) by formulating the stochastic differential equation in a matrix form. The extended version of the Langevin equation is given by:

$$du'_{\mathrm{s},i} = -G_{ij}\, u'_{\mathrm{s},j}\, dt + \sqrt{2\,\sigma^2_{\mathrm{SGS}}}\, B_{ij}\, dW_j\,. \tag{6.14}$$

Note that in Eq. (6.14) the superscript R is dropped, because the restriction of the model by Pozorski and Apte (2009) concerning the alignment of the relative velocity with one of the major axes of the fluid is not required in the above matrix formulation. In Eq. (6.14) G_{ij} and B_{ij} are the drift and diffusion matrices of the stochastic process, which are defined by (Minier et al., 2014):

$$G_{ij} = \frac{1}{\tau'_{\mathrm{L},\perp}}\,\delta_{ij} + \left(\frac{1}{\tau'_{\mathrm{L},\parallel}} - \frac{1}{\tau'_{\mathrm{L},\perp}}\right) r_i\, r_j, \tag{6.15}$$

$$B_{ij} = \frac{1}{\sqrt{\tau'_{\mathrm{L},\perp}}}\,\delta_{ij} + \left(\frac{1}{\sqrt{\tau'_{\mathrm{L},\parallel}}} - \frac{1}{\sqrt{\tau'_{\mathrm{L},\perp}}}\right) r_i\, r_j. \tag{6.16}$$

The definition of the time scales $\tau'_{\mathrm{L},\parallel}$ and $\tau'_{\mathrm{L},\perp}$ of the subgrid-scale fluctuations seen by the particles is the same as given by Eq. (6.11). The factors r_i are the respective vector components of the direction of the relative velocity of the particle to the fluid:

$$r_i = \frac{u_{\mathrm{r},i}}{|\boldsymbol{u}_\mathrm{r}|}. \tag{6.17}$$

One can readily see from Eqs. (6.15) and (6.16) that the matrices G_{ij} and B_{ij} yield the correct time scales of the subgrid scales. For example, in the case that the relative velocity is aligned with one of the major axes of the flow, the drift and diffusion matrices G_{ij} and B_{ij} given by Eqs. (6.15) and (6.16) are diagonal matrices. The diagonal components of G_{ij} and B_{ij} corresponding to the according Eulerian axis are given by $1/\tau'_{\mathrm{L},\parallel}$ and $1/\sqrt{\tau'_{\mathrm{L},\parallel}}$, respectively. The remaining two diagonal components correspond to the directions perpendicular to the relative velocity and, thus, the diagonal elements are $1/\tau'_{\mathrm{L},\perp}$ and $1/\sqrt{\tau'_{\mathrm{L},\perp}}$. Hence, the simple Langevin equation (6.10) by Pozorski and Apte (2009) is recovered. On the other hand, in the case that the relative velocity points in a direction not aligned with one of the major axes, the time scales over which the subgrid-scale fluctuations decay given by G_{ij} and B_{ij} are indeed larger than $\tau'_{\mathrm{L},\perp}$ but smaller than $\tau'_{\mathrm{L},\parallel}$.

The solution of Eq. (6.14) requires to specify the characteristic subgrid-scale velocity σ_SGS given by Eq. (6.13). Hence, the turbulent kinetic energy k_SGS associated with the subgrid scales has to be estimated. In the present thesis, this is done using an approach by Bardina et al. (1980) who proposed to double-filter the fluid velocity field:

$$k_\mathrm{SGS} = \frac{1}{2}\left(\overline{\boldsymbol{u}}_\mathrm{f} - \overline{\overline{\boldsymbol{u}}}_\mathrm{f}\right)^2. \tag{6.18}$$

The double-filtering of the fluid field in Eq. (6.18) relies on a filter width of $\tilde{\Delta} = 2\,\Delta$ by accounting for the 27 neighboring grid points with weighting factors based on a trilinear interpolation.

Lastly, it has to be noted that Pozorski and Apte (2009) devised their model to be applied to the case of decaying turbulence in a box. However, in many applications the flow is bounded by solid walls. Therefore, Breuer and Hoppe (2017) proposed an additional advancement of the approach by Pozorski and Apte (2009) by including wall effects in the modeling. This is achieved by taking the wall damping by van Driest (1956) into account. Hence, in Eq. (6.12) used to estimate the time scales τ_SGS of the subgrid-scale fluctuations, the filter width Δ is replaced by $\Delta \cdot f_\mathrm{wd}$ with f_wd given by Eq. (3.17).

In summary, in the form of Eq. (6.14) the subgrid-scale model by Pozorski and Apte (2009) extended by Breuer and Hoppe (2017) can account for the temporal coupling of the subgrid-scale velocity fluctuations with arbitrary orientations of the particle motion with respect to the Eulerian frame of reference. Additionally, the continuity effect and the crossing-trajectory effect are included in the modeling, since the time scales appearing in the matrices G_{ij} and B_{ij} include the factors of Csanady (1963). By incorporating the wall damping function of van Driest (1956) the present subgrid-scale model can be applied to wall-bounded flows.

6.4 Solution Method

The Langevin-based subgrid-scale model described in the previous section can be solved numerically in two ways, i.e., by an explicit Euler–Maruyama scheme or by an integration-based scheme. Both methods are presented in the following.

6.4.1 Euler–Maruyama Scheme

The first possibility is to directly solve Eq. (6.14) by an explicit Euler–Maruyama scheme (Kloeden and Platen, 1995). For example, this approach was used by Fede et al. (2006). The Euler–Maruyama scheme relies on the property (6.2b) of the Wiener process, i.e., that the increment of a Wiener process follows a Gaussian distribution with zero mean and a variance equal to the time-step size Δt. According to Kloeden and Platen (1995) this property can be used to model the increment $\mathrm{d}W_j$ of the Wiener process by the square-root of its variance:

$$\mathrm{d}W_j = \sqrt{\mathrm{Var}\left(\Delta W_j\right)}\,\xi_j = \sqrt{\left\langle \Delta W_j^2 \right\rangle}\,\xi_j = \sqrt{\Delta t}\,\xi_j\,. \tag{6.19}$$

In Eq. (6.19) ξ_j is a three-dimensional, normally distributed random vector with zero mean and unit variance, i.e., $\xi_j = \mathcal{N}(0,1)$. Consequently, Eq. (6.14) can be written in the form:

$$u_{\mathrm{s},i}^{\prime\,(n+1)} = u_{\mathrm{s},i}^{\prime\,(n)} - G_{ij}\,u_{\mathrm{s},j}^{\prime\,(n)}\,\Delta t + \sqrt{2\,\sigma_{\mathrm{SGS}}^2\,\Delta t}\,B_{ij}\,\xi_j\,, \tag{6.20}$$

where the superscripts (n) and $(n+1)$ denote the previous and the present time step, respectively. It is obvious that the main advantage of estimating the subgrid-scale fluctuations by an Euler–Maruyama scheme is the simple and straightforward implementation of Eq. (6.20). However, a scheme of the form of Eq. (6.20) is not unconditionally stable, i.e., restrictions in form of numerical instabilities exist. In other words, the Euler–Maruyama scheme has to fulfill the constraint:

$$\max\left(G_{ij}\,\Delta t\right) \ll 1, \tag{6.21}$$

for all elements of the drift matrix G_{ij}. If Eq. (6.21) is not satisfied, the Euler–Maruyama scheme becomes unstable. Remembering the definition (6.15) of the drift matrix G_{ij}, it becomes apparent that the stability constraint given by Eq. (6.21) depends on the filter width Δ and on the characteristic velocity of the subgrid scales σ_{SGS}. Inserting Eq. (6.15) into Eq. (6.21) allows to formulate the stability condition of the Euler–Maruyama scheme in form of an approximated restriction on the time-step size of the simulation:

$$\Delta t \ll \frac{\Delta}{\sigma_{\mathrm{SGS}}} = \frac{\Delta}{\sqrt{\frac{2}{3}\,k_{\mathrm{SGS}}}}. \tag{6.22}$$

It can be seen from Eq. (6.22) that the stability constraint of the Euler–Maruyama scheme is problematic in wall-bounded flows. As already argued in Section 3.3.1, in the case of a wall-resolved LES the grid spacing has to decrease in the vicinity of a solid wall imposing

harsh restrictions on the timer-step size Δt. Therefore, a scheme of the form of Eq. (6.20) is strongly unfavorable and unfeasible for the intended simulations.

6.4.2 Integration-based Scheme

An alternative to the Euler–Maruyama scheme was proposed by Minier et al. (2003) and Peirano et al. (2006). In their approaches the fact is used that a Langevin equation corresponding to an Ornstein–Uhlenbeck process can be solved by an analytic integration. Consequently, an integration-based scheme is obtained, which has the advantage that it is not restricted by the time step. Therefore, this approach was recommended by several authors (see, e.g., Berrouk et al., 2007, 2008; Pozorski and Apte, 2009).

Similar to the considerations made in Section 6.1, the present Langevin equation (6.14) can be integrated between the time instants t_0 and t yielding the subgrid-scale velocities seen by the particles:

$$u'_{\mathrm{s},i}(t) = E_{ij}(t,t_0)\,u'_{\mathrm{s},j}(t_0) + \sqrt{2\,\sigma^2_{\mathrm{SGS}}}\int_{t_0}^{t} E_{ik}(t,t')\,B_{kj}\,dW_j(t'). \tag{6.23}$$

Since Eq. (6.14) is a matrix equation, its solution is a matrix formulation as well. Hence, in Eq. (6.23) the matrix $E_{ij}(t,t_0)$ denotes the time-dependent matrix exponential of the drift matrix G_{ij}. The second term on the r.h.s. of Eq. (6.23) is the diffusion term of the stochastic process. A common definition of a matrix exponential is via the series expansion of the exponential function:

$$E_{ij}(t,t_0) = \sum_{n=0}^{\infty} \frac{(G_{ij})^n\,(t-t_0)^n}{n!}. \tag{6.24}$$

However, determining the matrix exponential of G_{ij} by Eq. (6.24) is unfavorable, because a large number of matrix multiplications is required. Fortunately, another advantage of the model by Pozorski and Apte (2009) is that the exponential of the drift matrix G_{ij} can be determined analytically. The reason behind this is that the drift matrix G_{ij} is symmetric. Hence, G_{ij} is diagonalizable, i.e., a normal, orthogonal transformation matrix S_{ij} exists fulfilling the characteristic equation:

$$G_{ij} = S_{ik}\,D_{kl}\,S^{-1}_{lj}. \tag{6.25}$$

In Eq. (6.25) the diagonal matrix $D_{kl} = \lambda^{(k)}\delta_{kl}$[1] contains the three eigenvalues ($\lambda^{(1)}$, $\lambda^{(2)}$, $\lambda^{(3)}$) of the drift matrix. One can readily confirm that in the present case the eigenvalues $\lambda^{(k)}$ of the drift matrix G_{ij} are given by the inverses of the time scales $1/\tau'_{\mathrm{L},\parallel}$ and $1/\tau'_{\mathrm{L},\perp}$. Note that $1/\tau'_{\mathrm{L},\perp}$ has to appear twice in the diagonal of D_{kl}, because two directions are perpendicular to the direction of the relative velocity.

[1] Note that the superscript (k) is supposed to indicate that three eigenvalues are considered for the three diagonal elements of D_{kl}. Hence, no summation over the index k is implied here.

The fact that G_{ij} is diagonalizable can be used to determine the matrix exponential $E_{ij}(t, t_0)$. The matrix exponential of a diagonalizable matrix is simply the matrix product of the exponential of the diagonal matrix with the corresponding transformation matrices S_{ik} and S_{lj}^{-1}. Hence, the matrix exponential of the drift matrix is defined by:

$$E_{ij}(t, t_0) = S_{ik} \exp\left[-\lambda^{(k)}\,(t - t_0)\right] \delta_{kl}\, S_{lj}^{-1}. \tag{6.26}$$

One can readily confirm that Eq. (6.26) is correct by inserting Eq. (6.25) into Eq. (6.24). By explicitly calculating the matrix multiplications and using the orthogonality of the transformation matrix ($S_{ij}\, S_{jk}^{-1} = \delta_{ik}$) one obtains Eq. (6.26). Consequently, it remains to specify a transformation matrix S_{ij} in order to fully determine the matrix exponential E_{ij}. One possible form of S_{ij} is given by:

$$S_{ij} = \begin{pmatrix} r_x & \dfrac{r_z}{\sqrt{r_x^2 + r_z^2}} & -\dfrac{r_x r_y}{\sqrt{r_x^2 + r_z^2}} \\ r_y & 0 & \dfrac{r_x^2 + r_z^2}{\sqrt{r_x^2 + r_z^2}} \\ r_z & -\dfrac{r_x}{\sqrt{r_x^2 + r_z^2}} & -\dfrac{r_y r_z}{\sqrt{r_x^2 + r_z^2}} \end{pmatrix}, \tag{6.27}$$

which can be confirmed by inserting Eq. (6.27) into Eq. (6.25). Since S_{ij} is a normal and orthogonal matrix, the inverse S_{ij}^{-1} of the transformation matrix is given by the transposed version of S_{ij}, i.e., $S_{ij}^{-1} = S_{ij}^{\mathrm{T}}$. Therefore, by inserting Eq. (6.27) into Eq. (6.26) one can explicitly determine the matrix exponential of the drift matrix G_{ij}:

$$E_{ij}(t, t_0) = E_{\perp}(t, t_0)\, \delta_{ij} + \left[E_{\parallel}(t, t_0) - E_{\perp}(t, t_0)\right] r_i\, r_j, \tag{6.28}$$

where the time-dependent coefficients $E_{\parallel}(t, t_0)$ and $E_{\perp}(t, t_0)$ are given by:

$$E_{\parallel}(t, t_0) = \exp\left(-\frac{t - t_0}{\tau'_{\mathrm{L},\parallel}}\right), \tag{6.29a}$$

$$E_{\perp}(t, t_0) = \exp\left(-\frac{t - t_0}{\tau'_{\mathrm{L},\perp}}\right). \tag{6.29b}$$

Since in the simulation t and t_0 are the present and previous instant in time, the difference between the time instants is equal to the time-step size, i.e., $t - t_0 = \Delta t$.

With $E_{ij}(t, t_0)$ specified, it remains to determine the stochastic integral appearing in Eq. (6.23). As already argued in Section 6.1, the integral over the Wiener process cannot be evaluated directly due to its stochastic nature. Hence, the integral is modeled by

multiplying the square-root of the covariance matrix of the stochastic process with a normally distributed random number (Minier et al., 2003; Peirano et al., 2006):

$$\sqrt{2\,\sigma_{\mathrm{SGS}}^2}\int_{t_0}^{t} E_{ik}(t,t')\,B_{kj}\,dW_j(t') = \sqrt{\mathrm{Cov}\left[u'_{\mathrm{s},i}(t)\,u'_{\mathrm{s},j}(t)\right]}\,\xi_j = W_{ij}(t,t_0)\,\xi_j. \tag{6.30}$$

In Eq. (6.30) the matrix W_{ij} is the square-root of the covariance matrix. In contrast to Section 6.1, where an one-dimensional stochastic process was considered, it is necessary to use the covariance matrix, since Eq. (6.14) is a matrix equation. Nevertheless, the considerations made in Section 6.1 are still valid. Hence, the covariance matrix is given by the first two moments of the stochastic process described by Eq. (6.23). Additionally, the initial conditions for both moments are assumed to be zero (Minier et al., 2003; Peirano et al., 2006). Due to this simplification, the first moment $\langle u'_{\mathrm{s},i}(t_0)\rangle$ and the second moment $\langle u'_{\mathrm{s},i}(t_0)\,u'_{\mathrm{s},j}(t_0)\rangle$ are zero at the time instant t_0. Consequently, the covariance matrix is reduced to:

$$\begin{aligned}\mathrm{Cov}\left[u'_{\mathrm{s},i}(t)\,u'_{\mathrm{s},j}(t)\right] &= 2\,\sigma_{\mathrm{SGS}}^2\int_{t_0}^{t} E_{ik}(t,t')\,B_{km}\,B_{ml}\,E_{lj}(t,t')\,dt' \\ &= 2\,\sigma_{\mathrm{SGS}}^2\,G_{ik}\int_{t_0}^{t} E_{kl}(t,t')\,E_{lj}(t,t')\,dt'.\end{aligned} \tag{6.31}$$

In order to obtain the final form of Eq. (6.31) the fact that the diffusion matrix B_{ij} is defined as the square-root of the drift matrix G_{ij} is used, i.e., $B_{km}\,B_{ml} = G_{kl}$. An advantageous property of the drift matrix is that it commutes with its own matrix exponential. Since $E_{ik}(t,t')\,G_{kl} = G_{ik}\,E_{kl}(t,t')$, the drift matrix can be pulled out of the integral resulting in the final form of Eq. (6.31). The integral in Eq. (6.31) can be evaluated by inserting Eq. (6.26) for the two matrix exponentials $E_{kl}(t,t')$ and $E_{lj}(t,t')$:

$$\begin{aligned}\int_{t_0}^{t} E_{kl}(t,t')\,E_{lj}(t,t')\,dt' &= \int_{t_0}^{t} S_{km}\,\exp\left[-2\,\lambda^{(m)}\,(t-t')\right]\,\delta_{ml}\,S_{lj}^{-1}\,dt' \\ &= \frac{1}{2}\,S_{km}\,\underbrace{(\lambda^{(m)})^{-1}\,\delta_{mn}}_{D_{mn}^{-1}}\,\exp\left[-2\,\lambda^{(n)}\,(t-t')\right]\,\delta_{nl}\,S_{lj}^{-1}\Bigg|_{t_0}^{t} \\ &= \frac{1}{2}\,\underbrace{S_{km}\,D_{mn}^{-1}\,S_{nh}^{-1}}_{G_{kh}^{-1}}\,\underbrace{S_{hf}\,\exp\left[-2\,\lambda^{(f)}\,(t-t')\right]\,\delta_{fl}\,S_{lj}^{-1}}_{E_{ho}(t,t')\,E_{oj}(t,t')}\Bigg|_{t_0}^{t} \\ &= \frac{1}{2}\,G_{kh}^{-1}\,(\delta_{hj} - E_{ho}(t,t_0)\,E_{oj}(t,t_0))\,.\end{aligned} \tag{6.32}$$

On the first line of Eq. (6.32) the orthogonality of the transformation matrix is used again. The second line is obtained by integrating the matrix expression over time, which results in the appearance of the inverse D_{mn}^{-1} of the diagonalized drift matrix defined by Eq. (6.25). Next, an unit matrix is inserted into Eq. (6.32) in the form of $I_{nf} = S_{nh}^{-1}\,S_{hf}$ allowing to merge the matrices into the inverse G_{kh}^{-1} of the drift matrix and the product

$E_{ho}(t,t')\,E_{oj}(t,t')$ of the matrix exponentials. In the last step of Eq. (6.32), the boundaries t_0 and t of the integration interval are inserted.

Inserting Eq. (6.32) into Eq. (6.31) yields the final expression of the covariance matrix of the stochastic process:

$$\mathrm{Cov}\left[u'_{\mathrm{s},i}(t)\,u'_{\mathrm{s},j}(t)\right] = \sigma^2_{\mathrm{SGS}}\left(\delta_{ij} - E_{io}(t,t_0)\,E_{oj}(t,t_0)\right). \tag{6.33}$$

Lastly, it remains to take the square-root of the covariance matrix, which can be achieved by inserting Eq. (6.26) for the matrix exponentials in Eq. (6.33) and factoring out the transformation matrices:

$$\mathrm{Cov}\left[u'_{\mathrm{s},i}(t)\,u'_{\mathrm{s},j}(t)\right] = \sigma^2_{\mathrm{SGS}}\,S_{ik}\left(\delta_{kl} - \exp\left[-2\,\lambda^{(k)}\,(t-t_0)\right]\delta_{kl}\right)S^{-1}_{lj}. \tag{6.34}$$

In the form of Eq. (6.34) the square-root W_{ij} of the covariance matrix is obtained by:

$$W_{ij} = \sqrt{\mathrm{Cov}\left[u'_{\mathrm{s},i}(t)\,u'_{\mathrm{s},j}(t)\right]} = \sigma_{\mathrm{SGS}}\,S_{ik}\sqrt{\left(\delta_{kl} - \exp\left[-2\,\lambda^{(k)}\,(t-t_0)\right]\delta_{kl}\right)}\,S^{-1}_{lj}. \tag{6.35}$$

Finally, the square-root of the covariance matrix is fully determined by inserting Eq. (6.27) for the transformation matrix S_{ij} into Eq. (6.35) yielding:

$$W_{ij}(t,t_0) = W_\perp(t,t_0)\delta_{ij} + \left[W_\parallel(t,t_0) - W_\perp(t,t_0)\right] r_i\,r_j, \tag{6.36}$$

with the time-dependent coefficients:

$$W_\parallel(t,t_0) = \sigma_{\mathrm{SGS}}\sqrt{1 - \exp\left[-2\,\frac{t-t_0}{\tau'_{\mathrm{L},\parallel}}\right]}, \tag{6.37a}$$

$$W_\perp(t,t_0) = \sigma_{\mathrm{SGS}}\sqrt{1 - \exp\left[-2\,\frac{t-t_0}{\tau'_{\mathrm{L},\perp}}\right]}. \tag{6.37b}$$

Summarizing the previous derivations, the subgrid-scale velocity fluctuations seen by the particles given by Eq. (6.23) can be modeled by:

$$u'^{(n+1)}_{\mathrm{s},i} = E_{ij}(t,t_0)\;u'^{(n)}_{\mathrm{s},j} + W_{ij}(t,t_0)\;\xi_j. \tag{6.38}$$

The matrix exponential $E_{ij}(t,t_0)$ of the drift matrix can be determined by Eq. (6.28), while the square-root $W_{ij}(t,t_0)$ of the covariance matrix is provided by Eq. (6.36). The term ξ_j again denotes a normally distributed random vector. The main advantage of the integration-based scheme over the Euler–Maruyama scheme (Eq. (6.20)) is that Eq. (6.38) is unconditionally stable. In the case that leads to stability problems in the Euler–Maruyama scheme ($\max\left(G_{ij}\,\Delta t\right) \ll 1$), the matrix exponential $E_{ij}(t,t_0)$ of the drift matrix vanishes, since the coefficients $E_\parallel(t,t_0)$ and $E_\perp(t,t_0)$ tend to zero. Simultaneously, the coefficients $W_\parallel(t,t_0)$ and $W_\perp(t,t_0)$ of the square-root of the covariance matrix tend

to σ_{SGS} resulting in a diagonal matrix $W_{ij} = \sigma_{\mathrm{SGS}}\,\delta_{ij}$. Consequently, the integral solution given by Eq. (6.38) reduces to:

$$u_{\mathrm{s},i}^{\prime\,(n+1)} = \sigma_{\mathrm{SGS}}\,\xi_i, \tag{6.39}$$

if the time-step size exceeds the constraint given by Eq. (6.22). From a physical point of view, this means that the time scales of the subgrid-scale fluctuations seen by the particles are much smaller than the time scales of the particle motion. Hence, the unresolved scales fluctuate so fast that the particle cannot adapt to the changes. Equation (6.39) is denoted as the *trivial* subgrid-scale model in the present work. Due to its simple form, the trivial model was used in several studies (see, e.g., Alletto and Breuer, 2012, 2013b; Almohammed and Breuer, 2016a) regardless of the time-step size. However, it has to be noted that the trivial model disregards several important features of the enhanced Langevin model given by Eq. (6.38). For example, the temporal correlation of the subgrid-scale fluctuations is neglected. Additionally, important effects like the crossing trajectory and the continuity effects are not accounted for by the trivial model. Thus, in the present thesis it is applied solely for comparison purposes.

7 Modeling of Bubble Coalescence

The modeling of bubble coalescence in the present thesis relies on the film drainage model of Jeelani and Hartland (1991). As already argued in the literature overview in Section 2.2, this model accounts for various important physical mechanisms commonly neglected by simpler approaches. The major drawback of the model by Jeelani and Hartland (1991) is its reduced applicability to flows containing a huge number of bubbles originating from the high computational costs associated with the determination of the transition time between inertial and viscous drainage. The objective of Section 7.1 is to explain the presently used film drainage model including some improvements introduced for the modeling. Next, in Section 7.2 the conditions required for bubble coalescence are presented. In Section 7.3 the approach made to circumvent the high computational costs required for the estimation of the transition time t_j is introduced. Lastly, in Section 7.4 the relation of the present coalescence model to simpler approaches is demonstrated. Note that most of the derivations shown in this chapter have already been published in Hoppe and Breuer (2017, 2018).

7.1 Improved Film Drainage Model

The starting point for the modeling of the coalescence of two colliding bubbles is the model by Jeelani and Hartland (1991), who describe coalescence by two simultaneous processes. On the one hand, the collision between two bubbles leads to a deformation of the bubbles resulting in a temporarily evolving contact area A_f between the two bubbles. On the other hand, the fluid trapped between the interface of the either clean or contaminated bubbles is forced out of the gap. Consequently, the drainage of the fluid leads to a reduction of the thickness of the liquid film. The varying size of the contact area is one of the important features of the model by Jeelani and Hartland (1991). As argued in Section 2.2.3, this aspect is neglected by other coalescence models, which usually assume a constant contact surface of a certain size.

7.1.1 Collision Process

Figure 7.1 schematically depicts the collision and the drainage process including important variables of the coalescence process. It is important to note that both the film thickness h and the size of the contact surface A_f are strongly enlarged in Fig. 7.1 in order to improve the overall visibility. In the modeling approach of Jeelani and Hartland (1991), the height of the liquid film is assumed to be small compared to the distance $x_\mathrm{rel} = |\boldsymbol{x}_{\mathrm{b},1} - \boldsymbol{x}_{\mathrm{b},2}|$ of the centers of the bubbles, i.e., $x_\mathrm{rel} \gg h$. Furthermore, it is assumed that the bubbles only

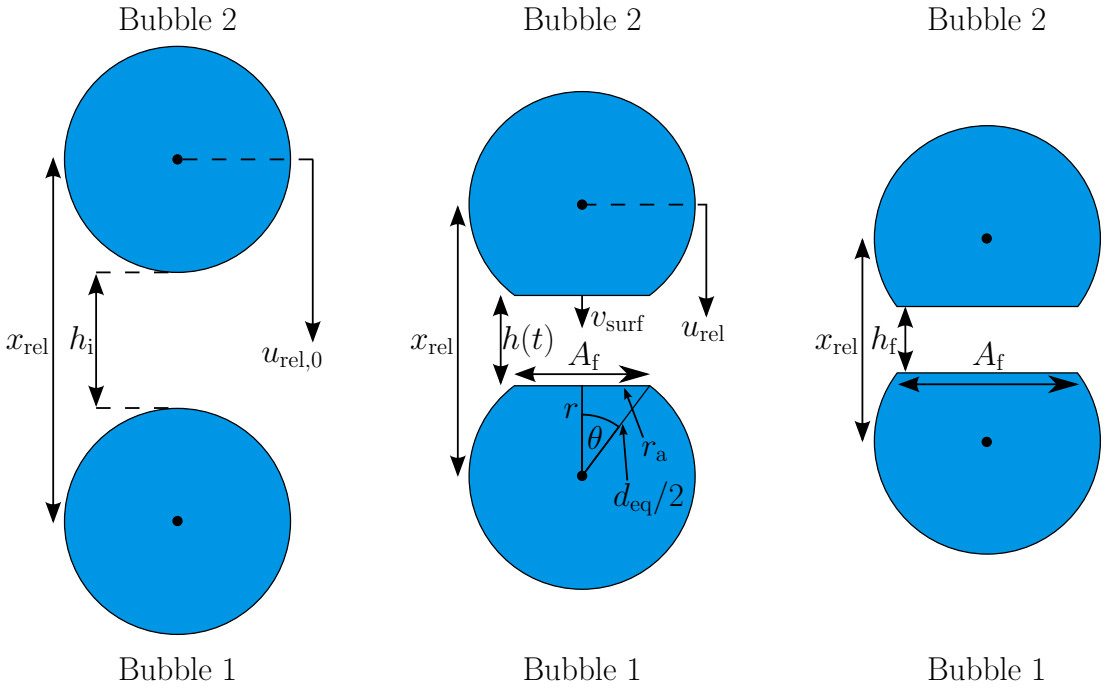

(a) Initial conditions. **(b)** During the drainage. **(c)** Final conditions.

Fig. 7.1. Schematic sketch of the collision process between two equally sized bubbles: (a) initial conditions at the onset of the deformation, (b) during the drainage of the liquid trapped between the deformed bubbles and (c) the final conditions reached when the relative motion of he bubble centers has stopped. The size of the contact surface and the film thickness are strongly enlarged for a better visibility. Figure taken from Hoppe and Breuer (2018).

slightly deform during the collision process. Hence, the radius r_{a} of the contact surface A_{f} is small compared to the radius of the bubbles $d_{\mathrm{eq}}/2$. Lastly, the approach velocity v_{surf} of the flat bubble surfaces is small compared to the relative velocity u_{rel} of the bubble centers, i.e., $u_{\mathrm{rel}} \gg v_{\mathrm{surf}}$.

Figure 7.1(a) depicts the colliding bubbles at the onset of the deformation process just before the drainage of the liquid begins. Initially, the centers of the undeformed bubbles are separated by the relative distance x_{rel}. Both centers approach each other with a relative velocity $u_{\mathrm{rel},0}$, where the center of the first bubble is arbitrarily chosen as the frame of reference. The surfaces of the still spherical bubbles are separated by a distance h_{i} also denoted as initial thickness of the liquid film. Afterwards, as shown in Fig. 7.1(b) the colliding bubbles deform resulting in a flat contact surface of varying size A_{f}. Since the film force F_{f} acts on the contact surface, the approach of the bubble centers towards each other is decelerated, i.e., the speed u_{rel} of the relative motion decreases. Simultaneously, the liquid trapped between the two bubbles is forced out of the gap. Consequently, the drainage of the liquid leads to a reduced film height $h(t)$. The corresponding velocity with which the two flat surfaces approach each other is v_{surf}. Note that the flat surface

of the first bubble is the frame of reference for this process. Lastly, in Fig. 7.1(c) the relative motion of the bubble centers has stopped, i.e., $u_{\mathrm{rel}} = 0$. Hence, the contact surface has reached its maximum. At this instant in time the bubbles coalesce, if the final film thickness h_{f} resulting from the drainage process is equal to or smaller than a certain critical film thickness h_{crit}, where the film ruptures. If this thickness is not reached, the bubbles rebound fully restoring their spherical form.

In the model of Jeelani and Hartland (1991) the above sketched collision process of the bubbles is determined by the force balance acting on the colliding bubbles. It has to be noted that Jeelani and Hartland (1991) derived their coalescence model for the collision of two equally sized bubbles. However, bubble-bubble collisions are typically comprised of two unequally sized partners. The following considerations are nevertheless valid, if the diameters $d_{\mathrm{b},1}$ and $d_{\mathrm{b},2}$ are replaced by a single equivalent diameter:

$$d_{\mathrm{eq}} = 2 \left(\frac{1}{d_{\mathrm{b},1}} + \frac{1}{d_{\mathrm{b},2}} \right)^{-1}. \tag{7.1}$$

The physical reason behind the applicability of Eq. (7.1) is that the pressure in the liquid film trapped between unequally sized bubbles is equal to the pressure in the liquid trapped between two equally sized bubbles of diameter d_{eq} (Abid and Chesters, 1994; Chesters and Hofman, 1982; Jeffreys and Davis, 1971). Consequently, the drainage of the liquid is equivalent in both cases as well. However, it has to be noted that differing bubble diameters have an influence on the contact time t_{c} (see below for more details).

According to the chosen frame of reference (sketched in Fig. 7.1), the force balance of the respective bubble describing the motion of the bubble during the collision process is given by (Jeelani and Hartland, 1991):

$$m \frac{\mathrm{d}^2 x_{\mathrm{rel}}}{\mathrm{d}t^2} = -m \frac{\mathrm{d}u_{\mathrm{rel}}}{\mathrm{d}t} = 2\, F_{\mathrm{f}}\,. \tag{7.2}$$

In Eq. (7.2) the film force F_{f} acting on the bubbles originates from the excess pressure inside the liquid film trapped between the bubbles. The factor of two is due to the fact that the film force acts on both bubbles. Since F_{f} is directed normal to the interface, the film force initially decelerates the bubbles during the collision process. If no coalescence occurs, the film force drives the bubbles away from each other restoring their spherical shape. In the work of Jeelani and Hartland (1991) the film force is given by:

$$F_{\mathrm{f}}^{\mathrm{Jeelani}} = \Delta p_{\mathrm{f}}\, A_{\mathrm{f}} = \frac{4\,\sigma}{d_{\mathrm{eq}}}\, A_{\mathrm{f}}. \tag{7.3}$$

The origin of the film force is the increased internal pressure inside the bubbles due to the surface tension σ. It is assumed by Jeelani and Hartland (1991) that the pressure in the liquid film is uniformly increased by Δp_{f} over the complete contact surface. This assumption can be justified by the Young–Laplace equation, which states that the internal pressure of the bubbles is increased by $\Delta p = 4\,\sigma / d_{\mathrm{eq}}$ compared with the surrounding liquid. Additionally, according to the Young–Laplace equation no pressure difference can exist

across a flat surface. The reason behind this is that the radii of curvature tend to infinity for a flat surface. Hence, the pressure in the liquid film trapped between the bubbles is constant, i.e., $\Delta p_\mathrm{f} = \Delta p$.

However, it can be shown that this approach contradicts the assumption of a radial outflow of the liquid: A pressure gradient driving the fluid flow out of the gap is required for both inertia and viscous-controlled drainage (Hartland, 1967; Jeffreys and Davis, 1971; Kirkpatrick and Lockett, 1974). Therefore, in the present thesis it is assumed that the pressure in the liquid film is only increased by $\Delta p = 4\,\sigma/d_\mathrm{eq}$ at the center of the contact surface. Away from the center, a quadratic decrease of the pressure is considered in the radial direction explained below. At the edge of the contact surface the film pressure equals the pressure in the surrounding liquid. The quadratic pressure distribution has been applied by several authors in their approaches (see, e.g., Chesters, 1975; Hartland, 1967; Jeffreys and Davis, 1971; Kirkpatrick and Lockett, 1974; Oolman and Blanch, 1986). Note that the quadratic decrease of the pressure is valid for both clean and contaminated bubbles. For the case of clean bubbles the quadratic pressure distribution can be derived with the help of Bernoulli's equation yielding a quadratic dependency of the pressure on the outflow velocity. On the other hand, the outflow velocity can be shown to be linearly related to the radius by applying the conservation of mass (Kirkpatrick and Lockett, 1974). In a similar manner, the case of contaminated bubbles can be explained, where the description is based again on the conservation of mass and additionally on the momentum equation of a laminar flow (Hartland, 1967; Jeffreys and Davis, 1971). For a more detailed derivation of the pressure distribution in the considered cases, see the aforementioned studies by Hartland (1967), Jeffreys and Davis (1971) and Kirkpatrick and Lockett (1974). By integrating the pressure distribution over the contact surface, it can be shown (see, e.g., Hartland, 1967; Kirkpatrick and Lockett, 1974) that the film force is now given by:

$$F_\mathrm{f}^\mathrm{present} = \frac{2\,\sigma}{d_\mathrm{eq}}\,A_\mathrm{f}. \tag{7.4}$$

The factor of two between Eqs. (7.3) and (7.4) originates from the quadratically decreasing pressure in the radial direction neglected by Jeelani and Hartland (1991).

The mass m appearing in Eq. (7.2) denotes the sum of the mass m_b of the bubble and the added mass m_AM of the fluid, which has to be displaced by the bubbles during their approach. Hence, m is given by:

$$m = m_\mathrm{b} + m_\mathrm{AM} = m_\mathrm{b}\left(1 + C'_\mathrm{m}\,\frac{\rho_\mathrm{f}}{\rho_\mathrm{b}}\right). \tag{7.5}$$

The factor C'_m is a modified[1] added-mass coefficient, which deviates from the standard added-mass coefficient of $C_\mathrm{m} = 0.5$ used for the added-mass force acting on individual bubbles, cf., Section 4.1.1.4. It has to be remembered that the added-mass force originates from the additional work needed to accelerate or decelerate the fluid surrounding an unsteadily moving bubble (Brennen, 1982, 2005; Crowe et al., 1998). Hence, it is obvious

[1] Indicated by the prime.

that an additional bubble in close vicinity of the considered bubble augments the required work. This phenomenon is accounted for by the modified added-mass coefficient C'_{m}. Following Jeelani and Hartland (1991), the modified added-mass coefficient was set to:

$$C'_{\mathrm{m}} = 0.8, \tag{7.6}$$

in Hoppe and Breuer (2018). The value corresponds to the added-mass coefficient in the case of two equally sized bubbles in direct contact with each other and is based on an expression (see Eq. (7.7)) analytically derived by Lamb (1932) based on the irrotational flow induced by two moving spheres.

However, it has to be noted that the expression of C'_{m} by Lamb (1932) deviates from Eq. (7.6) for unequally sized bubbles. Based on the work of Lamb (1932), Kamp et al. (2001) showed that the added-mass coefficient for two unequally sized bubbles can be written according to:

$$C'_{\mathrm{m}} = \frac{1}{8}\,\frac{L\,N - M^2}{L - 2\,M + N}\left(\frac{d_{\mathrm{b},1} + d_{\mathrm{b},2}}{d_{\mathrm{b},1}\,d_{\mathrm{b},2}}\right)^3, \tag{7.7}$$

where L, N and M are functions of the bubble diameters $d_{\mathrm{b},1}$ and $d_{\mathrm{b},2}$ defined by:

$$L = d_{\mathrm{b},1}^3\left[1 + 3\,\frac{d_{\mathrm{b},2}^3}{\left(d_{\mathrm{b},1} + 2\,d_{\mathrm{b},2}\right)^3} + 3\,\frac{d_{\mathrm{b},2}^3}{2\,\left(d_{\mathrm{b},1} + 3\,d_{\mathrm{b},2}\right)^3}\right], \tag{7.8a}$$

$$N = d_{\mathrm{b},2}^3\left[1 + 3\,\frac{d_{\mathrm{b},1}^3}{\left(2\,d_{\mathrm{b},1} + d_{\mathrm{b},2}\right)^3} + 3\,\frac{d_{\mathrm{b},1}^3}{3\,\left(d_{\mathrm{b},1} + 2\,d_{\mathrm{b},2}\right)^3}\right], \tag{7.8b}$$

$$M = \frac{251}{72}\left(\frac{d_{\mathrm{b},1}\,d_{\mathrm{b},2}}{d_{\mathrm{b},1} + d_{\mathrm{b},2}}\right)^3. \tag{7.8c}$$

The application of Eq. (7.7) leads to a variation of the added-mass coefficient from $C'_{\mathrm{m}} = 0.8$ for equally sized bubbles to $C'_{\mathrm{m}} = 0.2$, if one bubble is much larger than the other ($d_{\mathrm{b},1}/d_{\mathrm{b},2} \to \infty$). In the following it will be shown that the added-mass coefficient directly affects the time t_{c} the colliding bubbles are in contact with each other and the corresponding contact surface. Consequently, the form of the added-mass coefficient also influences the transition time t_{j} between inertia and viscous-controlled drainage in the case of contaminated bubbles (see Sections 7.2 and 7.3).

Equation (7.2) can be transformed into a differential equation of the contact surface A_{f} using several simple geometrical considerations (Jeelani and Hartland, 1991). Firstly, the contact surface A_{f}, the relative distance x_{rel} between the centers of mass of the bubbles and the corresponding relative velocity u_{rel} are expressed by the angle θ between the center of A_{f} and its edge at r_{a} (see Fig. 7.1(b)). One can readily show that:

$$A_{\mathrm{f}} = \pi\,r_{\mathrm{a}}^2 = \pi\left(\frac{d_{\mathrm{eq}}}{2}\,\sin\theta\right)^2 \approx \frac{\pi}{4}\,d_{\mathrm{eq}}^2\,\theta^2, \tag{7.9}$$

$$x_{\mathrm{rel}} \approx 2\,r = d_{\mathrm{eq}}\,\cos\theta \qquad \approx d_{\mathrm{eq}}\left(1 - \frac{1}{2}\,\theta^2\right), \tag{7.10}$$

$$u_{\mathrm{rel}} = -\frac{\mathrm{d}x_{\mathrm{rel}}}{\mathrm{d}t} \approx \frac{d_{\mathrm{eq}}}{2}\frac{\mathrm{d}\theta^2}{\mathrm{d}t}. \tag{7.11}$$

From the sketch of the geometry depicted in Fig. 7.1(b) it is visible that the radius of the contact surface is given by $r_{\mathrm{a}} = d_{\mathrm{eq}}/2 \sin\theta$. Due to the assumption that the deformation of the bubbles is small, the contact surface and, thus, the angle θ have to be small as well. Hence, the angular functions can be approximated for small angles ($\sin\theta \approx \theta$) leading to the final form of Eq. (7.9). Similarly, the relative distance x_{rel} between the bubble centers can be related to d_{eq} and θ, see Eq. (7.10). Here, the approximation $\cos\theta = 1 - \theta^2/2$ valid for small angles is applied. Lastly, Eq. (7.11) is obtained by simply taking the derivative of Eq. (7.10). Combining Eqs. (7.4) and (7.9) to (7.11) and inserting into the force balance (7.2) yields:

$$\frac{\mathrm{d}^2 A_{\mathrm{f}}}{\mathrm{d}t^2} = -\frac{2\,\pi\,\sigma}{m}\,A_{\mathrm{f}}\,, \tag{7.12}$$

describing the evolution of the contact surface between the onset of the deformation process and the separation of the bubbles. The general solution of Eq. (7.12) is given by:

$$A_{\mathrm{f}} = K_1 \sin\left(\pi\,\frac{t}{t_{\mathrm{c}}}\right) + K_2 \cos\left(\pi\,\frac{t}{t_{\mathrm{c}}}\right), \tag{7.13}$$

where K_1 and K_2 are two constants. The contact time t_{c} appearing in Eq. (7.16) describes the time span the two colliding bubbles are in contact with each other. It can be readily seen that the contact time is defined by:

$$t_{\mathrm{c}} = \sqrt{\frac{\pi\,m}{2\,\sigma}}. \tag{7.14}$$

The same expression of t_{c} has been derived by Kamp et al. (2001) using the principle of energy conservation during the collision process. In order to obtain the final expression of the evolving contact surface, the unknown constants K_1 and K_2 have to be determined by suitable initial conditions. Firstly, it has to be noted that the contact surface is zero at the onset of the deformation of the bubbles at $t = 0$. Hence, in order to fulfill this condition K_2 has to be zero. The remaining constant K_1 can be specified by noting that the relative approach velocity $u_{\mathrm{rel},0}$ is equal to the collision velocity at the beginning of the collision. Inserting Eqs. (7.9) and (7.13) into Eq. (7.11) one obtains the expression for the relative velocity at the instant $t = 0$:

$$u_{\mathrm{rel},0} = \frac{2}{\pi\,d_{\mathrm{eq}}}\frac{\mathrm{d}A_{\mathrm{f}}}{\mathrm{d}t}\bigg|_{t=0} = \frac{2\,K_1}{d_{\mathrm{eq}}\,t_{\mathrm{c}}}\,, \tag{7.15}$$

which can be readily solved for K_1. Therefore, the temporal evolution of the contact surface during the collision process is fully determined by:

$$A_{\mathrm{f}} = \frac{d_{\mathrm{eq}}\,u_{\mathrm{rel},0}\,t_{\mathrm{c}}}{2} \sin\left(\pi\,\frac{t}{t_{\mathrm{c}}}\right). \tag{7.16}$$

7.1.2 Liquid Drainage

Based on the temporal variation of the contact surface given by Eq. (7.16), the drainage equations of the liquid film can now be specified. Jeelani and Hartland (1991) distinguished two physical mechanisms: inertia controlled or viscous controlled outflow. In the first case the outflow of the liquid between the two bubbles is described by a plug flow with a spatially constant drainage or outflow velocity u_d. Hence, a free-slip boundary condition present on the surface of completely clean bubbles (Dijkhuizen et al., 2010; Tomiyama et al., 1998) is required. Consequently, it is assumed here that the outflow of the liquid trapped between clean bubbles is solely controlled by inertia forces. In the second case of a viscous controlled outflow, the velocity distribution in the gap is described by a parabolic profile with the velocity being zero at the surfaces of the bubbles. Such a flow behavior requires a no-slip condition at the surfaces of the bubbles, which is present on the surface of bubbles dispersed in contaminated liquids. As already described in Section 4.1.1.1, the contaminants accumulate on the bubble surface causing the surface to behave like a rigid interface (Tomiyama et al., 1998). Consequently, in the case of contaminated bubbles the drainage is dominated by viscous forces. However, Hartland et al. (1989) demonstrated that the drainage in that case is initially also controlled by inertia and only transforms to the viscous-dominated regime after a certain time t_j. In their study Hartland et al. (1989) showed that at the beginning of the outflow process the reduction of the film height estimated by the Bernoulli equation is identical to a numerical solution of the Navier–Stokes equations of the liquid outflow. Solely at later time instants differences occurred due to viscous effects becoming important. From a physical point of view this phenomenon can be understood by the fact that at the beginning of the collision the contact surface suddenly increases. Hence, the outflow of the liquid increases suddenly as well and, therefore, is dominated by inertia forces shortly after the onset of the deformation. This phenomenon is accounted for by the model of Jeelani and Hartland (1991).

The actual drainage equations describing the reduction of the film thickness in both inertia as well as the viscous regime are derived by relating the film force F_f (Eq. (7.4)) to the force required for the approach of two surfaces with a velocity v_surf and a certain amount of liquid trapped between them. Kirkpatrick and Lockett (1974) determine this force for the case of inertia-controlled outflow by solving the Bernoulli equation. The derived film force reads:

$$F_\mathrm{f}^\mathrm{inert} = \frac{\rho_\mathrm{f}\, A_\mathrm{f}^2\, v_\mathrm{surf}^2}{16\,\pi\, h^2}. \tag{7.17}$$

By combining Eqs. (7.4) and (7.17) and using the relation $v_\mathrm{surf} = -\mathrm{d}h/\mathrm{d}t$, one obtains the drainage equation for the inertia-controlled outflow (Jeelani and Hartland, 1991):

$$\frac{\mathrm{d}h}{\mathrm{d}t} = -k_\mathrm{i}\,\frac{h}{\sqrt{A_\mathrm{f}}} \quad \text{with} \quad k_\mathrm{i} = \sqrt{\frac{32\,\pi\,\sigma}{\rho_\mathrm{f}\, d_\mathrm{eq}}}. \tag{7.18}$$

Similarly, Hartland (1967) and Jeffreys and Davis (1971) provide the film force for the case of viscous-controlled drainage based on the momentum equation of a laminar flow:

$$F_{\mathrm{f}}^{\mathrm{visc}} = \frac{3\,\mu_{\mathrm{f}}\,A_{\mathrm{f}}^2\,v_{\mathrm{surf}}}{2\,\pi\,h^3}. \tag{7.19}$$

Inserting Eq. (7.19) into Eq. (7.4) yields the drainage equation for the case of viscous-dominated outflow (Jeelani and Hartland, 1991):

$$\frac{\mathrm{d}h}{\mathrm{d}t} = -k_{\mathrm{v}}\,\frac{h^3}{A_{\mathrm{f}}} \quad \text{with} \quad k_{\mathrm{v}} = \frac{4\,\pi\,\sigma}{3\,\mu_{\mathrm{f}}\,d_{\mathrm{eq}}}. \tag{7.20}$$

Hence, the drainage of the liquid trapped between both clean and contaminated bubbles is described by Eqs. (7.18) and (7.20). However, for the solution of Eqs. (7.18) and (7.20) the time-dependent contact surface A_{f} given by Eq. (7.16) has to be inserted into the drainage equations. Due to the sine function, the resulting differential equations cannot be solved analytically. Hence, Jeelani and Hartland (1991) proposed to approximate the sine function in the range $0 < t/t_{\mathrm{j}} \leq 1$ by the expression:

$$\sin\left(\pi\,\frac{t}{t_{\mathrm{c}}}\right) \approx 4\,\frac{t}{t_{\mathrm{c}}}\left(1 - \frac{t}{t_{\mathrm{c}}}\right) \quad \text{for} \quad 0 \leq \frac{t}{t_{\mathrm{c}}} < 1. \tag{7.21}$$

Inserting this approximation into Eqs. (7.18) and (7.20) yields differential equations that can be solved analytically by the separation of the variables. Subsequently, the film thickness can be integrated between the heights h_1 and h_2 at the time instants t_1 and t_2, respectively. In the case of inertial drainage (Eq. (7.18)) the reduction of the film height is given by:

$$\frac{h_2}{h_1} = \exp\left[-\frac{k_i}{\sqrt{d_{\mathrm{eq}}\,u_{\mathrm{rel},0}}}\sqrt{\frac{t_{\mathrm{c}}}{2}}\left\{\arcsin\left(2\,\frac{t_2}{t_{\mathrm{c}}} - 1\right) - \arcsin\left(2\,\frac{t_1}{t_{\mathrm{c}}} - 1\right)\right\}\right]. \tag{7.22}$$

In a similar manner, one can determine the reduction of the film thickness in the case of viscous-controlled outflow described by Eq. (7.20):

$$\frac{h_2}{h_1} = \left[1 + h_1^2\,\frac{k_v}{d_{\mathrm{eq}}\,u_{\mathrm{rel},0}}\left\{\ln\left(\frac{t_2}{t_{\mathrm{c}} - t_2}\right) - \ln\left(\frac{t_1}{t_{\mathrm{c}} - t_1}\right)\right\}\right]^{-\frac{1}{2}}. \tag{7.23}$$

It can be readily seen by comparing Eqs. (7.22) and (7.23) that the inertial drainage is considerably faster than the drainage controlled by viscous forces. In Eq. (7.22) the film thickness h_2 at the time instant t_2 is proportional to an exponential decrease, while the film thickness reduces with the inverse of a square-root in Eq. (7.23).

7.2 Coalescence Conditions

As already explained in Section 7.1.1, the deformation of the colliding bubbles starts at an initial film thickness h_i after which the film thickness reduces due to the drainage of the liquid trapped between the bubbles. Two distinctive cases have to be considered. Due to the free-slip boundary condition at the surface of clean bubbles, the drainage is purely controlled by inertia forces. Hence, only Eq. (7.22) is required to describe the reduction of the film thickness. For contaminated bubbles the drainage is initially inertia-controlled as well until viscous effects start to dominate. Thus, the reduction of the film thickness is given by Eq. (7.22) for an initial period of time until a certain instant in time denoted t_j. Afterwards, Eq. (7.23) describes the remaining liquid drainage. Coalescence occurs if the final film thickness h_f is equal or smaller than a certain critical film thickness h_crit at which the liquid film ruptures. Hence, the coalescence criterion is given by:

$$h_\mathrm{f} \leq h_\mathrm{crit}. \tag{7.24}$$

Note that both the initial film thickness h_i and the critical film thickness h_crit will be specified below. Furthermore, it has to be noted that for both clean and contaminated bubbles the drainage process occurs only during the approach of the bubble centers, i.e., during the first half of the contact time $t_\mathrm{c}/2$. In the second half of the contact time the bubbles separate from each other reducing the contact surface again. Consequently, it is plausible to assume that the film thickness only reduces during $t \leq t_\mathrm{c}/2$.

Based on the considerations in Section 7.1.2 the coalescence can be estimated for both clean and contaminated bubbles. For the case of clean bubbles the final film thickness h_f reached at $t_\mathrm{c}/2$ is solely given by Eq. (7.22). Hence, by setting $h_2 = h_\mathrm{f}$ and $h_1 = h_\mathrm{i}$ for the film thicknesses at the time instants $t_2 = t_\mathrm{c}/2$ and $t_1 = 0$, one obtains:

$$h_\mathrm{f} = h_\mathrm{i} \exp\left[-\frac{k_i}{\sqrt{d_\mathrm{eq}\, u_\mathrm{rel,0}}} \sqrt{\frac{t_\mathrm{c}}{2}}\, \frac{\pi}{2}\right]. \tag{7.25}$$

Note that in Eq. (7.25) the relations $\arcsin(0) = 0$ and $\arcsin(-1) = \pi/2$ are applied. Since Eq. (7.25) solely contains known quantities of the bubbles and the collision process, the coalescence of clean bubbles can be readily modeled by this expression.

The case of contaminated bubbles can be described in a similar manner. However, more effort is required due to the transformation of the responsible drainage regime after the transition time t_j. Consequently, the film thickness is initially decreased according to Eq. (7.22) from $h_1 = h_\mathrm{i}$ to the intermediate film thickness $h_2 = h_\mathrm{j}$ during the time interval $t_1 = 0$ to $t_2 = t_\mathrm{j}$ (Jeelani and Hartland, 1991). Hence, the intermediate film thickness reads:

$$h_\mathrm{j} = h_\mathrm{i} \exp\left[-\frac{k_i}{\sqrt{d_\mathrm{eq}\, u_\mathrm{rel,0}}} \sqrt{\frac{t_\mathrm{c}}{2}} \left\{\frac{\pi}{2} + \arcsin\left(2\,\frac{t_\mathrm{j}}{t_\mathrm{c}} - 1\right)\right\}\right]. \tag{7.26}$$

Subsequently, the drainage is controlled by viscous forces, i.e., Eq. (7.23) describes the reduction of the film thickness from the intermediate value $h_1 = h_\mathrm{j}$ at the time instant $t_1 = t_\mathrm{j}$ until the final film thickness is reached at $t_\mathrm{c}/2$:

$$h_\mathrm{f} = h_\mathrm{j} \left[1 + h_\mathrm{j}^2 \, \frac{k_\mathrm{v}}{d_\mathrm{eq} \, u_\mathrm{rel,0}} \, \ln\left(\frac{t_\mathrm{c}}{t_\mathrm{j}} - 1 \right) \right]^{-\frac{1}{2}}. \tag{7.27}$$

The major challenge arising in the model of Jeelani and Hartland (1991) is the estimation of the transition time t_j. Since Eq. (7.26) contains the two unknowns t_j and h_j, a second equation is required. In order to explicitly determine the two quantities, Jeelani and Hartland (1991) proposed that at the time instant t_j the drainage rates $\mathrm{d}h/\mathrm{d}t$ of the inertia-controlled drainage (Eq. (7.18)) and of the viscous-controlled outflow (Eq. (7.20)) should be equal. Since at this instant the transition from inertial to viscous drainage occurs, this assumption is meaningful from a physical point of view. By equating Eqs. (7.18) and (7.20) at the time instant t_j and the film thickness h_j and solving for the intermediate film thickness h_j one obtains:

$$h_\mathrm{j} = \sqrt{\frac{k_\mathrm{i}}{k_\mathrm{v}}} \sqrt[4]{\frac{d_\mathrm{eq} \, u_\mathrm{rel,0} \, t_\mathrm{c}}{2} \, \sin\left(\pi \, \frac{t_\mathrm{j}}{t_\mathrm{c}} \right)}. \tag{7.28}$$

Equations (7.26) and (7.28) solely contain t_j and h_j as unknowns. Hence, two equations are available for two unknown quantities, i.e., the problem is fully determined. For example, one can readily eliminate the intermediate film thickness h_j by equating Eqs. (7.26) and (7.28). The resulting expression reads:

$$\frac{1}{4} \, \ln\left[\sin\left(\pi \, \frac{t_\mathrm{j}}{t_\mathrm{c}} \right) \right] + c_1 = -c_2 \left[\frac{\pi}{2} + \arcsin\left(2 \, \frac{t_\mathrm{j}}{t_\mathrm{c}} - 1 \right) \right], \tag{7.29}$$

where the coefficients c_1 and c_2 introduced to abbreviate Eq. (7.29) solely depend on known quantities and are defined by:

$$c_1 = \frac{1}{2} \, \ln\left(\frac{k_\mathrm{i}}{k_\mathrm{v}} \right) + \frac{1}{4} \, \ln\left(\frac{d_\mathrm{eq} \, u_\mathrm{rel,0} \, t_\mathrm{c}}{2} \right) - \ln\left(h_\mathrm{i} \right), \tag{7.30a}$$

$$c_2 = \frac{k_\mathrm{i}}{\sqrt{d_\mathrm{eq} \, u_\mathrm{rel,0}}} \sqrt{\frac{t_\mathrm{c}}{2}}. \tag{7.30b}$$

Unfortunately, it is not possible to analytically solve Eq. (7.29) for the transition time t_j. Thus, a numerical root-finding algorithm has to be used. Especially in the case of large volume loadings this is a costly task, since the number of collisions is possibly huge and the transition time has to be determined for each collision individually. Therefore, the approach by Jeelani and Hartland (1991) is unfeasible for the prediction of coalescence in flows containing a large number of contaminated bubbles explaining why to the best of the author's knowledge the model by Jeelani and Hartland (1991) was not used prior to Hoppe and Breuer (2018).

7.3 Numerical Solution for the Transition Time

In order to circumvent the necessity to estimate the transition time by a root-finding algorithm for each individual collision process, an a-priori estimation of the relative transition time $t_\mathrm{j}/t_\mathrm{c}$ based on a two-step process was proposed by Hoppe and Breuer (2018). First, at the beginning of the simulation Eq. (7.29) is numerically solved for a pre-defined range of bubble parameters (see Sections 7.3.1 and 7.3.2). Thus, a map of relative transition times $t_\mathrm{j}/t_\mathrm{c}$ is defined. In a second step, a regression function $f_{t_\mathrm{j}/t_\mathrm{c}}$ is proposed, which approximately describes the relative transition time $t_\mathrm{j}/t_\mathrm{c}$ based on a parametric dependency on the chosen set of parameters. The parametric dependency of $f_{t_\mathrm{j}/t_\mathrm{c}}$ is determined by a non-linear least-squares fitting of the regression function to the data of the map. The idea behind this procedure is to estimate the regression function $f_{t_\mathrm{j}/t_\mathrm{c}}$ once at the beginning of the simulation. During the simulation the relative transition time required for the prediction of the coalescence of contaminated bubbles is approximated by the regression function, i.e., the properties of the colliding bubbles ($u_\mathrm{rel,0}$, $d_\mathrm{b,1}$ and $d_\mathrm{b,2}$) are inserted into the regression function $f_{t_\mathrm{j}/t_\mathrm{c}}$ yielding the corresponding transition time. In summary, only a simple function evaluation is required for the estimation of the transition time for each individual collision instead of a complete numerical root-finding procedure. Consequently, the numerical costs associated with the approach by Jeelani and Hartland (1991) are significantly reduced.

As explained, the above procedure requires the application of two numerical algorithms once at the beginning of the simulation: a root-finding method and a non-linear least-squares fit. In the present thesis the root-finding algorithm of Ridders (1979) is applied due to its beneficial properties (Press et al., 2007). The regression function $f_{t_\mathrm{j}/t_\mathrm{c}}$ is determined by the non-linear least-squares algorithm 'NL2SOL' by Dennis et al. (1981a,b), which is suggested to be used, for example, by Press et al. (2007).

Lastly, the set of parameters on which the relative transition time is supposed to depend on has to be chosen. It is obvious from Eq. (7.29) that the relative collision velocity $u_\mathrm{rel,0}$ and the equivalent diameter d_eq affect the relative transition time $t_\mathrm{j}/t_\mathrm{c}$. Hence, both bubble properties have to be taken into account for the map and the corresponding regression function $f_{t_\mathrm{j}/t_\mathrm{c}}$ used to approximate $t_\mathrm{j}/t_\mathrm{c}$. However, the added-mass coefficient C'_m also plays an important role, since according to Eq. (7.14) the contact time t_c is directly affected by C'_m. Here, two cases can be distinguished based on whether the added-mass coefficient is assumed to be a constant (Eq. (7.6)) as done by Jeelani and Hartland (1991) and, originally, by Hoppe and Breuer (2018), or if C'_m depends on the diameters of the colliding bubbles (Eq. (7.7)) as in Kamp et al. (2001). Presently, the latter option is implemented in $\mathcal{LESOCC}$.

7.3.1 Constant Added-Mass Coefficient

In the case that the added-mass coefficient is assumed to be a constant given by Eq. (7.6) the relative contact time depends solely on the relative collision velocity $u_\mathrm{rel,0}$ and the equivalent diameter d_eq. Hence, it is sufficient to define a range of velocities and equivalent diameters for which the map of $t_\mathrm{j}/t_\mathrm{c}$ is determined by the root-finding algorithm. Naturally,

the regression function f_{t_j/t_c} can only depend on $u_{rel,0}$ and d_{eq} in this case. While the exact form of the regression function is arbitrary, in the present thesis the relation:

$$f_{t_j/t_c} = \alpha_1 \, d_{eq}^{\alpha_2} \, \exp\left(\alpha_3 \, d_{eq}\right) \, u_{rel,0}^{\alpha_4} \, \exp\left(\alpha_5 \, u_{rel,0}\right) \tag{7.31}$$

originally proposed in Hoppe and Breuer (2018) is applied. It was found that Eq. (7.31) yields a good approximation of the relative transition time over the full range of the variables. The parameters α_1 to α_5 describe the actual parametric dependency of f_{t_j/t_c} on $u_{rel,0}$ and d_{eq} and are determined by the above mentioned algorithm of Dennis et al. (1981a,b).

In Fig. 7.2 the above described two-step procedure is demonstrated for a constant added-mass coefficient of $C'_m = 0.8$. The relative velocity and the equivalent diameter are exemplary chosen in the range $u_{rel,0} = 0.75 - 75\,\mathrm{mm/s}$ and $d_{eq} = 0.1 - 10\,\mathrm{mm}$, respectively. For both variables 200 data points are used. Hence, the map of the relative transition time t_j/t_c shown as a contour plot in Fig. 7.2(a) consists of 200×200 data points. It can be seen from Fig. 7.2(a) that the increase of the relative transition time with both variables is continuous but non-linear. In Fig. 7.2(b) the regression function obtained from the non-linear least-squares fit of the map displayed in Fig. 7.2(a) is shown, where the values of f_{t_j/t_c} are plotted against the corresponding values of t_j/t_c in form of a scatter plot. Since all points of the scatter plot are well aligned with the diagonal black line representing the correct transition times, the regression function f_{t_j/t_c} yields an accurate estimation of the t_j/t_c over the complete range of $u_{rel,0}$ and d_{eq}.

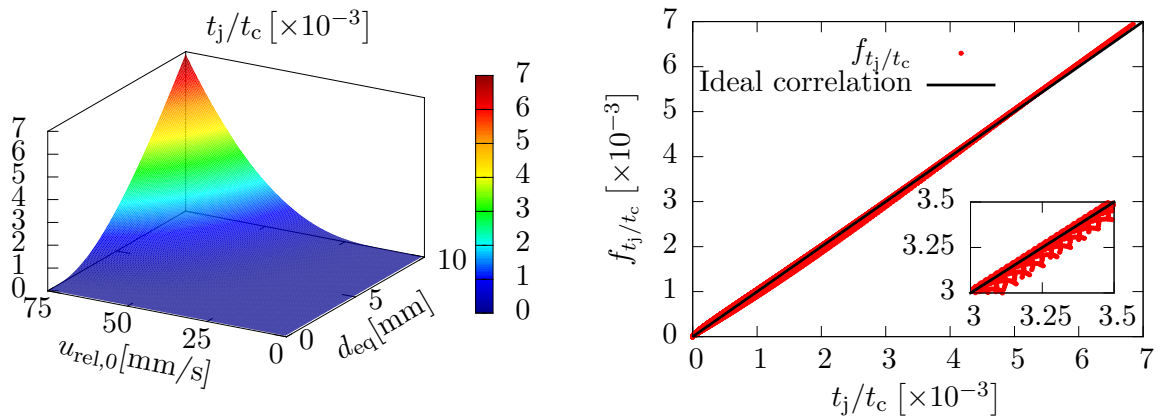

(a) Contour plot of the map of t_j/t_c.

(b) Scatter plot of f_{t_j/t_c} against t_j/t_c.

Fig. 7.2. Demonstration of the steps of the approximation method for the relative transition time for a constant added-mass coefficient of $C'_m = 0.8$. (a) Contour plot of the map of the relative transition time t_j/t_c as a function of $u_{rel,0}$ and d_{eq}. The map consists of 200×200 data points. (b) Scatter plot of the regression function f_{t_j/t_c} against the relative transition time t_j/t_c. The red dots denote the predicted values of f_{t_j/t_c} for 200×200 data points. The black line represents the ideal correlation. The inset shows a zoomed view. Figure taken from Hoppe and Breuer (2018).

7.3.2 Variable Added-Mass Coefficient

The methodology for determining the relative transition time in the case where the added-mass coefficient varies with the diameters $d_{b,1}$ and $d_{b,2}$ of the bubbles is equivalent to the one previously described in Section 7.3.1. Again, t_j/t_c is a function of the relative collision velocity $u_{rel,0}$ and the equivalent diameter d_{eq}. Hence, as in the case of a constant C'_m a range of velocities and equivalent diameters has to be defined. However, it is additionally required to account for the effect of the varying value of C'_m given by Eq. (7.7) on the relative transition time, i.e., both the map of t_j/t_c and the corresponding regression function f_{t_j/t_c} now depend on a third variable. According to Eq. (7.7) the added-mass coefficient can only vary in the range $C'_m = 0.2$ to 0.8 for $d_{b,1}/d_{b,2} = \infty$ and 1, respectively. Hence, it is sufficient to solely account for values in this interval.

Figure 7.3 demonstrates the influence of the added-mass coefficient on the relative transition time. Contour plots of the map of t_j/t_c are depicted for four different values of the added-mass coefficient, i.e., C'_m decreases from 0.8 to 0.2 in Figs. 7.3(a) to 7.3(d). The relative collision velocity and the equivalent diameter are again exemplary chosen in the range $u_{rel,0} = 0.75 - 75\,\mathrm{mm/s}$ and $d_{eq} = 0.1 - 10\,\mathrm{mm}$ with 200 data points for each variable, while the range of C'_m is divided into 60 points. Consequently, the map of t_j/t_c now consists of $200 \times 200 \times 60$ points. It is obvious that increasing the added-mass coefficient substantially decreases the relative transition time. For example, for $C'_m = 0.8$ shown in Fig. 7.3(a) the maximum value of the relative transition time is about $t_j/t_c = 7 \times 10^{-3}$, while in Fig. 7.3(d) with $C'_m = 0.2$ the maximum is $t_j/t_c \approx 14 \times 10^{-3}$. Consequently, the relative transition time is raised by a factor of two due to the decrease of the added-mass coefficient by a factor of four. This can be readily explained by the fact that the contact time t_c is proportional to the square-root of the mass m, see Eq. (7.14). According to Eq. (7.5) the mass m increases with increasing values of C'_m. On the other hand, the transition time t_j is not affected by the added-mass coefficient, since the transition solely relies on the transformation of the responsible (inertia or viscous controlled) drainage mechanism. Thus, a variation of C'_m directly influences the relative transition time.

In order to capture the effect of the added-mass coefficient on the relative transition time, the regression function has to be modified such that f_{t_j/t_c} also depends on C'_m with the actual form of the dependency being again arbitrary. In analogy to Eq. (7.31), it is proposed here to estimate the relative transition time by:

$$f_{t_j/t_c} = \alpha_1\, d_{eq}^{\alpha_2}\, \exp\left(\alpha_3\, d_{eq}\right)\, u_{rel,0}^{\alpha_4}\, \exp\left(\alpha_5\, u_{rel,0}\right)\, C_m'^{\alpha_6}\, \exp\left(\alpha_7\, C'_m\right). \tag{7.32}$$

Hence, the parametric dependency of the regression function on the added-mass coefficient is assumed to be equivalent to the relation of f_{t_j/t_c} to $u_{rel,0}$ and d_{eq}. Again the parameters α_1 to α_7 are determined based on the map of t_j/t_c. For the exemplary chosen range of variables (see above) the regression function resulting from the non-linear least-squares fitting is demonstrated in Fig. 7.4. It is apparent that the regression function proposed in Eq. (7.32) still yields an accurate estimation of the relative transition time, since all scatter points are in close vicinity to the diagonal representing the ideal correlation.

Presently, the variable added-mass coefficient is taken into account in the estimation of the relative transition time in $\mathcal{LESOCC}$. However, the results published in Hoppe

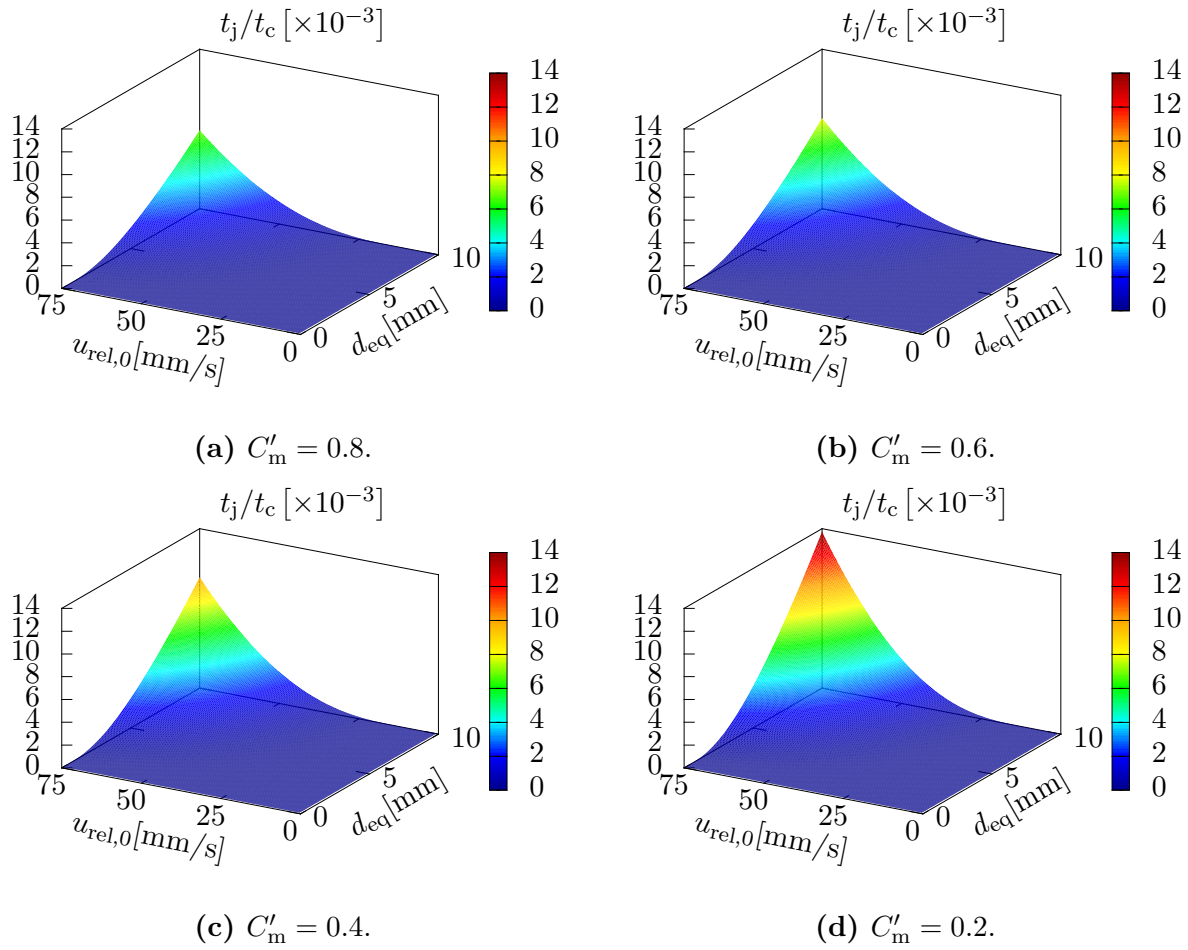

(a) $C'_m = 0.8$. **(b)** $C'_m = 0.6$.

(c) $C'_m = 0.4$. **(d)** $C'_m = 0.2$.

Fig. 7.3. Contour plots of the map of the relative transition time as a function of $u_{rel,0}$ and d_{eq} for varying added-mass coefficients.

and Breuer (2018) were obtained with a constant added-mass coefficient. Therefore, in Section 11.3 these results will be compared with more recent results. Note that the overall numerical effort associated with considering a variable added-mass coefficient is larger compared with the case of a constant added-mass coefficient. Obviously, the map of t_j/t_c generated at the beginning of the simulation contains sixty times more data points than in the former case, thus, requiring more computational storage. However, since the whole procedure proposed by Hoppe and Breuer (2018) is only performed once at the beginning of the simulation, the used storage can be deallocated after the regression function is determined. The computational effort associated with the non-linear least-squares approach apparently increases as well, due to the two additional parameters (α_6 and α_7) that have to be determined. Since the applied algorithm by Dennis et al. (1981a,b) is highly efficient (Press et al., 2007), the computational time is not noticeably extended. Lastly, during the simulation the determination of C'_m by Eq. (7.7) extends the computational effort due to the complicated coefficients L, N and M given by Eq. (7.8). However, the evaluation of the regression function f_{t_j/t_c} is still cost-efficient.

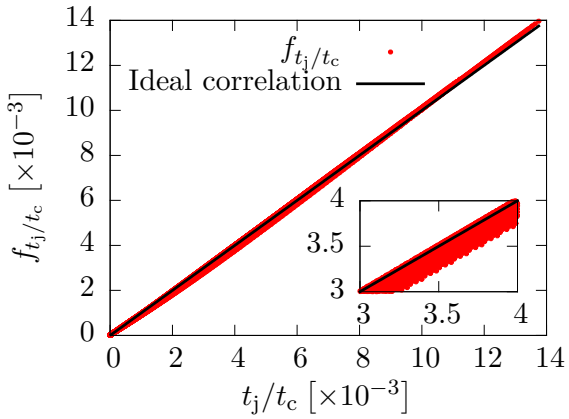

Fig. 7.4. Scatter plot of f_{t_j/t_c} against t_j/t_c. The regression function is obtained by a non-linear least-squares fit of the map shown in Fig. 7.3.

7.4 Relation to Simpler Coalescence Models

In Section 7.1 the varying contact surface was inserted into the drainage equations of inertial (Eq. (7.18)) and viscous (Eq. (7.20)) drainage. Subsequently, for both cases the reduction of the film thickness was determined by the separation of variables and integration. It is possible to retrieve the simpler coalescence models by Kirkpatrick and Lockett (1974) and Prince and Blanch (1990) for the inertial case and Hartland (1967) and Jeffreys and Davis (1971) for the viscous case by assuming that the contact surface is constant.

First, the value of the constant contact surface has to be specified. Following the suggestion of Prince and Blanch (1990) the projected area of the bubbles $A_f = \pi\, d_{eq}^2/4$ is used here. Consequently, integrating Eq. (7.18) between h_i and h_f at the time instants $t = 0$ and $t_c/2$ with a constant contact surface yields:

$$h_f = h_i \exp\left(-\frac{k_i}{\sqrt{A_f}}\,\frac{t_c}{2}\right) = h_i \exp\left(-\sqrt{\frac{128\,\sigma}{\rho_f\, d_{eq}^3}}\,\frac{t_c}{2}\right). \tag{7.33}$$

Equation (7.33) is equal to the model derived by Kirkpatrick and Lockett (1974) and Prince and Blanch (1990) for the purely inertia-controlled reduction of the film thickness between clean bubbles. In the same manner, one obtains for the film thickness reduction in the viscous-controlled case:

$$h_f = h_j \left(1 + h_j^2\,\frac{k_v}{A_f}\,t_c\right)^{-\frac{1}{2}} = h_j \left(1 + h_j^2\,\frac{16\,\sigma}{3\,\mu_f\, d_{eq}^3}\,t_c\right)^{-\frac{1}{2}}, \tag{7.34}$$

which corresponds to the results of Hartland (1967) and Jeffreys and Davis (1971). Since neither of these authors took the transition from inertial to viscous drainage into account, this effect is also not considered in Eq. (7.34). As already described in Section 2.2, the film

drainage between contaminated bubbles is solely dominated by viscous effects in these simpler coalescence models.

Additionally, it was argued in Section 2.2 that another drawback of these simpler models is the missing estimate of the contact time. Consequently, a separate model is required for this quantity. Aside from the approach by Kamp et al. (2001) who also obtained relation (7.14) for t_c using a different approach, the model by Sommerfeld et al. (2003) is quite popular in the literature (see, e.g., Darmana et al., 2006; Jain et al., 2014; Lau et al., 2014; Sungkorn et al., 2012). The contact time proposed by Sommerfeld et al. (2003) reads:

$$t_c = C_S \frac{d_{eq}}{2\, u_{rel,0}}, \tag{7.35}$$

with the model constant arbitrarily set to $C_S = 0.5$.

7.5 Initial and Critical Film Thickness

For a complete description of the film drainage by Eqs. (7.25) to (7.27) the initial and critical film heights h_i and h_{crit} have to be specified. Note that Jeelani and Hartland (1991) did not explicitly specify these quantities. In many studies on bubble coalescence (see, e.g., Darmana et al., 2006; Prince and Blanch, 1990; Sommerfeld et al., 2003; Sungkorn et al., 2012) fixed values are assumed for both the initial and the critical film thickness. A common choice suggested by Prince and Blanch (1990) is:

$$h_i = 10^{-4}\,\mathrm{m}, \tag{7.36}$$

$$h_{crit} = 10^{-8}\,\mathrm{m}, \tag{7.37}$$

where the values of h_i and h_{crit} were proposed by Kirkpatrick and Lockett (1974) and Kim and Lee (1987), respectively. Note that other values for h_i and h_{crit} exist in the literature. For example, Marrucci (1969) estimated the initial film height to be $h_i = 10^{-5}\,\mathrm{m}$, while Kirkpatrick and Lockett (1974) used $h_{crit} = 2.5 \times 10^{-8}\,\mathrm{m}$ for the critical film thickness.

From a physical point of view, it is likely that both the initial as well as the critical film height depend on the properties of the liquid and the bubbles. Therefore, in the present thesis the approach by Chesters (1975, 1991) is followed, who proposed relations for h_i and h_{crit}. Chesters (1975) assumes that the initial film thickness is given by the distance at which the pressure in the liquid between the approaching bubbles is sufficiently large to deform the bubbles. Hence, by relating the liquid pressure and the pressure required for the deformation Chesters (1975) obtains:

$$h_i = \frac{\rho_f\, u_{rel,0}^2\, d_{eq}^2}{16\,\sigma} \left(1 + \frac{8\,\mu_f}{\rho_f\, u_{rel,0}\, d_{eq}}\right). \tag{7.38}$$

In a similar manner, Chesters (1991) estimates the critical film thickness. It is remarked by Chesters (1991) that the van-der-Waals forces acting between the molecules of the liquid trapped between the bubbles are responsible for the destabilization and, thus, the

rupture of the liquid film. Hence, by equating the pressure in the liquid film and the pressure associated with the van-der-Waals forces the estimation:

$$h_{\mathrm{crit}} = \left(\frac{A_{\mathrm{H}}\, d_{\mathrm{eq}}}{24\,\pi\,\sigma} \right)^{\frac{1}{3}}, \tag{7.39}$$

is found. In Eq. (7.39) A_{H} denotes the Hamaker constant (Hamaker, 1937), which according to Hiemenz (1986) is typically of the order of $\mathcal{O}(10^{-20}\,\mathrm{J} - 10^{-19}\,\mathrm{J})$ depending on the liquid considered.

7.6 Post-Coalescence Conditions

Lastly, it remains to determine the post-coalescence conditions for the newly generated bubble. Since in the present thesis the two coalescing bubbles are assumed to consist of fully miscible gases of equal density, the generated bubble cannot possess any structure unlike, for example, solid agglomerates (Almohammed and Breuer, 2016a; Breuer and Almohammed, 2015). Consequently, the size $d_{\mathrm{b,n}}$ of the generated bubble is adequately modeled by a volume-equivalent sphere yielding the bubble diameter:

$$d_{\mathrm{b,n}} = \left(d_{\mathrm{b,1}}^3 + d_{\mathrm{b,1}}^3 \right)^{\frac{1}{3}}, \tag{7.40}$$

where the index 'n' denotes the newly generated bubble. The position $\boldsymbol{x}_{\mathrm{b,n}}$ of the new bubble is equal to the center of mass of the two colliding bubbles prior to coalescence. Hence, $\boldsymbol{x}_{\mathrm{b,n}}$ is given by:

$$\boldsymbol{x}_{\mathrm{b,n}} = \frac{m_{\mathrm{b,1}}\,\boldsymbol{x}_{\mathrm{b,1}} + m_{\mathrm{b,2}}\,\boldsymbol{x}_{\mathrm{b,2}}}{m_{\mathrm{b,n}}} = \frac{d_{\mathrm{b,1}}^3\,\boldsymbol{x}_{\mathrm{b,1}} + d_{\mathrm{b,2}}^3\,\boldsymbol{x}_{\mathrm{b,2}}}{d_{\mathrm{b,n}}^3}. \tag{7.41}$$

Note that $\mathcal{LESOCC}$ performs most calculations of the dispersed phase in the so-called computational space (see Section 9.1 for more details). Consequently, the bubble position given by Eq. (7.41) also has to be provided in the computational space, which is shown in Section 9.3.4. The last property required for the new bubble is its velocity. Since the total momentum of the colliding bubbles has to be conserved, a momentum balance provides the following expression for the velocity $\boldsymbol{u}_{\mathrm{b,n}}$ of the bubble after coalescence occurred:

$$\boldsymbol{u}_{\mathrm{b,n}} = \frac{d_{\mathrm{b,1}}^3\,\boldsymbol{u}_{\mathrm{b,1}} + d_{\mathrm{b,2}}^3\,\boldsymbol{u}_{\mathrm{b,2}}}{d_{\mathrm{b,n}}^3}. \tag{7.42}$$

In Eq. (7.42) the velocities $\boldsymbol{u}_{\mathrm{b,1}}$ and $\boldsymbol{u}_{\mathrm{b,2}}$ are the velocities of the coalescing bubbles immediately before the collision. Note that the angular momentum of the new bubble described by the corresponding conservation law is neglected. Similar to the argumentation in Section 4.1, the vanishing moment of inertia of the bubble is the reason behind this approach.

8 Modeling of Bubble Breakup

As explained in the literature review in Section 2.3, the breakup of small bubbles is mainly caused by turbulent velocity fluctuations in the inertial subrange of turbulence. Other mechanisms (surface instabilities and viscous shear stresses) briefly presented in Sections 2.3.1 and 2.3.2 only play a role for large bubbles and are not considered in the present thesis. Hence, the focus of the present chapter is the description of turbulence-induced bubble breakup. The starting point of the modeling is the approach by Hagesaether et al. (2002), which is chosen due to the reasonable physical assumptions considered in the modeling of the breakup process (see Section 2.3.3). In Section 8.1 the breakup criterion proposed by Hagesaether et al. (2002) is introduced. An additional advantage of the chosen model is the possibility to deterministically estimate the size of the daughter bubbles based on the breakup criterion. Nevertheless, one major challenge associated with breakup models is the transfer to the Euler–Lagrange framework, since these models are typically based on the Euler–Euler approach, where the exact properties of the individual bubbles are not considered. Hence, the formulation of suitable post-breakup conditions for the daughter bubbles is a critical issue for the breakup modeling presented in this chapter. This topic is explained in Section 8.2. Note that most of these considerations have been published in Hoppe and Breuer (2020).

8.1 Breakup Criterion by Hagesaether et al. (2002)

As described in Section 2.3.3, bubble breakup is a highly complex process requiring a simplifying representation for the modeling. A schematic depiction of the breakup process is shown in Fig. 8.1. Figure 8.1(a) depicts the starting point for the modeling of the breakup process. It is assumed that the parent bubble of diameter $d_{\mathrm{b,p}}$ interacts with a turbulent eddy of the same size. As shown in Fig. 8.1(b), the pressure fluctuations associated with the turbulent velocity fluctuations $\langle u_i' \, u_i' \rangle_{d_{\mathrm{b,p}}}$ potentially deform the parent bubble into a dumbbell-like shape. Furthermore, it is assumed here that the deformation occurs along a separation axis $\boldsymbol{x}_{\mathrm{sep}}$. Note that the dumbbell-shaped parent bubble spans a distance of d_{db} along this separation axis. A deformation of this type prior to breakup is in accordance with both experiments and fully-resolved simulations (see, e.g., Andersson and Andersson, 2006a; Qian et al., 2006; Risso and Fabre, 1998). If this deformation is sufficiently strong, the parent bubble cannot restore its original shape and breaks up. The conditions after breakup are shown in Fig. 8.1(c). Since only binary breakup is considered in the present work, the parent bubble breaks into two daughter bubbles of size $d_{\mathrm{b,s}}$ and $d_{\mathrm{b},\ell}$. Here, the subscripts 's' and 'ℓ' denote the smaller and the larger daughter bubble, respectively. This notation is also used in the case of equally-sized breakup. The daughter

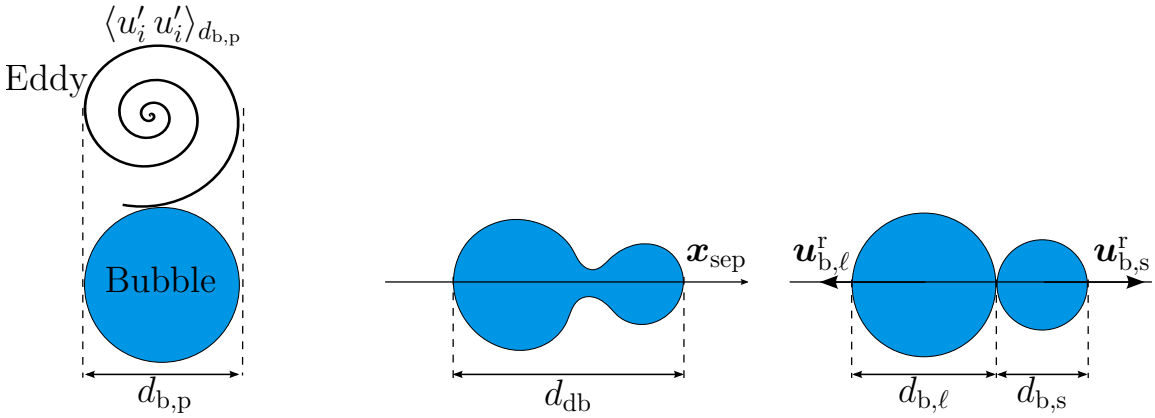

(a) Eddy impact. **(b)** Dumbbell-like bubble. **(c)** Bubble breakup.

Fig. 8.1. Schematic sketch of the turbulence-induced breakup: (a) The impact of a turbulent eddy (size $d_{b,p}$, associated fluctuations $\langle u_i' u_i' \rangle_{d_{b,p}}$) leads to (b) the dumbbell-shaped deformation of the parent bubble along the separation axis $\boldsymbol{x}_{sep}$. (c) If the neck ruptures, the bubble breaks into two daughters of size $d_{b,s}$ and $d_{b,\ell}$, which separate from each other along $\boldsymbol{x}_{sep}$ with the velocities $\boldsymbol{u}^r_{b,s}$ and $\boldsymbol{u}^r_{b,\ell}$. The process takes a breakup time of Δt_{break} to complete.

bubbles separate from each other with the relative velocities $\boldsymbol{u}^r_{b,s}$ and $\boldsymbol{u}^r_{b,\ell}$ along the separation axis $\boldsymbol{x}_{sep}$ along which the parent bubble has been deformed immediately before breakup. The superscript 'r' denotes that the post-breakup velocities are estimated in the frame of reference of the parent bubble moving with the velocity $\boldsymbol{u}_{b,p}$. Note that the whole process depicted in Fig. 8.1 takes a certain amount of time (Andersson and Andersson, 2006a). As proposed in Hoppe and Breuer (2020), the time span from the impact of the eddy (Fig. 8.1(a)) leading to the deformation of the parent bubble (Fig. 8.1(b)) to its breakup (Fig. 8.1(c)) is denoted the breakup time Δt_{break}.

In order to represent the breakup process described above, Hagesaether et al. (2002) assumed that the energy density w_t of the turbulent velocity fluctuations has to be equal to or higher than the surface energy $w_{b,s}$ of the smaller daughter bubble generated by the breakup process. Hence, the breakup criterion reads:

$$w_t \geq w_{b,s}. \tag{8.1}$$

Hagesaether et al. (2002) define the energy density of the turbulent eddy by the ratio of the turbulent kinetic energy E_t of the corresponding fluid fluctuations to the volume of the eddy. Since it is assumed that the parent bubble is deformed by velocity fluctuations of the same size, the volume of the eddy is equal to the volume $V_{b,p}$ of the parent bubble. Therefore, the energy density of the turbulent eddy responsible for the deformation of the parent bubble prior to breakup is given by:

$$w_t = \frac{E_t}{V_{b,p}} = \frac{1}{2} \rho_f \langle u_i' u_i' \rangle_{d_{b,p}}. \tag{8.2}$$

According to Hagesaether et al. (2002), the surface energy density is given by the surface energy $E_{\mathrm{s,s}} = \sigma\,\pi\,d_{\mathrm{b,s}}^2$ of the smaller daughter bubble divided by its volume:

$$w_{\mathrm{b,s}} = \frac{E_{\mathrm{s,s}}}{V_{\mathrm{b,s}}} = 6\,\frac{\sigma}{d_{\mathrm{b,s}}}. \tag{8.3}$$

Note that in the definition of the surface energy and in Eq. (8.3) the relations for the surface and the volume of a sphere are used. This implies that the smaller daughter bubble is also spherical. However, experiments by Andersson and Andersson (2006a) and Risso and Fabre (1998) show that this may not be true in reality, i.e., the generated daughter bubbles are typically non-spherical immediately after breakup. Therefore, the breakup criterion (8.1) by Hagesaether et al. (2002) is an inequality reflecting the fact that not necessarily the complete turbulent energy density of the eddy is transformed into the surface energy density of the smaller (spherical) daughter bubble. A part of w_{t} may be contained in the energy density associated with the deformation of the smaller daughter bubble, which is not accounted for by the model.

Furthermore, it has to be noted that the energy density of the turbulent velocity fluctuations (Eq. (8.2)) corresponds to the turbulent pressure fluctuations associated with the eddy. On the other hand, the surface energy density given by Eq. (8.3) describes the surface restoring pressure of the smaller daughter bubble. Consequently, the physical meaning behind the breakup criterion Eq. (8.1) is that breakup requires the turbulent pressure fluctuations to be larger than the surface restoring pressure of the smaller daughter bubble trying to prevent the contraction and the rupture of the neck of gas formed between the two volumes of gas of the dumbbell-like parent bubble. Consequently, the model by Hagesaether et al. (2002) provides a physically meaningful criterion for the direct breakup of bubbles. However, the breakup due to the pinch off of a small daughter bubble during the backflow inside the deformed parent bubble is not accounted for.

The breakup criterion by Hagesaether et al. (2002) can be formulated in dimensionless form by inserting Eqs. (8.2) and (8.3) into the inequality (8.1). After some minor rearrangements the breakup criterion containing the dimensionless Weber number reads:

$$\mathrm{We} \geq 12\,\frac{d_{\mathrm{b,p}}}{d_{\mathrm{b,s}}} = 12\,f_{\mathrm{V}}^{-\frac{1}{3}}. \tag{8.4}$$

In relation (8.4) the volume fraction $f_{\mathrm{V}} = d_{\mathrm{b,s}}^3/d_{\mathrm{b,p}}^3$ is defined by the volume of the smaller daughter bubble to the volume of the parent bubble. The dimensionless Weber number is given by:

$$\mathrm{We} = \frac{\rho_{\mathrm{f}}\,d_{\mathrm{b,p}}\,\langle u_i'\,u_i'\rangle_{d_{\mathrm{b,p}}}}{\sigma}. \tag{8.5}$$

It is obvious that the ratio $f_{\mathrm{V}}^{-1/3}$ reaches its smallest value for breakup into two equally-sized daughter bubbles, i.e., $f_{\mathrm{V,min}}^{-1/3} = 0.5^{-1/3} \approx 1.26$. Consequently, in order to break up

a bubble into two equally-sized daughter bubbles, the Weber number has to be equal to or larger than a minimum Weber number:

$$\mathrm{We}_{\mathrm{min}} = 12 \left(\frac{1}{2}\right)^{-\frac{1}{3}} \approx 15.12. \tag{8.6}$$

For breakup into unequally-sized daughter bubbles the Weber number has to be larger, since the volume fraction $f_{\mathrm{V}}^{-1/3}$ increases with a decreasing size of the smaller daughter bubble. The physical reason behind this behavior is the larger surface restoring pressure resisting the breakup associated with a smaller daughter bubble.

The prediction of breakup by Eq. (8.4) requires the estimation of the turbulent velocity fluctuations $\langle u_i' \, u_i' \rangle_{d_{\mathrm{b,p}}}$ over the size of the parent bubble. It is common practice in the modeling of turbulence-induced breakup to assume that the fluctuations are in the inertial subrange of turbulence (see, e.g., Lehr et al., 2002; Luo and Svendsen, 1996; Martínez-Bazán et al., 1999a; Prince and Blanch, 1990). For this specific case relations for the turbulent velocity fluctuations over a certain distance are available in the literature. According to Batchelor (1953) the fluctuations $\langle u_i' \, u_i' \rangle_{d_{\mathrm{b,p}}}$ over the diameter $d_{\mathrm{b,p}}$ of the parent bubble read:

$$\langle u_i' \, u_i' \rangle_{d_{\mathrm{b,p}}} = \beta \left(\epsilon \, d_{\mathrm{b,p}}\right)^{\frac{2}{3}}, \tag{8.7}$$

with β a proportionality constant, which is related to the Kolmogorov constant c_{K}. The term ϵ denotes the energy dissipation rate of the turbulent fluid flow at the position of the bubble. According to Batchelor (1953) the relation between the two constants is given by:

$$\beta = \frac{9}{5} \Gamma\left(\frac{1}{3}\right) c_{\mathrm{K}}, \tag{8.8}$$

where Γ denotes the Gamma-function, which has a value of $\Gamma(1/3) \approx 2.68$. The value of the Kolmogorov constant varies throughout the available literature. Batchelor (1953) used $c_{\mathrm{K}} = 1.7$, while Tennekes and Lumley (1972) gave a value of $c_{\mathrm{K}} = 1.5$. Based on a review of a large number of experimental studies on the value of the Kolmogorov constant, Sreenivasan (1995) proposed a value of:

$$c_{\mathrm{K}} = 1.62, \tag{8.9}$$

which is used in the present thesis as well. Therefore, Eq. (8.8) yields a value of $\beta \approx 7.81$ for the proportionality constant. It remains to determine the dissipation rate of the fluid at the position of the bubble. According to Hinze (1975), the dissipation rate can be estimated by:

$$\epsilon = 2 \, \nu_{\mathrm{f}} \, S_{ij} \, S_{ij}, \tag{8.10}$$

where S_{ij} is the strain rate tensor defined by Eq. (3.3). In the LES context this quantity is estimated by $\overline{S}_{ij}$ defined by Eq. (3.10). Thus, the filtered velocity field is used to approximate the strain rate tensor.

As already mentioned in Section 2.3, Castellano et al. (2019), Karimi and Andersson (2019) and Solsvik and Jakobsen (2016a,b) remarked that the assumption of bubbles being

solely subjected to turbulent fluctuations in the inertial subrange may not be correct. In contrast, according to these authors the whole spectrum of turbulence should be considered. For this purpose, Eq. (8.7) describing the turbulent velocity fluctuations has to be replaced by a different relation, which is based on model energy spectra like the ones by Hinze (1975) or Pope (2000). Based on the energy spectrum by Pope (2000), a highly complex relation describing the fluid fluctuations in the inertial and energy-containing subranges of turbulence was proposed by Solsvik and Jakobsen (2016b). Note that in this work the dissipative subrange of turbulence is not taken into account. Applying such a relation allows for a more physical description of the turbulence-induced breakup process. Nevertheless, Eq. (8.7) is used in the present thesis for the sake of simplicity, since the more complex approaches require a much higher computational effort. For example, the approach by Solsvik and Jakobsen (2016b) relies on a coefficient which has to be determined by a root-finding algorithm for each individual bubble at each time step. The choice of using the simple relation (8.7) is further motivated by the fact that the majority of the bubbles considered in the experiment by Martínez-Bazán et al. (1999a,b), which is chosen as the reference case for the present breakup model (Section 11.4), is within the inertial subrange, see Section 10.5 for an estimation. An overview on existing model energy spectra and the resulting estimations of the fluctuations is given by Solsvik and Jakobsen (2016a).

8.2 Post-Breakup Treatment

Aside from the appropriate description of the breakup process by criterion (8.4) presented in the previous section, the formulation of suitable post-breakup conditions for the generated daughter bubbles is the main challenge associated with the transfer of breakup models to the Euler–Lagrange framework. As depicted in Fig. 8.1 this includes the prediction of the diameters $d_{\mathrm{b},s}$ and $d_{\mathrm{b},\ell}$ of the daughter bubbles. Additionally, the axis $\boldsymbol{x}_{\mathrm{sep}}$ along which the bubbles separate from each other and the corresponding relative velocities $\boldsymbol{u}^{\mathrm{r}}_{\mathrm{b,s}}$ and $\boldsymbol{u}^{\mathrm{r}}_{\mathrm{b},\ell}$ are required. Lastly, the breakup time $\Delta t_{\mathrm{break}}$ has to be estimated.

8.2.1 Size of the Daughter Bubbles

Before the size of the daughter bubbles can be estimated, the number of bubbles resulting from a breakup process has to be specified. As already mentioned before in the literature overview on turbulence-induced breakup (Section 2.3.3), binary bubble breakup is most commonly observed by experiments (see, e.g., Andersson and Andersson, 2006a,b; Hesketh et al., 1991a,b; Martínez-Bazán et al., 1999a; Risso and Fabre, 1998; Stewart, 1995; Walter and Blanch, 1986). Non-binary breakup into up to ten fragments has been observed, for example, by Risso and Fabre (1998) and Solsvik and Jakobsen (2015). However, in these experiments the size of the bubbles is relatively large, i.e., $d_{\mathrm{b}} \gtrsim 2\,\mathrm{mm}$. In the present thesis mostly small bubbles of diameters less than 1.5 mm are considered. Consequently, the application of the common assumption of binary breakup is reasonable. Furthermore, note that in the experiments by Martínez-Bazán et al. (1999a,b) forming the basis for the

test case applied for the present breakup model (Sections 10.5 and 11.4) binary breakup was also the most common type of breakup. According to Martínez-Bazán et al. (1999a,b) binary breakup events are characterized by low to moderate Weber numbers, whereas non-binary breakup only occurs for the rare case of very large We. Hence, in the present thesis the breakup is assumed to be binary. However, it has to be kept in mind, that the non-binary breakup is at least a possibility, although such an event is not accounted for by the present model.

Since most breakup models are derived in the framework of a population balance equation incorporated in Euler–Euler predictions, the typical approach in the literature (see, e.g., Hagesaether et al., 2002; Luo and Svendsen, 1996; Martínez-Bazán et al., 1999a; Prince and Blanch, 1990) is to model the size of the daughter bubbles according to a size distribution. This idea was also followed in the Euler–Lagrange predictions of Jain et al. (2014) and Lau et al. (2014). However, this leads to the necessity to randomly choose the size of the daughter bubbles. In order to circumvent this drawback, it was proposed by Hoppe and Breuer (2020) that breakup only occurs, if criterion (8.4) is exactly fulfilled. Hence, the inequality is transformed into an equality and Eq. (8.4) can be readily solved for the diameter $d_{\mathrm{b,s}}$ of the smaller daughter bubble. Since the total volume of the parent bubble has to be conserved, the diameter of the corresponding larger daughter bubble is also determined. Thus, under the condition that the Weber number is sufficiently large for breakup to occur ($\mathrm{We} \geq \mathrm{We}_{\mathrm{min}}$), the sizes of the daughter bubbles are given by:

$$d_{\mathrm{b,s}} = \frac{12}{\mathrm{We}}\, d_{\mathrm{b,p}}, \tag{8.11a}$$

$$d_{\mathrm{b},\ell} = \left(d_{\mathrm{b,p}}^3 - d_{\mathrm{b,s}}^3\right)^{\frac{1}{3}}. \tag{8.11b}$$

From a physical point of view Eq. (8.11) means that the entire turbulent kinetic energy density is transformed into the surface energy density of the smaller daughter bubble. Note that Eq. (8.11) indeed yields two equally-sized daughter bubbles for $\mathrm{We} = \mathrm{We}_{\mathrm{min}}$. According to Eq. (8.11a) the size of the smaller daughter bubble decreases with increasing We, while $d_{\mathrm{b},\ell}$ tends to $d_{\mathrm{b,p}}$ (Eq. (8.11b)). This is plausible, since the stresses required to directly break off a small daughter bubble have to be larger as well.

8.2.2 Separation Axis

Subsequently, the separation axis $\boldsymbol{x}_{\mathrm{sep}}$ along which the parent bubble is deformed and the daughter bubbles separate from each other after breakup has to be estimated. To the best of the author's knowledge the axis of separation of bubbles has not been studied numerically or experimentally before. Since Euler–Euler predictions rely on population balance equations, it is not necessary to specify the separation axis in this approach. In the Euler–Lagrange based studies by Jain et al. (2014) and Lau et al. (2014) on bubble breakup the separation axis is chosen randomly. However, it is doubtful that this reflects the correct physical behavior.

Saha (2013) experimentally studied the direction of separation of *solid* fragments after the breakup of agglomerates. The experiments were conducted with a quasi-homogeneous

and isotropic turbulent flow inside a tank. About 100 binary breakup events have been observed by Saha (2013). Additionally, the fluid stresses around the agglomerates at the instance of breakup have been measured by tracking tracer particles. It was found that the axis of separation $\boldsymbol{x}_{\text{sep}}$ is mostly aligned with the direction of the largest fluid stresses. This observation can be explained by the fact that these stresses lead to the breakup of the agglomerate. Despite the circumstance that Saha (2013) considered solid particles, it is assumed in the present thesis that the breakup of gas bubbles is governed by a similar mechanism. Since the parent bubble is deformed into a dumbbell-like shape by the fluid stresses around its surface, it is plausible to assume that the associated stretching of the bubble (see Fig. 8.1(b)) is aligned with the direction of the largest stresses. Hence, the generated daughter bubbles should separate in the same direction after breakup (Hoppe and Breuer, 2020). Note that Breuer and Khalifa (2019a,b) successfully applied the idea of Saha (2013) in their improved Euler–Lagrange based model for the breakup of agglomerates due to turbulent stresses.

Saha (2013) determined the eigenvalues $\lambda^{(k)}$ and the corresponding eigenvectors $\boldsymbol{x}_{\text{eig}}^{(k)}$ of the strain rate tensor S_{ij} given by Eq. (3.3). Both quantities are defined by the characteristic equation:

$$S_{ij}\, x_{\text{eig},j}^{(k)} = \lambda^{(k)}\, x_{\text{eig},i}^{(k)}. \tag{8.12}$$

Since S_{ij} is a 3×3 matrix, it has three eigenvalues and eigenvectors, which are distinguished by the superscript (k). According to Saha (2013) there always exists one largest positive eigenvalue $\lambda^{(\ell)}$ and one smallest negative eigenvalue $\lambda^{(\text{s})}$. The third intermediate eigenvalue $\lambda^{(\text{m})}$ is either positive or negative. Here, a positive eigenvalue means that the fluid stresses stretch a fluid element in the direction of the corresponding eigenvalue, while a negative eigenvalue means that the fluid element is compressed (Saha, 2013). Hence, the largest fluid stresses leading to the most pronounced stretching are pointing in the direction of the eigenvector $\boldsymbol{x}_{\text{eig}}^{(\ell)}$ corresponding to the most extensional, positive eigenvector $\lambda^{(\ell)}$. Consequently, it is assumed that the deformation of the parent bubble and the corresponding axis of separation of the daughter bubbles is given by (Hoppe and Breuer, 2020):

$$\boldsymbol{x}_{\text{sep}} = \boldsymbol{x}_{\text{eig}}^{(\ell)}. \tag{8.13}$$

It remains to determine the largest eigenvalue and the corresponding eigenvector of the strain rate tensor S_{ij} or more precisely the strain rate tensor $\overline{S}_{ij}$ of the filtered velocity field. Since $\overline{S}_{ij}$ is a symmetric matrix, λ^{ℓ} and $\boldsymbol{x}_{\text{eig}}^{\ell}$ can be readily found by simple transformation algorithms (see, e.g., Press et al., 2007). In the first step, a Householder transformation is applied decomposing $\overline{S}_{ij}$ into an orthogonal matrix Q_{ij} and a real, symmetric and tridiagonal matrix A_{ij}. Afterwards, a lower triangular matrix L_{ij} is obtained by a QL-algorithm with implicit shifts (also see Press et al., 2007). The eigenvalues $\lambda^{(k)}$ of the strain rate tensor are found on the diagonal of L_{ij}. The major advantage of this procedure is that the eigenvectors are also determined. Hence, in the last step a simple sorting algorithm is required to find the largest eigenvalue $\lambda^{(\ell)}$ needed to identify the corresponding eigenvector $\boldsymbol{x}_{\text{eig}}^{(\ell)}$. Note that this procedure yields a normalized eigenvector making $\boldsymbol{x}_{\text{sep}}$ normalized as well.

8.2.3 Separation Velocity

It is known from experiments by Andersson and Andersson (2006a) and Risso and Fabre (1998) that the daughter bubbles do not overlap after the breakup. Hence, their centers of mass should be separated by a minimum distance equal to the sum of their radii. With the axis of separation determined in Section 8.2.2, it is in principle possible to set the positions of the daughter bubbles along $\boldsymbol{x}_{\mathrm{sep}}$ starting from the last position of the parent bubble. However, this poses several difficulties. Firstly, the daughter bubbles can overlap with other surrounding bubbles. Additionally, if the fluid phase is predicted using a block-structured grid on a parallel computer, the daughter bubbles may be moved out of the block executed by a certain processor due to the re-positioning after breakup. Hence, time-consuming exchange mechanisms between blocks are required. Related to this difficulty is the case, where breakup occurs close to a solid wall in such a way that a bubble-wall collision takes place. In order to circumvent the large computational effort associated with the solution of these challenges, the positions of the daughter bubbles are set equal to the position of the parent bubble. The immediate re-coalescence of the daughter bubbles is prevented by estimating the post-breakup relative velocities $\boldsymbol{u}_{\mathrm{b,s}}^{\mathrm{r}}$ and $\boldsymbol{u}_{\mathrm{b},\ell}^{\mathrm{r}}$ with which the daughter bubbles separate from each other. Note again that the superscript 'r' denotes that the velocities are determined in the moving frame of reference of the parent bubble (velocity $\boldsymbol{u}_{\mathrm{b,p}}$). Since the bubbles are assumed to separate along the axis $\boldsymbol{x}_{\mathrm{sep}}$, the velocities $\boldsymbol{u}_{\mathrm{b,s}}^{\mathrm{r}}$ and $\boldsymbol{u}_{\mathrm{b},\ell}^{\mathrm{r}}$ point in opposite directions along $\boldsymbol{x}_{\mathrm{sep}}$:

$$\boldsymbol{u}_{\mathrm{b,s}}^{\mathrm{r}} = \quad u_{\mathrm{b,s}}^{\mathrm{r}}\, \boldsymbol{x}_{\mathrm{sep}}, \tag{8.14}$$

$$\boldsymbol{u}_{\mathrm{b},\ell}^{\mathrm{r}} = -u_{\mathrm{b},\ell}^{\mathrm{r}}\, \boldsymbol{x}_{\mathrm{sep}}. \tag{8.15}$$

Note that the choice which velocity is positive and which is negative is arbitrary.

In order to estimate the actual velocities, an energy balance between the kinetic energies $E_{\mathrm{kin,s}}^{\mathrm{r}}$ and $E_{\mathrm{kin},\ell}^{\mathrm{r}}$ of the daughter bubbles in the moving frame of reference, the turbulent kinetic energy $E_{\mathrm{turb,db}}$ of the velocity fluctuations exerted on the deformed parent bubble during breakup and the turbulent kinetic energy E_{break} required for the breakup process is used. Hence, the energy balance reads:

$$E_{\mathrm{kin,s}}^{\mathrm{r}} + E_{\mathrm{kin},\ell}^{\mathrm{r}} = E_{\mathrm{turb,db}} - E_{\mathrm{break}} \tag{8.16}$$

As illustrated by Fig. 8.1(b) during the breakup process the parent bubble is deformed to a dumbbell-like shape, where the largest size associated with this deformation is given by the distance d_{db}. Since this size is larger than the diameter of the parent bubble, additional stresses are exerted on the deformed bubble. Hence, if the parent bubble breaks, these additional stresses act on the daughter bubbles driving them away from each other (Hoppe and Breuer, 2020). Therefore, in the present thesis it is assumed that the turbulent kinetic energy $E_{\mathrm{turb,db}}$ is related to the turbulent velocity fluctuations $\langle u_i' \, u_i' \rangle_{d_{\mathrm{db}}}$ over the size of the dumbbell-shaped parent bubble. These fluctuations are estimated by Eq. (8.7) given by Batchelor (1953), but with $d_{\mathrm{b,p}}$ replaced by d_{db}. Unfortunately, the size d_{db} of the deformed parent bubble during the breakup process is unknown. Hence, it was proposed

by Hoppe and Breuer (2020) to estimate d_{db} based on the sizes of the generated daughter bubbles:

$$d_{\mathrm{db}} = d_{\mathrm{b,s}} + d_{\mathrm{b},\ell}. \tag{8.17}$$

However, since the fluctuations $\langle u_i' \, u_i' \rangle_{d_{\mathrm{b,p}}}$ over the size of the parent bubble lead to the initial deformation of the parent bubble and the subsequent breakup, the corresponding kinetic energy E_{break} does not contribute to the relative separation velocities. Hence, it is assumed that E_{break} is completely consumed by the breakup process. Thus, only the excess turbulent kinetic energy ΔE is available for the separation velocity of the daughter bubbles:

$$\Delta E = E_{\mathrm{turb,db}} - E_{\mathrm{break}} = \frac{1}{2} \, m_{\mathrm{f}} \left(\langle u_i' \, u_i' \rangle_{d_{\mathrm{db}}} - \langle u_i' \, u_i' \rangle_{d_{\mathrm{b,p}}} \right). \tag{8.18}$$

In Eq. (8.18) $m_{\mathrm{f}} = \rho_{\mathrm{f}} \, V_{\mathrm{b,p}}$ is the mass of the fluid displaced by the parent bubble, since the fluid fluctuations are exerted on a fluid volume equal to the volume of the parent bubble. Consequently, the energy balance describing the relative velocities of the daughter bubbles (Eq. (8.16)) can be written in the form:

$$m_{\mathrm{s}} \left(u_{\mathrm{b,s}}^{\mathrm{r}} \right)^2 + m_{\ell} \left(u_{\mathrm{b},\ell}^{\mathrm{r}} \right)^2 = 2 \, \Delta E. \tag{8.19}$$

In Eq. (8.19) the fact that the separating bubbles have to accelerate the fluid surrounding them is accounted for. Hence, the masses m_{s} and m_{ℓ} are defined according to Eq. (7.5), i.e., they are a combination of the bubble masses $m_{\mathrm{b,s}}$ and $m_{\mathrm{b},\ell}$ and the corresponding added masses of the displaced fluid $m_{\mathrm{AM,s}}$ and $m_{\mathrm{AM},\ell}$:

$$m_{\mathrm{s}} = m_{\mathrm{b,s}} + m_{\mathrm{AM,s}} = \rho_{\mathrm{b}} \, V_{\mathrm{b,s}} \left(1 + C_{\mathrm{m}}' \, \frac{\rho_{\mathrm{f}}}{\rho_{\mathrm{b}}} \right), \tag{8.20}$$

$$m_{\ell} = m_{\mathrm{b},\ell} + m_{\mathrm{AM},\ell} = \rho_{\mathrm{b}} \, V_{\mathrm{b},\ell} \left(1 + C_{\mathrm{m}}' \, \frac{\rho_{\mathrm{f}}}{\rho_{\mathrm{b}}} \right). \tag{8.21}$$

Similar to Section 7.1, C_{m}' is the modified added-mass coefficient. Here, it is assumed that C_{m}' is given by Eq. (7.7).

In order to determine the relative velocities of the daughter bubbles after breakup, a second equation is required. For this purpose, the conservation of momentum is applied. Since the daughter bubbles are assumed to separate along $\boldsymbol{x}_{\mathrm{sep}}$ in the frame of reference moving with the velocity $\boldsymbol{u}_{\mathrm{b,p}}$, the momentum balance of the daughter bubbles has to read:

$$m_{\mathrm{s}} \, u_{\mathrm{b,s}}^{\mathrm{r}} - m_{\ell} \, u_{\mathrm{b},\ell}^{\mathrm{r}} = 0. \tag{8.22}$$

By solving Eq. (8.22) for the relative velocity of the larger daughter bubble and inserting into Eq. (8.19), a relation containing only the velocity of the smaller daughter bubble is obtained. Hence, the resulting expression can be readily solved for $u_{\mathrm{b,s}}^{\mathrm{r}}$, which then

can be inserted into Eq. (8.22) to determine the velocity of the larger daughter bubble. Consequently, the relative velocities are given by:

$$u_{\mathrm{b,s}}^{\mathrm{r}} = \left[\frac{1}{m_{\mathrm{s}} + m_{\ell}} \frac{m_{\ell}}{m_{\mathrm{s}}} 2\,\Delta E\right]^{\frac{1}{2}}, \tag{8.23}$$

$$u_{\mathrm{b},\ell}^{\mathrm{r}} = \left[\frac{1}{m_{\mathrm{s}} + m_{\ell}} \frac{m_{\mathrm{s}}}{m_{\ell}} 2\,\Delta E\right]^{\frac{1}{2}}. \tag{8.24}$$

By inserting Eqs. (8.23) and (8.24) into Eqs. (8.14) and (8.15) the velocities of the daughter bubbles after the breakup are obtained in the Eulerian frame of reference:

$$\boldsymbol{u}_{\mathrm{b,s}} = \boldsymbol{u}_{\mathrm{b,p}} + \left[\frac{1}{\frac{\rho_{\mathrm{b}}}{\rho_{\mathrm{f}}} + C'_{\mathrm{m}}} \frac{d_{\mathrm{b},\ell}^3}{d_{\mathrm{b,s}}^3} \left(\langle u_i' \, u_i' \rangle_{d_{\mathrm{db}}} - \langle u_i' \, u_i' \rangle_{d_{\mathrm{b,p}}}\right)\right]^{\frac{1}{2}} \boldsymbol{x}_{\mathrm{sep}}, \tag{8.25}$$

$$\boldsymbol{u}_{\mathrm{b},\ell} = \boldsymbol{u}_{\mathrm{b,p}} - \left[\frac{1}{\frac{\rho_{\mathrm{b}}}{\rho_{\mathrm{f}}} + C'_{\mathrm{m}}} \frac{d_{\mathrm{b,s}}^3}{d_{\mathrm{b},\ell}^3} \left(\langle u_i' \, u_i' \rangle_{d_{\mathrm{db}}} - \langle u_i' \, u_i' \rangle_{d_{\mathrm{b,p}}}\right)\right]^{\frac{1}{2}} \boldsymbol{x}_{\mathrm{sep}}. \tag{8.26}$$

8.2.4 Breakup Time

Another difficulty arising in the framework of Euler–Lagrange predictions of bubble breakup are the repeated breakups of the same bubble at several successive time steps. This phenomenon occurs when a large bubble breaks up due to strong fluid fluctuations. In this case one small and one large daughter bubble are generated. The larger daughter bubble immediately may fulfill the breakup criterion in the following time step. Hence, the bubble is further split into two daughter bubbles, where again the larger one is only slighter smaller than the previous daughter bubble. It is possible that this process is repeated multiple times until the breakup criterion is not fulfilled anymore. From a numerical point of view, this issue is related to the modeling of breakup in the presently applied Euler–Lagrange framework, i.e., the whole breakup process including the deformation of the parent bubble and the formation of the daughter bubbles is an instantaneous event taking place within one computational time step Δt. If no countermeasures are taken (e.g., in form of an idle time), this means that the original parent bubble is subject to an unphysical erosion process generating a large swarm of small daughter bubbles. The associated breakup rate is directly proportional to the numerical time-step size of the simulation and not based on physical arguments. Since for LES the chosen time steps are typically small, such an unphysical behavior can take place very quickly.

In order to inhibit this artificial erosion process, the further breakup of the daughter bubbles generated by the breakup of a parent bubble is prevented during a certain *idle time* Δt_{idle}. As depicted in Fig. 8.1 the deformation and subsequent breakup of the parent bubble takes a breakup time of $\Delta t_{\mathrm{break}}$ to complete. Hence, the idle time in which the daughter bubbles cannot breakup is estimated by the breakup time, i.e., $\Delta t_{\mathrm{idle}} = \Delta t_{\mathrm{break}}$. Since the breakup is caused by the turbulent velocity fluctuations of the fluid around the

parent bubble, it is plausible to assume that the breakup time is related to the turbulent time scale Δt_{turb} of the fluctuations, which can be estimated in different ways.

For example, Andersson and Andersson (2006a) proposed to estimate the breakup time by the time scale given by the ratio of the turbulent kinetic energy k of the fluctuations to the dissipation rate ϵ of the fluid. If the turbulent kinetic energy k is estimated by $\langle u_i' \, u_i' \rangle_{d_{\text{b,p}}}/2$ with the fluctuations given by Eq. (8.7), the turbulent time scale reads (Andersson and Andersson, 2006a):

$$\Delta t_{\text{turb,AA}} = \frac{k}{\epsilon} = \frac{\beta}{2} \frac{d_{\text{b,p}}^{\frac{2}{3}}}{\epsilon^{\frac{1}{3}}}. \tag{8.27}$$

In order to relate the turbulent time scale given by Eq. (8.27) with the breakup time, Andersson and Andersson (2006a) experimentally investigated the breakup process of air bubbles in a turbulent water flow at a Reynolds number of $\text{Re} = 66,000$. They observed that the breakup of a bubble with a diameter of 1 mm takes approximately 2 to 3.4 ms, which is roughly 1/2 to 2/3 of $\Delta t_{\text{turb,AA}}$. Consequently, the breakup time according to Andersson and Andersson (2006a) can be estimated by:

$$\Delta t_{\text{break,AA}} = C_{\text{break,AA}} \frac{d_{\text{b,p}}^{\frac{2}{3}}}{\epsilon^{\frac{1}{3}}}, \quad \text{with} \quad C_{\text{break,AA}} = C_{\text{AA}} \frac{\beta}{2}. \tag{8.28}$$

In Eq. (8.28) the constant $C_{\text{AA}} = 1/2$ to $2/3$ is the experimentally determined factor between the breakup and the turbulent time scale.

A second option for the estimation of the breakup time is to use the eddy turnover time obtained by dividing a characteristic length scale by a characteristic velocity:

$$\Delta t_{\text{turb,et}} = \frac{l_{\text{c}}}{v_{\text{c}}}. \tag{8.29}$$

Since the length scale of the turbulent fluctuations responsible for the breakup is the diameter of the parent bubble, $l_{\text{c}} = d_{\text{b,p}}$ is used in the present thesis. The characteristic velocity can be estimated in different ways. One possibility is to define v_{c} as the square-root of the turbulent kinetic energy $k^{1/2}$ with k estimated by the above relation. The resulting turbulent time scale based on the eddy turnover time and the square-root of k is given by:

$$\Delta t_{\text{turb,etk}} = \frac{d_{\text{b,p}}}{k^{\frac{1}{2}}} = \left(\frac{2}{\beta}\right)^{\frac{1}{2}} \frac{d_{\text{b,p}}^{\frac{2}{3}}}{\epsilon^{\frac{1}{3}}}, \tag{8.30}$$

Hence, the breakup time is given by:

$$\Delta t_{\text{break,etk}} = C_{\text{break,etk}} \frac{d_{\text{b,p}}^{\frac{2}{3}}}{\epsilon^{\frac{1}{3}}}, \quad \text{with} \quad C_{\text{break,etk}} = \left(\frac{2}{\beta}\right)^{\frac{1}{2}}. \tag{8.31}$$

Alternatively, the characteristic velocity can be obtained by taking the square-root of the turbulent fluctuations $\langle u_i' \, u_i' \rangle_{d_{\mathrm{b,p}}}^{1/2}$ leading to the expression:

$$\Delta t_{\mathrm{break,etf}} = C_{\mathrm{break,etf}} \frac{d_{\mathrm{b,p}}^{\frac{2}{3}}}{\epsilon^{\frac{1}{3}}}, \quad \text{with} \quad C_{\mathrm{break,etf}} = \left(\frac{1}{\beta} \right)^{\frac{1}{2}}. \tag{8.32}$$

By comparing Eqs. (8.31) and (8.32) it is obvious that both relations only differ by a factor of $\sqrt{2}$. Furthermore, it is noteworthy that all formulations of the breakup time (Eqs. (8.28), (8.31) and (8.32)) yield the same functional relationship composed of the diameter of the parent bubble and the dissipation rate of the fluid, but different proportionality constants.

It has to be noted that Coulaloglou and Tavlarides (1977) also define a breakup time based on the same functional dependency on the bubble diameter and the dissipation rate without specifying the proportionality constant. Based on this quantity Coulaloglou and Tavlarides (1977) and later other authors (e.g., Solsvik and Jakobsen, 2015) estimate a breakup frequency of the bubbles, i.e., a certain fraction of the bubbles always breaks up after this time period. It has to be clearly remarked that the case for the above defined breakup time used in the present thesis. Here, $\Delta t_{\mathrm{break}}$ defines a *minimum* period of time during which the daughter bubbles cannot break up after their formation. After this idle time is passed breakup is *possible* again but *not* mandatory. Hence, only if the local properties of the fluid and the bubbles at this new instant in time allow for the breakup condition to be fulfilled, breakup of the daughter bubbles occurs. Thus, the phenomenon of a breakup cascade, where daughter bubbles formed from one parent bubble repeatedly break up (Solsvik et al., 2016), can be captured.

In order to justify the preceding considerations and to select the most appropriate definition of the breakup time, Eqs. (8.28), (8.31) and (8.32) are compared with an experimental observation by Andersson and Andersson (2006a). The breakup time of a bubble with a diameter of $d_{\mathrm{b,p}} = 1\,\mathrm{mm}$ was measured to be $\Delta t_{\mathrm{break}} = 2.25\,\mathrm{ms}$, while the dissipation rate of the turbulent fluid flow was $\epsilon = 16\,\mathrm{m^2/s^3}$. Consequently, Eq. (8.28) by Andersson and Andersson (2006a) gives $\Delta t_{\mathrm{break,AA}} = 7.74\,\mathrm{ms}$ for $C_{\mathrm{AA}} = 1/2$ and $\Delta t_{\mathrm{break,AA}} = 10.3\,\mathrm{ms}$ for $C_{\mathrm{AA}} = 2/3$, respectively. Applying the relations based on the eddy turnover time yields breakup times of $\Delta t_{\mathrm{break,etk}} = 2.01\,\mathrm{ms}$ for Eq. (8.31) and $\Delta t_{\mathrm{break,etf}} = 1.42\,\mathrm{ms}$ for Eq. (8.32). It is obvious that the estimations of the breakup times based on the eddy turnover time ($\Delta t_{\mathrm{break,etk}}$ and $\Delta t_{\mathrm{break,etf}}$) provide the best agreements with the experiment. Furthermore, by comparing the results obtained by simulations of bubble breakup in a turbulent jet flow with the corresponding experimental data by Martínez-Bazán et al. (1999a), it can be shown that Eq. (8.32) yields the best agreement with the experiment (see Section 11.4.3). Thus, $\Delta t_{\mathrm{break,etf}}$ is applied in the present thesis. Lastly, the following procedure is used to prevent the immediate breakup of the daughter bubbles: The ratio of the breakup time to the time-step size of the simulation defines the number of time steps during which no further breakup can occur. This number is stored as a property of the bubble and transported through the flow field. After the corresponding number of time steps are performed, the daughter bubbles are again allowed to break up.

9 Numerical Methodology

The previous chapters covered the modeling of the bubble-laden flow, i.e., the determination of the continuous phase (Chapter 3), the Lagrangian tracking of the bubbles (Chapter 4) and the interaction between the two phases (Chapter 5). Additionally, it was explained in Chapters 6 to 8 how the modeling of the subgrid scales seen by the dispersed phase, the coalescence of the bubbles and their breakup is done in the present thesis. The numerical methodology applied to determine the solution of the corresponding governing equations of the fluid and the bubble has to be both efficient as well as robust. The objective of this chapter is to provide an overview over the numerical methods implemented in the in-house CFD code $\mathcal{LESOCC}$ (Breuer, 1998a,b, 2000, 2002) used at PfS. $\mathcal{LESOCC}$ is based on a three-dimensional finite-volume method using arbitrary curvilinear, block-structured and body-fitted grids with a collocated variable arrangement. The code is highly vectorized and parallelized by domain decomposition using MPI. The computational grids used in $\mathcal{LESOCC}$ are explained in Section 9.1. In Section 9.2 the prediction of the Eulerian phase based on the transformed governing equations of the fluid is described. Afterwards, the methods used for tracking the bubbles are presented in Section 9.3. Lastly, in Section 9.4 it is shown how the statistics of both phases are obtained.

9.1 Transformation to Curvilinear Coordinate Systems

As mentioned above, $\mathcal{LESOCC}$ utilizes curvilinear body-fitted block-structured grids allowing to predict (two-phase) fluid flows in complex flow geometries. Due to the decomposition of the computational domain into smaller blocks, the complexity of the representable geometry is increased. This grid arrangement offers a compromise between structured mono-block grids and unstructured grids. On the one hand, curvilinear block-structured grids can resolve more complex flow geometries than structured mono-block grids, which are restricted to relatively simple geometries. A prominent example of a grid arrangement posing a difficulty for structured mono-block grids are polar grids used for circular geometries. In the center of the circle the grid lines converge leading to a degeneration of the cells. On the other hand, the matrix of the algebraic equation system required to be solved still has a regular band structure in the case of (structured or) block-structured grids. Consequently, the solution methodology is more efficient than for unstructured grids, which do not have this beneficial property. The reason for this is that in block-structured grids each grid point of a curvilinear grid is uniquely identified by an index triple (i, j, k). Hence, the neighbors to an arbitrary grid point are readily given by changing the index by ± 1. The neighboring grid points are, for example, needed to predict the fluxes over

surfaces of the control volumes. In unstructured grids the connections to the neighbors have to be explicitly specified and stored. Consequently, the matrices of the algebraic system of equations are no longer structured leading to a much larger computational effort compared with block-structured grids. A detailed discussion of the advantages and drawbacks of such grids can be found in Ferziger and Perić (2002).

Due to the domain decomposition, an individual curvilinear coordinate system exists for each block. Consequently, the governing equations for the fluid and the bubbles have to be transformed from a representation in the physical or p-space (x, y, z) to a curvilinear coordinate system in the computational or c-space (ξ, η, ζ), see Fig. 9.1 illustrating this issue. The transformation requires to express the coordinates of the computational space depending on the coordinates in the physical space:

$$\xi = \xi(x, y, z), \tag{9.1a}$$
$$\eta = \eta(x, y, z), \tag{9.1b}$$
$$\zeta = \zeta(x, y, z). \tag{9.1c}$$

Note that in the entire transformation temporally non-varying coordinates are assumed. Based on Eq. (9.1), the changes along each direction (ξ, η, ζ) of the c-space can be determined according to:

$$\mathrm{d}\xi = \frac{\partial \xi}{\partial x}\,\mathrm{d}x + \frac{\partial \xi}{\partial y}\,\mathrm{d}y + \frac{\partial \xi}{\partial z}\,\mathrm{d}z, \tag{9.2a}$$
$$\mathrm{d}\eta = \frac{\partial \eta}{\partial x}\,\mathrm{d}x + \frac{\partial \eta}{\partial y}\,\mathrm{d}y + \frac{\partial \eta}{\partial z}\,\mathrm{d}z, \tag{9.2b}$$
$$\mathrm{d}\zeta = \frac{\partial \zeta}{\partial x}\,\mathrm{d}x + \frac{\partial \zeta}{\partial y}\,\mathrm{d}y + \frac{\partial \zeta}{\partial z}\,\mathrm{d}z. \tag{9.2c}$$

Equation (9.2) can be readily written in matrix form:

$$\begin{pmatrix} \mathrm{d}\xi \\ \mathrm{d}\eta \\ \mathrm{d}\zeta \end{pmatrix} = \underbrace{\begin{pmatrix} \xi_x & \xi_y & \xi_z \\ \eta_x & \eta_y & \eta_z \\ \zeta_x & \zeta_y & \zeta_z \end{pmatrix}}_{\mathbf{J}} \begin{pmatrix} \mathrm{d}x \\ \mathrm{d}y \\ \mathrm{d}z \end{pmatrix}, \tag{9.3}$$

where the abbreviation $\partial\xi/\partial x = \xi_x$ is used to denote a partial derivative. The matrix $\mathbf{J}$ is called a Jacobian matrix and its components $\xi_x, \xi_y, \ldots \zeta_z$ are the metric terms. Similar to Eq. (9.3), a back-transformation from the computational space to the physical space based on the inverse $\mathbf{J}^{-1}$ of the Jacobian is possible. Further important quantities required for the coordinate transformation to the c-space are the determinants of the Jacobian matrix $\mathbf{J}$ and its inverse $\mathbf{J}^{-1}$, i.e., $\mathrm{J} = |\mathbf{J}|$ and $\mathrm{J}^{-1} = |\mathbf{J}^{-1}|$. According to Ferziger and Perić (2002) the volumes $\Delta\mathrm{V}$ and $\Delta\mathrm{V_c}$ of the cells in the physical and the computational space are related to the determinants of the Jacobian and its inverse by the relations:

$$\Delta\mathrm{V} = \mathrm{J}^{-1}\,\Delta\xi\,\Delta\eta\,\Delta\zeta \qquad \text{and} \qquad \Delta\mathrm{V_c} = \Delta\xi\,\Delta\eta\,\Delta\zeta = \mathrm{J}\,\Delta x\,\Delta y\,\Delta z\,. \tag{9.4}$$

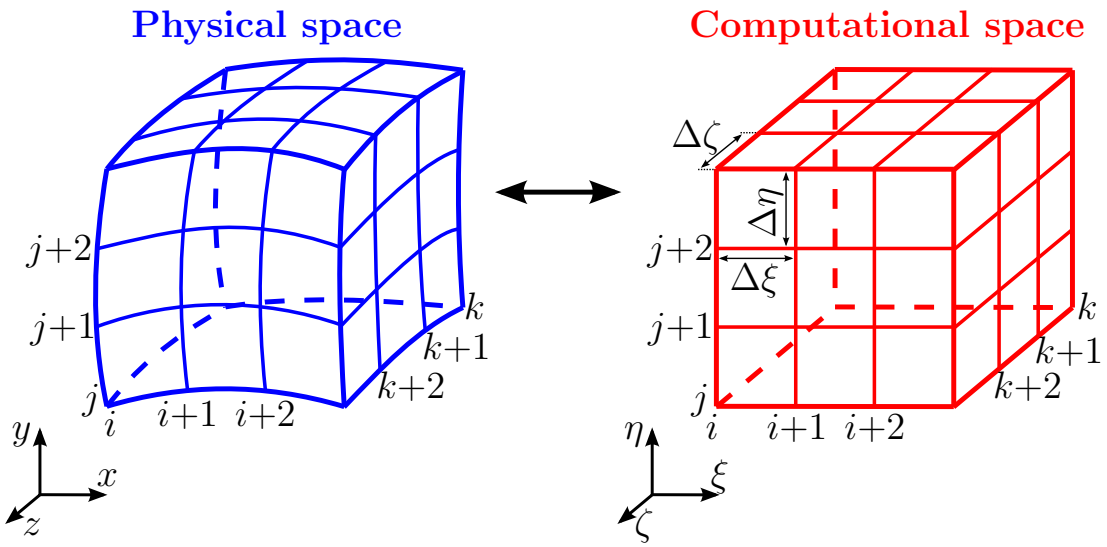

Fig. 9.1. Schematic sketch of the transformation of the coordinate system from the physical space to the computational space.

Since it is assumed that $\Delta\xi = \Delta\eta = \Delta\zeta = 1$, the volume of the cell in the computational space is equal to unity as well, i.e., $\Delta \mathrm{V_c} = 1$. Hence, it follows from Eq. (9.4) that the determinant of the Jacobian is $\mathrm{J} = 1/\Delta V$, while $\mathrm{J}^{-1} = \Delta V$.

Based on these considerations, the important differential operators appearing in the governing equations of the fluid and the dispersed phase (gradient of a scalar, divergence of a vector and the Laplace operator) can be transformed to a representation in the computational space. By applying the chain rule, one can readily show that the gradient of a scalar variable ϕ is given by:

$$\frac{\partial \phi}{\partial x_j} = \frac{\partial \phi}{\partial \xi}\frac{\partial \xi}{\partial x_j} + \frac{\partial \phi}{\partial \eta}\frac{\partial \eta}{\partial x_j} + \frac{\partial \phi}{\partial \zeta}\frac{\partial \zeta}{\partial x_j} = \left(\frac{\partial \phi}{\partial \xi_i}\right)\beta_{ij}\,\mathrm{J}, \tag{9.5}$$

where the notation $\xi_i = (\xi, \eta, \zeta)$ is used for the coordinates in the computational space. Additionally, in Eq. (9.5) the coefficient $\beta_{ij} = \mathrm{J}^{-1}\,(\partial \xi_i / \partial x_j)$ is defined. In a similar manner the divergence of a vector can be formulated in the computational space. Here, the filtered fluid velocity $\overline{u}_i$ is exemplary chosen:

$$\frac{\partial \overline{u}_i}{\partial x_i} = \frac{\partial (\overline{u}_k\,\beta_{ik})}{\partial \xi_i}\,\mathrm{J} = \frac{\partial (\overline{U}_i\,\mathrm{J}^{-1})}{\partial \xi_i}\,\mathrm{J}. \tag{9.6}$$

In the second step of Eq. (9.6) the contravariant velocities $\overline{U}_i = (\overline{U}, \overline{V}, \overline{W}) = \mathrm{J}\,(\overline{u}_k\,\beta_{ik})$ are defined. Lastly, the Laplace operator of a scalar quantity is given by:

$$\frac{\partial}{\partial x_i}\left(\frac{\partial \phi}{\partial x_i}\right) = \frac{\partial}{\partial \xi_j}\left(\frac{\partial \phi}{\partial \xi_k}\,\mathrm{J}\,B_{kj}\right)\mathrm{J}, \tag{9.7}$$

where the matrix $B_{kj} = \beta_{ki}\,\beta_{ji}$ is defined to abbreviate the resulting expression.

9.2 Numerical Methods for the Continuous Phase

With the coordinate transformation from the physical to the computational space described in the previous section, the methodology used in the present thesis to predict the continuous phase can be explained. Firstly, the governing equations (3.8) and (3.9) have to be written in a form corresponding to the computational space, i.e., the definitions (9.5) to (9.7) have to be applied. Consequently, the dimensionless conservation equations of mass and momentum for an incompressible fluid ($\rho_\mathrm{f} = 1$) read:

$$\frac{\partial\left(\overline{U}_j\,\mathrm{J}^{-1}\right)}{\partial\xi_j} = 0, \tag{9.8}$$

$$\mathrm{J}^{-1}\,\frac{\partial\overline{u}_i}{\partial t} + \frac{\partial(\overline{u}_i\,\overline{U}_j\,\mathrm{J}^{-1})}{\partial\xi_j} = -\frac{\partial\overline{p}}{\partial\xi_j}\,\beta_{ji} + \frac{\partial}{\partial\xi_j}\left[\left(\mu_\mathrm{T} + \frac{1}{\mathrm{Re}}\right)\left(\frac{\partial\overline{u}_i}{\partial\xi_m}\,\mathrm{J}\,B_{mj}\right)\right] + \mathrm{J}^{-1}\,\overline{f}_i. \tag{9.9}$$

Note that in the second term on the r.h.s. of Eq. (9.9) the terms for the molecular momentum transfer ($\overline{\tau}_{ij}^{\mathrm{mol}}$) and the momentum transfer due to the subgrid scales (τ_{ij}^{SGS}) appearing in Eq. (3.9) have been combined. This is possible since in the present thesis the subgrid-scale stress tensor τ_{ij}^{SGS} is modeled by one of the eddy-viscosity models described in Section 3.2.

In $\mathcal{LESOCC}$ the transformed conservation equations (9.8) and (9.9) are solved by a finite-volume method (Ferziger and Perić, 2002) based on cell-centered grids with a collocated variable arrangement. Consequently, all fluid properties ($\overline{u}$, $\overline{v}$, $\overline{w}$, $\overline{p}$) are stored at the center P of the control volume. Figure 9.2 visualizes the computational cell for a three-dimensional Cartesian grid together with the notation used in the present thesis.

9.2.1 Finite-Volume Method

In the following, the finite-volume method and the corresponding discretization are briefly explained exemplary using a general conservation equation of an arbitrary transport quantity ϕ in a curvilinear coordinate system:

$$\mathrm{J}^{-1}\left(\frac{\partial\phi}{\partial t}\right) + \frac{\partial\left(\phi\,U_j\,\mathrm{J}^{-1}\right)}{\partial\xi_j} = \frac{\partial}{\partial\xi_j}\left(\Gamma_\phi\frac{\partial\phi}{\partial\xi_m}\,\mathrm{J}\,B_{mj}\right) + S_\phi\,\mathrm{J}^{-1}, \tag{9.10}$$

where Γ_ϕ denotes the diffusion coefficient and S_ϕ is a source term for the quantity ϕ. Note that the following considerations can be readily applied to the Navier–Stokes equations (9.8) and (9.9). In this case the transport quantity ϕ represents the components of the

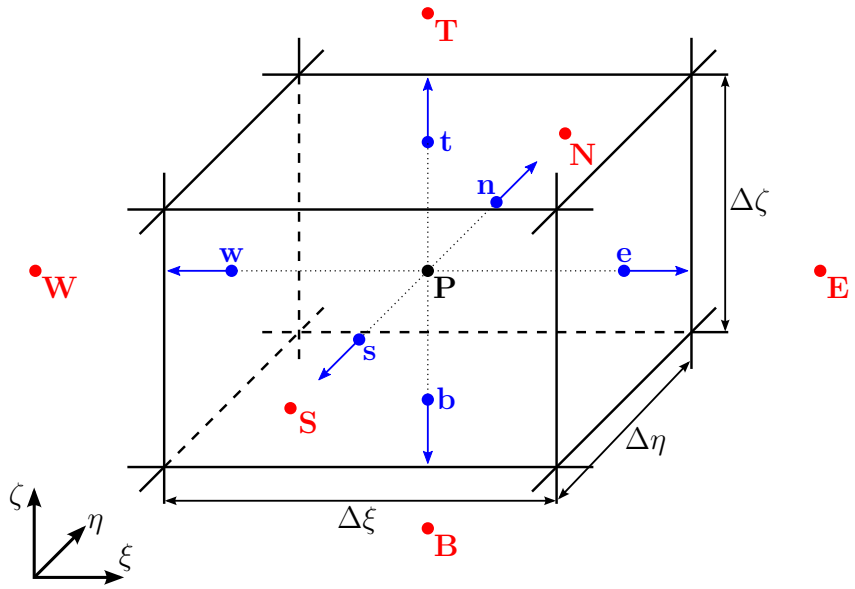

Fig. 9.2. Computational cell for a three-dimensional orthogonal grid with a collocated variable arrangement and the notation used in the present thesis.

(filtered) velocity field. Integrating expression (9.10) over the control volume ΔV_c in the c-space and applying Gauss's theorem yields after some re-arrangements:

$$\underbrace{\int\limits_{\Delta V_\mathrm{c}} \mathrm{J}^{-1}\left(\frac{\partial \phi}{\partial t}\right) \mathrm{d}V_\mathrm{c}}_{\text{local change}} + \underbrace{\int\limits_{\Delta S_\mathrm{c}} \left(\phi\, U_j\, \mathrm{J}^{-1}\right) \cdot n_j \,\mathrm{d}S_\mathrm{c}}_{\text{convective fluxes}} = \underbrace{\int\limits_{\Delta S_\mathrm{c}} \left(\Gamma_\phi \frac{\partial \phi}{\partial \xi_m}\, \mathrm{J}\, B_{mj}\right) \cdot n_j \,\mathrm{d}S_\mathrm{c}}_{\text{diffusive fluxes}} + \underbrace{\int\limits_{\Delta V_\mathrm{c}} S_\phi\, \mathrm{J}^{-1}\, \mathrm{d}V_\mathrm{c}}_{\text{sources}}, \quad (9.11)$$

where ΔS_c denotes the surface of the control volume in the c-space and n_j is the corresponding surface normal unit vector. In order to solve Eq. (9.11) the volume and the surface integrals appearing in the transport equation have to be discretized. Note that in Eqs. (9.10) and (9.11) the density ρ_f is assumed to be constant (incompressible fluid) and, thus, could be eliminated from the dimensionless conservation equations.

The volume integrals can be discretized by the second-order accurate midpoint rule (Ferziger and Perić, 2002). Here, the source term of Eq. (9.11) is exemplary chosen. Other volume integrals (the local change of ϕ for example) can be described in an equivalent manner. The integral over the control volume is replaced by the average $\langle S_\phi \rangle_{\Delta V_\mathrm{c}}$ of the source term S_ϕ over the control volume multiplied with the volume ΔV_c. Subsequently, the unknown average is estimated by the value $S_{\phi,\mathrm{P}}$ of the source term at the location

of the center of the control volume (denoted by the point P in Fig. 9.2). Hence, the discretized volume integral reads:

$$\int_{\Delta V_\mathrm{c}} S_\phi \, \mathrm{J}^{-1} \, \mathrm{d}V_\mathrm{c} = \langle S_\phi \rangle_{\Delta V_\mathrm{c}} \, \mathrm{J}^{-1} \, \Delta V_\mathrm{c} \approx \mathrm{J}^{-1} \, S_{\phi,\mathrm{P}}. \tag{9.12}$$

In the last step of Eq. (9.12) $\Delta V_\mathrm{c} = 1$ is utilized, which is possible since $\Delta\xi = \Delta\eta = \Delta\zeta = 1$. In a collocated variable arrangement all fluid properties are stored at the cell center position P. Thus, no interpolation of the respective quantities is required for the integration.

Next, the surface integrals of Eq. (9.11) describing the convective and diffusive fluxes of the transport quantity through the surface of the control volume have to be evaluated. Since the control volume is given by a hexahedron depicted in Fig. 9.2, in both cases the net flux is given by the sum of fluxes over the six faces of the control volume:

$$\int_{\Delta \mathrm{S_c}} f_j \cdot n_j \, \mathrm{d}S_\mathrm{c} = \sum_k \int_{\Delta S_{\mathrm{c},k}} \left(f_j \cdot n_j\right)_k \mathrm{d}S_\mathrm{c} = \sum_k F_k \qquad \text{with } k = \{\mathrm{e}, \mathrm{w}, \mathrm{n}, \mathrm{s}, \mathrm{t}, \mathrm{b}\}, \tag{9.13}$$

where $n_{j,k}$ is the surface normal vector of the cell face with index k and f_j represents either the convective ($f_j = \phi \, U_j \, \mathrm{J}^{-1}$) or the diffusive ($f_j = \Gamma_\phi \left(\partial\phi/\partial\xi_m\right) \mathrm{J} \, B_{mj}$) flux vectors of the transport equation (9.11). Similar to the discretization of the volume integral described above, the surface integral over one of the faces of the control volume can be expressed by the average $\langle f_k \rangle_{\Delta S_{\mathrm{c},k}}$ of the flux vector over the corresponding surface multiplied by its area $\Delta S_{\mathrm{c},k}$. Since the average is again unknown, it has to be approximated. In the present thesis the second-order accurate midpoint rule (Ferziger and Perić, 2002) is used resulting in the expression:

$$F_k = \int_{\Delta S_{\mathrm{c},k}} \left(f_j \cdot n_j\right)_k \mathrm{d}S_\mathrm{c} = \langle f_k \rangle_{\Delta S_{\mathrm{c},k}} \Delta S_{\mathrm{c},k} \approx f_k, \tag{9.14}$$

for the flux through the surface with index 'k'. Note that again $\Delta S_{\mathrm{c},k} = 1$, since in the present thesis $\Delta\xi = \Delta\eta = \Delta\zeta = 1$.

Applying this approximation to both surface integrals of the transport equation (9.11) allows to discretize the convective and diffusive fluxes. For the sake of simplicity, only the fluxes through the eastern surface of the control volume denoted by the index 'e' in Fig. 9.2 are considered. The remaining sides can be analogously described. For the discretization of the convective fluxes one has to account for the fact that in case of the momentum conservation equation (9.9) ϕ represents one of the three filtered velocity components ($\overline{u}_i$) causing the convective flux $F_\mathrm{e}^\mathrm{conv}$ to be a non-linear function of the velocity. Consequently, the convective flux has to be linearized before it can be discretized. This is achieved by assuming that the term $\left(\overline{U}_j \, n_j \, \Delta S_{\mathrm{c,e}} \, \mathrm{J}^{-1}\right)_\mathrm{e}$ is known. From a physical point of view this term is connected to the mass flow. In an explicit time marching approach as applied in the present thesis for the momentum equation (see Section 9.2.2), it can be approximated

by using the values of the subsequent time step. Consequently, after this linearization the convective flux of the momentum conservation equation (9.9) can be approximated by:

$$F_{\mathrm{e}}^{\mathrm{conv}} = \int_{\Delta S_{\mathrm{c,e}}} \left(\mathrm{J}^{-1}\, \overline{u}_i\, \overline{U}_j \cdot n_j \right)_{\mathrm{e}} \mathrm{d}S_{\mathrm{c}} \approx \overline{u}_{i,\mathrm{e}}\, \overline{U}_{\mathrm{e}}\, \mathrm{J}^{-1}. \tag{9.15}$$

Since in $\mathcal{LESOCC}$ a collocated variable arrangement is used, all variables are stored at the cell centers. Consequently, an interpolation of $\overline{u}_i$ to the faces of the control volume is required. In the present thesis, a first-order accurate linear interpolation is used for this task, which, however, applied in the context of the mid-point rule leads to an overall second-order accuracy. Thus, the linearly interpolated velocity $\overline{u}_{i,\mathrm{e}}$ is estimated based on the values $\overline{u}_{i,\mathrm{P}}$ and $\overline{u}_{i,\mathrm{E}}$ of the filtered fluid velocity stored at the centers of the control volume P and its eastern neighbor E; see Fig. 9.3 for an illustration of the variable arrangement, which is chosen to be two-dimensional for the sake of simplicity. The linear interpolation yields:

$$\overline{u}_{i,\mathrm{e}} = g_e\, \overline{u}_{i,\mathrm{E}} + (1 - g_{\mathrm{e}})\, \overline{u}_{i,\mathrm{P}}, \tag{9.16}$$

where the interpolation factor g_{e} to the eastern cell surface is defined according to:

$$g_{\mathrm{e}} = \frac{|\boldsymbol{x}_{\mathrm{e}} - \boldsymbol{x}_{\mathrm{P}}|}{|\boldsymbol{x}_{\mathrm{E}} - \boldsymbol{x}_{\mathrm{P}}|} = \frac{l_{\mathrm{Pe}}}{l_{\mathrm{PE}}}\,. \tag{9.17}$$

The interpolation factor is given by the ratio of the distance l_{Pe} between the cell center P and the eastern cell face and the distance l_{PE} between the neighboring cell centers P and E. Note that both distances are determined based on the positions $\boldsymbol{x}_{\mathrm{P}}$, $\boldsymbol{x}_{\mathrm{E}}$ and $\boldsymbol{x}_{\mathrm{e}}$ in the physical space.

Coming back to the discretization of the convective flux in case of the mass conservation, $\phi = 1$ and, thus, $f_j = \overline{U}_j\, \mathrm{J}^{-1}$. For this mass flow through the cell face it is important to note that using the linear interpolation scheme defined by Eq. (9.16) for the estimation of $\overline{U}_{\mathrm{e}}$ at the eastern surface of the control volume can lead to unphysical oscillations in the flow and pressure fields. In order to prevent these oscillations caused by a pressure-velocity decoupling, the momentum interpolation technique by Rhie and Chow (1983) is applied in the $\mathcal{LESOCC}$; see Section 9.2.3 for more details on the method.

Lastly, the diffusive fluxes $F_{\mathrm{e}}^{\mathrm{diff}}$ appearing in Eq. (9.9) have to be discretized. According to the midpoint rule defined in Eq. (9.14), the diffusive fluxes can be approximated by:

$$F_{\mathrm{e}}^{\mathrm{diff}} = \int_{\Delta S_{\mathrm{c,e}}} \Gamma_{\mathrm{e}} \left[\frac{\partial \overline{u}_i}{\partial \xi_m}\, \mathrm{J}\, B_{mj}\, n_j \right]_{\mathrm{e}} \mathrm{d}S_{\mathrm{c}} \approx \Gamma_{\mathrm{e}} \left[\frac{\partial \overline{u}_i}{\partial \xi_m}\, \mathrm{J}\, B_{mj}\, n_j \right]_{\mathrm{e}}. \tag{9.18}$$

The value of the gradient $(\partial \overline{u}/\partial \xi_m)_{\mathrm{e}}$ at the eastern surface of the control volume again has to be approximated. Using a central finite-difference scheme, the estimated gradient reads:

$$\left(\frac{\partial \overline{u}_i}{\partial \xi_m} \right)_{\mathrm{e}} = \frac{\overline{u}_{i,\mathrm{E}} - \overline{u}_{i,\mathrm{P}}}{\xi_{m,\mathrm{E}} - \xi_{m,\mathrm{P}}}. \tag{9.19}$$

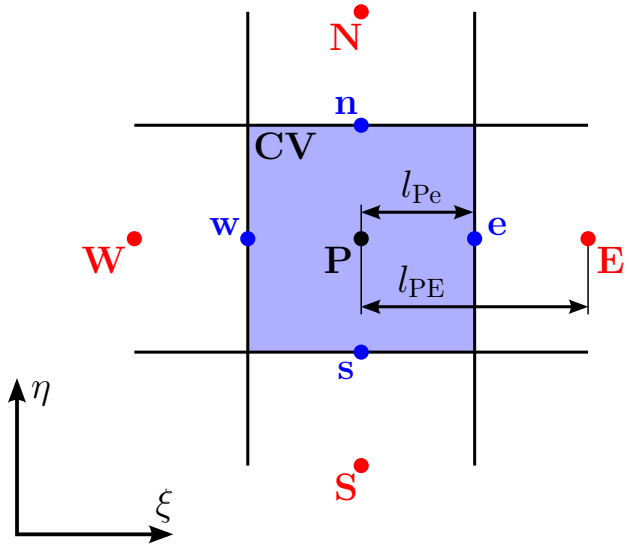

Fig. 9.3. Example for the illustration of the linear interpolation for a two-dimensional grid with a cell-centered variable arrangement.

Note that in Eq. (9.18) the diffusion coefficient $\Gamma_{\mathrm{e}} = (\mu_{\mathrm{T}} + 1/\mathrm{Re})$ is linearly interpolated to the eastern cell face by Eq. (9.16). The discretization of the diffusive fluxes is also second-order accurate.

9.2.2 Temporal Discretization

Applying the finite-volume method described in Section 9.2.1 to the conservation equation (9.9) of the fluid momentum yields a non-linear differential equation of the following form:

$$\frac{\partial \overline{u}_{i,\mathrm{P}}}{\partial t} = \frac{1}{\mathrm{J}^{-1}} \left[\mathcal{R}(\overline{u}_i) - \mathcal{F}\left(\frac{\partial \overline{p}}{\partial \xi_i} \right) \right] \tag{9.20}$$

for the filtered fluid velocity at the center of the computational cells. In Eq. (9.20) $\mathcal{R}(\overline{u}_i)$ is a non-linear function of the fluid velocities at the cell center position P and its six neighbors, while $\mathcal{F}(\partial\overline{p}/\partial\xi_i)$ depends on the pressure gradient. Integrating Eq. (9.20) in time between $t^{(n)}$ and $t^{(n+1)}$ representing the old and the new instant in time, respectively, and applying a simple explicit Euler scheme for this purpose, results in the following temporal discretization:

$$\overline{u}_{i,\mathrm{P}}^{(n+1)} = \overline{u}_{i,\mathrm{P}}^{(n)} + \frac{\Delta t}{\mathrm{J}^{-1}} \left[\mathcal{R}\left(\overline{u}_i^{(n)} \right) - \mathcal{F}^{(n)} \left(\frac{\partial \overline{p}}{\partial \xi_i} \right) \right]. \tag{9.21}$$

Here, the superscript (n) denotes the values at the previous time step and Δt is the time-step size.

In the present thesis the temporal integration is performed by a low-storage three-step Runge–Kutta method, which is second-order accurate in time (Binninger, 1989). Accordingly, the three sub-steps of the integration are:

$$\bar{u}_{i,\mathrm{P}}^{(1)} = \bar{u}_{i,\mathrm{P}}^{(n)} + \alpha_1 \frac{\Delta t}{\mathrm{J}^{-1}} \left[\mathcal{R}\left(\bar{u}_i^{(n)}\right) - \mathcal{F}^{(n)}\left(\frac{\partial \bar{p}}{\partial \xi_i}\right) \right] \qquad \text{with } \alpha_1 = \frac{1}{3}, \tag{9.22a}$$

$$\bar{u}_{i,\mathrm{P}}^{(2)} = \bar{u}_{i,\mathrm{P}}^{(n)} + \alpha_2 \frac{\Delta t}{\mathrm{J}^{-1}} \left[\mathcal{R}\left(\bar{u}_i^{(1)}\right) - \mathcal{F}^{(n)}\left(\frac{\partial \bar{p}}{\partial \xi_i}\right) \right] \qquad \text{with } \alpha_2 = \frac{1}{2}, \tag{9.22b}$$

$$\bar{u}_{i,\mathrm{P}}^{(3)} = \bar{u}_{i,\mathrm{P}}^{(n)} + \alpha_3 \frac{\Delta t}{\mathrm{J}^{-1}} \left[\mathcal{R}\left(\bar{u}_i^{(2)}\right) - \mathcal{F}^{(n)}\left(\frac{\partial \bar{p}}{\partial \xi_i}\right) \right] \qquad \text{with } \alpha_3 = 1, \tag{9.22c}$$

$$\bar{u}_{i,\mathrm{P}}^{(*)} = \bar{u}_{i,\mathrm{P}}^{(3)}. \tag{9.22d}$$

It has to be noted that the velocity field resulting from Eq. (9.22) is not divergence-free. Consequently, the above described Runge–Kutta method is applied within a predictor-corrector scheme, where the intermediate velocity $\bar{u}_{i,\mathrm{P}}^{(*)}$ given by Eq. (9.22d) is the result of the predictor step. This also explains why the operator $\mathcal{F}$ is evaluated at the previous time step and the intermediate velocity has to be updated in the corrector step.

9.2.3 Predictor-Corrector Scheme

Since the velocity field $\bar{u}_{i,\mathrm{P}}^{(*)}$ resulting from Eq. (9.22) in the predictor step is not divergence-free, a corrector step is required in which the pressure field is adjusted such that the continuity equation is fulfilled. For the sake of simplicity, in the following the corrector scheme is described in the physical space. Afterwards, the final expression used to determine the velocity correction is transformed to the computational space by using the considerations of Section 9.1.

The starting point for the method used in the corrector step is the momentum equation (Breuer, 2013; Ferziger and Perić, 2002). The conservation of momentum at the location P can be written in semi-discrete form according to:

$$\frac{\bar{u}_{i,\mathrm{P}}^{(*)} - \bar{u}_{i,\mathrm{P}}^{(n)}}{\Delta t} = -\left[\frac{\partial\left(\bar{u}_i\,\bar{u}_j\right)}{\partial x_j}\right]_{\mathrm{P}}^{(n)} - \left[\frac{1}{\mathrm{Re}}\frac{\partial \bar{\tau}_{ij}^{\mathrm{mol}}}{\partial x_j} + \frac{\partial \tau_{ij}^{\mathrm{SGS}}}{\partial x_j}\right]_{\mathrm{P}}^{(n)} - \frac{\partial \bar{p}_{\mathrm{P}}^{(*)}}{\partial x_i}. \tag{9.23}$$

Since the intermediate pressure $\bar{p}_{\mathrm{P}}^{(*)}$ is unknown and has to be approximated, in $\mathcal{LESOCC}$ the pressure field $\bar{p}_{\mathrm{P}}^{(n)}$ of the preceding time step is used. Note that the viscous stress tensor $\bar{\tau}_{ij}^{\mathrm{mol}}$ and the subgrid-scale stress tensor τ_{ij}^{SGS} vary in space and time. In order to obtain a correction term for the velocity, it is assumed that the pressure $\bar{p}_{\mathrm{P}}^{(n+1)}$ at the next time step is known allowing to write the semi-discrete momentum conservation equation in its correct form as follows:

$$\frac{\bar{u}_{i,\mathrm{P}}^{(n+1)} - \bar{u}_{i,\mathrm{P}}^{(n)}}{\Delta t} = -\left[\frac{\partial\left(\bar{u}_i\,\bar{u}_j\right)}{\partial x_j}\right]_{\mathrm{P}}^{(n)} - \left[\frac{1}{\mathrm{Re}}\frac{\partial \bar{\tau}_{ij}^{\mathrm{mol}}}{\partial x_j} + \frac{\partial \tau_{ij}^{\mathrm{SGS}}}{\partial x_j}\right]_{\mathrm{P}}^{(n)} - \frac{\partial \bar{p}_{\mathrm{P}}^{(n+1)}}{\partial x_i}. \tag{9.24}$$

Here, $\overline{u}_{i,\mathrm{P}}^{(n+1)}$ is the divergence-free velocity at the next time step. Subtracting Eq. (9.23) from Eq. (9.24) yields the expression:

$$\frac{\overline{u}_{i,\mathrm{P}}^{(n+1)} - \overline{u}_{i,\mathrm{P}}^{(*)}}{\Delta t} = -\left(\frac{\partial \overline{p}_{\mathrm{P}}^{(n+1)}}{\partial x_i} - \frac{\partial \overline{p}_{\mathrm{P}}^{(*)}}{\partial x_i} \right). \tag{9.25}$$

Since $\overline{u}_{i,\mathrm{P}}^{(n+1)}$ is supposed to be divergence-free, applying the divergence operator to Eq. (9.25) yields the Poisson equation:

$$\frac{\partial}{\partial x_i} \left(\frac{\partial \overline{p}'_{\mathrm{P}}}{\partial x_i} \right) = \frac{1}{\Delta t} \left(\frac{\partial \overline{u}_{i,\mathrm{P}}^{(*)}}{\partial x_i} \right) \tag{9.26}$$

for the pressure correction $\overline{p}'_{\mathrm{P}} = \overline{p}_{\mathrm{P}}^{(n+1)} - \overline{p}_{\mathrm{P}}^{(*)}$. After a transformation to the computational space based on Eqs. (9.6) and (9.7), Eq. (9.26) reads:

$$\frac{\partial}{\partial \xi_j} \left(\frac{\partial \overline{p}'}{\partial \xi_k} \, \mathrm{J} \, B_{kj} \right)_{\mathrm{P}} = \frac{1}{\Delta t} \left(\frac{\partial \overline{U}_i^{(*)}}{\partial \xi_i} \, \mathrm{J}^{-1} \right)_{\mathrm{P}}. \tag{9.27}$$

Based on Eq. (9.27) the pressure correction $\overline{p}'_{\mathrm{P}}$ can be determined resulting in a divergence-free velocity field. In $\mathcal{LESOCC}$ the Poisson equation (9.27) is numerically solved by the incomplete LU decomposition method proposed by Stone (1968), which is an iterative solver for linear equation systems with sparsely populated matrices (see Ferziger and Perić, 2002; Stone, 1968, for details).

The whole predictor-corrector procedure is summarized as follows: In the predictor step the not divergence-free velocity $\overline{u}_{i,\mathrm{P}}^{(*)}$ is determined by Eq. (9.22). Afterwards, Eq. (9.27) is solved in the corrector step resulting in the pressure correction $\overline{p}'_{\mathrm{P}}$. Then, an improved estimation of the fluid field $\overline{u}_{i,\mathrm{P}}^{(n+1)}$ is obtained from the corrected pressure $\overline{p}_{\mathrm{P}}^{(n+1)} = \overline{p}_{\mathrm{P}}^{(*)} + \overline{p}'_{\mathrm{P}}$ based on Eq. (9.25). For a general curvilinear non-staggered grid $\overline{u}_{i,\mathrm{P}}^{(n+1)}$ is not divergence-free after the correction step. The reason are several numerical approximations used for the discretization procedure. Thus, the correction step has to be repeated several times. For this purpose, the improved velocity field and the corrected pressure field are inserted into Eq. (9.27) again to obtain further pressure corrections $\overline{p}'$ and, thus, also a new estimate of the velocity $\overline{u}_{i,\mathrm{P}}^{(n+1)}$ at the new time step. The whole procedure is repeated until the velocity $\overline{u}_{i,\mathrm{P}}^{(n+1)}$ fulfills a pre-defined criterion (typically of the order of $\mathcal{O}(10^{-8})$) regarding the divergence of the velocity field.

Lastly, it has to be noted that in the context of the finite-volume method the estimation of the divergence of the velocity field is based on the evaluation of the mass balance through the surfaces of the control volumes. As previously mentioned in Section 9.2.1, unphysical oscillations caused by a pressure-velocity decoupling can arise on non-staggered grids, if the mass fluxes are interpolated to the cell faces by the linear interpolation scheme defined in Eq. (9.16). In order to prevent these oscillations of the solution, the momentum interpolation technique by Rhie and Chow (1983) is applied in $\mathcal{LESOCC}$ for the mass

fluxes. According to Rhie and Chow (1983) the corrected velocity (in p-space) at the eastern cell face of a control volume in the context of an explicit time-marching scheme reads (Ferziger and Perić, 2002):

$$\bar{u}_{i,\mathrm{e}}^{\mathrm{cor}} = \bar{u}_{i,\mathrm{e}} + \left[\bar{p}_{\mathrm{P}} - \bar{p}_{\mathrm{E}} - \frac{1}{2}\left(\bar{p}_{\mathrm{w}} - \bar{p}_{\mathrm{ee}}\right)\right] \frac{\Delta t}{\Delta x_i}, \tag{9.28}$$

where $\bar{u}_{i,\mathrm{e}}$ is the velocity linearly interpolated to the eastern cell face by Eq. (9.16). Likewise, in the correction term (second term on the r.h.s. of Eq. (9.28)) $\bar{p}_{\mathrm{w}}$ is the pressure linearly interpolated to the western cell face of the control volume, while $\bar{p}_{\mathrm{ee}}$ is the interpolated pressure of the eastern cell face of the control volume E located east of the considered control volume. In the case that pressure oscillations are present in the flow field, the correction term of Eq. (9.28) is non-vanishing, since the pressure appears in the formulation of the mass flux. Consequently, the pressure terms induce a mass flow, which leads to improved, less oscillating pressure and velocity fields in the subsequent iterations of the solver. In summary, the method by Rhie and Chow (1983) achieves a sufficient coupling between the pressure and the velocity fields similar to the application of staggered grids.

9.3 Numerical Methods for the Dispersed Phase

After the fluid field has been described in the previous section, the numerical methodology used to individually track the bubbles through the flow is described next. Since at several instances the tracking procedure requires fluid properties at the position of the bubble center, the available interpolation schemes are presented in Section 9.3.1. Afterwards, in Section 9.3.2 the bubble tracking algorithm is explained. Lastly, in order to account for four-way coupling, an efficient collision detection scheme is necessary. In Section 9.3.3 the detection method presently applied in $\mathcal{LESOCC}$ is introduced.

9.3.1 Interpolation of Fluid Quantities to the Bubble Position

As mentioned before, the tracking of the bubbles relies on the knowledge of fluid properties at the position of the bubble. Most prominently, the (filtered) fluid velocity is required for the solution of the governing equation (4.33) of the bubbles. Another example is the dissipation rate ϵ used to estimate the dimensionless Weber number of the bubbles in the context of breakup (see Section 8.1). Two interpolation schemes are utilized in $\mathcal{LESOCC}$.

9.3.1.1 Trilinear Interpolation

The first available scheme used to interpolate an arbitrary fluid quantity ϕ_{f} to the bubble position is the trilinear interpolation (see, e.g., Breuer et al., 2006a). This method relies on the values of ϕ_{f} stored at the eight cell centers surrounding the bubble weighted by the distances to the respective nodes.

$$\phi_{\mathrm{f}}|_{\mathrm{bubble}} = \Delta\xi^{-}\,\Delta\eta^{-}\,\Delta\zeta^{-} \cdot \phi_{\mathrm{f}}|_{(i,j,k)} \qquad + \Delta\xi^{+}\,\Delta\eta^{-}\,\Delta\zeta^{-} \cdot \phi_{\mathrm{f}}|_{(i+1,j,k)} \qquad +$$

$$\begin{aligned}
&\Delta\xi^- \Delta\eta^+ \Delta\zeta^- \cdot \phi_\mathrm{f}|_{(i,j+1,k)} \quad + \Delta\xi^- \Delta\eta^- \Delta\zeta^+ \cdot \phi_\mathrm{f}|_{(i,j,k+1)} \quad + \\
&\Delta\xi^+ \Delta\eta^+ \Delta\zeta^- \cdot \phi_\mathrm{f}|_{(i+1,j+1,k)} + \Delta\xi^+ \Delta\eta^- \Delta\zeta^+ \cdot \phi_\mathrm{f}|_{(i+1,j,k+1)} \quad + \\
&\Delta\xi^- \Delta\eta^+ \Delta\zeta^+ \cdot \phi_\mathrm{f}|_{(i,j+1,k+1)} + \Delta\xi^+ \Delta\eta^+ \Delta\zeta^+ \cdot \phi_\mathrm{f}|_{(i+1,j+1,k+1)}
\end{aligned} \tag{9.29}$$

In Eq. (9.29) the weighting factors $\Delta\xi^+$, $\Delta\eta^+$ and $\Delta\zeta^+$ denote the distances in the computational space of the bubble to the node defined by the index triple (i, j, k). The remaining distances are defined by $\Delta\xi^- = 1 - \Delta\xi^+$, $\Delta\eta^- = 1 - \Delta\eta^+$ and $\Delta\zeta^- = 1 - \Delta\zeta^+$. The trilinear interpolation defined by Eq. (9.29) represents a weighted average of the values of ϕ_f at the neighboring cell centers. Note that applying Eq. (9.29) for the estimation of the fluid velocity at the position of tiny particles leads to a pronounced filtering effect on the fluid velocity making it impossible to accurately reproduce second-order statistics (Alletto, 2014; Marchioli et al., 2007). Therefore, in the present thesis the trilinear interpolation scheme is not used for this task, but only for less critical quantities like the dissipation rate ϵ. The estimation of the fluid velocity at the bubble position is performed by the second interpolation scheme described in the following section.

9.3.1.2 Taylor Series Expansion

The second interpolation scheme included in $\mathcal{LESOCC}$ was proposed by Marchioli et al. (2007) and is based on a Taylor series expansion at the cell center closest to the bubble position. Since this interpolation scheme is solely used for the fluid velocity $\boldsymbol{u}_\mathrm{f}|_\mathrm{bubble}$ in order to prevent the unphysical filtering effect found by Alletto (2014) and Marchioli et al. (2007), the method is only specified for the velocity and not for a general fluid quantity. Hence, in the physical space with Cartesian coordinates the fluid velocity at the bubble position reads:

$$\begin{aligned}
\boldsymbol{u}_\mathrm{f}|_\mathrm{bubble} = \boldsymbol{u}_\mathrm{f}|_\mathrm{N} + \left.\frac{\partial \boldsymbol{u}_\mathrm{f}}{\partial x}\right|_\mathrm{N} \Delta x + \left.\frac{\partial \boldsymbol{u}_\mathrm{f}}{\partial y}\right|_\mathrm{N} \Delta y + \left.\frac{\partial \boldsymbol{u}_\mathrm{f}}{\partial z}\right|_\mathrm{N} \Delta z + \\
\mathcal{O}\left(\Delta x^2, \Delta y^2, \Delta z^2, \Delta x\,\Delta y, \Delta x\,\Delta z, \Delta y\,\Delta z\right),
\end{aligned} \tag{9.30}$$

where the index N denotes the nearest cell center with respect to the position of the bubble found at the position (i, j, k) in the computational space. Note that Marchioli et al. (2007) suggested to truncate the Taylor series expansion after the linear terms, i.e., only the first derivatives appear in Eq. (9.30). Consequently, the interpolation scheme proposed by Marchioli et al. (2007) is second-order accurate in space.

Since $\mathcal{LESOCC}$ works on a curvilinear coordinate system, the derivatives appearing in Eq. (9.30) have to be transformed to the computational space using the considerations made in Section 9.1. Consequently, by applying Eq. (9.5), the first derivatives in the c-space are given by:

$$\left.\frac{\partial \boldsymbol{u}_\mathrm{f}}{\partial x}\right|_\mathrm{N} = \left.\frac{\partial \boldsymbol{u}_\mathrm{f}}{\partial \xi}\right|_\mathrm{N} \left.\frac{\partial \xi}{\partial x}\right|_\mathrm{N} + \left.\frac{\partial \boldsymbol{u}_\mathrm{f}}{\partial \eta}\right|_\mathrm{N} \left.\frac{\partial \eta}{\partial x}\right|_\mathrm{N} + \left.\frac{\partial \boldsymbol{u}_\mathrm{f}}{\partial \zeta}\right|_\mathrm{N} \left.\frac{\partial \zeta}{\partial x}\right|_\mathrm{N}, \tag{9.31a}$$

$$\left.\frac{\partial \boldsymbol{u}_\mathrm{f}}{\partial y}\right|_\mathrm{N} = \left.\frac{\partial \boldsymbol{u}_\mathrm{f}}{\partial \xi}\right|_\mathrm{N} \left.\frac{\partial \xi}{\partial y}\right|_\mathrm{N} + \left.\frac{\partial \boldsymbol{u}_\mathrm{f}}{\partial \eta}\right|_\mathrm{N} \left.\frac{\partial \eta}{\partial y}\right|_\mathrm{N} + \left.\frac{\partial \boldsymbol{u}_\mathrm{f}}{\partial \zeta}\right|_\mathrm{N} \left.\frac{\partial \zeta}{\partial y}\right|_\mathrm{N}, \tag{9.31b}$$

$$\left.\frac{\partial \boldsymbol{u}_\mathrm{f}}{\partial z}\right|_\mathrm{N} = \left.\frac{\partial \boldsymbol{u}_\mathrm{f}}{\partial \xi}\right|_\mathrm{N} \left.\frac{\partial \xi}{\partial z}\right|_\mathrm{N} + \left.\frac{\partial \boldsymbol{u}_\mathrm{f}}{\partial \eta}\right|_\mathrm{N} \left.\frac{\partial \eta}{\partial z}\right|_\mathrm{N} + \left.\frac{\partial \boldsymbol{u}_\mathrm{f}}{\partial \zeta}\right|_\mathrm{N} \left.\frac{\partial \zeta}{\partial z}\right|_\mathrm{N}. \tag{9.31c}$$

Note that the metric coefficients are only computed once and then stored in arrays. It remains to specify the derivatives of the fluid velocity with respect to the coordinates (ξ, η, ζ) of the computational space. In the present thesis a central difference scheme is used for this purpose. Hence, the approximated derivatives in the c-space read:

$$\left.\frac{\partial \boldsymbol{u}_\mathrm{f}}{\partial \xi}\right|_\mathrm{N} = \frac{1}{2}\left[\boldsymbol{u}_\mathrm{f}|_{i+1,j,k} - \boldsymbol{u}_\mathrm{f}|_{i-1,j,k}\right] + \mathcal{O}\left(\Delta\xi^2\right), \tag{9.32a}$$

$$\left.\frac{\partial \boldsymbol{u}_\mathrm{f}}{\partial \eta}\right|_\mathrm{N} = \frac{1}{2}\left[\boldsymbol{u}_\mathrm{f}|_{i,j+1,k} - \boldsymbol{u}_\mathrm{f}|_{i,j-1,k}\right] + \mathcal{O}\left(\Delta\eta^2\right), \tag{9.32b}$$

$$\left.\frac{\partial \boldsymbol{u}_\mathrm{f}}{\partial \zeta}\right|_\mathrm{N} = \frac{1}{2}\left[\boldsymbol{u}_\mathrm{f}|_{i,j,k+1} - \boldsymbol{u}_\mathrm{f}|_{i,j,k-1}\right] + \mathcal{O}\left(\Delta\zeta^2\right). \tag{9.32c}$$

The resulting interpolation scheme is second-order accurate in space.

9.3.2 Bubble Tracking Algorithm

As argued in Section 4.1, the tracking of the bubbles through the continuous phase is based on a Lagrangian approach, i.e., the forces acting on the bubbles displace them. Consequently, the bubble position at a new time step is determined by integrating Eq. (4.33) twice in time. The first integration yielding the new dimensionless velocity $\boldsymbol{u}_\mathrm{b}$ of the bubble is carried out in the physical space. For this purpose, Eq. (4.33) is written in the following form[1]:

$$\frac{\mathrm{d}\boldsymbol{u}_\mathrm{b}}{\mathrm{d}t} = f_\mathrm{D}\left(\boldsymbol{u}_\mathrm{f} - \boldsymbol{u}_\mathrm{b}\right) + \underbrace{\frac{1}{f_\mathrm{m}}\left(\boldsymbol{f}_\mathrm{G+B} + \boldsymbol{f}_\mathrm{L} + \boldsymbol{f}^\mathrm{mod}_\mathrm{AM+PG}\right)}_{\boldsymbol{f}}, \tag{9.33}$$

where the acceleration term $\boldsymbol{f}$ is introduced to abbreviate the expression. The terms contained in $\boldsymbol{f}$ are defined by Eqs. (4.34b) to (4.34e). The factor f_D of the drag force is given by:

$$f_\mathrm{D} = \frac{C_\mathrm{D}}{f_\mathrm{m}}\frac{3}{4}\frac{|\boldsymbol{u}_\mathrm{f} - \boldsymbol{u}_\mathrm{b}|}{d_\mathrm{b}\,\rho_\mathrm{b}}. \tag{9.34}$$

The equation of motion (9.33) of the bubble is solved either analytically by a direct integration of the differential equation or numerically based on a fourth-order Runge–Kutta scheme (Schäfer, 2006). The distinction between these approaches is necessary, since the Runge–Kutta scheme is not unconditionally stable. Hence, in the present thesis the two methods are distinguished based on the parameter $\beta = f_\mathrm{D}\,\Delta t$, where Δt is the time-step size. According to Antia (2012) the numerical Runge–Kutta approach is unconditionally stable for $0 < \beta \leq 2.78$. Consequently, in $\mathcal{LESOCC}$ the numerical method

[1] Note that here the prime denoting dimensionless variables in Chapter 4 is dropped for the sake of convenience.

is used, if $\beta \leq 2$. Otherwise, the analytical integration is chosen. The integration of Eq. (9.33) by the Runge–Kutta scheme is given by the following expression:

$$\boldsymbol{u}_\mathrm{b}^{(n+1)} = \boldsymbol{u}_\mathrm{b}^{(n)} + \frac{1}{6}\left(\boldsymbol{k}_1 + 2\,\boldsymbol{k}_2 + 2\,\boldsymbol{k}_3 + \boldsymbol{k}_4\right), \tag{9.35}$$

with $\boldsymbol{u}_\mathrm{b}^{(n+1)}$ denoting the bubble velocity at the new time step. The coefficients of the four sub-steps of Eq. (9.35) are defined by:

$$\boldsymbol{k}_1 = \Delta t \left\{ f_\mathrm{D}^{(n)} \left[\boldsymbol{u}_\mathrm{f} - \boldsymbol{u}_\mathrm{b}^{(n)}\right] + \boldsymbol{f}^{(n)} \right\}, \tag{9.36a}$$

$$\boldsymbol{k}_2 = \Delta t \left\{ f_\mathrm{D}^{(n)} \left[\boldsymbol{u}_\mathrm{f} - \left(\boldsymbol{u}_\mathrm{b}^{(n)} + \frac{1}{2}\,k_1\right)\right] + \boldsymbol{f}^{(n)} \right\}, \tag{9.36b}$$

$$\boldsymbol{k}_3 = \Delta t \left\{ f_\mathrm{D}^{(n)} \left[\boldsymbol{u}_\mathrm{f} - \left(\boldsymbol{u}_\mathrm{b}^{(n)} + \frac{1}{2}\,k_2\right)\right] + \boldsymbol{f}^{(n)} \right\}, \tag{9.36c}$$

$$\boldsymbol{k}_4 = \Delta t \left\{ f_\mathrm{D}^{(n)} \left[\boldsymbol{u}_\mathrm{f} - \left(\boldsymbol{u}_\mathrm{b}^{(n)} + k_3\right)\right] + \boldsymbol{f}^{(n)} \right\}. \tag{9.36d}$$

Note that the acceleration term $\boldsymbol{f}^{(n)}$ contains, among others, the lift force, which according to Eq. (4.34c) depends on the bubble velocity (see Section 4.1.1.3). Hence, the lift force should ideally also be updated within the four sub-steps of the Runge-Kutta method. However, for the sake of simplicity and since the lift is typically smaller than the drag force by at least one order of magnitude, the lift force is only determined once. In the case that the stability condition of the Runge–Kutta approach is not satisfied, i.e., if $\beta > 2$, Eq. (9.33) is analytically integrated. Thus, the bubble velocity at the new time step is given by:

$$\boldsymbol{u}_\mathrm{b}^{(n+1)} = \boldsymbol{u}_\mathrm{f} + \left(\boldsymbol{u}_\mathrm{b}^{(n)} - \boldsymbol{u}_\mathrm{f}\right) \exp\left(-\beta\right) + \frac{1}{f_\mathrm{D}^{(n)}}\,\boldsymbol{f}\left[1 - \exp\left(-\beta\right)\right]. \tag{9.37}$$

Note that the time-step size Δt in Eqs. (9.35) and (9.37) is equal to the time step used for the prediction of the continuous phase. In principle, it is possible that two different time steps are used for both phases. However, this is not done in the present thesis to prevent run-time overheads caused by the interpolation of the fluid velocity between two time steps of the continuous phase (Breuer et al., 2006a). Additionally, this interpolation of the fluid velocity between two time steps leads to numerical errors due to the interpolation.

After the new bubble velocity is calculated based on either Eq. (9.35) or (9.37), the new bubble position can be determined by a second integration with respect to time. In contrast to the first integration explained above, the second integration is done in the computational space, see Fig. 9.4 for a schematic sketch. The reason behind this approach is that the identification of the position in the c-space based on a location in the p-space requires time-consuming search algorithms. These would be necessary after each integration in time, since the bubble might reach another computational cell. As indicated in Fig. 9.4(a) the physical coordinates of the bubble and the index of the computational cell where the bubble is located are not directly related. However, such an explicit relation exists in the computational space:

$$i_\mathrm{b} = \mathrm{int}\left(\xi_\mathrm{b}\right), \quad j_\mathrm{b} = \mathrm{int}\left(\eta_\mathrm{b}\right) \quad \text{and} \quad k_\mathrm{b} = \mathrm{int}\left(\zeta_\mathrm{b}\right). \tag{9.38}$$

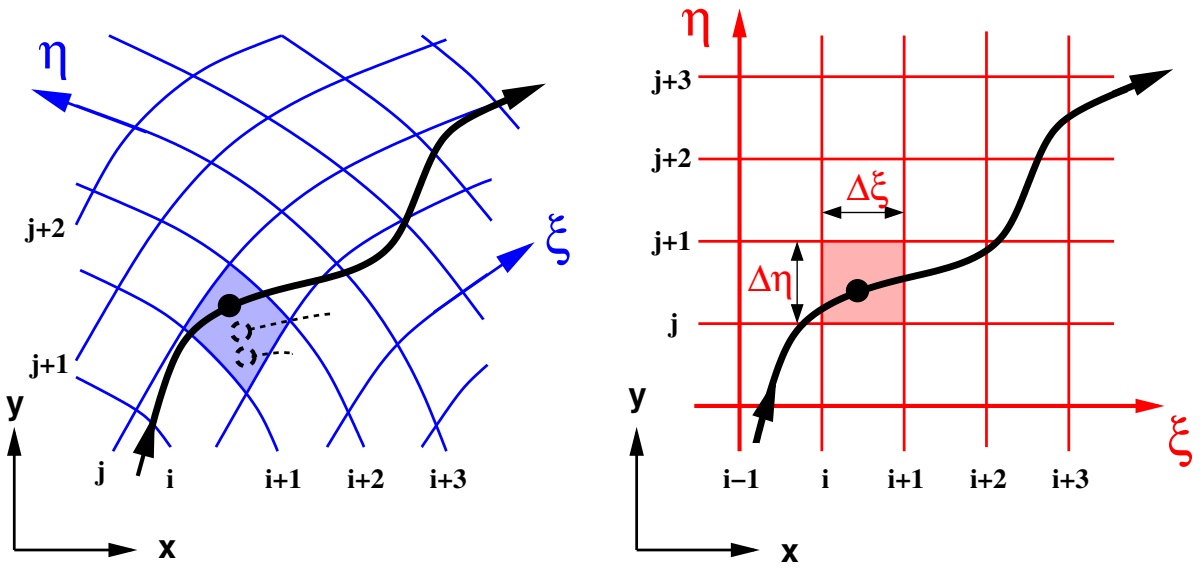

(a) Physical space. **(b)** Computational space.

Fig. 9.4. Schematic sketch of the bubble tracking: (a) in the physical space and (b) in the computational space. Taken from Breuer et al. (2007).

In Eq. (9.38) $\boldsymbol{\xi}_\mathrm{b} = (\xi_\mathrm{b}, \eta_\mathrm{b}, \zeta_\mathrm{b})$ denotes the position of the bubble in the c-space and the index triple $(i_\mathrm{b}, j_\mathrm{b}, k_\mathrm{b})$ defines the computational cell the bubble is located in (see Fig. 9.4(b)). The function int (.) represents the integer function, i.e., int (ξ_b) gives the integer value of the bubble position ξ_b.

In order to determine the position $\boldsymbol{\xi}_\mathrm{b}$ of the bubble in the computational space, Eq. (4.2) has to be transformed to its formulation in c-space, which reads:

$$\frac{\mathrm{d}\boldsymbol{\xi}_\mathrm{b}}{\mathrm{d}t} = \boldsymbol{U}_\mathrm{b}\,, \tag{9.39}$$

with $\boldsymbol{U}_\mathrm{b}$ the contravariant velocity of the bubble. Based on Eq. (9.2), the components of $\boldsymbol{U}_\mathrm{b}$ in c-space are given by:

$$U_\mathrm{b} = \frac{\mathrm{d}\xi_\mathrm{b}}{\mathrm{d}t} = \left.\frac{\partial\xi}{\partial x}\right|_\mathrm{b} u_\mathrm{b} + \left.\frac{\partial\xi}{\partial y}\right|_\mathrm{b} v_\mathrm{b} + \left.\frac{\partial\xi}{\partial z}\right|_\mathrm{b} w_\mathrm{b}, \tag{9.40a}$$

$$V_\mathrm{b} = \frac{\mathrm{d}\eta_\mathrm{b}}{\mathrm{d}t} = \left.\frac{\partial\eta}{\partial x}\right|_\mathrm{b} u_\mathrm{b} + \left.\frac{\partial\eta}{\partial y}\right|_\mathrm{b} v_\mathrm{b} + \left.\frac{\partial\eta}{\partial z}\right|_\mathrm{b} w_\mathrm{b}, \tag{9.40b}$$

$$W_\mathrm{b} = \frac{\mathrm{d}\zeta_\mathrm{b}}{\mathrm{d}t} = \left.\frac{\partial\zeta}{\partial x}\right|_\mathrm{b} u_\mathrm{b} + \left.\frac{\partial\zeta}{\partial y}\right|_\mathrm{b} v_\mathrm{b} + \left.\frac{\partial\zeta}{\partial z}\right|_\mathrm{b} w_\mathrm{b}. \tag{9.40c}$$

Note that the velocity components $\boldsymbol{u}_\mathrm{b} = (u_\mathrm{b}, v_\mathrm{b}, w_\mathrm{b})$ in the physical space appearing in Eq. (9.40) are known from the first integration of Eq. (9.33). In order to estimate the metric coefficients at the bubble position $\partial\xi/\partial x|_\mathrm{b}, \partial\xi/\partial y|_\mathrm{b}, \ldots, \partial\zeta/\partial z|_\mathrm{b}$ a trilinear

interpolation defined in Section 9.3.1 is used. The transformed equation (9.39) is then integrated in time by a fourth-order Runge–Kutta scheme yielding the new bubble position in the computational space according to:

$$\boldsymbol{\xi}^{(n+1)} = \boldsymbol{\xi}^{(n)} + \frac{1}{6}\left(\boldsymbol{k}_1 + 2\,\boldsymbol{k}_2 + 2\,\boldsymbol{k}_3 + \boldsymbol{k}_4\right), \tag{9.41}$$

with the coefficients of the four sub-steps defined by:

$$\boldsymbol{k}_1 = \Delta t\,\boldsymbol{U}_\mathrm{b}, \tag{9.42a}$$

$$\boldsymbol{k}_2 = \Delta t\left(\boldsymbol{U}_\mathrm{b} + \frac{1}{2}\,\boldsymbol{k}_1\right), \tag{9.42b}$$

$$\boldsymbol{k}_3 = \Delta t\left(\boldsymbol{U}_\mathrm{b} + \frac{1}{2}\,\boldsymbol{k}_2\right), \tag{9.42c}$$

$$\boldsymbol{k}_4 = \Delta t\left(\boldsymbol{U}_\mathrm{b} + \boldsymbol{k}_3\right). \tag{9.42d}$$

Note that the above described procedure is highly efficient. Especially, the determination of the bubble position in the computational space is beneficial. According to Schäfer and Breuer (2002), the CPU-time requirements of tracking schemes performing the second integration of Eq. (9.33) in c-space are up to one order of magnitude lower than schemes working in p-space. Additionally, it is noteworthy that no back-transformation to the physical space is required during the algorithm. The only exception is the visualization of the results, where the coordinates in the p-space are obtained by a trilinear interpolation.

9.3.3 Collision Detection

As already argued in Section 5.3, bubble-bubble collisions become important, if the volume fraction of the bubbles is sufficiently large. The detection of collisions in this four-way coupling regime is a critical point of the numerical methodology, since the computational costs can be extremely large. For example, in simple brute-force detection algorithms, where for each bubble it is checked if it collides with any of the other bubbles within the present time step, the numerical effort is of the order of $\mathcal{O}(N_\mathrm{b}^2)$. In order to reduce the computational costs, the deterministic collision detection algorithm by Breuer and Alletto (2012) is applied in $\mathcal{LESOCC}$, which is based on the uncoupling technique by Bird (1976). Consequently, the bubble trajectories are computed in two steps (Breuer and Alletto, 2012):

1. Bubbles are moved according to the equation of motion neglecting bubble-bubble collisions.

2. The occurrence of collisions is examined for all bubbles. If a collision is detected, the velocities of the collision pair are replaced by the post-collision velocities. The positions of the colliding bubbles are not changed, which is advantageous for parallelization.

Displacing the bubbles after a collision is associated with the risk of an overlap with a third bubble, which could disarrange the procedure (Wunsch et al., 2008). Therefore, the

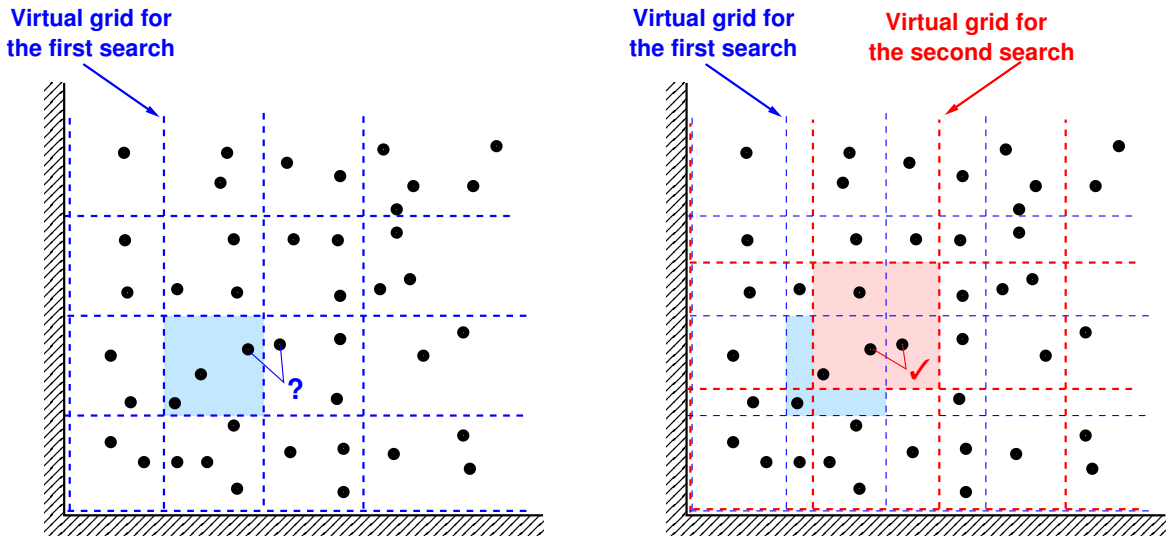

(a) First search. **(b)** Second search.

Fig. 9.5. Deterministic collision detection by a two-step search algorithm using virtual cells. Figures taken from Breuer and Alletto (2012).

displacement is neglected in the present thesis. It has to be noted that the statistical results in non-homogeneous flows may be altered by disregarding the displacement (Wunsch et al., 2008). However, the effect is assumed to be a marginal due to the small time-step size typically used for LES.

As argued before, the actual detection of the colliding bubbles is a critical issue for the cost-efficiency of the collision-detection algorithm. In the present thesis, a two-step procedure is employed (Breuer and Alletto, 2012). In a first step, likely collision partners are identified. Since in LES the time-step size is small, it can be assumed that only neighboring bubbles can collide within one time step. In order to determine the corresponding bubbles, the computational domain is divided into virtual cells. The search for likely collisions is then only carried out within those virtual cells depicted in Fig. 9.5(a). Using this approach reduces the associated numerical costs from the aforementioned order of $\mathcal{O}(N_\mathrm{b}^2)$ to a much lower order of $\mathcal{O}(N_\mathrm{b})$ (Breuer and Alletto, 2012). The size of the virtual cells is dynamically adapted during the simulation to guarantee an optimized cell size. Furthermore, to account for collisions of bubbles present close to the interface between two neighboring virtual cells during the first search shown in Fig. 9.5(a), a second search schematically depicted in Fig. 9.5(b) is performed with a slightly modified cell size. In the present thesis the length of the edges of the virtual cells used during the second search are increased by a factor of $17/13 \approx 1.3$ compared to the original edges. Consequently, the necessity for overlapping cells or taking the 26 surrounding virtual cells into account is avoided. Note that this concept was successfully applied in various studies (see, e.g., Hopkins and Louge, 1991; Viccione et al., 2008; Wunsch et al., 2008).

After the likely collision partners within one virtual cell are identified, it is sufficient to restrict the collision detection to these bubbles in the following second step. In the

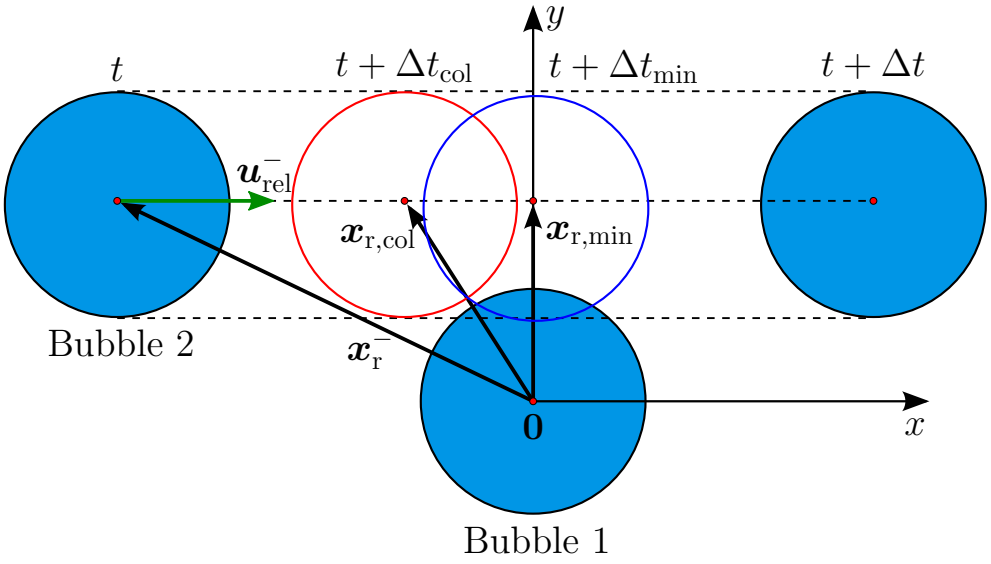

Fig. 9.6. Schematic sketch of the relative motion between two colliding bubbles. Based on Breuer and Alletto (2012) and Tanaka and Tsuji (1991).

procedure proposed by Breuer and Alletto (2012), it is assumed that the bubbles move with a constant velocity within one time step (Chen et al., 1999; Tanaka and Tsuji, 1991; Yamamoto et al., 2001), i.e., the bubble displacement is assumed to be linear. This assumption is reasonable for the small time steps applied in LES. Consequently, binary bubble collisions can be detected solely based on the following kinematic conditions (Breuer and Alletto, 2012):

I. The collision partners have to approach each other as depicted in Fig. 9.6. This is expressed by the condition:

$$\boldsymbol{x}_{\mathrm{r}}^{-} \cdot \boldsymbol{u}_{\mathrm{rel}}^{-} < 0\,, \tag{9.43}$$

where $\boldsymbol{x}_{\mathrm{r}}^{-} = \boldsymbol{x}_2^{-} - \boldsymbol{x}_1^{-}$ and $\boldsymbol{u}_{\mathrm{rel}}^{-} = \boldsymbol{u}_{\mathrm{b},2}^{-} - \boldsymbol{u}_{\mathrm{b},1}^{-}$ are the relative distance between the bubble centers and their relative velocity prior to the possible collision, respectively. In the present case bubble 1 denotes the reference. Only bubbles within a virtual cell fulfilling condition (9.43) need to be checked for a collision based on the second criterion.

II. The minimum distance $\boldsymbol{x}_{\mathrm{r,min}}$ between the possible collision partners within the considered time step has to be smaller than the sum l_{12} of their radii:

$$|\boldsymbol{x}_{\mathrm{r,min}}| \leq l_{12} = r_{\mathrm{b},1} + r_{\mathrm{b},2} = \frac{1}{2}\left(d_{\mathrm{b},1} + d_{\mathrm{b},2}\right)\,. \tag{9.44}$$

In other words, the second condition (9.44) means that the bubbles have to come into contact with each other during the linear displacement of the considered time step, see Fig. 9.6.

Based on the assumption of a linear displacement of the bubbles, the minimum separation between the (possible) collision partners within one time step is given by:

$$\boldsymbol{x}_{\mathrm{r,min}} = \boldsymbol{x}_{\mathrm{r}}^{-} + \boldsymbol{u}_{\mathrm{rel}}^{-}\,\Delta t_{\mathrm{min}}\,, \tag{9.45}$$

where Δt_{min} denotes the time interval after which the separation distance between the bubbles has its smallest value. According to Breuer and Alletto (2012), this time interval can be calculated according to:

$$\Delta t_{\mathrm{min}} = -\frac{\boldsymbol{x}_{\mathrm{r}}^{-}\cdot\boldsymbol{u}_{\mathrm{rel}}^{-}}{\left|\boldsymbol{u}_{\mathrm{rel}}^{-}\right|^{2}}. \tag{9.46}$$

Consequently, bubble-bubble collisions within a virtual cell are found if the following conditions are satisfied:

$$(\Delta t_{\mathrm{min}} \leq \Delta t \quad \text{and} \quad |\boldsymbol{x}_{\mathrm{r,min}}| \leq l_{12}) \quad \text{or} \quad \left|\boldsymbol{x}_{\mathrm{r}}^{-}\right| \leq l_{12}\,. \tag{9.47}$$

On the one hand, the first condition of Eq. (9.47) expresses that a collision takes place if the time interval Δt_{min} given by Eq. (9.46) is smaller than or equal to the time-step size Δt. Additionally, the separation distance of the bubble centers at the corresponding time instant has to be smaller than l_{12}. On the other hand, the third condition defined by Eq. (9.47) means that the considered bubbles are already separated by a distance less than l_{12} at the beginning of the time step leading automatically to a collision.

If the collision conditions defined by Eq. (9.47) are satisfied, a collision between the two considered bubbles takes place within the present time step. Hence, the collision model described in Section 5.3 can be applied to determine the post-collision velocities of the bubbles. This requires to specify the collision-normal unit vector $\boldsymbol{n}_{\mathrm{c}}$, which is given by the relation (see Eq. (5.7) in Section 5.3):

$$\boldsymbol{n}_{\mathrm{c}} = \frac{\boldsymbol{x}_{\mathrm{r,col}}}{|\boldsymbol{x}_{\mathrm{r,col}}|}\,. \tag{9.48}$$

Here, $\boldsymbol{x}_{\mathrm{r,col}}$ denotes the relative distance vector of the bubble centers at the time instant of the collision. Based on the linear displacement of the bubbles, the distance vector obtained after the collision time interval Δt_{col} reads:

$$\boldsymbol{x}_{\mathrm{r,col}} = \boldsymbol{x}_{\mathrm{r}}^{-} + \boldsymbol{u}_{\mathrm{rel}}^{-}\,\Delta t_{\mathrm{col}}\,. \tag{9.49}$$

Note that the corresponding distance is simply given by $|\boldsymbol{x}_{\mathrm{r,col}}| = l_{12}$, since the bubbles exactly touch each other at the instant of the collision. The collision time interval Δt_{col} can be readily determined by squaring Eq. (9.49) leading to the expression:

$$\left|\boldsymbol{x}_{\mathrm{r}}^{-} + \boldsymbol{u}_{\mathrm{rel}}^{-}\,\Delta t_{\mathrm{col}}\right|^{2} = |\boldsymbol{x}_{\mathrm{r,col}}|^{2} = l_{12}^{2}\,. \tag{9.50}$$

Solving Eq. (9.50) yields the collision time interval (Chen et al., 1999):

$$\Delta t_{\mathrm{col}} = \Delta t_{\mathrm{min}} \left(1 - \sqrt{1 - K_1\, K_2}\right), \tag{9.51}$$

$$\text{with} \quad K_1 = \frac{\left|\boldsymbol{x}_{\mathrm{r}}^{-}\right|^2 \left|\boldsymbol{u}_{\mathrm{rel}}^{-}\right|^2}{\left(\boldsymbol{x}_{\mathrm{r}}^{-} \cdot \boldsymbol{u}_{\mathrm{rel}}^{-}\right)^2} \quad \text{and} \quad K_2 = 1 - \frac{l_{12}^2}{\left|\boldsymbol{x}_{\mathrm{r}}^{-}\right|^2}. \tag{9.52}$$

Consequently, inserting the value of the collision time interval Δt_{col} obtained from Eq. (9.51) into Eq. (9.49) provides the relative distance vector $\boldsymbol{x}_{\mathrm{r,col}}$ at the instant of the bubble collision, which is required for the estimation of the collision normal vector $\boldsymbol{n}_{\mathrm{c}}$.

9.3.4 Description of Bubble Coalescence

In the case that the coalescence of the colliding bubbles is taken into account, the model described in Chapter 7 is applied in the present thesis. By using the extended film drainage model by Hoppe and Breuer (2018), coalescence is found if the coalescence criterion (7.24) is satisfied. Otherwise a rebound takes place with the post-collision conditions given by the collision model explained in Section 5.3.

If two bubbles coalesce, the post-coalescence conditions of the newly formed bubble are given by Eqs. (7.40) to (7.42) defined in Section 7.6. Here, it is important to remember that in the present CFD code the position of the bubbles is solely tracked in the computational space. Consequently, Eq. (7.41) defining the position of the new bubble in the physical space has to be transformed to the computational space. For a general curvilinear non-staggered grid the position $\boldsymbol{\xi}_{\mathrm{b,n}}$ of the newly generated bubble in c-space has to be approximated by:

$$\boldsymbol{\xi}_{\mathrm{b,n}} \approx \frac{m_{\mathrm{b,1}}\, \boldsymbol{\xi}_{\mathrm{b,1}} + m_{\mathrm{b,2}}\, \boldsymbol{\xi}_{\mathrm{b,2}}}{m_{\mathrm{b,n}}} = \frac{d_{\mathrm{b,1}}^3\, \boldsymbol{\xi}_{\mathrm{b,1}} + d_{\mathrm{b,2}}^3\, \boldsymbol{\xi}_{\mathrm{b,2}}}{d_{\mathrm{b,n}}^3}, \tag{9.53}$$

where $\boldsymbol{\xi}_{\mathrm{b,1}}$ and $\boldsymbol{\xi}_{\mathrm{b,2}}$ are the c-space positions of the two coalescing bubbles, respectively. Additionally, from a numerical point of view the linear arrays in which the bubble properties (position, velocity, etc.) are stored have to be re-adjusted, since a coalescence process decreases the total number of bubbles in the computational domain by one. In $\mathcal{LESOCC}$ the properties of the new bubble are stored at the array positions of one of the bubbles participating in the coalescence process. The second bubble is removed from the simulation by moving the variables of the last bubble in the array to the array position of the second bubble overwriting its values in the process. Thus, linear arrays are retained.

9.3.5 Description of Bubble Breakup

In order to describe the bubble breakup phenomenon, the model by Hoppe and Breuer (2020) is used in the present thesis. Recalling the considerations made in Chapter 8, a breakup process takes place if the turbulent surface deforming pressure fluctuations associated with an eddy are larger than the surface restoring pressure of the smaller

daughter bubble. Mathematically, this criterion is described by Eq. (8.4) leading to the requirement of We $\gtrsim 15.12$ defined in Eq. (8.6). In order to estimate the Weber number of the bubble, the dissipation rate ϵ at the position of the bubble is approximated from the values of ϵ stored at the eight cell centers surrounding the bubble by the trilinear interpolation scheme described in Section 9.3.1. As described in Section 8.1, the dissipation rate itself is predicted based on the instantaneous filtered velocities.

The post-breakup conditions of the two daughter bubbles are described in Section 8.2. Here, it is noteworthy that the daughter bubbles are not shifted in space after the breakup, but the positions of both bubbles are set to the center of mass of the parent bubble, i.e., $\boldsymbol{\xi}_{\mathrm{b,s}} = \boldsymbol{\xi}_{\mathrm{b,l}} = \boldsymbol{\xi}_{\mathrm{b,p}}$. Furthermore, the immediate breakup of the daughter bubbles in the subsequent time steps is prevented by introducing the idle time defined by Eq. (8.32) in Section 8.2.4. Similar to Section 9.3.4, the occurrence of a breakup event requires an adjustment of the arrays storing the bubble properties. Since it is assumed in the present thesis that the parent bubble breaks into two daughter bubbles, it is a natural choice to store the properties of one daughter bubble at the array positions of the parent bubble. The corresponding variables of the second daughter bubble are simply appended to the array.

9.4 Determination of the Statistics

The statistics of the results obtained by the present simulation framework are calculated on-the-fly by the updating formalism of Youngs and Cramer (1971). Hence, at every averaging instant (also called events) the instantaneous realization of an arbitrary (fluid or bubble) quantity $\phi(x, y, z)$ located at the position (x, y, z) is included in the averaging process. Consequently, the average of the considered quantity obtained after N events is given by (Youngs and Cramer, 1971):

$$\langle\phi\rangle_{(N)}(x, y, z) = \frac{1}{N}\left[(N-1)\langle\phi\rangle_{(N-1)}(x, y, z) + \phi(x, y, z)\right], \tag{9.54}$$

where $\langle\phi\rangle_{(N-1)}$ denotes the average before the present value of $\phi(x, y, z)$ is included. The fluctuation $\langle\phi'\,\varphi'\rangle_{(N)}(x, y, z)$, where $\phi' = \phi - \langle\phi\rangle$ and $\varphi' = \varphi - \langle\varphi\rangle$ also represent arbitrary fluid or bubble quantities, is determined by the formula (Youngs and Cramer, 1971):

$$\langle\phi'\,\varphi'\rangle_{(N)}(x, y, z) = \frac{1}{N-1}\Big[(N-2)\langle\phi'\,\varphi'\rangle_{(N-1)}(x, y, z) + \frac{N}{N-1}(\phi'\,\varphi')(x, y, z)\Big], \tag{9.55}$$

with $(\phi'\,\varphi')(x, y, z)$ the present realization of the fluctuation. Note that in the case that a fluid quantity is averaged, N denotes the actual number of averaging time steps, $N = N_{\mathrm{av}}$, considered up to the present time step. If a bubble quantity is averaged, N is the total number of bubbles which have contributed to the average. Hence, N equals the accumulated number of bubbles $N_{\mathrm{b}}(x, y, z)$ found in a computational cell located at the

position (x, y, z). In other words, at an averaging instant the present bubble properties are included in the averaging and stored at the cell center of the control volume the bubble is located in.

Afterwards, the three-dimensional statistics obtained by this temporal averaging procedure can be further averaged during the post-processing. This is possible if the considered turbulent flow possesses homogeneous directions, in which the average flow does not vary. Prominent examples are the streamwise and spanwise directions of a channel flow. In these homogeneous directions the averages and the fluctuations of a certain quantity ϕ stored at the centers of the computational cells have to be averaged up, i.e., the total average of ϕ and the associated total fluctuations have to be calculated. For this purpose, the formulas by Chan et al. (1983) are used in the present thesis in form of an updating scheme. Hence, if the total average $\langle\phi\rangle_{(N_{\mathrm{tot}}^{\mathrm{prev}})}$ of a quantity ϕ has been calculated considering all previous averages up to a certain control volume, the new total average $\langle\phi\rangle_{(N_{\mathrm{tot}}^{\mathrm{new}})}$ including the average in the next cell $\langle\phi\rangle_{(N_{\mathrm{cell}})}$ is obtained by:

$$\langle\phi\rangle_{(N_{\mathrm{tot}}^{\mathrm{new}})} = \frac{1}{N_{\mathrm{tot}}^{\mathrm{new}}}\left[N_{\mathrm{tot}}^{\mathrm{prev}} \cdot \langle\phi\rangle_{(N_{\mathrm{tot}}^{\mathrm{prev}})} + N_{\mathrm{cell}} \cdot \langle\phi\rangle_{(N_{\mathrm{cell}})}\right]. \tag{9.56}$$

where $N_{\mathrm{tot}}^{\mathrm{prev}}$ denotes the number of events that have contributed to the previous total average $\langle\phi\rangle_{(N_{\mathrm{tot}}^{\mathrm{prev}})}$. The average $\langle\phi\rangle_{(N_{\mathrm{cell}})}$, which is added to the total average, consists of N_{cell} events (e.g., collisions, coalescence or breakup processes). Therefore, the new total number of events is given by $N_{\mathrm{tot}}^{\mathrm{new}}) = N_{\mathrm{tot}}^{\mathrm{prev}} + N_{\mathrm{cell}}$.

The associated fluctuation $\langle\phi'\,\varphi'\rangle_{(N_{\mathrm{tot}}^{\mathrm{new}})}$ is determined in a slightly different manner. In order to reduce the number of required computations in each updating step, the total of the sum:

$$S_{(N_{\mathrm{tot}}^{\mathrm{new}})} = (N_{\mathrm{tot}}^{\mathrm{new}} - 1) \cdot \langle\phi'\,\varphi'\rangle_{(N_{\mathrm{tot}}^{\mathrm{new}})} \tag{9.57}$$

along the homogeneous direction is calculated in a first step. According to Chan et al. (1983) the total sum is given by the following formula:

$$\begin{aligned} S_{(N_{\mathrm{tot}}^{\mathrm{new}})} = {} & S_{(N_{\mathrm{tot}}^{\mathrm{prev}})} + (N_{\mathrm{cell}} - 1) \cdot \langle\phi'\,\varphi'\rangle_{(N_{\mathrm{cell}})} \\ & + \frac{N_{\mathrm{tot}}^{\mathrm{prev}}\, N_{\mathrm{cell}}}{N_{\mathrm{tot}}^{\mathrm{prev}} + N_{\mathrm{cell}}} \cdot \left(\langle\phi\rangle_{(N_{\mathrm{tot}}^{\mathrm{prev}})} - \langle\phi\rangle_{(N_{\mathrm{cell}})}\right)\left(\langle\varphi\rangle_{(N_{\mathrm{tot}}^{\mathrm{prev}})} - \langle\varphi\rangle_{(N_{\mathrm{cell}})}\right), \end{aligned} \tag{9.58}$$

where $S_{(N_{\mathrm{tot}}^{\mathrm{prev}})}$ denotes the total sum over all computational cells preceding the present one. Since the fluctuation $\langle\phi'\,\varphi'\rangle_{(N_{\mathrm{cell}})}$ is stored at the center of the computational cells, the fluctuation has to be multiplied by $N_{\mathrm{cell}} - 1$ in order to be added to the total sum (second term on the r.h.s. of Eq. (9.58)). After the total sum along a homogeneous direction is obtained by Eq. (9.58), the associated total fluctuation can be calculated by:

$$\langle\phi'\,\varphi'\rangle_{(N_{\mathrm{tot}})}^{\mathrm{new}} = \frac{S_{(N_{\mathrm{tot}})}^{\mathrm{new}}}{(N_{\mathrm{tot}}^{\mathrm{new}} - 1)}. \tag{9.59}$$

10 Description and Numerical Setup of the Test Cases

The Euler–Lagrange framework for turbulent bubble-laden flows described in the previous chapters is validated and investigated based on various test cases. In the following, the test cases and the respective numerical setups used throughout this thesis are presented. The first test case described in Section 10.1 represents a bubble-laden downward channel flow at a Reynolds number of $\mathrm{Re}_\tau = 150$. This setup is used for the validation of the numerical methodology and partly for the investigation on the influence of the subgrid-scale model seen by the dispersed phase on both phases. Afterwards, the setup of a second channel flow at a higher Reynolds number ($\mathrm{Re}_\tau = 644$) laden with solid particles is described, which is utilized for further investigations on the subgrid-scale model. The coalescence model is tested in two different setups. The first setup (Section 10.3) considers the coalescence of a single bubble vertically rising in a stagnant fluid with a free surface. The second setup used to study bubble coalescence is a bubble column outlined in Section 10.4. Lastly, the breakup model for bubbles is investigated in a fully developed turbulent jet flow, where the details of the setup are given in Section 10.5.

10.1 Low-Reynolds Number Channel Flow with Bubbles

To validate the numerical methodology for the bubble tracking and to investigate the influence of the enhanced Langevin subgrid-scale model, the downward channel flow setup by Molin et al. (2012) is used. Note that their DNS of a channel flow is based on an earlier work by Giusti et al. (2005). The half-width of the considered channel is $\delta = 20\,\mathrm{mm}$, while the wall-shear stress velocity is set to $u_\tau = 7.5 \times 10^{-3}\,\mathrm{m/s}$ by Molin et al. (2012), where the flow is driven by a constant dimensionless pressure gradient $\partial \bar{p}^*/\partial x^* = -1$ leading to a variable mass flow. Consequently, a Reynolds number of $\mathrm{Re}_\tau = 150$ based on the wall-shear stress velocity is obtained for a typical kinematic viscosity $\nu = 10^{-6}\,\mathrm{m}^2/\mathrm{s}$ of water. In the DNS of Molin et al. (2012) a computational domain of the size of $4\,\pi\,\delta \times 2\,\delta \times 2\,\pi\,\delta$ in streamwise, wall-normal and spanwise direction is considered. The same dimensions of the computational domain are chosen in the present thesis in order to ensure the same flow features. Furthermore, the no-slip boundary condition is applied at the walls, while in streamwise and spanwise direction periodic boundary conditions are used.

For the validation of the bubble tracking in Section 11.1 a grid consisting of $256 \times 128 \times 256$ control volumes in streamwise, wall-normal and spanwise direction is applied. The resulting equidistant grid spacings in streamwise and spanwise direction are $\Delta x^+ = 7.35$ and $\Delta z^+ = 3.68$, respectively. The first cell center is located at a distance of $\Delta y^+ = 0.225$

from the wall. The size of the cells in the wall-normal direction increases according to a geometric series with a stretching factor of $r = 1.044$. The idea behind using such a fine grid is to validate the bubble tracking methodology without spurious effects of the subgrid-scale models for both the continuous and the dispersed phase. Consequently, neither the subgrid-scale models for the fluid presented in Section 3.2 nor the present Langevin-based model (Chapter 6) are applied.

The investigation on the influence of the particle subgrid-scale model on the bubble-laden flow in Section 11.2.1 is performed using a coarser grid in streamwise and spanwise direction containing $128 \times 128 \times 128$ control volumes. The first cell center is still located at a distance of $\Delta y^+ = 0.225$ from the wall with the cell sizes increasing with the same stretching factor as above. The equidistant grid spacing in streamwise and spanwise direction increases to $\Delta x^+ = 14.7$ and $\Delta z^+ = 7.36$, respectively. Consequently, the conditions for a wall-resolved LES ($y^+ < 2$ for the first cell center and $\Delta x^+ \lesssim 50 - 150$ and $\Delta z^+ \lesssim 15 - 40$) by Piomelli and Chasnov (1996) are still fulfilled. The influence of the subgrid scales on the continuous phase is taken into account by the Smagorinsky model, where the model constant is $C_\mathrm{S} = 0.065$ and the van Driest damping near solid walls is used. The dimensionless time-step size of the simulation is set to $\Delta t\, u_\tau/\delta = 1 \times 10^{-4}$.

In all cases the diameter of the bubbles is $d_\mathrm{b} = 0.22\,\mathrm{mm}$ corresponding to a dimensionless diameter of $d_\mathrm{b}^* = d_\mathrm{b}/\delta = 0.011$. A total of $N_\mathrm{b} = 21,940$ bubbles are tracked through the turbulent channel flow. Consequently, the total averaged volume fraction of the bubbles is $\Phi_{\mathrm{V,tot}} = 1 \times 10^{-4}$. The density ratio of the bubbles to the fluid is $\rho_\mathrm{b}/\rho_\mathrm{f} = 1.3 \times 10^{-3}$ yielding a very low mass loading of $\eta_\mathrm{b} = 1.3 \times 10^{-7}$. The resulting bubble response time of $\tau_\mathrm{b} = \rho_\mathrm{b}\, d_\mathrm{b}^2/18\,\mu_\mathrm{f} = 3.5 \times 10^{-6}\,\mathrm{s}$ corresponds to a dimensionless Stokes number built with the characteristic fluid time scale based on the wall-shear stress velocity and the kinematic viscosity of the fluid of $\mathrm{St}^+ = \tau_\mathrm{b}\, u_\tau^2/\nu_\mathrm{f} = 1.97 \times 10^{-4}$. The dimensionless gravitational acceleration pointing in the main flow direction is $g\,\delta/u_\tau^2 = 3488$. As in the work by Molin et al. (2012), the bubbles are assumed to be contaminated by surfactants. According to Pallas and Harrison (1990) the surface tension of air bubbles suspended in water at a temperature of 20° C is $\sigma = 72.86 \times 10^{-3}\,\mathrm{N/m}$, which is applied here as well. The resulting dimensionless Eötvös number is $\mathrm{Eo} = 6.5 \times 10^{-3}$. Hence, the bubbles are nearly spherical. Since the volume fraction of the bubbles is well within the regime where according to Elghobashi (1991, 1994) only two-way coupling plays a major role (see Section 5.2), only two-way coupling is considered, while bubble-bubble collisions are neglected. Bubble-wall collision are described by the inelastic hard-sphere model given in Section 4.2.4 with the normal restitution coefficient $e_\mathrm{n,w} = 1$, while the tangential restitution coefficient $e_\mathrm{t,w}$ and the static and kinetic friction coefficients $\mu_\mathrm{st,w}$ and $\mu_\mathrm{kin,w}$ are set to zero. However, note that bubble-wall collisions do not play any role in this setup, since the bubbles never reach the walls due to the influence of the lift force (cf. Section 11.2.1).

After their release into the turbulent channel flow, the bubbles are allowed to disperse in the channel for a dimensionless period of time of $\Delta T\, u_\tau/\delta = 25$. With a mean streamwise fluid velocity of $u_\mathrm{bulk}/u_\tau \approx 12$ and a length of the channel of $4\,\pi\,\delta$, this time period corresponds to roughly 25 flow-through times, which ensures a statistically steady simulation. Afterwards, the statistics of the bubbles and the flow are averaged over the same period of time, which is sufficient to obtain stable averages.

The choice of the reference data by Molin et al. (2012) has to be critically annotated. As already remarked by Molin et al. (2012) the point-bubble approximation has intrinsic limitations if the ratio of the bubble diameter to the grid spacing gets large as in the case of the channel flow close to the walls. As shown for example by Horwitz and Mani (2016) the drag force models become inaccurate under this circumstance. Nevertheless, this case is chosen here for comparison purposes for the following reasons: **1.** Since appropriate experimental data or DNS data considering a large number of fully resolved bubbles are missing, these DNS data are the most suitable choice. **2.** In the present study solely the downward channel flow is considered, where due to lift forces the bubbles are transported away from the walls and thus the above mentioned problem is strongly reduced. **3.** Since the present LES predictions are affected in the same manner as the DNS data, the effect can be approximately suppressed in the direct comparison of the data.

10.2 High-Reynolds Number Channel Flow with Particles

In order to further investigate the influence of the subgrid-scale modeling in general and the present extended Langevin model in particular, a second test case strongly differing from the bubble-laden channel flow at low Re by Giusti et al. (2005) and Molin et al. (2012) described in Section 10.1 is applied. For this purpose, a downward channel flow at a high Reynolds number containing solid particles is chosen. While the focus of this thesis is the prediction of bubble-laden flows, this setup is considered to illuminate the influence of the subgrid-scale model for a completely different density ratio of the dispersed to the continuous phase and different sizes of the entities of the Lagrangian phase. The setup chosen has been used before in various studies, e.g., by Breuer and Alletto (2012) and Breuer and Almohammed (2015). Consequently, a detailed description can be found therein.

As already mentioned, the flow Reynolds number is much larger than in the bubble-laden case, i.e., $\mathrm{Re}_\mathrm{b} = 11,900$ based on the half-width of the channel $\delta = 20\,\mathrm{mm}$ and the bulk fluid velocity u_bulk. This bulk Reynolds number corresponds to a shear Reynolds number of $\mathrm{Re}_\tau = 644$. Another major difference to the test case for the bubbles is that here the flow is driven by a variable pressure gradient, which allows to achieve a constant mass flow, cf. Eq. (3.35) in Section 3.3.5. The computational domain has a size of $2\,\pi\,\delta \times 2\,\delta \times \pi\,\delta$ in streamwise, wall-normal and spanwise direction, respectively. The grid used to resolve the fluid flow consists of $128 \times 128 \times 128$ control volumes in the respective directions. The first cell center from the wall is located at $\Delta y^+ = 0.63$ and the grid is geometrically stretched in wall-normal direction with a stretching factor of 1.05. In streamwise and spanwise direction the grid spacing is $\Delta x^+ = 61.76$ and $\Delta z^+ = 30.88$, respectively. The Smagorinsky model with $C_\mathrm{S} = 0.065$ and the van Driest damping near solid walls is applied to account for the influence of the unresolved scales on the continuous phase. The time-step size is set to $\Delta t\, u_\mathrm{bulk}/\delta = 5 \times 10^{-3}$.

The turbulent channel flow is laden with $N_\mathrm{p} = 6 \times 10^6$ fused quartz particles with a dimensionless diameter[1] of $d^*_{\mathrm{p},1.67} = 2 \times 10^{-4}$ and a density ratio of $\rho_\mathrm{p}/\rho_\mathrm{f} = 1814$. Hence, the Stokes number based on the wall-shear stress velocity and the kinematic viscosity ν_f of the fluid is $\mathrm{St}^+ = 1.67$. This leads to a total averaged volume fraction of $\Phi_{\mathrm{V,tot}} = 6.78 \times 10^{-7}$ and a corresponding mass loading of $\eta_\mathrm{p} = 1.23 \times 10^{-3}$, which is four orders of magnitude larger than in the bubble-laden case (Section 10.1). An additional set of simulations with altered particle properties is carried out for further studies on the effect of the subgrid scales. In those cases the particle diameters are reduced to the dimensionless values of $d_{\mathrm{p},1.00} = 1.55 \times 10^{-4}$ and $d_{\mathrm{p},0.10} = 5 \times 10^{-5}$. Since the number of particles is kept constant, this results in total volume fractions of $\Phi_{\mathrm{V,tot},1.00} = 3.14 \times 10^{-7}$ and $\Phi_{\mathrm{V,tot},0.10} = 1.06 \times 10^{-8}$ and mass loadings of $\eta_{\mathrm{p},1.00} = 5.70 \times 10^{-4}$ and $\eta_{\mathrm{p},0.10} = 1.92 \times 10^{-5}$, respectively. Therefore, the Stokes numbers of the additional cases are $\mathrm{St}^+ = 1.00$ and $\mathrm{St}^+ = 0.10$, respectively. Note that the remaining properties of the continuous and the dispersed phase remain unchanged. The gravitational acceleration acting on the particles points in the main flow direction and its dimensionless value is set to $g\,\delta/u^2_\mathrm{bulk} = 2.4 \times 10^{-3}$. The collisions of particles with a smooth solid wall are described by an approach devised by Breuer et al. (2012). The coefficients describing the momentum loss due to particle-wall collisions are the tangential and wall-normal restitution coefficients $e_\mathrm{t,w} = 0.44$ and $e_\mathrm{n,w} = 0.97$ and the static and kinetic friction coefficients $\mu_\mathrm{st,w} = 0.94$ and $\mu_\mathrm{kin,w} = 0.092$. The corresponding restitution and friction coefficients for particle-particle collisions are set to identical values based on the assumption that the wall and the particles have the same material properties, i.e., $e_\mathrm{t,p} = 0.44$, $e_\mathrm{n,p} = 0.97$, $\mu_\mathrm{st,p} = 0.94$ and $\mu_\mathrm{kin,p} = 0.092$. The description of the inter-particle collision process is done by the scheme of Breuer and Alletto (2012). In all cases of the high-Re channel flow the particles are allowed to disperse in the flow field for a dimensionless time interval of $\Delta T\,u_\mathrm{bulk}/\delta = 200$ (32 flow-through times) after their release. Afterwards, the statistics of the developed flow and the particles are averaged over a period of time of $\Delta T\,u_\mathrm{bulk}/\delta = 400$ corresponding to 64 flow-through times, which is again sufficient for stable statistics.

10.3 Free Surface

The validation of the present coalescence model (Chapter 7) is done by a comparison with the experimental results by Zawala and Malysa (2011) and Kosior et al. (2014), who investigated the coalescence of clean and contaminated bubbles with a free surface. In both experiments single air bubbles of varying size are released from a capillary orifice into a stagnant liquid. In the case of clean bubbles (Zawala and Malysa, 2011) distilled water is used, while in the contaminated case (Kosior et al., 2014) the distilled water contains n-octanol acting as a surfactant. Due to the buoyancy force the bubbles rise vertically upwards towards the free surface of the liquid column. There, the bubbles coalesce with the free surface, if the coalescence condition is satisfied. Otherwise, a rebound occurs.

[1] The number 1.67 in the subscript indicates the associated Stokes number St^+ based on the wall-shear stress velocity.

The reflected bubble is then accelerated towards the free surface again by the buoyancy force leading to a second or even further approaches.

It has to be noted that the results by Kosior et al. (2014) and Zawala and Malysa (2011) obtained for this experimental setup cannot readily be transferred to binary bubble coalescence, which is the topic of the present thesis. The reason for this is the fact that the process of coalescence with a free surface is not exactly identical to the binary coalescence of bubbles. For example, the impact of a bubble on a free surface vertically deforms the free surface (Kosior et al., 2014; Zawala and Malysa, 2011). Therefore, the assumption of a flat contact surface made for the derivation of the present coalescence model (see Section 7.1) is violated. While this is also not true for the coalescence of similar-sized bubbles, where dimples form in the film (see, e.g., Chan et al., 2011; Chesters and Hofman, 1982), the deformation is more pronounced in the case of a free surface. Additionally, it was observed in the experiments by Kosior et al. (2014) and Zawala and Malysa (2011) that the contact area between the free surface and the bubble becomes large during the impact, which contradicts the assumption made for the derivation of Eqs. (7.9) to (7.11). Nevertheless, the experiments by Kosior et al. (2014) and Zawala and Malysa (2011) are used for the validation of the present coalescence model by assuming the coalescence with a free surface to be equivalent to the coalescence with an infinitely large bubble. This is necessary since experiments performed under controlled conditions are rare in the literature or lack detailed information about the properties of the individual bubbles. Furthermore, bubble breakup can play a significant role in such experiments, i.e., coalescence and breakup processes balance each other resulting in bubble size distributions of a certain form. Such data are therefore inappropriate for the validation of the coalescence model.

The experimental setup of Kosior et al. (2014) and Zawala and Malysa (2011) is mimicked by releasing single bubbles into a stagnant liquid. Due to the influence of the buoyancy force (gravitational acceleration $g = 9.81\,\mathrm{m/s^2}$), the bubbles rise until they collide with a second bubble of infinite size hold in place at a certain position. The release position of the bubbles is chosen far below ($\Delta h = 120\,\mathrm{mm}$) the free surface ensuring that the rising bubbles reach their respective terminal rise velocities of $u_\mathrm{b} = 0.29\,\mathrm{m/s}$ and $u_\mathrm{b} = 0.37\,\mathrm{m/s}$ for the small and large clean bubbles and $u_\mathrm{b} = 0.14\,\mathrm{m/s}$ for the contaminated bubble. Based on the experiments, the diameters of the released bubble are set to $d_\mathrm{b} = 1.0\,\mathrm{mm}$ and $d_\mathrm{b} = 1.48\,\mathrm{mm}$ in the case of clean bubbles (Zawala and Malysa, 2011) and $d_\mathrm{b} = 1.32\,\mathrm{mm}$ in the case of contaminated bubbles (Kosior et al., 2014). In all cases the ratio of the densities of the bubble and the fluid is $\rho_\mathrm{b}/\rho_\mathrm{f} = 1.3 \times 10^{-3}$. The surface tension of the clean bubbles dispersed in distilled water is set to the value of $\sigma = 72.86 \times 10^{-3}\,\mathrm{N/m}$ for air bubbles dispersed in water at a temperature of 20° C given by Pallas and Harrison (1990). According to Kosior et al. (2014), the addition of $1 \times 10^{-3}\,\mathrm{kg/mol}$ n-octanol to the distilled water leads to a reduction of the surface tension to $\sigma = 51.5 \times 10^{-3}\,\mathrm{N/m}$ in the contaminated case. The Hamaker constant is set to $A_\mathrm{H} = 3.7 \times 10^{-20}\,\mathrm{J}$, which corresponds to the value for water molecules interacting in a vacuum (Israelachvili, 2011).

The initial film heights estimated by Eq. (7.38) are depending on the collision velocity and, thus, vary for each impact on the free surface. For example, in case of the small clean bubble the initial film thickness is $h_\mathrm{i} = 2.97 \times 10^{-4}\,\mathrm{m}$ and $h_\mathrm{i} = 7.60 \times 10^{-5}\,\mathrm{m}$ for the first and second collision, respectively. The initial thickness of the large clean bubble

varies between $h_\mathrm{i} = 1.01 \times 10^{-3}\,\mathrm{m}$ and $1.20 \times 10^{-4}\,\mathrm{m}$ for the first and the third approach, respectively. For the contaminated bubble the corresponding values are $h_\mathrm{i} = 1.78 \times 10^{-4}\,\mathrm{m}$ and $1.44 \times 10^{-7}\,\mathrm{m}$. Similarly, the respective critical thicknesses are given by Eq. (7.39) and read $h_\mathrm{crit} = 1.89 \times 10^{-8}\,\mathrm{m}$ and $h_\mathrm{crit} = 2.15 \times 10^{-8}\,\mathrm{m}$ for the smaller and the larger clean bubbles and $h_\mathrm{crit} = 2.33 \times 10^{-8}\,\mathrm{m}$ for the contaminated bubble.

Since $\mathcal{LESOCC}$ works with dimensionless variables, the aforementioned quantities have to be made dimensionless utilizing suitable reference values. In the present case of a single bubble rising in a stagnant liquid, the fluid velocity is zero. Hence, the reference values are arbitrarily chosen based on the case of the low-Re bubble-laden channel flow described in Section 10.1. The variables are summarized in Table 10.1. The dimensionless parameters of the present test case are given in Table 10.2.

Tab. 10.1. Arbitrarily chosen reference values used to make the simulation of the test case of single bubbles coalescing with a free surface dimensionless and the corresponding Reynolds number.

$u_\mathrm{ref}\,[\mathrm{m/s}]$	$L_\mathrm{ref}\,[\mathrm{m}]$	$\nu\,[\mathrm{m^2/s}]$	Re
7.5×10^{-3}	20×10^{-3}	1×10^{-6}	150

Tab. 10.2. Dimensionless parameters of the test case of single bubbles coalescing with a free surface.

g^*	A_H^*	σ^*		d_b^*		
		clean	cont.	small clean	large clean	contaminated
3488	8.2×10^{-14}	64.76	45.78	0.05	0.074	0.066

10.4 Bubble Column

In order to further investigate the present coalescence model, a second test case in the form of a bubble column filled with a liquid at rest is considered (Hoppe and Breuer, 2018). The bubble column is of cylindrical shape with a diameter of $d_\mathrm{c} = 0.05\,\mathrm{m}$, which is used as the reference length in the following. The column is assumed to be filled with water ($\nu = 10^{-6}\,\mathrm{m^2/s}$, $\rho_\mathrm{f} = 10^3\,\mathrm{kg/m^3}$) up to a dimensionless height of $h_\mathrm{c}^* = h_\mathrm{c}/d_\mathrm{c} = 30$, see Fig. 10.1 depicting the setup of the test case. Mono-disperse bubbles are released uniformly distributed over the entire cross-sectional area of the column in the height $h_\mathrm{r}/d_\mathrm{c}$ between 4 and 5 above the bottom. Due to the buoyancy force, the bubbles rise upwards, thereby, inducing a flow in the column. The average flow velocity over the cross-section is however zero. Therefore, the reference velocity is arbitrarily chosen to be $u_\mathrm{ref} = 7.07 \times 10^{-2}\,\mathrm{m/s}$ resulting in a Reynolds number of $\mathrm{Re} = u_\mathrm{ref}\,d_\mathrm{c}/\nu_\mathrm{f} = 3535$. Note that

the aforementioned values (d_c, h_c, u_{ref}, Re) are based on the downward bubble column experiment by Majumder et al. (2006).

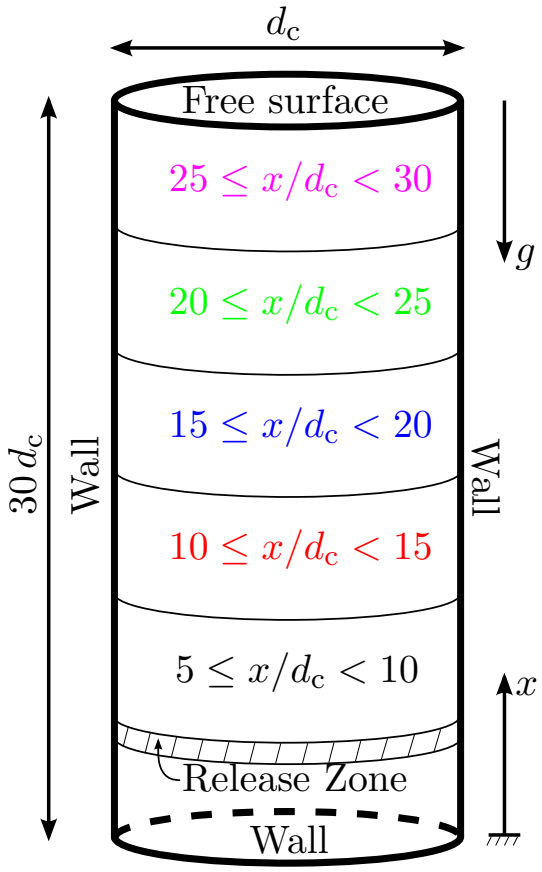

Fig. 10.1. Schematic sketch of the bubble column and the definition of specific regions for the evaluation. Taken from Hoppe and Breuer (2018).

The column is confined by a wall (no-slip boundary condition) at the bottom and the lateral area. At the top a free surface is assumed, see Sections 3.3.2 and 4.2.1 for details how the fluid and the bubbles are described at this boundary. Note that in contrast to the free surface setup described in Section 10.3, the bubbles are not assumed to rebound from the free surface but to leave the domain. In other words, the bubbles are removed from the computational domain, when they reach the top of the column. The domain is discretized by a curvilinear, block-structured grid consisting of a total of 9.2×10^6 control volumes split into five patches with 200 cells used in the direction of the pipe axis. A cross-section of the grid depicting the grid point distribution and the five blocks is shown in Fig. 10.2. The grid is chosen to be equidistant in the streamwise direction resulting in a dimensionless grid spacing of $\Delta x^* = 0.15$. In the radial direction the first cell center is located at a dimensionless distance of $\Delta r^* = 4.65 \times 10^{-4}$ from the wall. In order to assess the grid resolution in wall coordinates, a fully developed turbulent pipe flow at the same Reynolds number of Re = 3535 is assumed, which corresponds to a Reynolds

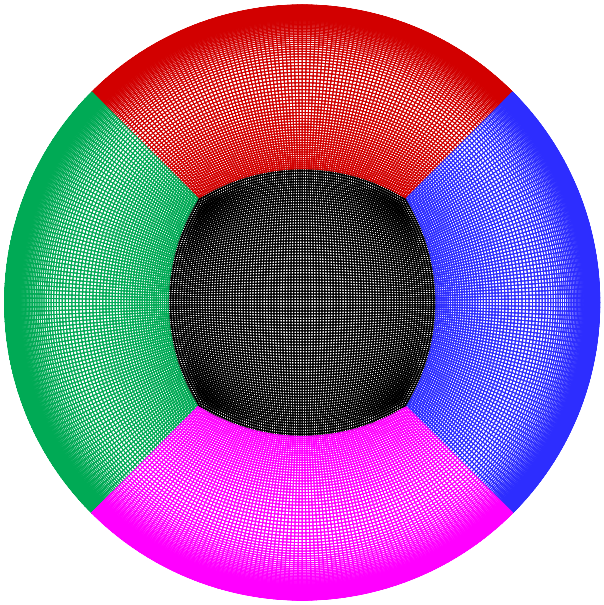

Fig. 10.2. Sketch of the cross-section of the grid applied for the present test case. The five patches are visualized by different colors.

number of $\mathrm{Re}_\tau = u_\tau\, d_\mathrm{c}/\nu_\mathrm{f} = 236$ based on the wall-shear stress velocity. Consequently, the resolution in streamwise direction corresponds to $\Delta x^+ = 35.4$ and a distance of $\Delta r^+ = 0.1$ for the first cell center from the wall in radial direction. Hence, the grid is sufficiently fine fulfilling the requirements for a wall-resolved LES by Piomelli and Chasnov (1996). The grid is only refined towards the lateral wall but not towards the bottom. Since the bubbles are released far away from this boundary, the non-refined grid is not critical. Again, the subgrid-scale model by Smagorinsky (1963) is applied, where the model constant is $C_\mathrm{S} = 0.065$ and the van Driest damping near solid walls is taken into account. In order to account for the unresolved scales of the flow and their effect on the bubbles the extended Langevin subgrid-scale model (Chapter 6) is applied. The dimensionless time step of the simulation is set to $\Delta t\, u_\mathrm{ref}/d_\mathrm{c} = 5 \times 10^{-4}$.

The dimensionless density of the bubbles is again set to $\rho_\mathrm{b}/\rho_\mathrm{f} = 1.3 \times 10^{-3}$. The dimensionless gravitational acceleration in the axial direction of the column is $g_x^* = g_x\, d_\mathrm{c}/u_\mathrm{ref}^2 = -98.13$. Similar to Section 10.3, a Hamaker constant of $A_\mathrm{H} = 3.7 \times 10^{-20}\,\mathrm{J}$ (Israelachvili, 2011) is applied, which corresponds to $A_\mathrm{H}^* = A_\mathrm{H}/(\rho_\mathrm{f}\, u_\mathrm{ref}^2\, d_\mathrm{c}^3) = 5.92 \times 10^{-17}$ in dimensionless form. A constant dimensionless volume flux of the bubbles of $\dot{Q}_\mathrm{b}^* = 1.89 \times 10^{-4}$ is assumed. In the present thesis, two different sizes of the inserted mono-disperse bubbles are considered: One case with small primary bubbles of $d_\mathrm{pb,small} = 125\,\mu\mathrm{m}$ and a second case with a larger diameter of $d_\mathrm{pb,large} = 156\,\mu\mathrm{m}$. These diameters correspond to $d_\mathrm{pb,small}^* = d_\mathrm{pb,small}/d_\mathrm{c} = 2.5 \times 10^{-3}$ and $d_\mathrm{pb,large}^* = d_\mathrm{pb,large}/d_\mathrm{c} = 3.12 \times 10^{-3}$ in dimensionless form. The dimensionless volumes are $V_\mathrm{pb,small}^* = 8.18 \times 10^{-9}$ and $V_\mathrm{pb,large}^* = 1.59 \times 10^{-8}$, respectively. Hence, in order to achieve the desired volume flux, 11 of the small or 6 of the large gas bubbles are released at each time step, respectively. As mentioned before, these are randomly distributed over the cross-section and the height in the range

$4 \leq x/d_c \leq 5$. For both bubble sizes the effect of clean and contaminated surface conditions is investigated. As in the investigation by Hoppe and Breuer (2018), a surface tension of $\sigma = 72.86 \times 10^{-3}\,\mathrm{N/m}$ (Pallas and Harrison, 1990) corresponding to $\sigma^* = \sigma/(\rho_f\, u_{ref}^2\, d_c) = 0.292$ is assumed. Remember that the initial film thickness and the critical film thickness are estimated by Eqs. (7.38) and (7.39) for each individual collision, respectively. In all cases the normal restitution coefficient for the bubble-bubble collisions $e_{n,b}$ is set to unity, while the remaining coefficients $e_{t,b}$, $\mu_{st,b}$ and $\mu_{kin,b}$ are all set to zero. Similarly, the restitution and friction coefficients of the bubble-wall collisions are set to $e_{n,w} = 1$, $e_{t,w} = \mu_{st,w} = \mu_{kin,w} = 0$. Thus, bubbles are reflected at the walls without any loss.

In order to ensure a fully developed system (flow and bubble distribution), the bubbles are allowed to disperse in the column for a dimensionless time period of $\Delta T\, u_{ref}/d_c = 187.5$ after the release of the first bubbles. Afterwards, statistics are averaged over a dimensionless period of time of $\Delta T\, u_{ref}/d_c = 150$, which is sufficiently to obtain stable statistics, i.e., it was verified that all graphs shown in Section 11.3.2 retain their form independently of the averaging period.

Lastly, it is worth mentioning that up to about 600,000 bubbles are simultaneously present in the bubble column. Nevertheless, the computational time spent for the coalescence model is not high, i.e., only 1 to 2% of the total CPU-time is required for the prediction of the collisions and the estimation of the coalescence. Overall, about 11 to 14% of the total CPU-time is required for the description of the dispersed phase, i.e., for the tracking of the bubbles, the prediction of bubble-wall and bubble-bubble collisions and the estimation of the bubble feedback on the fluid.

10.5 Turbulent Jet Flow

Lastly, the bubble breakup model (Chapter 8) is assessed by tracking the evolution of bubbles inserted into an unsteady spatially evolving jet flow (Hoppe and Breuer, 2020). The setup is based on the experiments by Martínez-Bazán et al. (1999a,b), who observed the breakup of bubbles injected into a fully developed jet flow. The water jet in the experiment discharges from the bottom vertically upwards into a hexagonal tank with a height of $h_t = 1.8\,\mathrm{m}$ and a minimal diameter (separation distance of the parallel sides) of $d_{t,m} = 0.597\,\mathrm{m}$. At the top of the tank the water is allowed to overflow minimizing the appearance of recirculation of fluid caused by the high-momentum jet flow. The diameter of the jet nozzle used by Martínez-Bazán et al. (1999a,b) is $d_j = 3 \times 10^{-3}\,\mathrm{m}$. The corresponding exit velocity of the jet is set to $u_0^E = 17\,\mathrm{m/s}$ resulting in a jet Reynolds number of $\mathrm{Re}_j^E = u_0^E\, d_j/\nu_f = 51,000$, where $\nu_f = 1 \times 10^{-6}\,\mathrm{m^2/s}$ again denotes the kinematic viscosity of water. However, it has to be noted that in the experiments by Martínez-Bazán et al. (1999a,b) the bubbles are injected into the jet flow through a tube with a diameter of $d_t = 1.5 \times 10^{-3}\,\mathrm{m}$, which passes through the center of the jet nozzle. Consequently, the open section of the jet, where fluid can exit the nozzle, is reduced. The diameter of the open section is given by $d_{j,o} = (d_j^2 - d_t^2)/(d_j + d_t) = 1.5 \times 10^{-3}\,\mathrm{m}$ (Martínez-Bazán, 2018). Hence, the jet Reynolds number based on the exit velocity u_0^E, the open section diameter $d_{j,o}$ and the kinematic viscosity ν_f is $\mathrm{Re}_{j,o}^E = 25,500$ (Martínez-Bazán et al., 1999a,b). Furthermore,

note that a jet flow exiting a nozzle of diameter d_j, but without taking the tube through the center of the nozzle into account, requires a lower flow velocity u_0 in order to ensure that the mass flow rate is equivalent to the experiment by Martínez-Bazán et al. (1999a,b). Based on the ratio of the area of the open section of the jet and the total area of the complete nozzle, the required velocity can be determined to be $u_0 = u_0^\mathrm{E}(d_\mathrm{j}^2 - d_\mathrm{t}^2)/d_\mathrm{j}^2 = 12.75\,\mathrm{m/s}$ resulting in a jet Reynolds number of $\mathrm{Re_j} = u_0\,d_\mathrm{j}/\nu_\mathrm{f} = 38,250$. Since the inner tube is not taken into account in the simulations, the latter definition is used in the present study.

The air bubbles are injected into the flow through a needle mounted at the end of the aforementioned tube at an axial position of $x/d_\mathrm{j} = 15$. The diameter of the needle is $d_\mathrm{n} = 0.394 \times 10^{-3}\,\mathrm{m}$. The gas flow rate is set to $Q_\mathrm{g} = 1.2 \times 10^{-6}\,\mathrm{m^3/s}$ corresponding to a superficial gas velocity of $u_\mathrm{g} = 9.84\,\mathrm{m/s}$. Figure 10.3 displays the bubble size distribution in form of a volumetric probability density function provided by Martínez-Bazán et al. (1999a,b) at an axial position of $x/d_\mathrm{j} = 16.1$. Additionally, the dimensionless mean diameter of the released bubbles $\langle d^*_\mathrm{b,rel}\rangle = \langle d_\mathrm{b,rel}\rangle/d_\mathrm{j} = 0.514$ is included. In dimensional form the mean bubble diameter is given by $\langle d_\mathrm{b,rel}\rangle = 1.542 \times 10^{-3}\,\mathrm{m}$. The void fraction of the bubbles is less than $\Phi_\mathrm{V} = 10^{-5}$ in the experiments. Hence, according to Martínez-Bazán et al. (1999a,b) bubble-bubble collisions rarely happen making coalescence negligible. The individual bubbles and their respective sizes are identified by a camera system using a white light source positioned opposite to the camera to uniformly illuminate the flow. Due to the low volume fraction of the bubbles and the corresponding low number of simultaneously present bubbles in the flow, the overlapping of bubbles is not a difficulty for the image processing technique (Martínez-Bazán et al., 1999a,b).

In the present simulations the experimental setup by Martínez-Bazán et al. (1999a,b) is represented by a fully developed jet flow. However, the tube passing through the center of the jet nozzle in the experiment is neglected for the sake of simplicity. This choice is further motivated by the fact that Martínez-Bazán et al. (1999a,b) also assumed the flow to be unaffected by the tube during their analysis of the results. The Reynolds number of the jet flow is thus set to 38,250 based on the same diameter d_j of the circular nozzle as in the experiments and a jet velocity ensuring an equivalent mass flow as in the experiments. In order to prevent numerical problems due to entrainment at the outer boundaries, the jet is placed in a weak co-flow. Hence, the walls of the tank are not taken into account, since they are far away from the region of interest. The corresponding dimensionless velocity of the co-flow is set to $u^*_\mathrm{co} = u_\mathrm{co}/u_0 = 0.025$ with $u_0 = 12.75\,\mathrm{m/s}$ the above defined reduced exit velocity of the jet. Consequently, the Reynolds number is based on the jet diameter d_j and the velocity difference $\Delta u = u_\mathrm{jc} - u_\mathrm{co} = u_0$ between the center of the jet and the co-flow in order to ensure a $\mathrm{Re_j} = \Delta u\,d_\mathrm{j}/\nu_\mathrm{f} = 38,250$. Therefore, the dimensionless velocity in the center of the jet is $u^*_\mathrm{jc} = u_\mathrm{jc}/u_0 = 1.025$

The computational domain containing the jet flow is of cylindrical form with a dimensionless radius of $R/d_\mathrm{j} = 10$, which is sufficient to prevent an influence of the lateral boundary on the jet flow. The total length of the computational domain in the downstream direction is $x_\mathrm{d}/d_\mathrm{j} = 40$ allowing a comparison of the simulation results with the experimental data by Martínez-Bazán et al. (1999a,b). The setup is depicted in Fig. 10.4. The flow is resolved by a block-structured grid containing about 10.65×10^6 control volumes. The grid is split into 5 geometric blocks with one block placed in the middle and four geometric

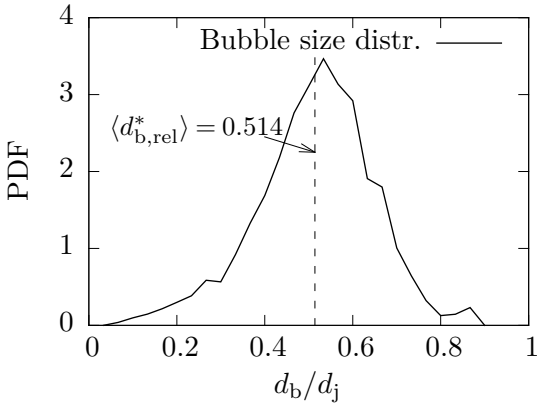

Fig. 10.3. Volumetric size distribution of the bubbles in the experiments by Martínez-Bazán et al. (1999a,b) shortly after their release from the air injection needle at an axial position of $x/d_\mathrm{j} = 16.1$. Taken from Hoppe and Breuer (2020).

blocks arranged around the central block building an O-grid arrangement similar to the one used in Section 10.4, see Fig. 10.2. In order to resolve the large velocity gradients occurring in the shear layer of the jet, the grid is refined in this region, especially near the inflow plane. In streamwise direction a total of 512 control volumes with increasing size according to a geometric series is used. The first cell in streamwise direction has a size of $\Delta x_1/d_\mathrm{j} = 2.5 \times 10^{-2}$, while the stretching factor is set to $q \approx 1.0039$ resulting in a size of the last cell of $\Delta x_{512}/d_\mathrm{j} = 0.1784$. The dimensionless sizes of the control volumes of the central block are set to 1.2×10^{-2} in the y- and the z-direction. In the surrounding O-grid blocks a total number of $N_\mathrm{r} = 120$ and $N_\theta = 160$ control volumes are used in the radial and circumferential direction, respectively. A geometric stretching of the control volumes is applied in the radial direction with a stretching factor of 1.0044 up to a radius of $r/d_\mathrm{j} = \sqrt{y^2 + z^2}/d_\mathrm{j} \leq 0.8$. This results in a cell size of $\Delta r/d_\mathrm{j} = 1.35 \times 10^{-2}$ in the radial direction at $r/d_\mathrm{j} = 0.5$. Note that at this radial position the largest velocity gradients are found in the shear layer close to the inflow plane. Afterwards, the stretching factor is increased to 1.0444 for $r/d_\mathrm{j} > 0.8$. In the circumferential direction the cells are chosen to be equally spaced with a size of $\Delta\theta = 2\,\pi/N_\theta \approx 3.93 \times 10^{-2} = 2.25°$.

This grid is the result of a series of preliminary studies, which were performed to gradually improve the applied mesh. For example, during these studies the shape of the computational domain was adjusted by testing a truncated cone geometry. Other adjustments involve the overall size of the computational cells or the stretching factors of the geometric series. One important factor largely improving the quality of the simulation results was the stretching of the cell size in the streamwise direction allowing for a refined resolution close to the jet inlet, where the largest velocity gradients are located. Overall, the present grid described above yields reliable results for the turbulent jet flow (see Section 11.4.1) with a reasonable numerical effort.

At the base of the cylindrical computational domain an inflow boundary condition is applied for the continuous phase. The dimensional streamwise velocity profile supposed to

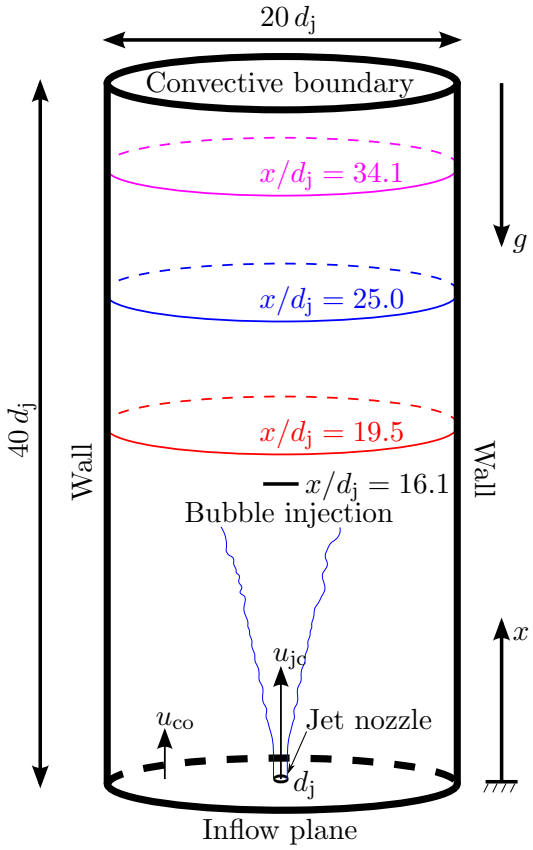

Fig. 10.4. Schematic sketch of the jet flow and the definition of the axial planes at which the bubble size distributions are averaged.

mimic a jet flow shortly downstream of a typical nozzle exit is approximated by (Michalke, 1984; Morris, 1976):

$$u(r) = u_{co} + \frac{u_0}{2}\left[1 - \tanh\left\{b\left(\frac{r}{r_j} - \frac{r_j}{r}\right)\right\}\right], \tag{10.1}$$

where $r_j/d_j = 1/2$ is the dimensionless radius of the nozzle. Note that this is a steady profile without any fluctuations. The factor $b = 0.25\, r_j/\delta_2$ depends on the momentum thickness δ_2 of the shear layer at the inlet of the jet (Michalke, 1984) with the exact magnitude of δ_2/r_j varying throughout the literature. Here, the common value (see, e.g., Bogey and Bailly, 2006; Gohil et al., 2011, 2014) of $\delta_2/r_j = 1/20$ is applied. At the lateral surface of the domain a no-slip boundary condition is used with the velocity set to the velocity of the co-flow. Lastly, at the outlet at the top surface of the domain a convective boundary condition is applied. The corresponding dimensionless convection velocity is set to the fixed value of $u^*_{conv} = 0.21$, which is slightly larger than the average centerline velocity of a jet flow at a distance of $x/d_j = 40$ downstream of the nozzle, i.e., $u^*_c = 0.161$ (Hussein et al., 1994). The dimensionless time step is set to $\Delta t^* = \Delta t\, u_0/d_j = 6 \times 10^{-3}$. In order to ensure a fully developed flow field, the jet flow is allowed to evolve for a dimensionless

time period of $\Delta T\, u_0/d_\mathrm{j} = 250$. Afterwards, bubbles are continuously released into the flow. A dimensionless time period of $\Delta T\, u_0/d_\mathrm{j} = 300$ is sufficient for obtaining a fully developed bubble distribution allowing to start taking the averaged statistics of the breakup parameters over a dimensionless time interval of $\Delta T\, u_0/d_\mathrm{j} = 6000$. The influence of the unresolved scales on the resolved large eddies is described by the subgrid-scale model of Smagorinsky (1963), where the Smagorinsky '*constant*' is dynamically determined by the procedure of Germano et al. (1991) and Lilly (1992), see Section 3.2.2.

The bubbles are inserted at an axial position of $x/d_\mathrm{j} = 16.1$, i.e., the position where Martínez-Bazán et al. (1999a,b) provide the bubble size distribution. In order to account for the radial migration of the bubbles after their detachment from the tip of the injection needle, the bubbles are uniformly distributed within a dimensionless radius of $r^*_\mathrm{in} = 0.2$ from the centerline of the jet. The diameter of the inserted bubbles is randomly chosen based on the probability density function (Fig. 10.3) provided by Martínez-Bazán et al. (1999a,b) using an inverse sampling method (Devroye, 1986). Individual bubbles are inserted with a dimensionless time lag of $\Delta T_\mathrm{int}\, u_0/d_\mathrm{j} = 6.798$ between successive releases, i.e., a single bubble is released every 1133 time steps. Based on the dimensionless average size of $\langle d^*_\mathrm{b,rel}\rangle = 0.514$ of the released bubbles, the dimensionless volumetric flow rate $Q^*_\mathrm{b} = \pi\,\langle d^*_\mathrm{b,rel}\rangle^3/(6\,\Delta T^*_\mathrm{int})$ of the bubbles is 1.046×10^{-2}. Hence, the flow rate of the bubbles is equal to the experimental value given by Martínez-Bazán et al. (1999a,b). The time lag $\Delta T_\mathrm{int}\, u_0/d_\mathrm{j}$ between successive releases of the bubbles results in a total of 883 bubbles being inserted into the flow during the averaging time period, with an average number of about 100 bubbles simultaneously present in the computational domain. The initial velocity of the bubbles is set to the actual fluid velocity at the position of the bubble center. This measure is based on the observations by Martínez-Bazán et al. (1999a,b), who found that the mean bubble velocity is equal to the mean fluid velocity shortly after the detachment of the bubbles from the needle.

Martínez-Bazán et al. (1999a,b) used regular tap water in the experiments. Hence, the surface of the bubbles is contaminated by surfactants. Consequently, the surface condition of contaminated bubbles is used for the simulations. The surface tension of the bubbles is again $\sigma = 72.86\,\mathrm{N/m}$ corresponding to a dimensionless value of $\sigma^* = \sigma/(\rho_\mathrm{f}\, u_0^2\, d_\mathrm{j}) = 1.49 \times 10^{-4}$. For the purpose of studying the effect of variations of the bubble properties, additional simulations applying a 30 percent smaller surface tension of $\sigma = 51.0 \times 10^{-3}\,\mathrm{N/m}$ and a 70 percent larger value of $\sigma = 123.86 \times 10^{-3}\,\mathrm{N/m}$ are performed. The corresponding dimensionless values are $\sigma^* = 1.05 \times 10^{-4}$ and 2.54×10^{-4}, respectively. The previously applied Hamaker constant of $A_\mathrm{H} = 3.7 \times 10^{-20}\mathrm{J}$ (Israelachvili, 2011) is re-used, which is $A^*_\mathrm{H} = A_\mathrm{H}/(\rho_\mathrm{f}\, u_0^2\, d_\mathrm{j}^3) = 8.43 \times 10^{-18}$ in dimensionless form. The dimensionless gravitational acceleration of $g^* = g\, d_\mathrm{j}/u_0^2 = 1.8103 \times 10^{-4}$ is directed against the mean flow direction of the jet.

Again, the extended Langevin model described in Chapter 6 is applied to estimate the influence of the unresolved subgrid scales on the bubbles. The collisions of bubbles with each other are again treated by the hard-sphere model described in Section 5.3 with the normal restitution coefficient $e_\mathrm{n,b}$ set to unity and the remaining coefficients set to zero. In all simulations the coalescence of the bubbles is taken into account by the extended coalescence model (Chapter 7), except for one specific case, where the model is deactivated

in order to study the effect of coalescence. Since the bubbles are contaminated, the relative transition time $t_\mathrm{j}/t_\mathrm{c}$ between inertia-controlled and viscous-dominated drainage has to be determined for the estimation of coalescence. The added-mass coefficient C'_m is variably adjusted according to Eq. (7.7). Additionally, it has to be remarked that the idle time Δt_idle during which the daughter bubbles formed by a breakup event cannot further break up is estimated by the breakup time $\Delta t_\mathrm{break,etf}$ described by Eq. (8.32). As already described in Section 8.2.4, this approach yields the best agreement with the experimental results by Martínez-Bazán et al. (1999a,b).

Lastly, it has to be ensured that the bubbles injected into the flow are actually within the inertial subrange of turbulence, since otherwise Eq. (8.7) would not be valid, see Section 8.1, where this was critically annotated. Pope (2000) provides the well-known relation $l_\mathrm{ID} \approx 60\,\eta$ for the boundary between the inertial and the dissipative subranges of turbulence, where η is the Kolmogorov length scale. Using the experimental measurement of $\eta/d_\mathrm{j} \approx 2 \times 10^{-3}$ (Sadeghi et al., 2018) for jet flows at Reynolds numbers of $\mathrm{Re} = 30,000$ and $50,000$, one can estimate that the boundary is given for a length of about $l_\mathrm{ID}/d_\mathrm{j} = 0.12$. Consequently, the majority of the presently considered bubbles have a larger diameter and, therefore, are within the inertial subrange of turbulence.

11 Results and Discussion

Finally, the results obtained with the present Euler–Lagrange simulation framework for the tracking of bubbles are presented. Firstly, the numerical methodology used for the tracking of the bubbles is validated in Section 11.1. Afterwards, in Section 11.2 the influence of the Langevin subgrid-scale model is investigated for channel flows laden with bubbles and particles. Next, the coalescence model is validated by comparison with experimental results of bubble coalescence with a free surface in Section 11.3. Subsequently, the turbulent two-phase flow in a bubble column is considered to further investigate bubble coalescence. Lastly, in Section 11.4 the breakup model is validated based on bubble breakup experiments in a turbulent jet flow. Note that the main results of these investigations were recently published in international journals, see, Breuer and Hoppe (2017, 2018) for the subgrid-scale model, Hoppe and Breuer (2017, 2018) for the coalescence model and Hoppe and Breuer (2020) for the breakup model.

11.1 Validation of the Lagrangian Tracking Methodology for Bubbles

Prior to the present thesis, the simulation methodology for the case of solid particles has been validated several times (see, e.g., Alletto and Breuer, 2012; Breuer and Alletto, 2012; Breuer et al., 2012). For the bubble-laden case the simulation methodology has been first validated in Breuer and Hoppe (2017) by a comparison with the results of Molin et al. (2012). This validation, which is based on the setup described in Section 10.1, is presented here again.

Molin et al. (2012) carried out a DNS of a downward channel flow using a pseudo-spectral solver with Lagrangian bubble tracking. Owing to the lack of bubble-laden DNS predictions relying on resolved bubbles of sufficient number, the uncertainties of these reference data due to the drag force models or the interpolation schemes used for the transfer of the forces between the Eulerian and the Lagrangian frame of reference as demonstrated in Garg et al. (2007, 2009) have to be accepted.

The validation of the numerical methodology applying the fine grid (Section 10.1) starts in Fig. 11.1 with the mean streamwise velocities of the continuous and the dispersed phases. Both the results for the fluid (Fig. 11.1(a)) and the bubbles (Fig. 11.1(b)) agree very well with the reference results by Molin et al. (2012). In the present simulation the streamwise fluid velocity is slightly overestimated in the center of the channel ($y^+ > 20$). Consequently, minor differences in the streamwise bubble velocity compared with the reference data are observable. Note that the streamwise velocity profiles of the bubbles do not extend below $y^+ = 2$ in the present case and below $y^+ = 5$ in the case of Molin et al.

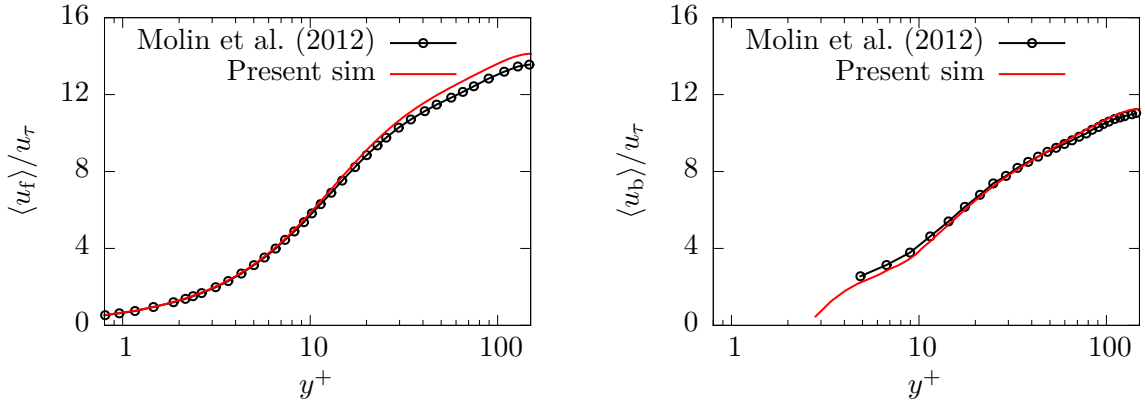

(a) Fluid. **(b)** Bubbles.

Fig. 11.1. Comparison of the mean streamwise velocities of the present simulation with the results of Molin et al. (2012). Taken from Breuer and Hoppe (2017).

(2012), because no bubbles are found near the walls during the averaging. The reason behind this observation is the shear-driven lift force, which is directed away from the walls in the case of the downward channel flow. Hence, the bubbles are pushed towards the center of the channel limiting the presence of bubbles close to the walls to rare instances. The minor differences between the present simulation and the results of Molin et al. (2012) can be attributed to a different formulation of the lift coefficient. In the present study the model of Legendre and Magnaudet (1998) described in Section 4.1.1.3 is applied, whereas Molin et al. (2012) based the formulation of the lift force on the models by Kurose and Komori (1999) and McLaughlin (1991). Furthermore, Molin et al. (2012) include the effects of wall-induced lift forces (Takemura and Magnaudet, 2003). Since wall-induced lift forces are depending on the distance of the bubble to the wall, these lift forces can easily be incorporated into a code specialized for Cartesian grids. However, in a general-purpose code relying on curvilinear grids like $\mathcal{LESOCC}$ utilized in the present thesis, the numerical costs associated with considering these forces are very large. Therefore, they are omitted here. For more details see Molin et al. (2012).

The effect of the different formulations of the lift force described above is also visible in Fig. 11.2, which depicts the volume fraction Φ_V of the bubbles normalized by the total averaged volume fraction of the bubbles $\Phi_{\mathrm{V,tot}} = 1 \times 10^{-4}$ in the channel. Both the present results as well as the data by Molin et al. (2012) show that nearly no bubbles are present close to the walls. Hence, the normalized volume fraction $\Phi_\mathrm{V}/\Phi_{\mathrm{V,tot}}$ is zero in the vicinity of the walls. Then a steep increase in the volume fraction is visible, which occurs at $y^+ \approx 7$ slightly further away from the wall in the present study compared with $y^+ \approx 5$ in the reference by Molin et al. (2012). Again this observation is most likely due to the different lift coefficients mentioned above. However, note that the slope of the volume fraction is equal in both cases. A very good agreement with the results of Molin et al. (2012) is reached in the center of the channel for $y^+ > 20$. For example, the local peak of the volume fraction at about $y^+ = 30$ shown by Molin et al. (2012) is well predicted by the present simulation. It is worth mentioning that this peak of the volume fraction found

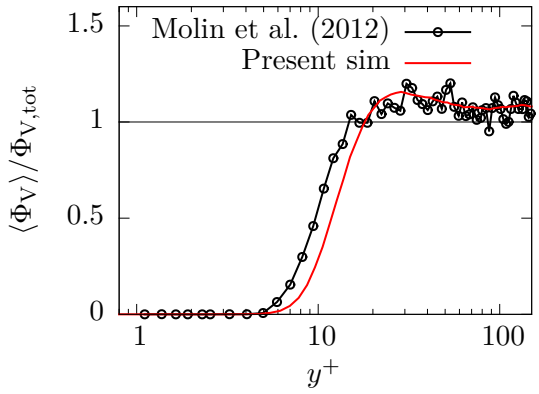

Fig. 11.2. Comparison of the bubble volume fraction of the present simulation with the results of Molin et al. (2012). Taken from Breuer and Hoppe (2017).

immediately after the steep increase of $\Phi_V/\Phi_{V,tot}$ was also observed by Lu and Tryggvason (2006), who performed a fully-resolved DNS of a channel flow ($Re_b = 1893$) laden with 72 bubbles of a diameter $d_b = 1.53\,mm$. Additionally, the magnitude of the volume fraction in the center of the channel ($\Phi_V/\Phi_{V,tot} = 1.1$) closely agrees with the reference data by Molin et al. (2012). Again, Lu and Tryggvason (2006) found a similarly increased volume fraction in the center of the channel ($\Phi_V/\Phi_{V,tot} = 1.3$) albeit for a slightly different configuration.

To complete the comparison of the present results with the reference case of Molin et al. (2012), the velocity fluctuations of both the fluid and the bubbles are displayed in Fig. 11.3. The results of the streamwise velocity fluctuations of the fluid and the bubbles are compared in Figs. 11.3(a) and (b), respectively. Again, a high level of agreement with the DNS results is achieved by the present simulation, both for the fluid and the bubble velocity fluctuations. A slight deviation is found around the peaks of the velocity fluctuations of the fluid, which is also present in the statistics of the bubbles. The same is true for the wall-normal fluid fluctuations shown in Fig. 11.3(c) and the respective fluctuations of the bubble velocity displayed in Fig. 11.3(d). Lastly, the spanwise velocity fluctuations of the fluid and the bubbles are displayed in Figs. 11.3(e) and (f). The comparison of these fluctuations has not been presented in Breuer and Hoppe (2017) for the sake of brevity. It is obvious that the spanwise velocity fluctuations of the fluid (Fig. 11.3(e)) and the bubbles (Fig. 11.3(f)) exhibit similar features as the fluctuations in the other two spatial directions, i.e., the peaks of the respective fluctuations are predicted slightly too low in the present simulation compared with the reference data by Molin et al. (2012). In the center of the channel the spanwise fluctuations of the fluid and the bubbles are slightly too large. It has to be noted that the large peaks of the spanwise bubble fluctuations close to the walls displayed in Fig. 11.3(f) are not a physical phenomenon, but are caused by the very small number of bubbles contributing to the on-the-fly averaging process in the near-wall regions. The shear stresses $\langle u'_{f/b}\, u'_{f/b}\rangle/u_\tau^2$ of the fluid and the bubbles are omitted here, since Molin et al. (2012) did not provide any reference data.

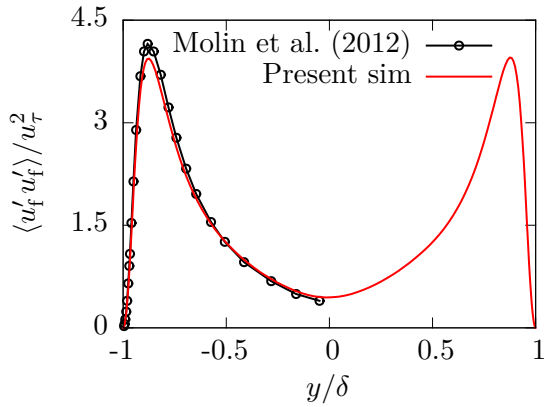

(a) Fluid, streamwise direction.

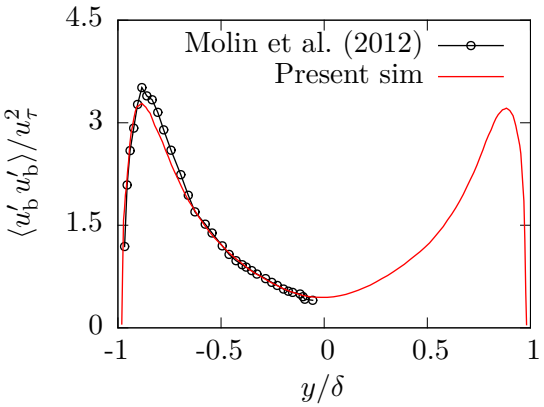

(b) Bubbles, streamwise direction.

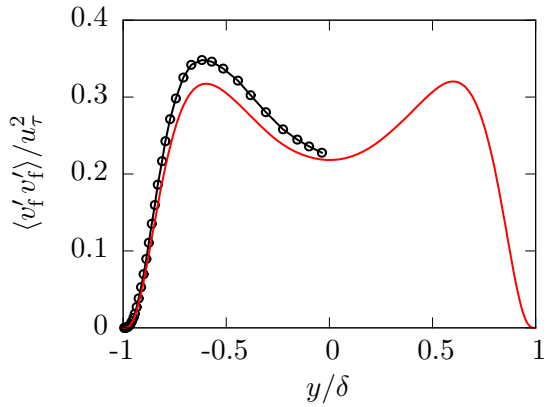

(c) Fluid, wall-normal direction.

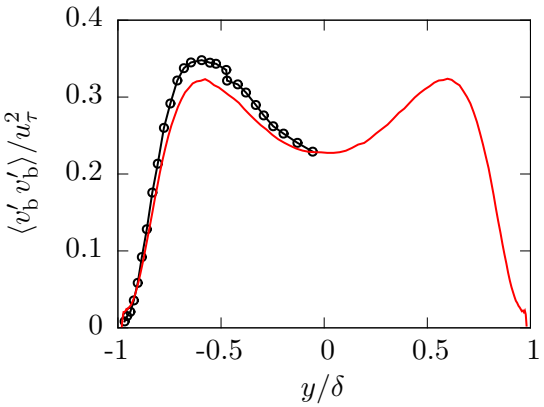

(d) Bubbles, wall-normal direction.

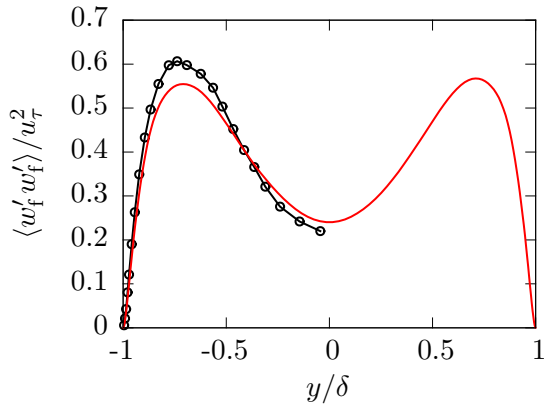

(e) Fluid, spanwise direction.

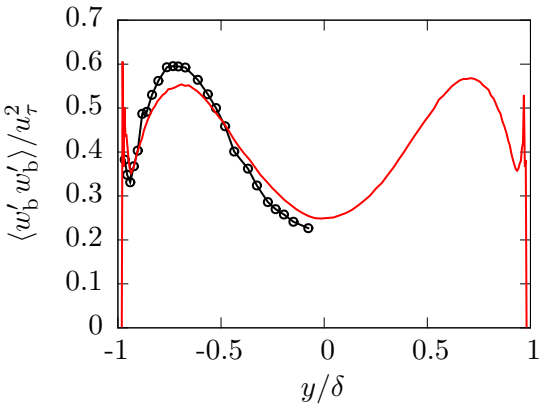

(f) Bubbles, spanwise direction.

Fig. 11.3. Comparison of the velocity fluctuations of the present simulation with the results by Molin et al. (2012). Partially taken from Breuer and Hoppe (2017).

Summarizing the comparison of the results obtained with the present numerical methodology and the DNS data by Molin et al. (2012) in Figs. 11.1 to 11.3, an overall satisfactory agreement is achieved. The minor deviations to the reference case are probably caused by the fact that the DNS by Molin et al. (2012) relies on a pseudo-spectral solver, which provides an improved accuracy but is limited to relatively simple geometries, whereas $\mathcal{LESOCC}$ is based on a finite-volume method for arbitrary curvilinear grids, see Chapter 9. The validation study shows that the entire simulation methodology used in the present thesis including the Lagrangian bubble tracking (Section 4.1) and the two-way coupling (Section 5.2) correctly predicts the motion of bubbles dispersed in turbulent flows.

11.2 Influence of the Subgrid-Scale Model on Dispersed Two-Phase Flows

In the present section the influence of the enhanced Langevin subgrid-scale model (Chapter 6) on dispersed turbulent flows is investigated. In the present thesis two different cases are considered. First, a bubble-laden channel flow at a relatively low Reynolds number ($\mathrm{Re}_\tau = 150$) is analyzed. The setup of this test case is described in Section 10.1. Afterwards, a particle-laden channel flow with a Reynolds number of $\mathrm{Re}_\tau = 644$ is considered, see Section 10.2 for the description of the test case. The reasons for choosing such a completely different setup are manifest. Firstly, since the effect of the subgrid-scale model is found to be marginal at low Re, the investigation on the influence at a higher fluid Reynolds number is meaningful. Secondly, the effect of a different density ratio of the fluid to the dispersed entities and a smaller particle size on the results predicted by the subgrid-scale model should be evaluated. Thirdly, it is important to test the Langevin subgrid-scale model first proposed by Breuer and Hoppe (2017) for the case of solid particles, since the model is also applied to particle-laden flows by other authors at PfS (see, e.g., Almohammed, 2018; Almohammed and Breuer, 2016b; Breuer and Khalifa, 2019a,b).

11.2.1 Bubble-Laden Channel Flow

The influence of the subgrid-scale modeling on the dispersion of the bubbles is investigated by applying the extended Langevin-based subgrid-scale model derived in Section 6.3 and the trivial model (Eq. (6.39) in Section 6.4) to the downward channel flow described in Section 10.1. Additionally, a simulation without a model for the subgrid scales affecting the dispersed phase is carried out. In contrast to the validation of the numerical methodology presented in Section 11.1 a coarser grid is applied for the prediction of the fluid flow. Additionally, the Smagorinsky model is activated now. Note that the results presented in this section have been published earlier in Breuer and Hoppe (2017).

In Fig. 11.4 averaged results of the three cases with the Langevin model, with the trivial model and without a model for the subgrid-scale fluctuations seen by the bubbles are compared. Figure 11.4(a) displays the mean streamwise bubble velocities normalized by the constant wall-shear stress velocity u_τ, while Fig. 11.4(b) shows the corresponding ratio of the averaged volume fractions of the bubbles to the total averaged volume fraction.

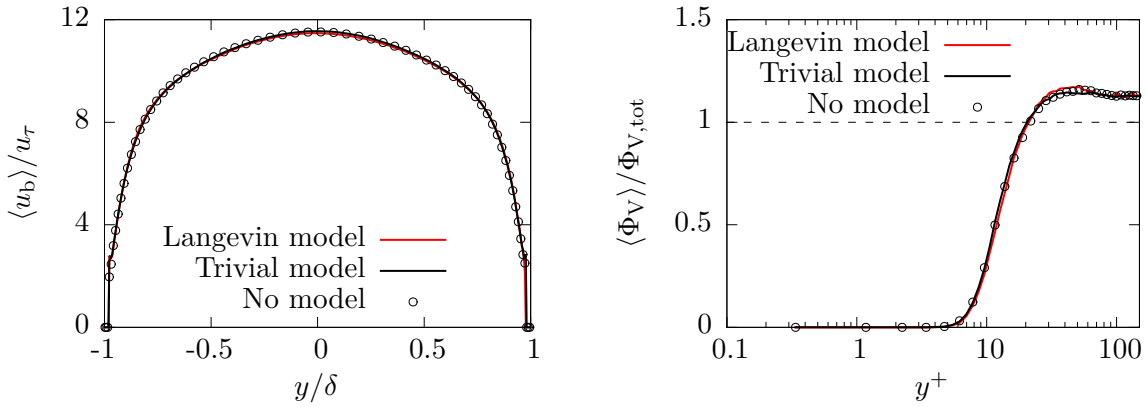

(a) Streamwise bubble velocity. **(b)** Bubble volume fraction.

Fig. 11.4. Averaged bubble properties obtained by the extended Langevin model, the trivial model and without a model for the subgrid scales seen by the bubbles. Taken from Breuer and Hoppe (2017).

It is obvious that no perceptible difference between the results of the three cases exist. Consequently, on average neither the trivial subgrid-scale model nor the Langevin model have a visible influence on the bubble velocity. Similarly, the distribution of the bubbles in the channel is not affected by the subgrid scales in this case.

In Fig. 11.5 the velocity fluctuations of the bubbles in streamwise (Fig. 11.5(a)), wall-normal (Fig. 11.5(b)) and spanwise (Fig. 11.5(c)) direction are shown together with the Reynolds shear stress (Fig. 11.5(d)). Again, only minor deviations between the three cases are observed. Especially, the fluctuations in the streamwise and spanwise directions as well as the Reynolds shear stress of the bubbles are nearly unaffected by the subgrid-scale modeling. Only the fluctuations in the wall-normal direction exhibit a minor effect of the subgrid scales, i.e., the wall-normal fluctuations of the bubbles slightly increase if the Langevin model or the trivial model are applied. Summarized, in the present case the influence of the subgrid scales on the statistics of the bubbles is marginal. Consequently, the influence of the subgrid-scale modeling on the averaged velocities and the corresponding fluctuations of the fluid due to two-way coupling is also negligibly small. Hence, the results are omitted here for the sake of brevity.

In order to investigate why both the Langevin and the trivial model have such a minor influence, the subgrid scales estimated by the Langevin model are analyzed. The mean subgrid-scale velocities of the fluid seen by the bubbles in streamwise, wall-normal and spanwise direction and the corresponding fluctuations are displayed in Figs. 11.6(a) and (b), respectively. Note that these quantities are obtained by the averaging process for the bubbles described in Section 9.4. Hence, every time a bubble is found in a certain control volume, the subgrid-scale fluid velocities seen by the bubble and the corresponding fluctuations are arithmetically averaged up based on Eqs. (9.54) and (9.55) and stored at the center of the corresponding cell. Afterwards, one-dimensional averages are obtained by Eqs. (9.56) and (9.58) during the post-processing. Nevertheless, the results are partially not smooth, especially in the near-wall regions, where only a few bubbles are present.

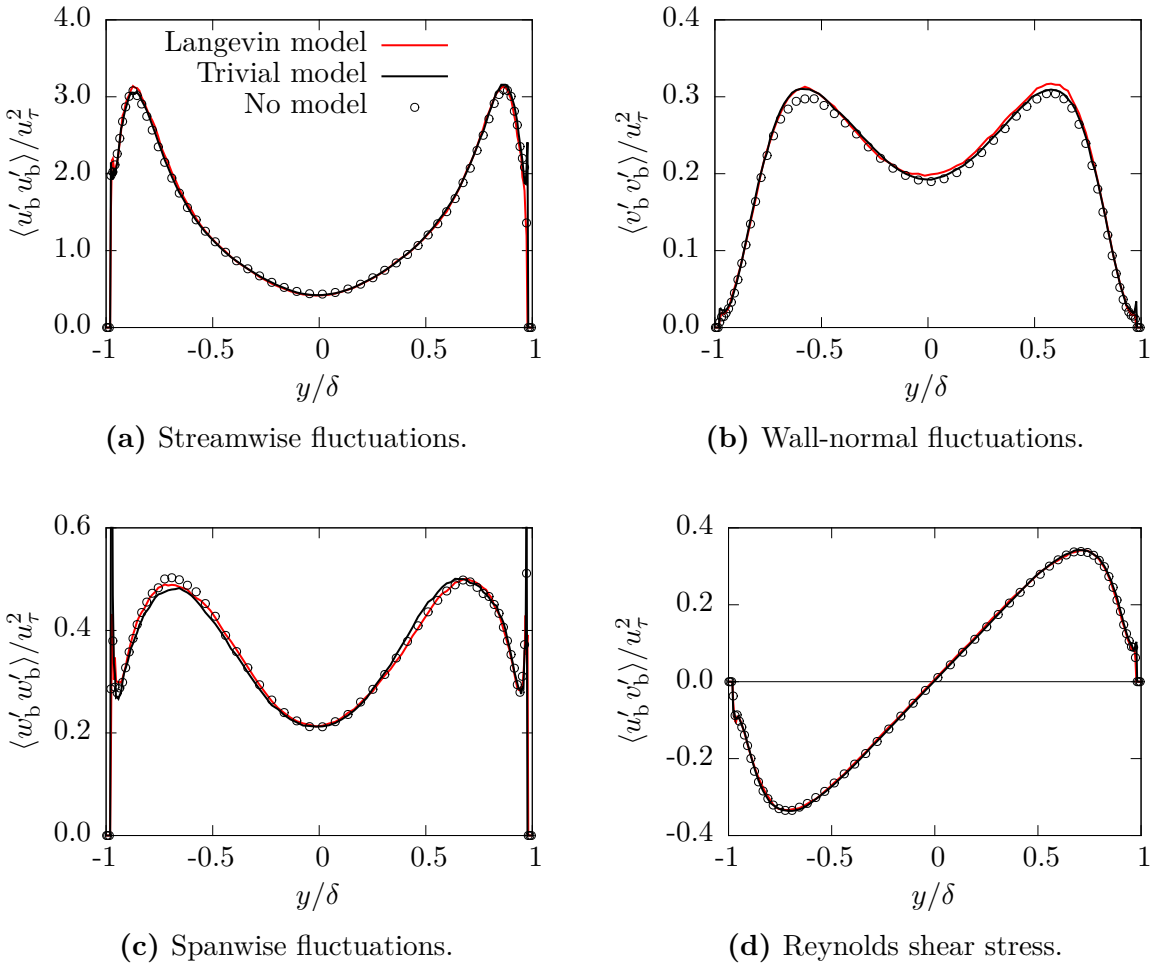

(a) Streamwise fluctuations.

(b) Wall-normal fluctuations.

(c) Spanwise fluctuations.

(d) Reynolds shear stress.

Fig. 11.5. Velocity fluctuations in the streamwise, wall-normal and spanwise directions and the Reynolds shear stress of the bubbles. Taken from Breuer and Hoppe (2017).

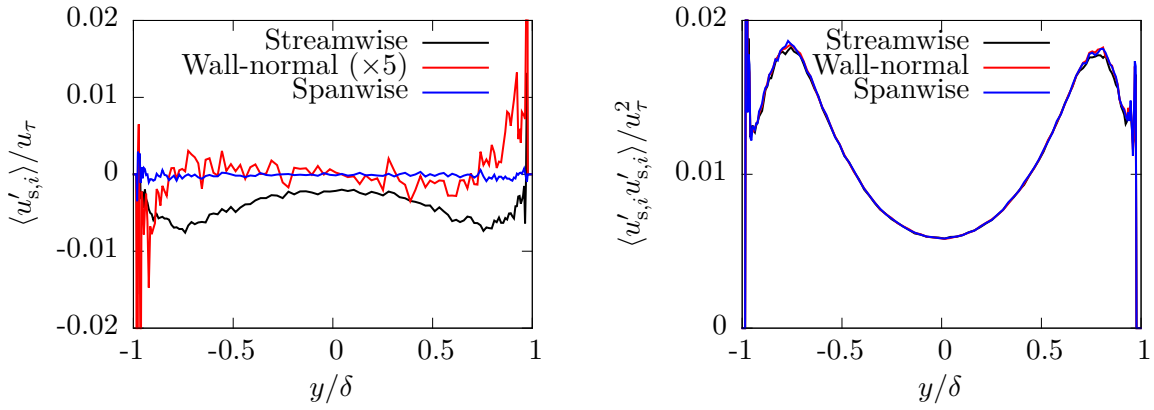

(a) Averaged velocities.

(b) Fluctuations.

Fig. 11.6. Statistics of the subgrid-scale velocities seen by the bubbles obtained by the extended Langevin model. Taken from Breuer and Hoppe (2017).

It is apparent from Fig. 11.6(a) that the mean streamwise subgrid-scale velocities seen by the bubbles are non-vanishing but are largely negative over the channel width. According to Eq. (5.2) provided in Section 5.1 the subgrid-scale velocities obtained by the Langevin model are added to the resolved fluid velocity at the position of the bubbles. Hence, the overall negative streamwise subgrid-scale velocity depicted in Fig. 11.6(a) implies that on average the total streamwise fluid velocity seen by the bubbles is smaller than the resolved fluid velocity. It is important to note that the mean values of the subgrid-scale velocities obtained by the extended Langevin subgrid-scale model have to tend to zero according to Eq. (6.5), if the averaging is done in an Eulerian frame of reference, i.e., at fixed positions in the flow. However, this is not necessarily the case for the above described averaging process, where averages are taken at the bubble positions. Since bubbles can preferentially accumulate in regions where the flow exhibits specific characteristics, this circumstance leads to a preferred sampling of the data in these zones. In case of the non-vanishing streamwise subgrid-scale velocity shown in Fig. 11.6(a), one can deduce that the bubbles preferentially accumulate in regions where the corresponding velocity component predicted by the extended Langevin subgrid-scale model is on average negative. Similar results have been reported by Bianco et al. (2012), who investigated the unresolved velocities which a subgrid-scale model should provide. Bianco et al. (2012) also considered a channel flow at $\mathrm{Re}_\tau = 150$, but one that is laden with solid particles of Stokes numbers equal to or larger than unity. Furthermore, only the drag force was acting on the particles, i.e., the lift force, the gravitational force and the buoyancy force were neglected making a detailed comparison impossible. However, the averaged negative streamwise subgrid-scale velocity obtained from the extended Langevin model is consistent with the results of Bianco et al. (2012).

The averaged subgrid-scale velocity in wall-normal direction is also non-zero, see Fig. 11.6(a). Note that this component is magnified by a factor of five for the sake of a better visibility of the results. It can be seen from Fig. 11.6(a) that the subgrid-scale velocity seen by the bubbles is directed towards the walls for the regions $y/\delta < -0.8$ and $y/\delta > 0.8$, respectively. The opposite is true further away from the walls, i.e., in the center of the channel the velocity seen by the bubbles is directed away from the walls. Comparing this observation with the wall-normal component of the subgrid-scale velocity fluctuations of the fluid depicted in Fig. 11.6(b) reveals that the wall-normal velocity of the subgrid scales is directed away from the regions of the largest fluctuations, since the maxima of the fluctuations are located at $y/\delta \approx \pm 0.8$. In other words, the wall-normal subgrid-scale velocity seen by the bubbles is directed away from the regions of the highest turbulent kinetic energy of the subgrid scales, see Fig. 11.7(a). Bianco et al. (2012) showed in their study that the wall-normal velocity of the subgrid scales should have the opposite behavior. However, it has to be remembered that Bianco et al. (2012) used particles for their study, which have completely different properties ($\mathrm{St} \geq 1$), and considered solely the drag force. Yet, in contrast to the streamwise and spanwise directions of the flow, the lift force plays an important role for the behavior of the bubbles in wall-normal direction. Hence, a final conclusion on the present results in wall-normal direction is not possible.

The last component shown in Fig. 11.6(a) is the spanwise subgrid-scale velocity, which is the only component which does not exhibit any special characteristics but tends to zero

over the whole width of the channel. Here, Bianco et al. (2012) found a similar behavior confirming that the profile of the subgrid-scale velocity component in spanwise direction is reasonable.

Despite the non-zero profiles of the streamwise and wall-normal subgrid-scale velocities in Fig. 11.6(a), their magnitudes are small compared with the resolved velocities of the fluid and the bubble velocities. Comparing Figs. 11.4(a) and 11.6(a) it can be seen that the streamwise subgrid-scale velocity seen by the bubbles is approximately three orders of magnitude smaller than the bubble velocity in the corresponding direction. Hence, in the present case the influence of the subgrid scales is negligibly small. The same observation can be made for the fluctuations of the subgrid-scale velocities depicted in Fig. 11.6(b). Comparing the streamwise fluctuations of the subgrid-scale velocities with the corresponding bubble fluctuations (Fig. 11.5(a)) shows that the fluctuations of the subgrid scales are roughly two orders of magnitude smaller than the bubble fluctuations. Similarly, the wall-normal fluctuations of the unresolved scales estimated by the extended Langevin model are more than one order of magnitude smaller than the corresponding bubble fluctuations. Since this difference is not as pronounced as in the streamwise direction, the bubble fluctuations in the wall-normal direction are slightly affected by the subgrid-scale model, see Fig. 11.5(b).

Note that all fluctuations of the subgrid-scale velocities are nearly identical in Fig. 11.6(b). This stems from the assumption of homogeneous and isotropic turbulence made by Pozorski and Apte (2009) for the derivation of their model. Since the presently used extended Langevin model by Breuer and Hoppe (2017) is based on the model by Pozorski and Apte (2009), anisotropy is not accounted for. The different time scales of the subgrid scales, $\tau'_{\mathrm{L},\parallel}$ and $\tau'_{\mathrm{L},\perp}$ defined in Eq. (6.11), are distinguished for including the crossing-trajectory effect and the continuity effect (see Sections 2.1 and 6.2). However, both effects are bubble effects and not related to the anisotropy of the turbulent flow.

Lastly, the distribution of the averaged turbulent kinetic energy $\langle k_{\mathrm{SGS}}^{\mathrm{seen}} \rangle = \langle u'_{\mathrm{s},i}\, u'_{\mathrm{s},i} \rangle / 2$ of the subgrid scales seen by the bubbles is investigated in Fig. 11.7. In Fig. 11.7(a) $\langle k_{\mathrm{SGS}}^{\mathrm{seen}} \rangle$ is compared with the averaged unresolved kinetic energy of the fluid $\langle k_{\mathrm{SGS}} \rangle$, which is estimated by Eq. (6.18). In Fig. 11.7(b) the comparison of $\langle k_{\mathrm{SGS}}^{\mathrm{seen}} \rangle$ with the averaged resolved turbulent kinetic energy $\langle k_{\mathrm{res}} \rangle = \langle u'_{\mathrm{f},i}\, u'_{\mathrm{f},i} \rangle / 2$ of the fluid is depicted. Figure 11.7(a) demonstrates that the extended Langevin model estimates the correct level of the turbulent kinetic energy of the subgrid scales. This observation agrees with the results by Cernick et al. (2015), who performed an a-priori analysis using DNS data combined with a similar Langevin model. The difference of the turbulent kinetic energy of the subgrid scales seen by the bubbles $\langle k_{\mathrm{SGS}}^{\mathrm{seen}} \rangle$ and the unresolved turbulent kinetic energy of the fluid $\langle k_{\mathrm{SGS}} \rangle$ is probably caused by the averaging process. The former quantity is determined solely at the positions of the bubbles and is then averaged up along the homogeneous directions of the channel flow, while the latter is calculated over the complete fluid domain by averaging the values of k_{SGS} stored in all computational cells in the streamwise and spanwise directions. Therefore, the fact that $\langle k_{\mathrm{SGS}}^{\mathrm{seen}} \rangle$ and $\langle k_{\mathrm{SGS}} \rangle$ do not overlap leads to the conclusion that the bubbles preferentially accumulate in regions of higher turbulent kinetic energy yielding larger values of $\langle k_{\mathrm{SGS}}^{\mathrm{seen}} \rangle$ on average. In Fig. 11.7(b) it can be seen that the subgrid-scale turbulent kinetic energy seen by the bubbles is negligibly small compared with the resolved

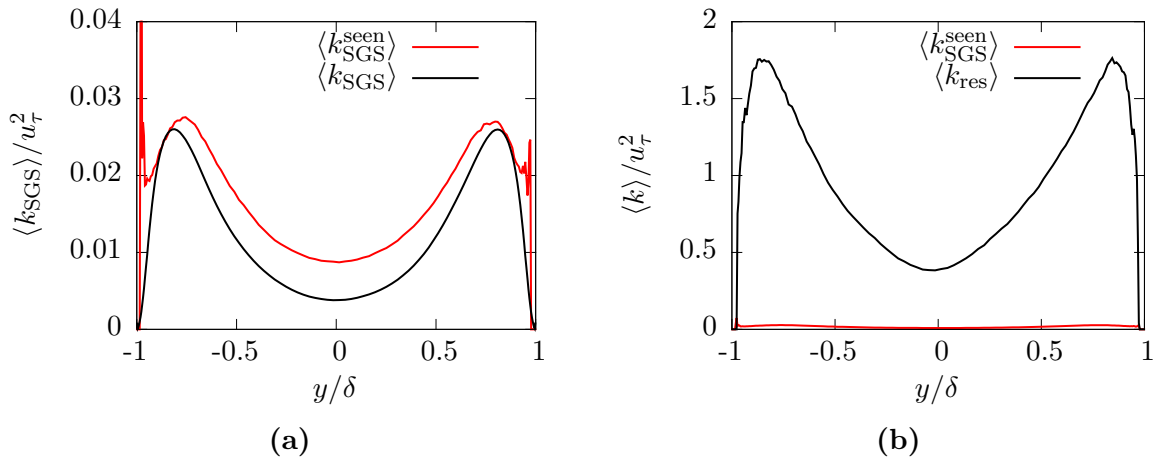

Fig. 11.7. Comparison of the turbulent kinetic energy of the subgrid scales seen by the bubbles with (a) the unresolved and (b) the resolved turbulent kinetic energy of the fluid. Taken from Breuer and Hoppe (2017).

turbulent kinetic energy $\langle k_{res} \rangle$ of the fluid. This explains why the subgrid-scale velocities and fluctuations shown in Fig. 11.6 are so small compared with the corresponding bubble properties (Figs. 11.4 and 11.5) and, therefore, the overall small influence of the extended Langevin model in the present case.

11.2.2 Particle-Laden Channel Flow with a Fixed Stokes Number

As already mentioned before, the model for the subgrid scales seen by the dispersed phase is further investigated in a second channel flow at $\mathrm{Re_b} = 11,900$ laden with solid particles, cf. Section 10.2 for details of the setup. The idea is to assess the influence of the subgrid-scale modeling under completely different conditions (Breuer and Hoppe, 2017). First, the impacts of the extended Langevin model and the trivial model are compared with results obtained without any subgrid-scale model for the case of solid particles with a Stokes number of $\mathrm{St}^+ = 1.67$.

In Fig. 11.8 the resulting statistics of the particles obtained with the Langevin model, the trivial model and without a model for the subgrid scales are shown. Note that in contrast to Section 11.2.1 the bulk velocity of the fluid flow u_{bulk} is used for the normalization of the velocities and not the wall-shear stress velocity u_τ. The reason is that in the particle-laden channel flow the mass flow is fixed (varying pressure gradient) and, hence, the bulk velocity is kept constant regardless of the mass loading. Figure 11.8(a) depicts the mean streamwise particle velocity for the three cases. Again, no visible difference between the results obtained with the Langevin or the trivial subgrid-scale model and without a model exists. Similarly, the results of the velocity fluctuations of the particles in streamwise direction depicted in Fig. 11.8(b) are nearly identical. Here, the extended Langevin model leads to a slight increase of the peaks of the fluctuations. The average particle velocity in the wall-normal direction is depicted in Fig. 11.8(c). It is apparent that the trivial subgrid-scale model does not affect the velocity distribution compared

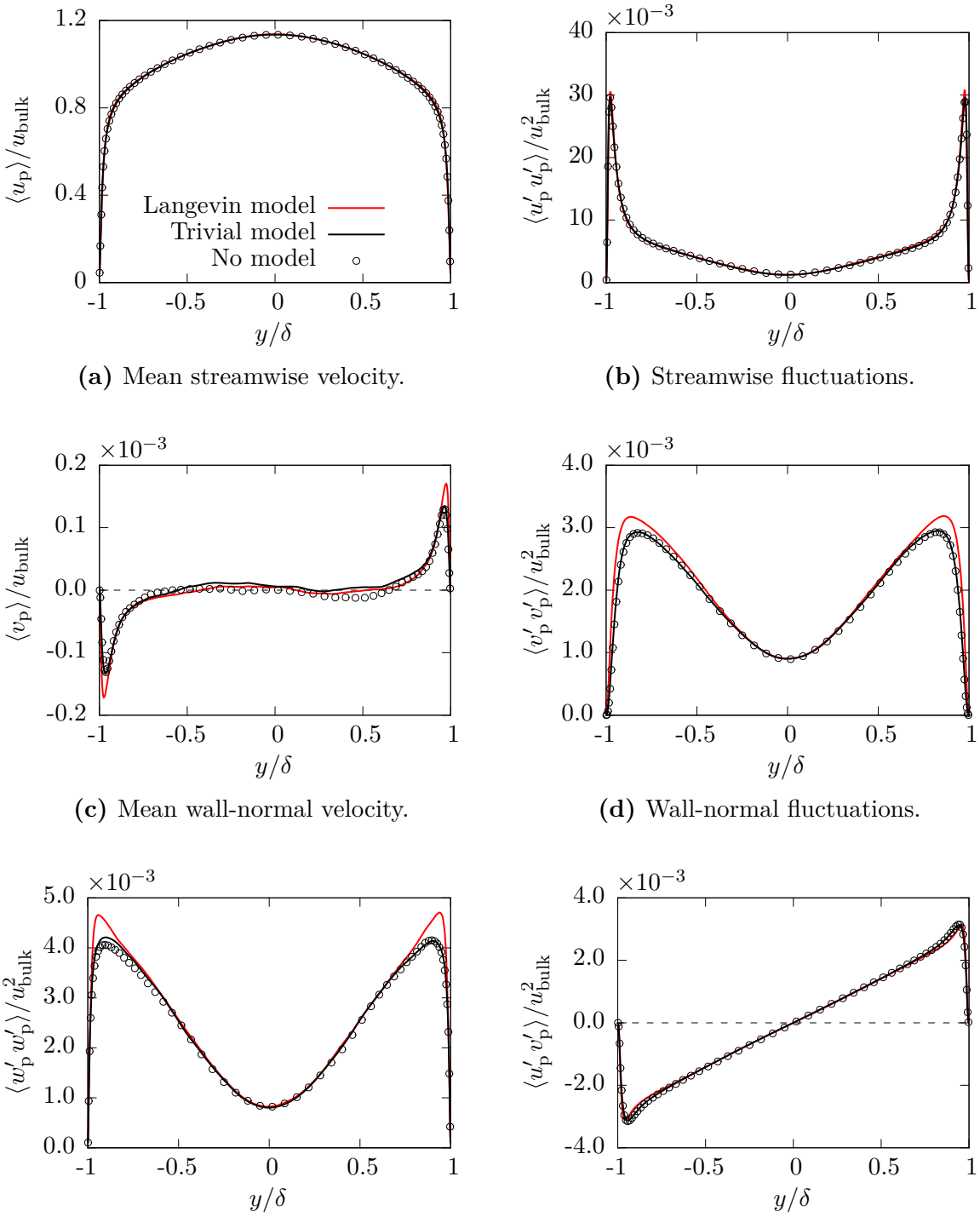

(a) Mean streamwise velocity.

(b) Streamwise fluctuations.

(c) Mean wall-normal velocity.

(d) Wall-normal fluctuations.

(e) Spanwise fluctuations.

(f) Reynolds shear stress.

Fig. 11.8. Statistics of the particles obtained with the Langevin subgrid-scale model, the trivial subgrid-scale model and without any model for the subgrid scales. Taken from Breuer and Hoppe (2017).

with the case without any model. However, applying the Langevin model leads to a visibly increased wall-normal velocity towards the walls in the direct vicinity of the wall. The corresponding velocity fluctuations shown in Fig. 11.8(d) exhibit a similar effect, i.e., the wall-normal velocity fluctuations are enhanced around the peaks near the solid walls compared with the results obtained with the trivial and without any model. Likewise, the peak fluctuations in the spanwise direction (Fig. 11.8(e)) are increased by the Langevin model, while the trivial model has no apparent influence on the spanwise fluctuations compared with the case without a model. Lastly, it is obvious from Fig. 11.8(f) that the Reynolds shear stress between the streamwise and the wall-normal components is only marginally affected by the subgrid-scale modeling. The Langevin model moves the peaks of the Reynolds shear stress slightly closer to the wall, but it does not alter the magnitude of the peak value.

In summary, the results shown in Fig. 11.8 clearly demonstrate that the trivial subgrid-scale model does not affect the statistics of the particle velocities with respect to the results obtained without any model for the unresolved scales. However, the extended Langevin model devised by Breuer and Hoppe (2017) leads to a visible modification of the mean velocities and the corresponding fluctuations of the particles. Yet, the overall influence is small despite the relatively high Reynolds number of the flow.

Although the influence of the subgrid scales on the averaged velocities of the particles is small, the subgrid-scale modeling significantly alters the distribution of the volume fractions in the vicinity of the solid walls depicted in Fig. 11.9. The application of the trivial subgrid-scale model leads to a twice as large volume fraction close to the walls compared with the case without any model for the unresolved scales. In case of the extended Langevin model the increase is even stronger, i.e., the volume fraction is by a factor of more than ten larger than for the case without any subgrid-scale model. The reason for this increase of the volume fraction close to the walls is caused by the augmented wall-normal velocity of the particles (Fig. 11.8(c)) directed towards the walls and the increased wall-normal fluctuations (Fig. 11.8(d)) observed for the Langevin model.

The increased volume fraction close to the walls agrees with the observations of Marchioli et al. (2008), who compared the results of a-priori and a-posteriori large-eddy simulations with the DNS of a particle-laden channel flow at $\mathrm{Re}_\tau = 150$. Marchioli et al. (2008) found that the filtering process in the a-priori and the a-posteriori LES reduces the volume fraction of the particles in the vicinity of the walls. Hence, a model for the unresolved scales of the flow seen by the particles should ideally compensate this filtering error. Figure 11.9 demonstrates that both the trivial and to an even larger extent the Langevin model counteract the decrease of the volume fraction close to the walls. It has to be noted that a direct comparison with the results of Marchioli et al. (2008) is not possible, since their study is based on a flow with a lower Reynolds number and neglects particle-particle collisions.

The increased volume fraction close to the walls has an important impact on two other physical phenomena, i.e., agglomeration and deposition of particles. For example, the application of the extended Langevin model leads to an increased number of inter-particle collisions caused by the denser particle distribution close to the walls. In the present case with the Langevin model the number of particle-particle collisions is found to be about

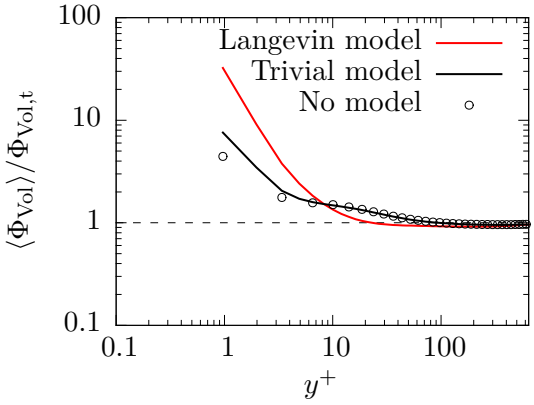

Fig. 11.9. Comparison of the volume fractions of the solid particles obtained by the extended Langevin subgrid-scale model, the trivial model and without any subgrid-scale model. In all cases the total average volume fraction is $\Phi_{\mathrm{V,tot}} = 6.78 \times 10^{-7}$. Taken from Breuer and Hoppe (2017).

6% higher than without a model for the unresolved scales, which is known to have a non-negligible effect on the agglomeration of particles (Almohammed, 2018; Almohammed and Breuer, 2016a). Since the agglomeration of solid particles is not the scope of the present work, this topic is not further pursued in the present thesis. However, Almohammed (2018) demonstrated that the application of the extended Langevin model by Breuer and Hoppe (2017) to an identical channel flow setup yields a significantly reduced agglomeration rate compared to the cases with the trivial model and without any model. Furthermore, the number of large agglomerates containing more than two primary particles is strongly reduced. According to Almohammed (2018) the physical mechanism responsible for these observations are the higher relative velocities between the collision partners due to the increased velocity fluctuations of the particles. Hence, while the particles are more likely to collide, the possibility for a successful agglomeration is reduced due to the augmented repulsive force and weaker cohesive force (Almohammed, 2018).

A similar effect of the Langevin model can be observed for the deposition of particles on the wall. For the purpose of investigating this phenomenon, additional simulations are carried out in the present study, including a particle-wall adhesion model by Almohammed and Breuer (2016b) accounting for van-der-Waals forces between dry, electrostatically neutral particles and the walls. The characteristic properties of the particles and the walls are taken from Almohammed and Breuer (2016b). The results of this investigation are summarized in Table 11.1 in form of the dimensionless frequencies of the particle-wall collisions $f_{\mathrm{col}}^{\mathrm{pw}\,*}$ and the deposition processes f_{dep}^{*}. In the present case of particles with $\mathrm{St}^{+} = 1.67$ the larger volume fraction near the wall in case of the Langevin model leads to a significantly increased number of particle-wall collisions compared with the case without a model. This translates to an augmentation of the collision frequency $f_{\mathrm{col}}^{\mathrm{pw}\,*}$ by more than two orders of magnitude (factor of 443.1) due to the Langevin model. At the same time, the deposition frequency f_{dep}^{*} increases by a factor of about 20 compared with the simulation without a subgrid-scale model for the dispersed phase. Hence, the

Tab. 11.1. Dimensionless frequencies of the particle-wall collisions $f_{\mathrm{col}}^{\mathrm{pw}\,*}$ and the deposition processes f_{dep}^{*} without a subgrid-scale model and with the extended Langevin subgrid-scale model. The frequencies $f_{\mathrm{col}}^{\mathrm{pw}\,*}$ and f_{dep}^{*} are defined by the number of particle-wall collisions $N_{\mathrm{col}}^{\mathrm{pw}}$ and deposition events N_{dep} within a dimensionless time interval (here $\Delta T^{*} = 100$) divided by ΔT^{*} expressing how many collisions and depositions take place in a dimensionless time unit, respectively. Note that for these additional simulations the elastic particle-wall collision model with friction is replaced by the particle-wall adhesion model (Almohammed and Breuer, 2016b). Taken from Breuer and Hoppe (2017).

St^{+}	$f_{\mathrm{col}}^{\mathrm{pw}\,*}$			f_{dep}^{*}		
	No model	Langevin model	Ratio	No model	Langevin model	Ratio
1.67	2.7×10^{2}	1.2×10^{5}	443.1	1.7×10^{2}	3.4×10^{3}	19.9
1.00	7.0×10^{1}	8.4×10^{4}	1197.9	5.2×10^{1}	2.8×10^{3}	55.4
0.10	8.7×10^{0}	3.1×10^{4}	3518.7	8.5×10^{0}	2.1×10^{3}	247.6

deposition rate $f_{\mathrm{dep}}^{*}/f_{\mathrm{col}}^{\mathrm{pw}\,*}$ decreases by applying the Langevin model: While about 63% of the wall collisions result in a deposition of the particle if no subgrid-scale model is used, the ratio $f_{\mathrm{dep}}^{*}/f_{\mathrm{col}}^{\mathrm{pw}\,*}$ drops to about 2.8% in the case with the Langevin model. Since the deposition model by Almohammed and Breuer (2016b) is to a great extend similar to the agglomeration model by Breuer and Almohammed (2015), the reason for this observation is likely to be similar to the reason for the reduced agglomeration probability due to the Langevin model found by Almohammed (2018). While the Langevin subgrid-scale model increases the number of particle-wall collisions by augmenting the volume fraction close to the walls, the collision velocity is also significantly enhanced, see Figs. 11.8(c) and (d). Thus, the repulsive force is larger if the extended Langevin model is applied reducing the likelihood for a successful deposition process.

In order to further investigate the reason for the effects of the present subgrid-scale model shown in Figs. 11.8 and 11.9 and Table 11.1, the subgrid-scale velocities seen by the particles and the associated fluctuations are depicted in Fig. 11.10. Note that the statistics are much smoother than in Fig. 11.6 for the bubble-laden case, since the number of particles is about 300 times larger than the number of bubbles. It is obvious from Fig. 11.10(a) that the streamwise subgrid-scale velocity estimated by the Langevin model has a similar appearance as the corresponding component obtained for the bubbles (Fig. 11.6(a)). The streamwise velocity shown in Fig. 11.10(a) is negative over nearly the complete channel width following the same characteristic profile visible for the case of the bubbles. The only exception is found in the direct vicinity of the walls, where positive peaks appear, which are not present in Fig. 11.6(a). Considering the fact that bubbles are seldom found in the direct vicinity of the walls due to the lift force and, consequently, the statistics are not smooth close to the walls, it is possible that this peak is a feature of the subgrid-scale velocities estimated by the extended Langevin model, which is simply not captured in the bubble case depicted in Fig. 11.6(a).

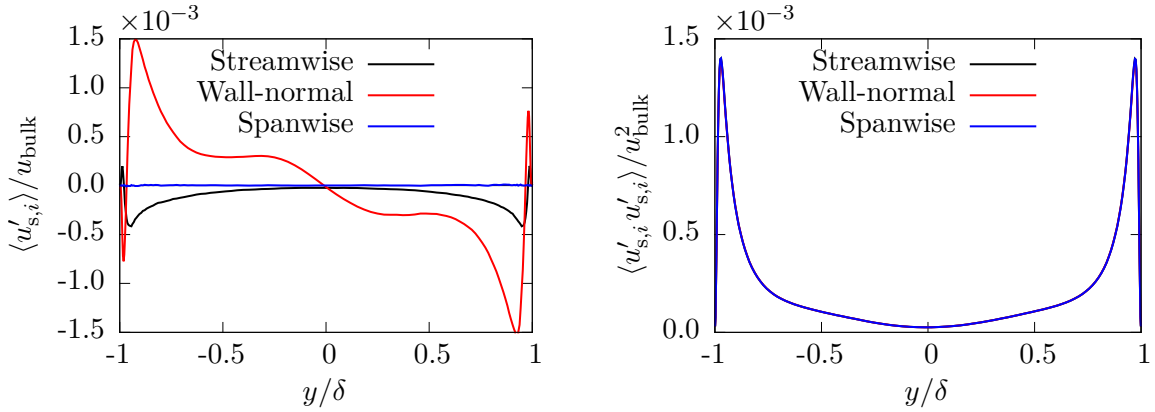

(a) Averaged velocities. **(b)** Fluctuations.

Fig. 11.10. Statistics of the subgrid-scale velocities seen by the particles obtained by the extended Langevin subgrid-scale model. Taken from Breuer and Hoppe (2017).

The wall-normal subgrid-scale velocity is now the largest of the three components. Note that in contrast to Fig. 11.6(a) the velocity component is not magnified in Fig. 11.10(a). The wall-normal component is fully anti-symmetric and non-zero over the complete width of the channel. In the direct vicinity of the walls a first local extremum of the subgrid-scale velocity pointing in the direction towards the walls is found. A second, larger extremum directed away from the walls is located slightly further away from the walls at $y/\delta = \pm 0.9$. Comparing these results with the fluctuations of the subgrid-scale velocities shown in Fig. 11.10(b), it becomes apparent that the mean wall-normal velocity seen by the particles is directed away from the location of the highest fluctuations corresponding to the highest turbulent kinetic energy of the subgrid scales, compare Fig. 11.11. Similar characteristics have been found for the case of the bubbles, see Section 11.2.1. The spanwise component of the subgrid-scale velocity is again tending to zero over the complete channel width. Furthermore, the fluctuations of the velocities of the unresolved scales (Fig. 11.10(b)) are nearly identical for all three spatial directions. The explanation for this behavior provided in Section 11.2.1 is valid for the present case as well.

Similar to the bubble case, a direct comparison with the results of Bianco et al. (2012) is difficult due to the fact that the latter considers a somewhat different setup, i.e., a lower Reynolds number of $\mathrm{Re}_\tau = 150$ and the important lift force is neglected in their study. Nevertheless, some conclusions can be drawn from the comparison of the results. Firstly, the mainly negative velocity of the unresolved scales in the streamwise direction are also found by Bianco et al. (2012) with the only exception of the small positive peaks very close to the walls in Fig. 11.10(a). Secondly, the spanwise component tends to zero in both the present study and the work by Bianco et al. (2012). Lastly, in the present case the wall-normal component is found to deviate from the results of Bianco et al. (2012). However, similar to the reasoning given for the case of a bubble-laden channel flow (Section 11.2.1), this discrepancy may be explained by the neglect of the lift force by Bianco et al. (2012).

Similar to Fig. 11.7, the distribution of the averaged turbulent kinetic energy of the unresolved scales seen by the particles $\langle k_{\mathrm{SGS}}^{\mathrm{seen}} \rangle$ over the channel width is shown in Fig. 11.11.

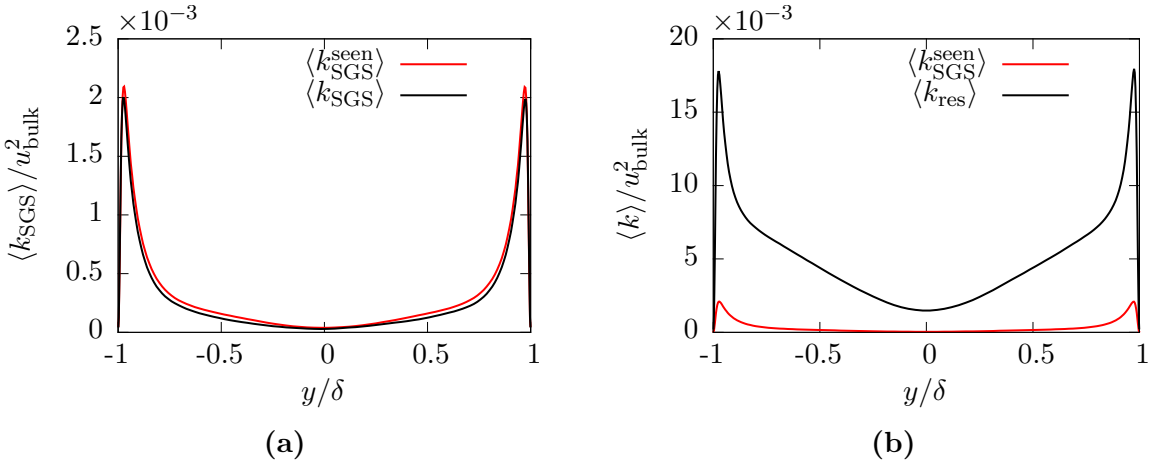

Fig. 11.11. Comparison of the turbulent kinetic energy of the subgrid scales seen by the particles with (a) the unresolved and (b) the resolved turbulent kinetic energy of the fluid. Taken from Breuer and Hoppe (2017).

The comparison of $\langle k_{\mathrm{SGS}}^{\mathrm{seen}} \rangle$ with the unresolved turbulent kinetic energy of the fluid $\langle k_{\mathrm{SGS}} \rangle$ estimated by Eq. (6.18) in Fig. 11.11(a) reveals that on average the profile of $\langle k_{\mathrm{SGS}}^{\mathrm{seen}} \rangle$ is very similar to $\langle k_{\mathrm{SGS}} \rangle$. Hence, in contrast to the bubble-laden case (Section 11.2.1), particles do not preferentially concentrate to a significant extent in regions of higher turbulent kinetic energy. The behavioral difference between bubbles and particles can be attributed to the much higher inertia of the solid particles, which prevents them from being as easily affected by the unresolved scales as the low-inertia bubbles. Figure 11.11(b) compares $\langle k_{\mathrm{SGS}}^{\mathrm{seen}} \rangle$ with the turbulent kinetic energy $\langle k_{\mathrm{res}} \rangle$ of the resolved scales showing that $\langle k_{\mathrm{SGS}}^{\mathrm{seen}} \rangle$ is much smaller than $\langle k_{\mathrm{res}} \rangle$ over the complete channel width. In more detail, the turbulent kinetic energy of the subgrid scales is on average less than 10% of the turbulent kinetic energy of the resolved scales explaining the globally rather small influence of the Langevin subgrid-scale model on the results.

11.2.3 Particle-Laden Channel Flow with a Varying Stokes Number

As a last investigation on the impact of the Langevin subgrid-scale model on the dispersed phase, the Stokes number of the solid particles is varied. In the particle-laden channel flow described in Section 11.2.2, the dispersed entities had a dimensionless diameter of $d_{\mathrm{p},1.76}^{*} = 2 \times 10^{-4}$ and a dimensionless density of $\rho_{\mathrm{p}}/\rho_{\mathrm{f}} = 1814$ yielding a Stokes number of $\mathrm{St}^{+} = 1.67$. Now, two additional simulations are carried out considering smaller particles ($d_{\mathrm{p},1.00}^{*} = 1.55 \times 10^{-4}$ and $d_{\mathrm{p},0.10}^{*} = 5 \times 10^{-5}$) with the same density ratio resulting in Stokes numbers of $\mathrm{St}^{+} = 1.00$ and $\mathrm{St}^{+} = 0.10$, respectively. Section 10.2 contains the details of the setup. The objective of the present section is to analyze how the Langevin subgrid-scale model impacts particles of varying Stokes number. Note that the trivial model is no longer considered in the following.

Figure 11.12 displays the velocities of the unresolved scales obtained by the extended Langevin model in streamwise and spanwise direction for the three particle Stokes numbers.

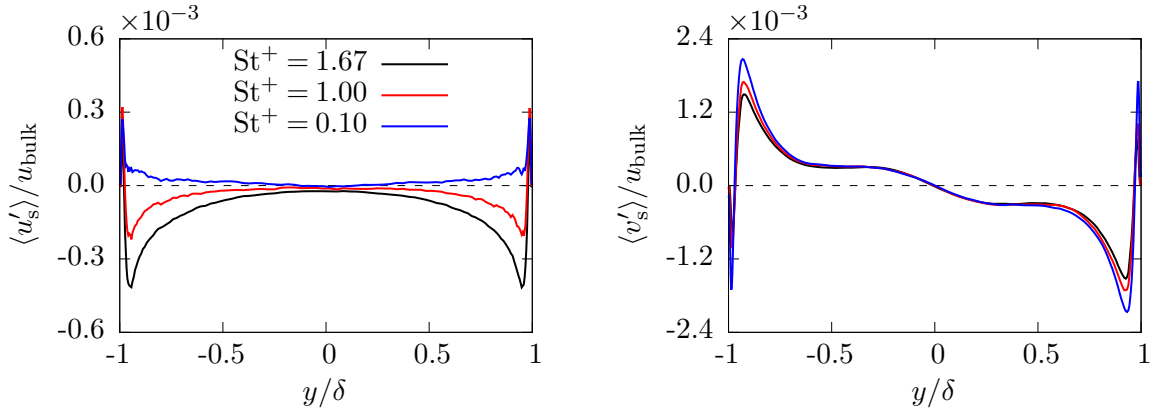

(a) Streamwise direction. **(b)** Wall-normal direction.

Fig. 11.12. Subgrid-scale velocities obtained by the extended Langevin subgrid-scale model for varying Stokes numbers. Taken from Breuer and Hoppe (2017).

It is apparent from Fig. 11.12(a) that the particle Stokes number has a significant influence on the averaged results in streamwise direction. For example, the negative values of the mean streamwise velocity of the subgrid scales are reduced by a factor of roughly two if the Stokes number is reduced from $\mathrm{St}^+ = 1.67$ to $\mathrm{St}^+ = 1.00$. Further decreasing the Stokes number to $\mathrm{St}^+ = 0.10$ leads to a small positive streamwise subgrid-scale velocity over the complete channel width. Additionally, the characteristic double-peak structure present for the cases with $\mathrm{St}^+ \geq 1$ vanishes for the case of a Stokes number smaller than unity. Since the subgrid-scale velocities obtained by the extended Langevin model are added to the filtered fluid velocities at the particle position according to Eq. (5.2), the fluid velocity seen by the particles of $\mathrm{St}^+ = 0.10$ is on average increased by the application of the present subgrid-scale model. In contrast, the full fluid velocity at the position of the particles with $\mathrm{St}^+ \geq 1$ is largely decreased by the extended Langevin model. Considering the explanation on the effect of preferential accumulation of the bubbles on the averaged subgrid-scale velocities depicted in Fig. 11.6 and explained in Section 11.2.1, it is apparent that particles of $\mathrm{St}^+ < 1$ tend to accumulate in regions of a positive streamwise subgrid-scale velocities, while heavier particles ($\mathrm{St}^+ \geq 1$) prefer regions where the corresponding velocity component is mostly negative. Note that the case of particles of $\mathrm{St}^+ = 0.10$ cannot be directly compared with the results shown in Fig. 11.6(a) obtained for bubbles, since the density ratio is completely different for the case of bubbles. The resulting buoyancy force has a significant effect on the bubbles, which is not relevant for solid particles. Hence, despite the fact that in both cases the Stokes numbers are smaller than unity, a different behavior of bubbles and particles with $\mathrm{St}^+ = 0.10$ is observed.

The averaged wall-normal velocities of the subgrid scales obtained by the Langevin model depicted in Fig. 11.12(b) also exhibit an influence of the considered Stokes number of the particles. However, the effect is less pronounced than in the streamwise direction. Most noticeable, the peak values of the subgrid-scale velocities in the vicinity of the wall increase if the Stokes number is reduced. However, the characteristic fully anti-symmetric profile over the complete channel width is still observable regardless of the Stokes number.

Note that the mean spanwise subgrid-scale velocity is omitted here as it was done in Breuer and Hoppe (2017), since the corresponding profiles simply tend to zero. That is similar to the case described above (for example in Figs. 11.6(a) and 11.10(a)) for the bubbles and the particles with $St^+ = 1.67$.

Again, results similar to the present study have been reported by Bianco et al. (2012). For example, for particles with a Stokes number larger than or equal to unity the negative peaks of the streamwise subgrid-scale velocity are found to be strongly augmented with increasing Stokes numbers. Furthermore, Bianco et al. (2012) showed that the wall-normal component is only affected to a small extent by the Stokes number similar to the results in Fig. 11.12(b). Likewise, the spanwise subgrid-scale velocities did not show any dependency on the Stokes number. However, it has to be noted that Bianco et al. (2012) did not consider Stokes numbers smaller than unity preventing any conclusion to be drawn for the case of particles with $St^+ = 0.10$.

The velocity fluctuations of the unresolved scales in streamwise direction are shown in Fig. 11.13(a). No visible differences between the results of the three Stokes numbers are observable. Thus, although the particles of different Stokes number tend to accumulate in regions with on average different subgrid-scale velocities, the corresponding velocity fluctuations of the subgrid-scales do not deviate. Based on the explanation of the identical subgrid-scale fluctuations in all spatial directions seen in Figs. 11.6(b) and 11.10(b) provided above, it is no surprise that that the fluctuations of the subgrid-scale velocities in wall-normal direction (Fig. 11.13(b)) do not deviate from the corresponding fluctuations in streamwise direction. The fluctuations in the spanwise direction are not depicted here for the same reason. Likewise, the comparison of the turbulent kinetic energy of the subgrid scales seen by the particles with resolved and the unresolved turbulent kinetic energy of the fluid is omitted here, since the results do not deviate from the profiles already shown in Fig. 11.11 for the case of a single fixed Stokes number of $St^+ = 1.67$.

The averaged particle velocities in streamwise and wall-normal direction obtained by the application of the extended Langevin subgrid-scale model and without any subgrid-scale model are shown in Fig. 11.14. In Figs. 11.14(a) and (c) the results obtained by the Langevin subgrid-scale model are depicted, while Figs. 11.14(b) and (d) show the averaged profiles obtained without any model. Comparing the results in the streamwise direction (Figs. 11.14(a) and (b)), no distinguishable difference between the mean streamwise particle velocities is observed. Hence, it can be concluded that neither the Langevin subgrid-scale model nor the Stokes number of the particles play a major role here. On the other hand, the wall-normal velocities exhibit a dependency on both the application of the subgrid-scale model for the particles as well as the Stokes number. It is obvious from the comparison of Fig. 11.14(c) with (d) that the Langevin subgrid-scale model yields increased peaks of the wall-normal velocity in the vicinity of the walls. This effect is observed for all three Stokes numbers considered in the present case. Furthermore, the inertia of the particles also affects the results: Reducing the Stokes number leads to increased peaks of the wall-normal velocity. While this effect is present in both Figs. 11.14(c) and (d), in case of the Langevin subgrid-scale model the augmentation of the peak of the wall-normal particle velocity is considerably stronger.

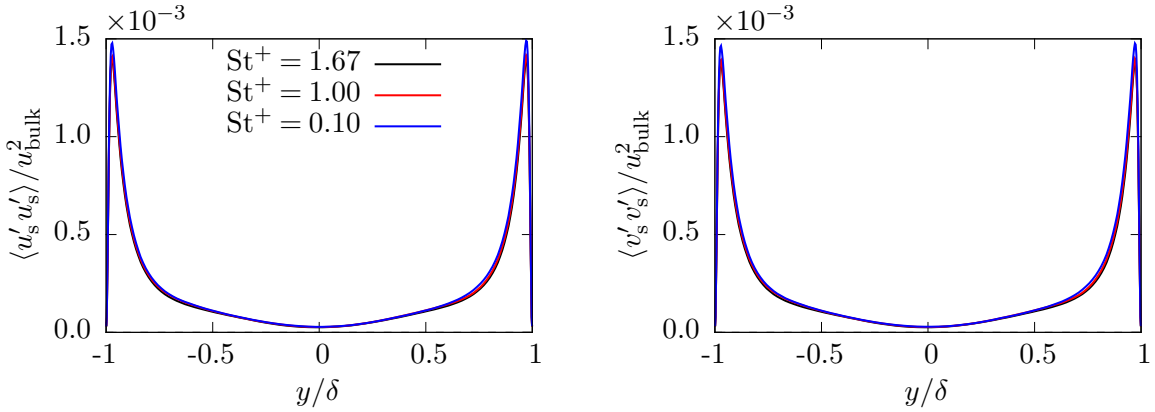

(a) Streamwise direction. **(b)** Wall-normal direction.

Fig. 11.13. Fluctuations of the subgrid-scale velocities obtained by the extended Langevin subgrid-scale model for varying Stokes numbers. Taken from Breuer and Hoppe (2017).

In Fig. 11.15 the normalized volume fractions of the particles resulting from the application of the Langevin subgrid-scale model and without any subgrid-scale model are shown. Note that the total volume fractions vary for the three Stokes numbers due to the changing particle diameters, see Section 10.2. Consequently, the total averaged volume fractions used for the normalization of the volume fraction profiles are $\Phi_{\mathrm{V,tot,0.10}} = 1.06 \times 10^{-8}$, $\Phi_{\mathrm{V,tot,1.00}} = 3.14 \times 10^{-7}$ and $\Phi_{\mathrm{V,tot,1.67}} = 6.78 \times 10^{-7}$ for the Stokes numbers $\mathrm{St}^+ = 0.10$, $\mathrm{St}^+ = 1.00$ and $\mathrm{St}^+ = 1.67$, respectively. It is obvious from Fig. 11.15 that the results are strongly affected by the application of the Langevin model as well as the variation of the Stokes number. In the case without a subgrid-scale model for the fluid velocity seen by the particles (Fig. 11.15(b)) the volume fraction close to the walls increases with increasing Stokes number. In particular, it is noteworthy that the volume fraction for particles with a Stokes number of $\mathrm{St}^+ = 0.10$ decreases towards the wall, while in the cases with $\mathrm{St}^+ \geq 1$ the volume fraction increases towards the wall. Applying the Langevin subgrid-scale model changes the observed behavior, i.e., the volume fraction increases towards the wall regardless of the Stokes number. This phenomenon is probably caused by the augmented wall-normal velocity of the particles due to the Langevin subgrid-scale model shown in Fig. 11.14(c). The effect of the Stokes number remains the same as in Fig. 11.15(a), i.e., the larger the particle Stokes number, the higher the normalized volume fraction of the particles close to the walls.

The fact that the Langevin subgrid-scale model changes the behavior of the dispersed phase is reasonable. Marchioli et al. (2008) showed that the volume fraction of the particles decreases in the vicinity of the walls if the flow is predicted by an a-priori or a-posteriori LES (without a subgrid-scale model for the particles) compared with a reference DNS. Consequently, the subgrid-scale model for the particles should increase the volume fraction close to the walls to counteract the aforementioned filtering effect. Note that Marchioli et al. (2008) neglected the lift force acting on the particles, i.e., the dispersed phase is solely affected by the drag force. Since in a downward channel flow the lift force acting on

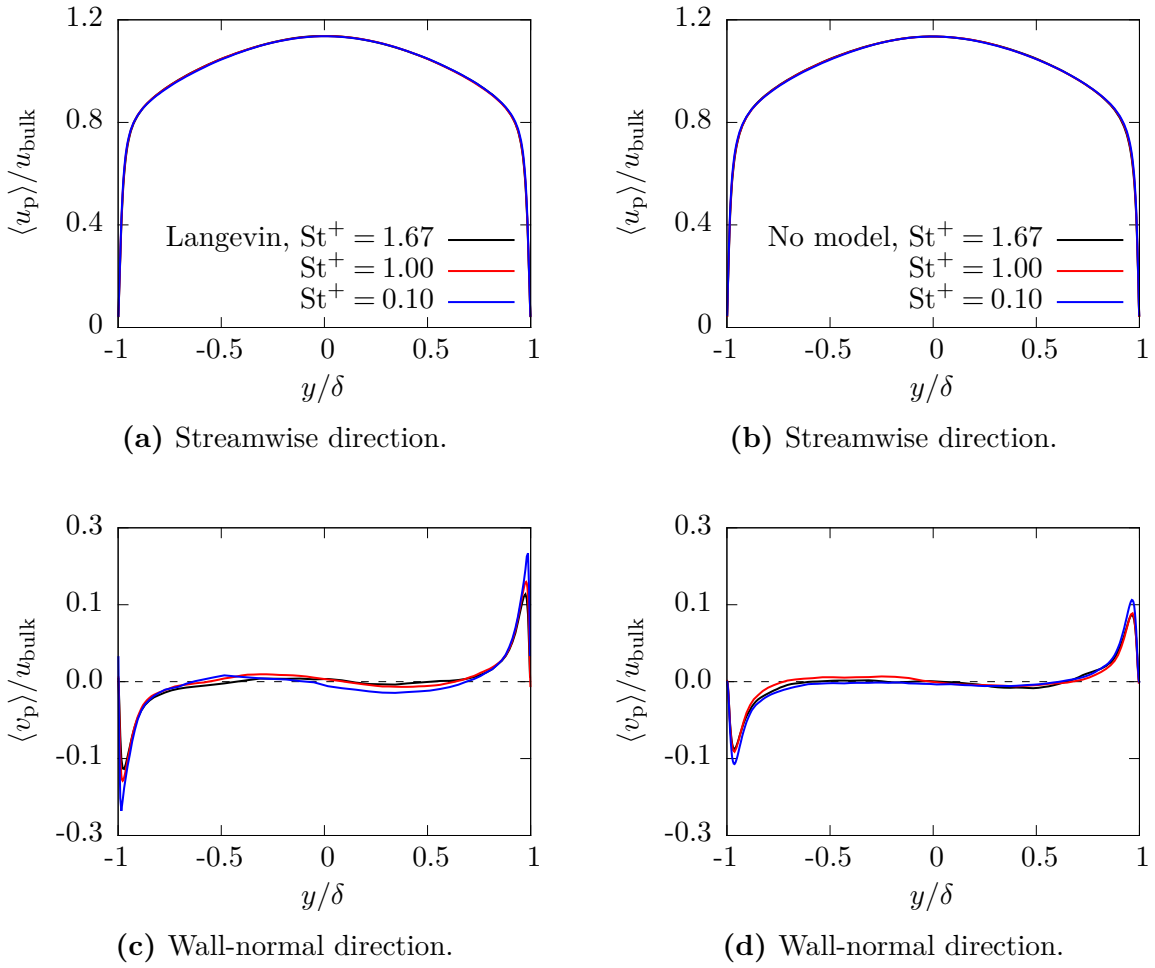

(a) Streamwise direction. **(b)** Streamwise direction.

(c) Wall-normal direction. **(d)** Wall-normal direction.

Fig. 11.14. Average particle velocities obtained by the Langevin subgrid-scale model (left column) and without a subgrid-scale model for the particles (right column). Taken from Breuer and Hoppe (2017).

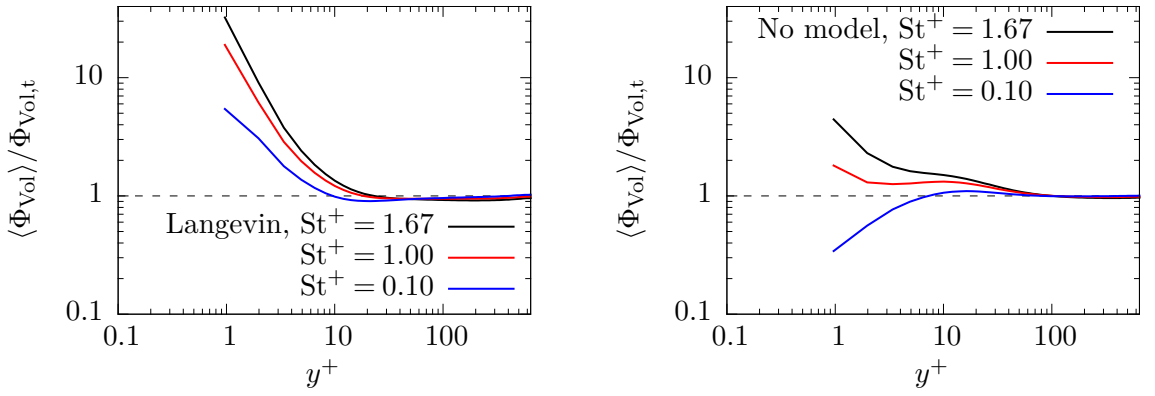

(a) Langevin subgrid-scale model. **(b)** No subgrid-scale model.

Fig. 11.15. Distribution of the normalized particle volume fraction. Taken from Breuer and Hoppe (2017).

solid particles ($\rho_\mathrm{p}/\rho_\mathrm{f} > 1$) points in the direction of the walls, particles are driven towards the walls causing an increased volume fraction. This effect is further amplified by the extended Langevin subgrid-scale model.

The increased volume fraction of the particles in the direct vicinity of the walls has a significant impact on the particle-wall collisions. As already argued before in Section 11.2.2 for the case of $\mathrm{St}^+ = 1.67$, the extended Langevin subgrid-scale model substantially augments the frequency of the particle-wall collisions. Table 11.1 demonstrates that the same is true for the cases with a smaller Stokes number. For $\mathrm{St}^+ = 1.00$ the application of the extended Langevin subgrid-scale model increases the particle-wall collision frequency by a factor of about 1200 compared with the result obtained without a subgrid-scale model for the unresolved scales seen by the particles. Further reducing the Stokes number ($\mathrm{St}^+ = 0.10$) amplifies the ratio between the frequencies obtained with the Langevin subgrid-scale model and without any model to about 3500. At the same time, the deposition frequencies are also augmented by the Langevin subgrid-scale model leading to ratios of about 56 and 248 for Stokes numbers $\mathrm{St}^+ = 1.00$ and $\mathrm{St}^+ = 0.10$, respectively. However, similar to the case of $\mathrm{St}^+ = 1.67$ described in Section 11.2.2 the overall deposition rate $f^*_\mathrm{dep}/f^{\mathrm{pw}\,*}_\mathrm{col}$ for the other two Stokes numbers also decreases due to the Langevin subgrid-scale model. For $\mathrm{St}^+ = 1.00$ the deposition rate decreases from $f^*_\mathrm{dep}/f^{\mathrm{pw}\,*}_\mathrm{col} \approx 74.3\%$ without any subgrid-scale model to roughly 3.3% with the extended Langevin subgrid-scale model. Likewise, in the case of the smallest Stokes number considered here $f^*_\mathrm{dep}/f^{\mathrm{pw}\,*}_\mathrm{col}$ drops from 97.7% to about 6.8%. The explanation for this observation given in Section 11.2.2 remains valid for the cases with smaller Stokes numbers.

Figure 11.16 depicts the velocity fluctuations of the particles in the three spatial directions for all three Stokes numbers considered. The left column represents the results obtained by the extended Langevin subgrid-scale model, while the results shown in the right column are obtained without any model for the subgrid scales seen by the particles. Again the Langevin subgrid-scale model slightly enhances the peak velocity fluctuations in the streamwise direction, compare Figs. 11.16(a) and (b). In both cases the peak values are to a minor extent affected by the Stokes number of the particles. Similar as before (Fig. 11.8(d)) the effect of the Langevin subgrid-scale model is more pronounced in the wall-normal direction. The application of the Langevin subgrid-scale model enhances the peaks of the wall-normal velocity fluctuations of the particles shown in Fig. 11.16(c) compared with the corresponding fluctuations without any model (Fig. 11.16(d)) for all three Stokes numbers. Additionally, an influence of the Stokes number can be observed, i.e., particles with a smaller Stokes number exhibit stronger velocity fluctuations. While this effect is rather small in the simulations without any model for the subgrid scales seen by the particles, a more distinct increase of the wall-normal velocity fluctuations is visible in Fig. 11.16(c), where the Langevin subgrid-scale model is applied. The same effect is observable in the spanwise direction displayed in Fig. 11.16(e) for the case of the Langevin subgrid-scale model and in Fig. 11.16(f) for the case without any model. For all Stokes numbers the peaks are augmented by the subgrid-scale model for the particles, with the strongest increase found for the smallest Stokes number. Note that in the spanwise direction the effect of the Stokes number on the fluctuations is indistinctive if no subgrid-scale model is considered (see Fig. 11.16(f)). Lastly, it is mentioned that the Reynolds shear

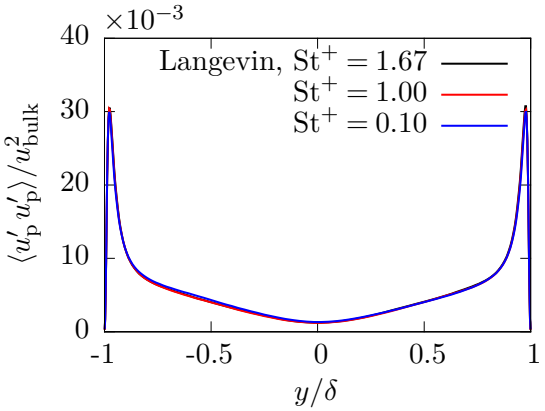

(a) Streamwise direction.

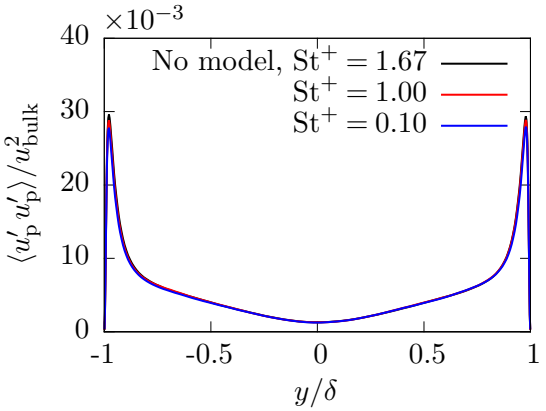

(b) Streamwise direction.

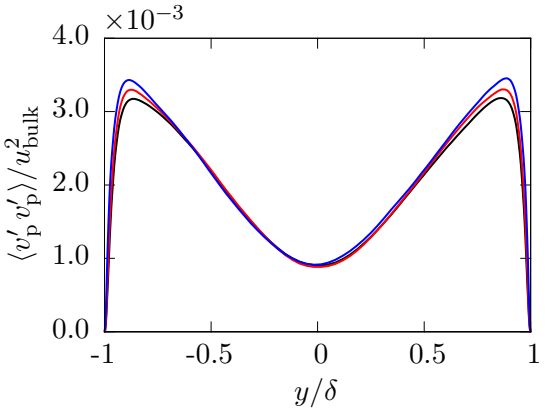

(c) Wall-normal direction.

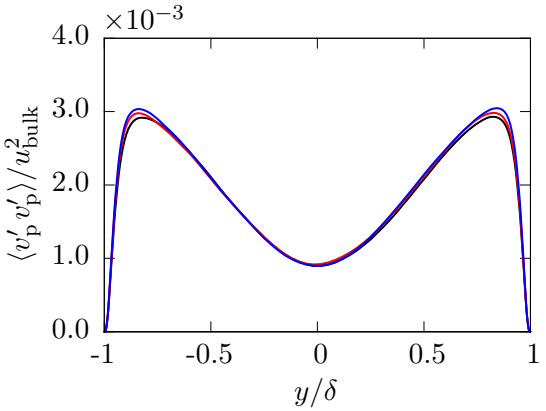

(d) Wall-normal direction.

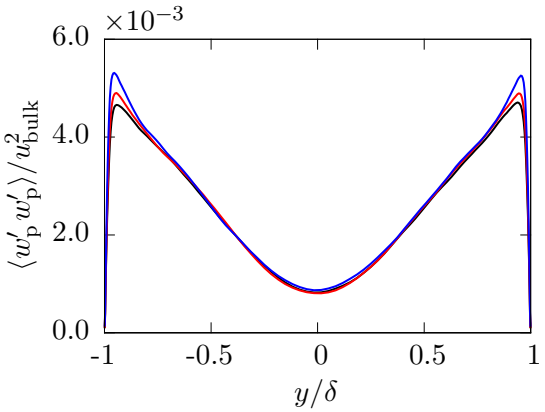

(e) Spanwise direction.

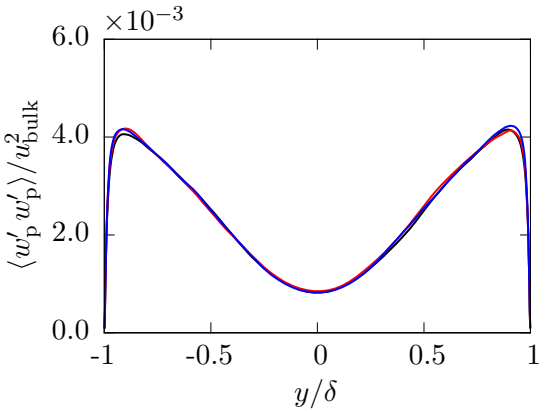

(f) Spanwise direction.

Fig. 11.16. Particle velocity fluctuations obtained by the extended Langevin subgrid-scale model (left column) and without subgrid-scale model for the particles (right column). Taken from Breuer and Hoppe (2017).

stress between the streamwise and the wall-normal direction is largely unaffected by the application of the Langevin subgrid-scale model, similar to the results for $\mathrm{St}^+ = 1.67$ shown in Fig. 11.8(f). However, an influence of the Stokes number of the particles on the peaks of the shear stress is observable, i.e., reducing St^+ reduces the peak values. Yet, the extent of this dependency is rather small, wherefore the presentation of the Reynolds shear stress distribution is omitted here.

11.2.4 Summary of the Results

Summarizing the results presented in Section 11.2, it can be concluded that the overall impact of the extended Langevin subgrid-scale model on averaged statistics is relatively small. The application of the Langevin subgrid-scale model to a bubble-laden channel flow at $\mathrm{Re}_\tau = 150$ leads to marginal deviations of the averaged bubble properties (mean streamwise velocity, velocity fluctuations and volume fraction) from the results obtained by the trivial subgrid-scale model or without any model for the unresolved scales. The reason for this observation is identified to be the small magnitude of the subgrid-scale velocities and the associated fluctuations obtained by the Langevin subgrid-scale model at this low Re_τ. However, the average level of the turbulent kinetic energy of the subgrid scales seen by the particles is correctly estimated by the present model. Additionally, it is shown that bubbles tend to accumulate in regions of high turbulent kinetic energy.

Further investigations showed that even in the case of a higher Reynolds number flow containing solid particles of $\mathrm{St}^+ = 1.67$ the Langevin subgrid-scale model has a relatively small influence on the averaged results. While the subgrid-scale velocities in streamwise and wall-normal direction show the characteristic profiles already found for the case of bubbles, their influence on the mean velocities of the particles is again found to be rather weak. While the phenomenon of agglomeration was not investigated in the present thesis, it was demonstrated by Almohammed (2018) that the agglomeration rate significantly decreases due to the application of the extended Langevin subgrid-scale model, despite the fact that the rate of inter-particle collisions increases. Hence, the evolution of the dispersed phase is nevertheless strongly affected by the extended Langevin subgrid-scale model.

Finally, a variation of the Stokes number of the particles is performed. The results of this variation reveal that the effects of the Langevin model on the dispersed phase are susceptible to changes of the Stokes number. Especially, the volume fraction of the particles is shown to be strongly altered by the application of the Langevin model for all Stokes numbers, which is a desired effect as explained above (see, e.g., Marchioli et al., 2008). As a consequence, the frequency of particle-wall collisions and subsequently the frequency of deposition process is augmented by the present subgrid-scale model. Yet, the deposition rate $f^*_{\mathrm{dep}}/f^{\mathrm{pw}\,*}_{\mathrm{col}}$ decreases, which is caused by the increased collision velocity.

Consequently, the initial impression of the small influence of the extended Langevin subgrid-scale model resulting from the small effect on the averaged statistics (velocity and fluctuations) is rebutted. Additionally, it is apparent that the influence of the subgrid-scale model increases with an increasing Reynolds number, since a larger part of the turbulent spectrum has to be mimicked by the subgrid-scale model and, thus, its impact rises.

11.3 Coalescence of Bubbles

The first part of this section is concerned with the validation of the coalescence model described in Chapter 7. For this purpose, the experiments by Kosior et al. (2014) and Zawala and Malysa (2011) are mimicked in order to compare the results obtained by the present coalescence model with the experimental data. The experiments by Kosior et al. (2014) and Zawala and Malysa (2011) and the corresponding numerical setup are described in Section 10.3. It has to be mentioned that most of the following results are based on the work published in Hoppe and Breuer (2017, 2018). However, in these studies the added-mass coefficient C'_{m} required for the estimation of the total mass $m = m_{\mathrm{b}} + m_{\mathrm{AM}}$ by Eq. (7.5) was assumed to be constant (Eq. (7.6)). It was realized later that a variable added-mass coefficient defined by Eq. (7.7) allows for a more reasonable description of the collision process. Hence, in Section 11.3.1 the results obtained by the coalescence model assuming a constant added-mass coefficient previously shown in Hoppe and Breuer (2017, 2018) are presented again. Afterwards, the results obtained for an added-mass coefficient variably adjusted by the coalescence model are compared with the previous results in order to demonstrate the influence of the added-mass coefficient. It has to be remembered that the added-mass coefficient C'_{m} used for the estimation of the added mass of a bubble-bubble collision (Section 7.1.1) is independent of the added-mass coefficient $C_{\mathrm{m}} = 0.5$ applied for the tracking of a single bubble, see Section 4.1.1.4. Hence, any variation of C'_{m} does not affect the bubble tracking. In the second part, further investigations on the influence of bubble coalescence on bubble-laden flows are carried out by applying the coalescence model to the bubble rise in a bubble column (Section 10.4 for the setup of the test case).

11.3.1 Validation of the Coalescence Model / Bubble at Free Surface

As mentioned before, the coalescence model by Hoppe and Breuer (2018) is validated by comparing simulations of the impact of clean ($d_{\mathrm{b}} = 1.0\,\mathrm{mm}$ and $d_{\mathrm{b}} = 1.48\,\mathrm{mm}$) and contaminated ($d_{\mathrm{b}} = 1.32\,\mathrm{mm}$) bubbles on a free surface with the results by Kosior et al. (2014) and Zawala and Malysa (2011). Firstly, results by Hoppe and Breuer (2018) obtained by the coalescence model assuming a constant added-mass coefficient of $C'_{\mathrm{m}} = 0.8$ are shown.

11.3.1.1 Results Obtained for a Constant Added-Mass Coefficient

Figure 11.17 displays the velocities observed in the experiments together with the results of the present simulations. Additionally, results obtained by applying the simple coalescence models for clean and contaminated bubbles described in Section 7.4 are shown. These simple models represent the coalescence models of Kirkpatrick and Lockett (1974) and Prince and Blanch (1990) for clean bubbles and Hartland (1967) and Jeffreys and Davis (1971) for contaminated bubbles, which are all highly popular and frequently applied in the literature. Since neither of these models provide an estimate of the contact time,

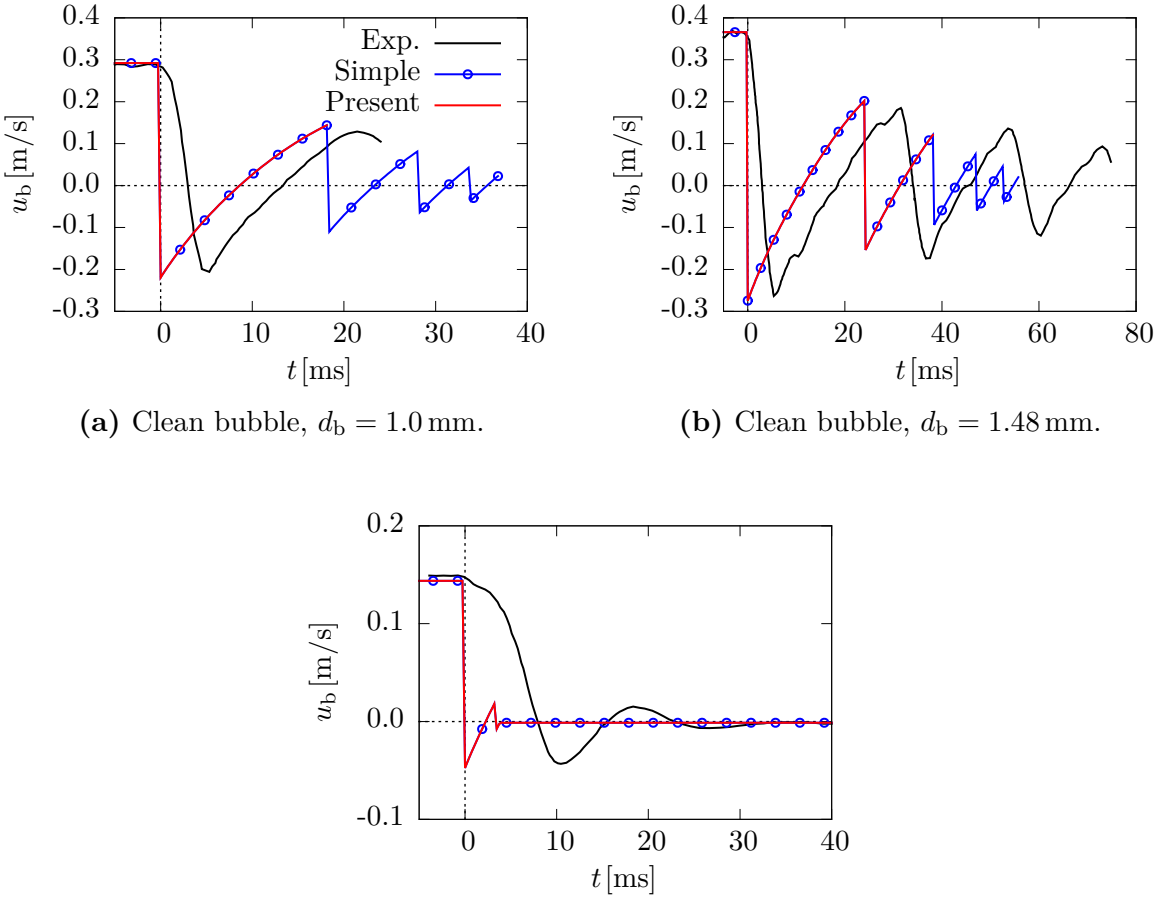

(a) Clean bubble, $d_b = 1.0\,\text{mm}$.

(b) Clean bubble, $d_b = 1.48\,\text{mm}$.

(c) Contaminated bubble, $d_b = 1.32\,\text{mm}$.

Fig. 11.17. Bubble velocity with collisions described by the present coalescence model (red line) assuming a constant added-mass coefficient (Eq. (7.6)) and the simple model (blue line with symbols) compared with experimental results (black line) by Kosior et al. (2014) and Zawala and Malysa (2011). Taken from Hoppe and Breuer (2018).

the simple approaches are combined with the ansatz of Sommerfeld et al. (2003) for t_c also described in Section 7.4. Furthermore, it has to be noted that in the simple models the added mass of the fluid is not considered. Hence, the improved formulation of the added-mass coefficient is not taken into account.

In the experiments shown in Fig. 11.17 the bubbles impact on the free surface with their respective terminal rise velocities, which has a positive sign in the figure. The impact defines $t = 0$. Due to the impact the bubbles are rapidly decelerated and reflected. Note that in the experiment none of the considered bubbles coalesce with the free surface during the first collision. After this initial impact the bubbles are accelerated again by the buoyancy force acting on the bubbles leading to another approach on the surface with a reduced impact velocity. The clean bubble with a diameter of $d_b = 1.0\,\text{mm}$ (Fig. 11.17(a)) coalesces during its second impact on the free surface. The large clean bubble of $d_b = 1.48\,\text{mm}$ (Fig. 11.17(b)) is reflected again with the coalescence ultimately

taking place at the fourth approach (Zawala and Malysa, 2011). Lastly, the contaminated bubble of $d_\mathrm{b} = 1.32\,\mathrm{mm}$ shown in Fig. 11.17(c) does not coalesce at all during the approaches on the surface but comes to rest. According to Kosior et al. (2014) the contaminated bubble remained at this position for several minutes until coalescence finally occurred.

It is apparent from Fig. 11.17 that in all cases considered here the numerically predicted terminal rise velocity of the bubbles agree well with the corresponding experiments. Hence, the Lagrangian tracking methodology and, especially, the drag coefficients for clean and contaminated bubbles used in this thesis are further validated. It has to be remembered that in the present framework collisions are handled by a hard-sphere approach, see Section 5.3. Hence, in the simulations the velocities of the bubbles are instantaneously reversed by a collision making the modeling of the deceleration not possible. Additionally, the instantaneous reversion of the bubble velocity leads to the compression of the temporal axis visible in Fig. 11.17. In order to make the comparison of the results easier, the normal restitution coefficients of the collisions are approximated. Based on the average ratio between the bubble velocities before and after the collisions observed in the experiments by Kosior et al. (2014) and Zawala and Malysa (2011), a normal restitution coefficient of $e_\mathrm{n,b}^\mathrm{clean} = 0.75$ is obtained for the case of the clean bubbles. Note that the first collision of the small clean bubble (Fig. 11.17(a)) and the first three collisions of the large clean bubble (Fig. 11.17(b)) are considered for the determination of this value. For the case of contaminated bubbles a normal restitution coefficient of $e_\mathrm{n,b}^\mathrm{cont} = 0.33$ is extracted from the first two impacts shown in Fig. 11.17(c). Note that these coefficients are solely used for the present comparison and are not universally valid.

In the case of the smaller clean bubble (Fig. 11.17(a)) the present model assuming a constant added-mass coefficient given by Eq. (7.6) predicts coalescence at the second approach in agreement with the experiment by Zawala and Malysa (2011). It has to be remarked that the bubble velocity at the instant of coalescence is slightly higher in the simulation than in the experiment. Coalescence takes place at a velocity of $u_\mathrm{b} = 0.147\,\mathrm{m/s}$ in the simulation, while the bubble velocity is $u_\mathrm{b} = 0.129\,\mathrm{m/s}$ in the experiment. A similar observation can be made for the larger clean bubble shown in Fig. 11.17(b). Here, the present model predicts coalescence at the third impact on the free surface at a velocity of $u_\mathrm{b} = 0.125\,\mathrm{m/s}$, which is found to be slightly smaller than the experimental value of $u_\mathrm{b} = 0.136\,\mathrm{m/s}$ at the third approach. In the experiments the bubble coalesces during the fourth impact on the surface at a velocity of $u_\mathrm{b} = 0.094\,\mathrm{m/s}$. The slightly too low impact velocity at the third approach compared to the experimental velocity is caused by the non-ideal restitution coefficient of $e_\mathrm{n,b}^\mathrm{clean} = 0.75$, which leads to a good agreement with the experiment for the first rebound. However, at subsequent approaches the agreement is worse. While a larger restitution coefficient would improve the results for the second and third impacts, it would lead to a worse agreement for the first collision.

Lastly, it can be seen from Fig. 11.17(c) that the present coalescence model predicts that the contaminated bubble does not coalesce with the free surface in the time period considered. The same observations are made in the experiments by Kosior et al. (2014), where coalescence did not occur for several minutes. Hence, the results obtained by the present coalescence model assuming a constant added-mass coefficient agree reasonably well with

the experiments despite the discrepancies between bubble/bubble and bubble/free-surface coalescence mentioned earlier in Section 10.3.

Figure 11.17 also depicts the results of simulations where the coalescence is described by the simple models of Kirkpatrick and Lockett (1974) and Prince and Blanch (1990) for clean bubbles and Hartland (1967) and Jeffreys and Davis (1971) for contaminated bubbles in combination with the estimation of the contact time by Sommerfeld et al. (2003). It is obvious that in most cases these models lead to a less satisfactory agreement with the experimental results. For example, in Fig. 11.17(a) coalescence is predicted during the fifth approach of the clean bubble of $d_\mathrm{b} = 1.0\,\mathrm{mm}$ at a much smaller impact velocity of $u_\mathrm{b} = 0.018\,\mathrm{m/s}$ compared with the results by Zawala and Malysa (2011), who observed coalescence during the second approach at $u_\mathrm{b} = 0.129\,\mathrm{m/s}$. Similarly, in Fig. 11.17(b) for the larger clean bubble of $d_\mathrm{b} = 1.48\,\mathrm{mm}$ the predicted coalescence takes place during a later approach (sixth compared with the fourth in the experiments) at a much lower velocity ($u_\mathrm{b} = 0.017\,\mathrm{m/s}$ compared with $u_\mathrm{b} = 0.094\,\mathrm{m/s}$). Apparently, the simple model for clean bubbles predicts coalescence only for much smaller impact velocities leading to an increased number of rebounds. Solely, the simple model for contaminated bubbles is capable of correctly estimating the absence of coalescence in the case depicted in Fig. 11.17(c).

The less accurate predictions by the simple model in the case of clean bubbles are caused by two drawbacks the simple approaches have compared with the extended present model: the assumption of a constant contact surface (see Section 7.4) and the estimation of the contact time by the model of Sommerfeld et al. (2003). Based on the assumption of a constant contact surface a larger amount of liquid is trapped between the colliding bubbles in the simple model. Hence, the drainage of the trapped liquid takes longer than in the present coalescence model, where the reduction of the film thickness is fast especially during the initial stages of the drainage process, since the contact area is still small. Consequently, the simple model predicts coalescence at later approaches of the clean bubbles, since the drainage process is slower than in the present coalescence model. Note that this argumentation also applies to contaminated bubbles, where the drainage process described by the simple model is also considerably slower than the drainage predicted by the present model. However, for contaminated bubbles this has no critical implications, since in both predictions the final film thickness obtained from the models is not equal to or smaller than the critical film thickness required for coalescence.

The estimation of the contact time by Eq. (7.35) proposed by Sommerfeld et al. (2003) is the second drawback of the simple approach. Table 11.2 summarizes the contact times from the initial contact until the bubbles rebound from it. The table is limited to the first two collisions of the clean and the contaminated bubbles, since in the experiments the small clean bubble coalesces after a time period of approximately 2.5 ms during the second approach and the contaminated bubble comes to rest at the free surface during the third approach. Note that the present model assuming a constant added-mass coefficient of $C'_\mathrm{m} = 0.8$ correctly predicts coalescence during the second collision, albeit at a too high impact velocity. It can be seen from Table 11.2 that the present model typically predicts somewhat too large contact times for the collisions. For example, for the first impact of the small clean bubble $t_\mathrm{c} = 8.5\,\mathrm{ms}$ according to the present model, whereas a

Tab. 11.2. Contact times t_c of the clean bubbles ($d_b = 1.0\,\text{mm}$ and $d_b = 1.48\,\text{mm}$) and the contaminated bubble ($d_b = 1.32\,\text{mm}$) with the free surface. The estimations of the present coalescence model based on the work of Jeelani and Hartland (1991) and of the simple approach by Sommerfeld et al. (2003) are compared with the experiments by Kosior et al. (2014) and Zawala and Malysa (2011). Taken from Hoppe and Breuer (2018).

Collision	t_c [ms]								
	$d_b^{clean} = 1.0\,\text{mm}$			$d_b^{clean} = 1.48\,\text{mm}$			$d_b^{cont} = 1.32\,\text{mm}$		
#	Exp.	Present	Simple	Exp.	Present	Simple	Exp.	Present	Simple
1.	5.9	8.5	1.7	6.4	15.3	2.0	10.2	15.3	4.6
2.	Coal.	Coal.	3.4	6.4	15.3	3.6	9.5	15.3	28.7

contact time of $t_c = 5.9\,\text{ms}$ is observed in the experiments. Similar results are obtained by the present coalescence model for the remaining collisions shown in Table 11.2. The overestimation probably has three reasons. Firstly, the deformation to a non-flat shape of the contact surface is neglected. Secondly, the contact surface is assumed to be small for the derivation of the present model, which is shown by Kosior et al. (2014) and Zawala and Malysa (2011) not to be the case in the experiment. Lastly, as described in Section 7.1 the contact time depends on the added mass of the fluid and, hence, on the added-mass coefficient. It has to be remembered that the above results originally published by Hoppe and Breuer (2018) are obtained using a constant coefficient of $C'_m = 0.8$.

The simple approach by Sommerfeld et al. (2003) predicts a too small contact time for most collisions shown in Table 11.2. The only exception to this underprediction is the second impact of the contaminated bubble on the surface, where t_c is largely overestimated. Furthermore, Table 11.2 shows that the contact time is approximately constant for all collisions of a specific bubble. Hence, the contact time appears to depend on the size of the bubbles but not on the collision velocity. A physical explanation for this observation is that a bubble impacting with a larger velocity deforms to a larger extent. Consequently, the contact surface becomes larger leading to an increase of the film force decelerating the bubbles more quickly. Hence, the effect of the collision velocity is (nearly) compensated by the resulting film forces making the contact time independent of the collision velocity. The estimation of t_c by Eq. (7.14) in the present model correctly captures this feature. In contrast, the model by Sommerfeld et al. (2003) is not able to reproduce this behavior, since Eq. (7.35) explicitly depends on the inverse of the collision velocity. Hence, the contact time is initially too low for the first approach estimated by the simple model in Table 11.2 but then significantly increases during later approaches with a decreasing approach velocity. This is especially obvious for the contaminated bubble, where the contact time for the second collision is more than six times larger than for the first impact.

11.3.1.2 Results Obtained for a Variable Added-Mass Coefficient

As already mentioned earlier the results shown above were obtained by the present coalescence model assuming a constant added-mass coefficient of $C'_{\mathrm{m}} = 0.8$ and published in Hoppe and Breuer (2018). However, it became apparent later that according to Kamp et al. (2001) and Lamb (1932) the added-mass coefficient is actually depending on the sizes of the colliding bubbles. Hence, an estimation of C'_{m} according to Eq. (7.7) is supposed to influence the results of the present coalescence model.

Figure 11.18 compares the results obtained by the present coalescence model with a constant added-mass coefficient and corresponding results, where the added-mass coefficient is variable. The experimental results by Kosior et al. (2014) and Zawala and Malysa (2011) are included for reference. It has to be noted that the notation '*var.*' is supposed to indicate that in the corresponding predictions C'_{m} is adjusted according to Eq. (7.7) in the coalescence model depending on the properties of the bubbles and is *not* a-priori defined. Since in the present case the rising bubble collides and coalesces with a free surface mimicked by a bubble of $d_{\mathrm{b}} = \infty$, the resulting added-mass coefficient is equal to $C'_{\mathrm{m}} = 0.2$ for all collisions of the three bubbles considered, see Section 7.1.1. Note again that in the previous case $C'_{\mathrm{m}} = 0.8$ was applied.

It can be seen in Fig. 11.18(a) that the present coalescence model predicts coalescence of the smaller clean bubble with the free surface at the third approach if the added-mass coefficient is variable, in contrast to the second approach observed by the experiment and the prediction of the present model with a constant coefficient. However, it has to be remembered that the normal restitution coefficient of $e_{\mathrm{n,b}}^{\mathrm{clean}}$ used in the simulations is not ideal, i.e., the impact velocity of $u_{\mathrm{b}} = 0.147\,\mathrm{m/s}$ at the second approach of the simulation is larger than the value of $u_{\mathrm{b}} = 0.129\,\mathrm{m/s}$ found by Zawala and Malysa (2011). While the present model assuming a constant added-mass coefficient predicts coalescence for this too large value, applying a variable C'_{m} leads to a rebound. Subsequently, the coalescence occurs at the third approach, where the bubble velocity is reduced to $u_{\mathrm{b}} = 0.085\,\mathrm{m/s}$. For the larger clean bubble (Fig. 11.18(b)) the outcome is opposite to the previous case. Here the number of rebounds increases by one due to the variable added-mass coefficient, i.e., the bubble coalesces at the fourth impact with a velocity of $u_{\mathrm{b}} = 0.078\,\mathrm{m/s}$. Hence, a better agreement with the experiment is achieved compared with the previous case, where a constant added-mass coefficient is assumed. Lastly, no deviations of the simulations are obtained for the case of a contaminated bubble shown in Fig. 11.18(c).

The observed differences for the clean bubbles are caused by the lower added-mass coefficient, which is adjusted to be $C'_{\mathrm{m}} = 0.2$ by the coalescence model in case of a variable added-mass constant. In comparison, the fixed value of $C'_{\mathrm{m}} = 0.8$ is used in case of a constant coefficient. According to Eq. (7.5) the lower added-mass coefficient leads to a lower total mass m[1] and, subsequently, to a lower contact time defined by Eq. (7.14). Consequently, the period of time during which the liquid film is drained is shortened leading to a smaller reduction of the film thickness. Hence, coalescence is less likely to occur, see, e.g., the second impact of the small clean bubble (Fig. 11.18(a)), where the present coalescence model with a variable added-mass coefficient predicts a rebound.

[1] Note that the dependency is non-linear.

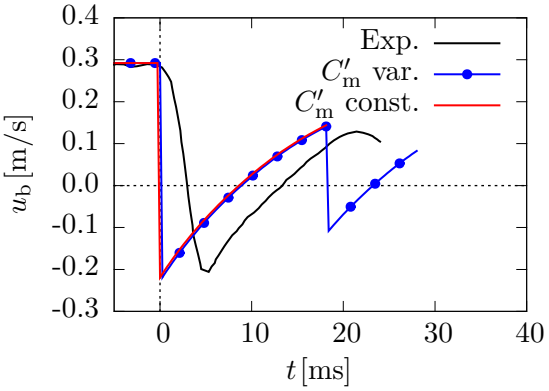

(a) Clean bubble, $d_b = 1.0\,\text{mm}$.

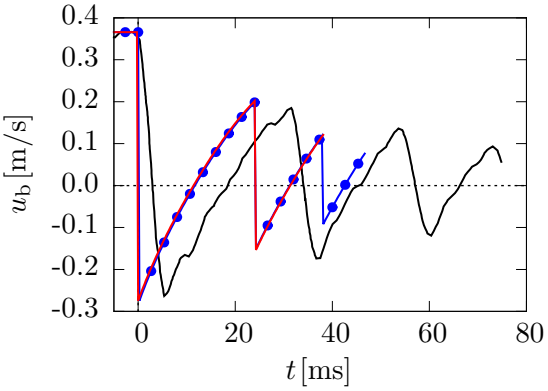

(b) Clean bubble, $d_b = 1.48\,\text{mm}$.

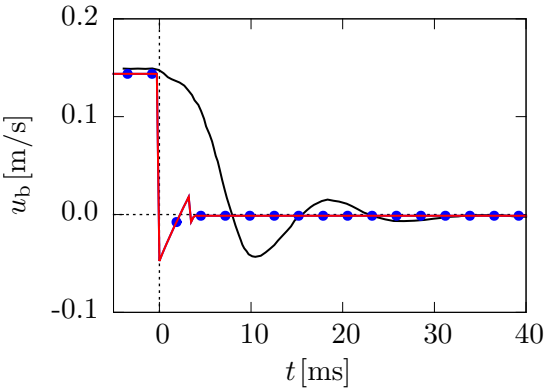

(c) Contaminated bubble, $d_b = 1.32\,\text{mm}$.

Fig. 11.18. Bubble velocity with collisions described by the present coalescence model with a constant (red line) and a variable (blue line with symbols) added-mass coefficient compared with experimental results by Kosior et al. (2014) and Zawala and Malysa (2011).

Table 11.3 summarizes the contact times for the present coalescence model with a constant added-mass coefficient and a variable added-mass coefficient for the first two impacts of the small and the large clean bubbles and the contaminated bubble. It is apparent that in all cases, where the added-mass coefficient is assumed to be variable, the contact times are more than halved compared with the case of a constant coefficient, e.g., $t_c = 4.1\,\text{ms}$ compared with $t_c = 8.5\,\text{ms}$ for the small clean bubble. Except for the case of the large clean bubble, the contact times estimated by assuming a variable added-mass coefficient are smaller than the contact times observed by Kosior et al. (2014) and Zawala and Malysa (2011). Nevertheless, the reduction of the contact time due to the smaller added-mass coefficient leads to an overall better agreement with the experiments. Especially, in the cases of the large clean bubble and the contaminated bubble taking a variable added-mass coefficient into account leads to a smaller deviation from the experimental values.

Tab. 11.3. Comparison of the contact times t_c estimated by the present coalescence model assuming a constant added-mass coefficient and a variable estimation of C'_m by Eq. (7.7) with the experimental results by Kosior et al. (2014) and Zawala and Malysa (2011).

Collision	t_c [ms]								
	$d_b^{clean} = 1.0$ mm			$d_b^{clean} = 1.48$ mm			$d_b^{cont} = 1.32$ mm		
	Exp.	Present C'_m		Exp.	Present C'_m		Exp.	Present C'_m	
#		const.	var.		const.	var.		const.	var.
1.	5.9	8.5	4.1	6.4	15.3	7.4	10.2	15.3	7.4
2.	Coal.	Coal.	4.1	6.4	15.3	7.4	9.5	15.3	7.4

11.3.1.3 Summary of the Results

In summary, the present coalescence model is able to provide results that agree overall well with the experimental results by Kosior et al. (2014) and Zawala and Malysa (2011) for both the assumption of a constant added-mass coefficient and a variable description. Furthermore, in both cases the results are demonstrated to be significantly improved compared with the results of the simpler coalescence models coupled with the model for the contact time by Sommerfeld et al. (2003). The results by Hoppe and Breuer (2018) obtained by assuming a constant added-mass coefficient show some deviations to the experiment, especially in terms of the predicted contact times. However, as shown in Fig. 11.17 these deviations are not critical. The improvement of a variable adjustment of the added-mass coefficient by the model made in the course of this thesis yields a better agreement of the predicted contact times with the experiments. The influence on the predicted bubble coalescence (Fig. 11.18) is rather small, with the most noticeable effect being that a smaller impact velocity is required for coalescence compared with the case of a constant added-mass coefficient. Hence, it can be stated that the description of the added mass by a variable formulation leads to a small improvement of the predicted results. Note that the present test case of bubble coalescence with a free surface represents an extreme case, i.e., the free surface is mimicked by a bubble of infinitely large diameter. As mentioned above, this configuration results in a decrease of the added-mass coefficient from $C'_m = 0.8$ for equally-sized bubbles to a value of $C'_m = 0.2$. However, in typical flow problems like the turbulent bubble column also considered by Hoppe and Breuer (2018) and shown in the following section, such a strong reduction of the added-mass coefficient by the model (Eq. (7.7)) is highly unlikely, since the ratio of the diameters of the colliding bubbles usually do not tend to infinity. Hence, in those cases the influence of the added-mass coefficient is not as pronounced as in the present case, see Section 11.3.2.2 below.

11.3.2 Turbulent Two-Phase Flow in a Bubble Column Including Coalescence

In order to investigate bubble coalescence in turbulent flows containing a large number of bubbles, additional simulations are carried out considering a cylindrical bubble column (Hoppe and Breuer, 2018). After the release of the mono-disperse bubbles at the bottom ($4 \leq x/d_c \leq 5$) of the column, they rise upwards due to the buoyancy force. During their rise the bubbles collide with each other and eventually coalesce forming larger bubbles. The emphasis of the present study is put on the influence of the bubble parameters on the overall coalescence behavior observed in the column, which is studied by varying the size of the primary bubbles and considering both clean and contaminated surface conditions. The setup is described in more detail in Section 10.4. Note that similar results have been previously published in Hoppe and Breuer (2018). However, as already mentioned before, in this study the added-mass coefficient was assumed to be constant (Eq. (7.6)). Since it was found in Section 11.3.1 that the estimation of a variable added-mass coefficient leads to an improved representation of the coalescence process, the results presented in the following are obtained by using C'_m variably adjusted according to Eq. (7.7). Firstly, the effects of the size of the primary bubbles and their contamination with surfactants are considered in Section 11.3.2.1. Afterwards, the impact of the added-mass coefficient C'_m is analyzed in Section 11.3.2.2, i.e., it is studied whether the variable estimation of C'_m leads to significantly different results compared with the predictions by Hoppe and Breuer (2018), who assumed a constant added-mass coefficient.

11.3.2.1 Influence of the Bubble Size and the Contamination with Surfactants

In the present study small and large primary bubbles with dimensionless diameters of $d^*_{pb,small} = 2.5 \times 10^{-3}$ and $d^*_{pb,large} = 3.12 \times 10^{-3}$ are considered. The corresponding dimensionless volumes are $V^*_{pb,small} = 8.18 \times 10^{-9}$ and $V^*_{pb,large} = 1.59 \times 10^{-8}$, respectively. Additionally, for both bubble sizes clean and contaminated surface conditions are taken into account. In order to give an impression of the evolution of the dispersed phase due to coalescence, snapshots of the bubbles at three different sections of the bubble column are shown in Figs. 11.19 to 11.22 for the four cases considered by the present study. In all figures the three chosen heights correspond to the lowermost averaging section ($5 \leq x/d_c < 10$) just above the bubble injection, the middle section ($15 \leq x/d_c < 20$) and the uppermost section ($25 \leq x/d_c < 30$) of the bubble column defined in Fig. 10.1. Note that only bubbles with coordinates within the central range $-0.1 \leq z/d_c \leq 0.1$ are shown in order to improve the visibility. Furthermore, the bubbles are magnified by a factor of three to make them more distinguishable. The color of the bubbles is chosen according to the ratio V_b/V_{pb} of the actual bubble volume to the respective volume of the released primary bubbles. Hence, primary bubbles ($V_b/V_{pb} = 1$) are plotted in dark blue, bubbles containing about ten primary bubbles are green and large bubbles of $V_b/V_{pb} > 20$ are red.

Figure 11.19 displays the case of small clean primary bubbles. It is apparent that in the lowermost section (Fig. 11.19(a)) mostly primary bubbles are encountered, which is expected due to the close vicinity to the injection region ($4 \leq x/d_c \leq 5$) of the

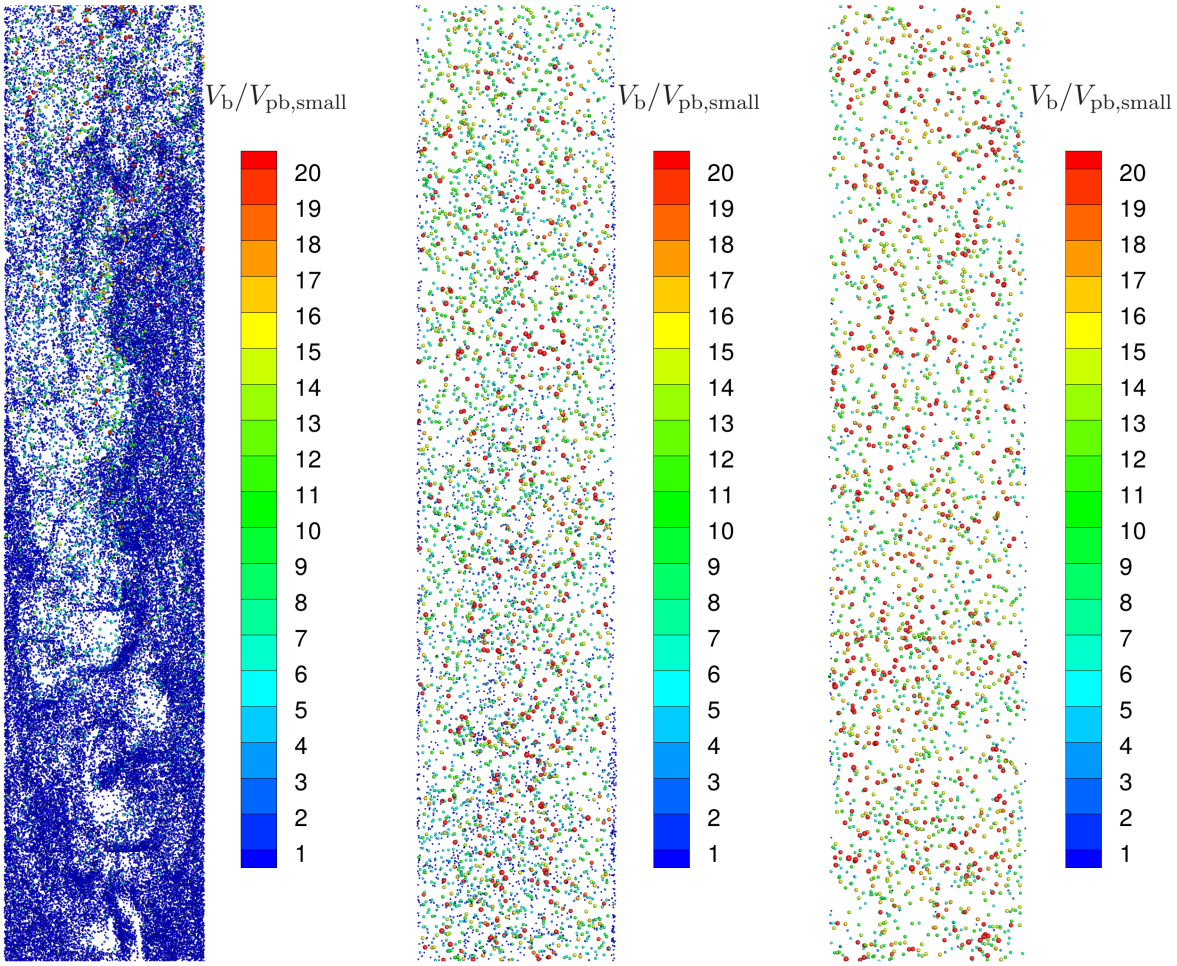

(a) $5 \leq x/d_c < 10$ **(b)** $15 \leq x/d_c < 20$ **(c)** $25 \leq x/d_c < 30$

Fig. 11.19. Snapshots of three sections of the bubble column for the case of small clean bubbles. Only bubbles with coordinates in the range $-0.1 \leq z/d_c \leq 0.1$ are shown. Colors chosen according to $V_b/V_{pb,small}$. Note that the bubbles are magnified by a factor of three. Based on Hoppe and Breuer (2018).

bubbles. With an increasing vertical position the number of primary bubbles reduces due to coalescence processes, see Fig. 11.19(b) depicting the middle section of the bubble column. Consequently, the number of larger bubbles increases. This process is continued towards the uppermost section shown in Fig. 11.19(c), where the normalized volume of the majority of bubbles is within a range of $5 \lesssim V_b/V_{pb,small} \lesssim 20$. Yet, on close inspection of Fig. 11.19(c) a significant number of primary bubbles can be found. Additionally, bubbles containing more than 20 primary bubbles are existing as well.

Comparing these observations with Fig. 11.20 depicting the case of small contaminated bubbles reveals several differences in the evolution of the bubbles. It is obvious that the number of primary bubbles decreases faster compared with the case of clean bubbles, e.g., in the upper part of the lowermost section of the column containing small contaminated bubbles (Fig. 11.20(a)) a large amount of already coalesced bubbles is present, whereas in

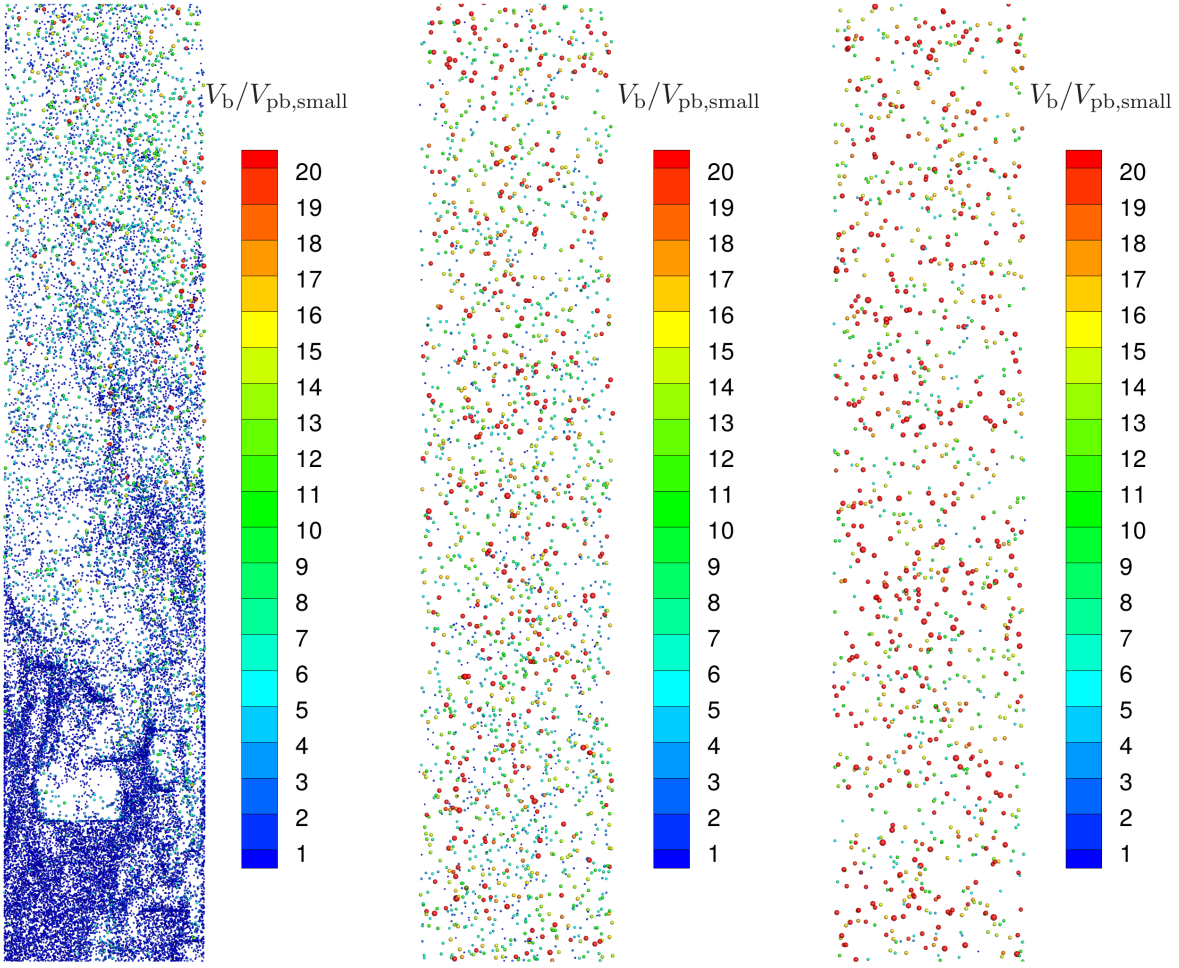

(a) $5 \leq x/d_c < 10$ **(b)** $15 \leq x/d_c < 20$ **(c)** $25 \leq x/d_c < 30$

Fig. 11.20. Snapshots of three sections of the bubble column for the case of small contaminated bubbles. Only bubbles with coordinates in the range $-0.1 \leq z/d_c \leq 0.1$ are shown. Colors chosen according to $V_b/V_{pb,small}$. Note that the bubbles are magnified by a factor of three. Based on Hoppe and Breuer (2018).

the clean case (Fig. 11.19(a)) the lowermost section is mostly filled with primary bubbles. Similar results are obtained for the sections further away from the bottom of the column. In the case of contaminated bubbles the middle section (Fig. 11.20(b)) is significantly more devoid of small primary bubbles than in the case of clean bubbles, since the majority of the primary bubbles has coalesced before. This leads to the fact that no primary bubble is visible in Fig. 11.20(c) anymore, i.e., in the uppermost section of the bubble column mostly large ($V_b/V_{pb,small} \geq 10$) bubbles are present. Furthermore, the number of very large bubbles of $V_b/V_{pb,small} \geq 20$ is also visibly increased compared with the case of clean bubbles shown in Fig. 11.19(c).

A completely different behavior of the bubbles is found for the case of large clean primary bubbles. In all three sections depicted in Fig. 11.21 a very large number of primary bubbles exists. For example, the lowermost section (Fig. 11.21(a)) of the column

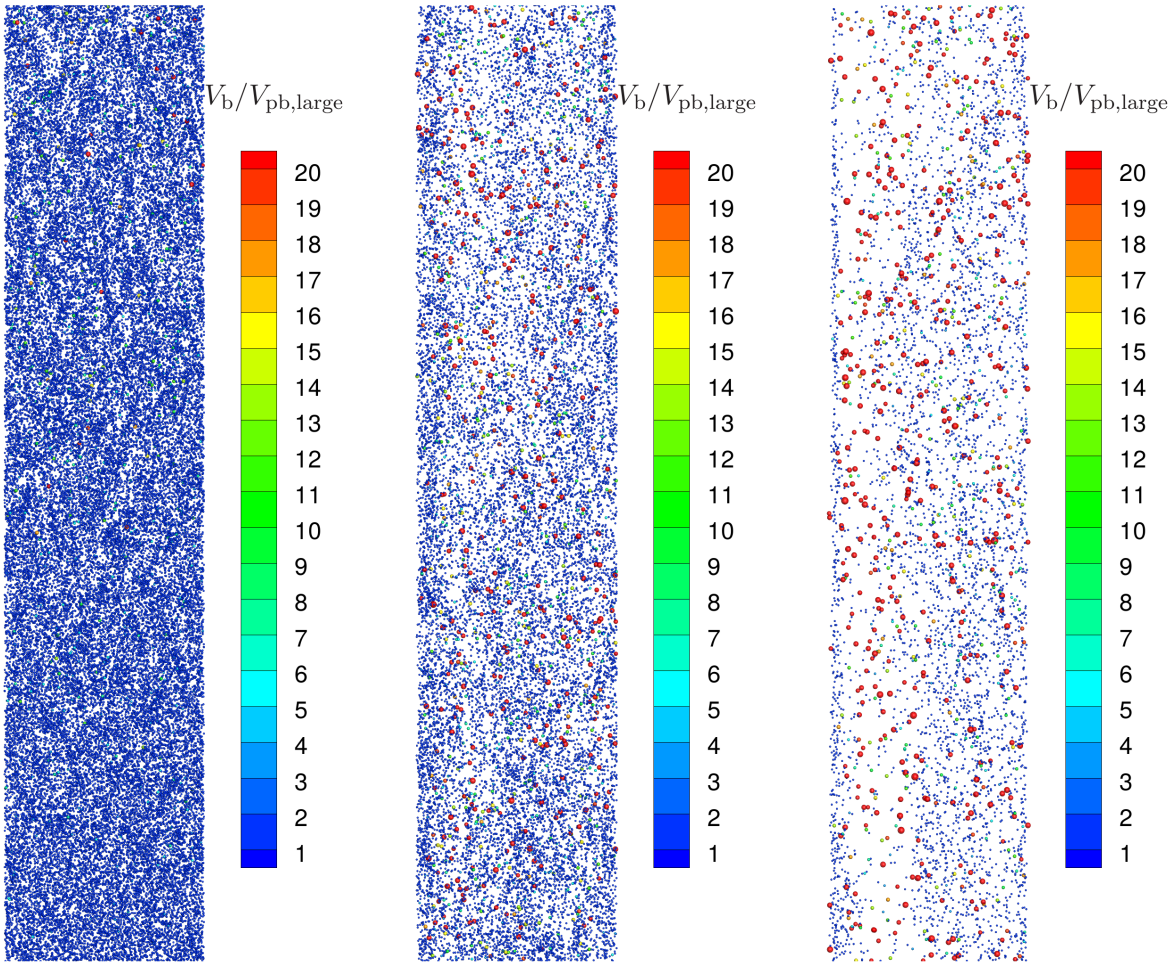

(a) $5 \leq x/d_c < 10$ **(b)** $15 \leq x/d_c < 20$ **(c)** $25 \leq x/d_c < 30$

Fig. 11.21. Snapshots of three sections of the bubble column for the case of large clean bubbles. Only bubbles with coordinates in the range $-0.1 \leq z/d_c \leq 0.1$ are shown. Colors chosen according to $V_b/V_{pb,large}$. Note that the bubbles are magnified by a factor of three. Based on Hoppe and Breuer (2018).

is nearly exclusively occupied by bubbles of $V_b/V_{pb,large} = 1$. Consequently, coalescence processes are only rarely found in this region, see Fig. 11.26 shown below quantifying this observation. Similarly, in the middle (Fig. 11.21(b)) and uppermost (Fig. 11.21(c)) sections primary bubbles represent the vast majority of all bubbles. While larger bubbles generated by coalescence processes are also present in the upper regions of the column, they are encountered less frequently than the primary bubbles.

Again, considering contaminated bubbles significantly alters the coalescence behavior in the column compared with the case of large clean primary bubbles. The evolution of the bubbles according to the vertical position in the column is shown in Fig. 11.22. It is obvious that the number of primary bubbles strongly decreases with an increasing distance from the bottom of the column, i.e., Fig. 11.22(a) demonstrates that in the upper part of the lowermost section a significant number of large bubbles has already been generated

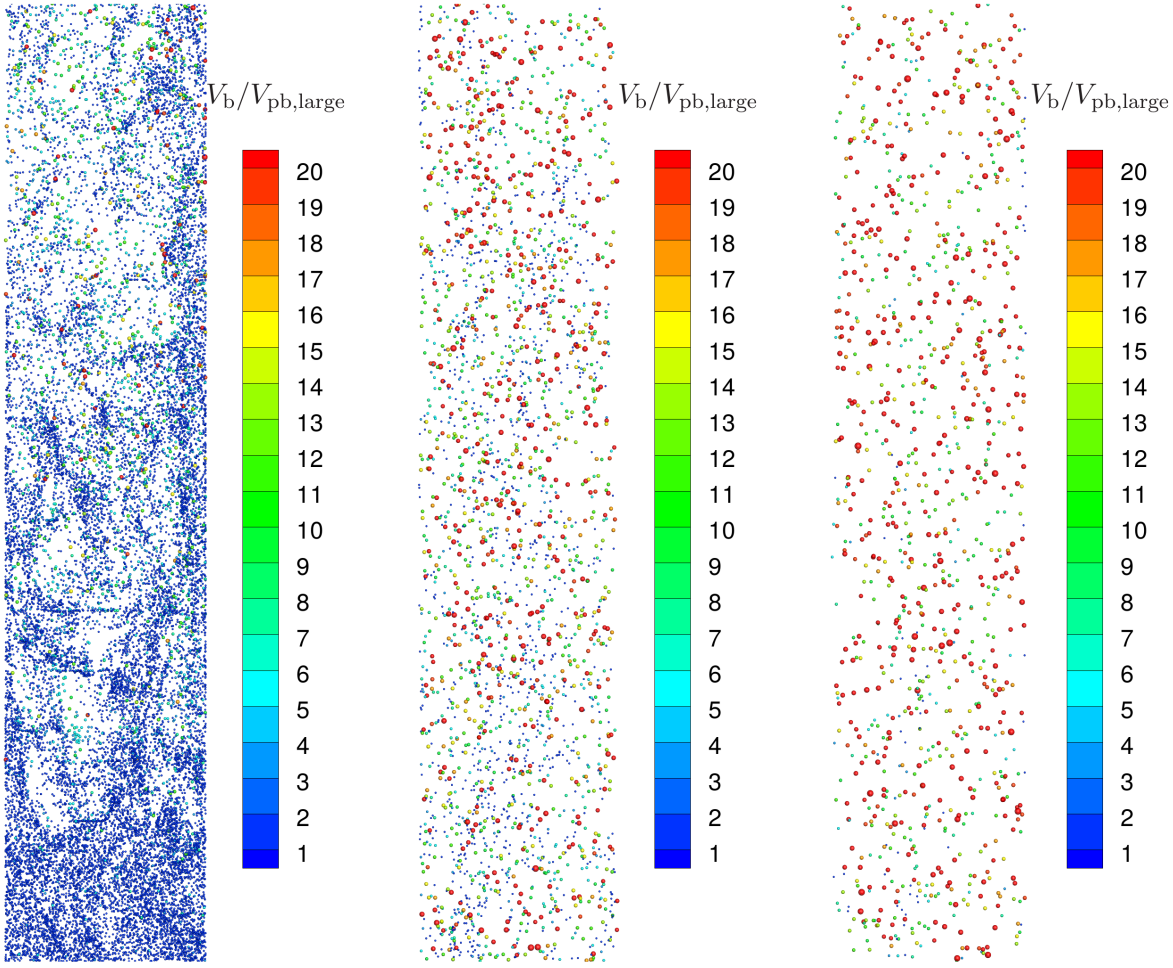

(a) $5 \leq x/d_c < 10$ **(b)** $15 \leq x/d_c < 20$ **(c)** $25 \leq x/d_c < 30$

Fig. 11.22. Snapshots of three sections of the bubble column for the case of large contaminated bubbles. Only bubbles with coordinates in the range $-0.1 \leq z/d_c \leq 0.1$ are shown. Colors chosen according to $V_b/V_{pb,large}$. Note that the bubbles are magnified by a factor of three. Based on Hoppe and Breuer (2018).

by coalescence processes. Consequently, in the middle (Fig. 11.22(b)) and especially in the uppermost section (Fig. 11.22(c)) only a few primary bubbles remain, while large previously coalesced bubbles make up the majority of the existing bubbles.

Comparing the snapshots of the lowermost sections of the four cases considered (subfigure **(a)** of Figs. 11.19 to 11.22, respectively) reveals significant difference between them. The large clean primary bubbles shown in Fig. 11.21(a) are uniformly distributed inside the column. In contrast, the small clean and contaminated bubbles as well as the large contaminated bubbles shown in Figs. 11.19(a), 11.20(a) and 11.22(a) are distributed more irregularly in the lowermost section of the bubble column, i.e., a significant number of areas with a low bubble number density can be seen for these cases, whereas in other regions of the lowermost section of the column the number density is visibly higher. Since bubbles tend to closely follow the fluid velocity at their position, it is likely that the

inhomogeneities observed in Figs. 11.19(a), 11.20(a) and 11.22(a) are caused by turbulent eddies of the flow. Figure 11.23 depicts snapshots of the two-dimensional contour plots of the instantaneous velocity of the fluid in the vertical direction for the lowermost section ($5 \leq x/d_c \leq 10$) of the bubble column for all cases considered. It can be seen that for the cases of small clean and contaminated bubbles as well as for the case of large contaminated bubbles (Figs. 11.23(a), (b) and (d), respectively) turbulent fluid structures are indeed present. However, in the case of large clean bubbles (Fig. 11.23(c)) no velocity fluctuations are visible, which agrees with the previous observations. These velocity fluctuations, which can only be excited by the bubbles since they are the only source of momentum, cause an increased number of inter-bubble collisions resulting in an augmented coalescence of the bubbles. Hence, it appears that in the case of large clean primary bubbles turbulent fluid fluctuations cannot be excited as effectively as in the other cases, where the turbulent fluid structures seen in Figs. 11.23(a), (b) and (d) are responsible for the irregular distribution of the bubbles in the lowermost section of the column. Consequently, a vastly different evolution of the dispersed phase is obtained for large clean primary bubbles. The reasons for the differences are discussed below.

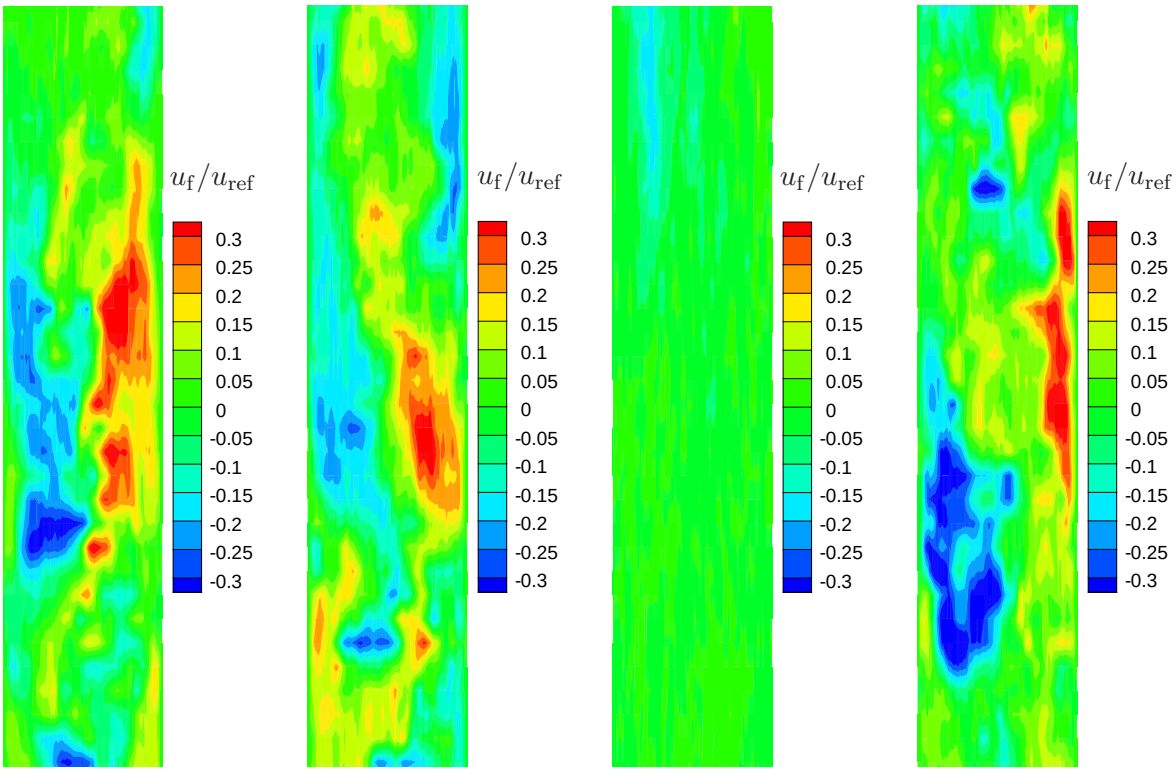

(a) Small clean primary bubbles. **(b)** Small cont. primary bubbles. **(c)** Large clean primary bubbles. **(d)** Large cont. primary bubbles.

Fig. 11.23. Two-dimensional contour plots of the instantaneous fluid velocity in the vertical direction for the lowermost section ($5 \leq x/d_c \leq 10$) of the column.

In order to further investigate the coalescence in a bubble column in a more quantitative manner, Fig. 11.24 depicts the bubble size distributions in form of probability density

functions (PDF) averaged at different sections (see Fig. 10.1) of the bubble column. The probability density functions are based on the ratio of the bubble volume to the volume of the corresponding primary bubbles released into the fluid at the bottom of the bubble column. The probability density functions shown in Fig. 11.24 are obtained by counting the occurrence of each bubble within a certain size interval $\Delta V_\mathrm{b}/V_\mathrm{pb}$ during the averaging period of time in the respective sections of the bubble column. Since breakup is not considered in this study due to the small turbulent stresses, bubbles with a size larger than the respective primary bubbles can only be generated by coalescence. Furthermore, the volumes of the bubbles can only be a multiple of the primary bubble volume. Hence, in the context of the present bubble column it is meaningful to set the width of the size interval to $\Delta V_\mathrm{b}/V_\mathrm{pb} = 1$, i.e., each bubble of a given size is counted for the calculation of the probability density function. Afterwards, the numbers of bubbles of size $V_\mathrm{b}/V_\mathrm{pb}$ are normalized by the total number of recorded bubbles and the width of the size interval $\Delta V_\mathrm{b}/V_\mathrm{pb} = 1$.

It is apparent from Fig. 11.24 that in all cases the bubble size distributions evolve with an increasing height of the considered averaging section. This evolution exhibits significant effects of the primary bubble size and the contamination of the bubbles. For the case of small clean primary bubbles (Fig. 11.24(a)) the probability density function at the lowermost averaging section between $5 \leq x/d_\mathrm{c} < 10$ (black line in Fig. 11.24) is close to unity for $V_\mathrm{b}/V_\mathrm{pb,small} = 1$ and then strongly decreases towards large bubble volumes. This means that in this region of the bubble column most of the bubbles are still primary bubbles, which has also been observed in Fig. 11.19(a). The probability density function transforms to a profile with a distinct double-peak structure at $25 \leq x/d_\mathrm{c} < 30$ (magenta line in Fig. 11.24). The first sharp peak is found at $V_\mathrm{b}/V_\mathrm{pb,small} = 1$ and a second broad peak at $V_\mathrm{b}/V_\mathrm{pb,small} \approx 8$. This result agrees with the snapshots in Figs. 11.19(b) and (c) of the bubbles in case of small clean primary bubbles, i.e., at the top of the column most of the bubbles consist of about 5 to 20 primary bubbles due to prior coalescence processes, while a significant number of primary bubbles remains.

Comparing Figs. 11.24(a) and (b) reveals that the contamination of the primary bubbles by surfactants causes a shift of the averaged probability density functions towards larger bubble diameters in all sections of the bubble column. For example, in the lowermost section the probability density function nearly extends up to $V_\mathrm{b}/V_\mathrm{pb,small} = 30$ in Fig. 11.24(b), while it only reaches up to $V_\mathrm{b}/V_\mathrm{pb,small} = 20$ for the clean bubbles (Fig. 11.24(a)). Especially in the sections further away from the injection region a strong reduction of the probability density function of the contaminated primary bubbles is visible, which is not present for clean bubbles. Again, this agrees with the qualitative results shown in Fig. 11.20 that the contaminated bubbles possess a much stronger tendency for coalescence than the clean bubbles.

Lastly, as already expected from the discussion of the snapshots the differences between the probability density functions of clean and contaminated bubbles are even more pronounced for large primary bubbles. Figure 11.24(c) depicts the probability density functions for the case of clean bubbles. It is apparent that the PDFs in the lower size range vary only slightly with an increased height in the column, i.e., in all sections the probability density is close to unity for the primary bubbles. The probability density function is

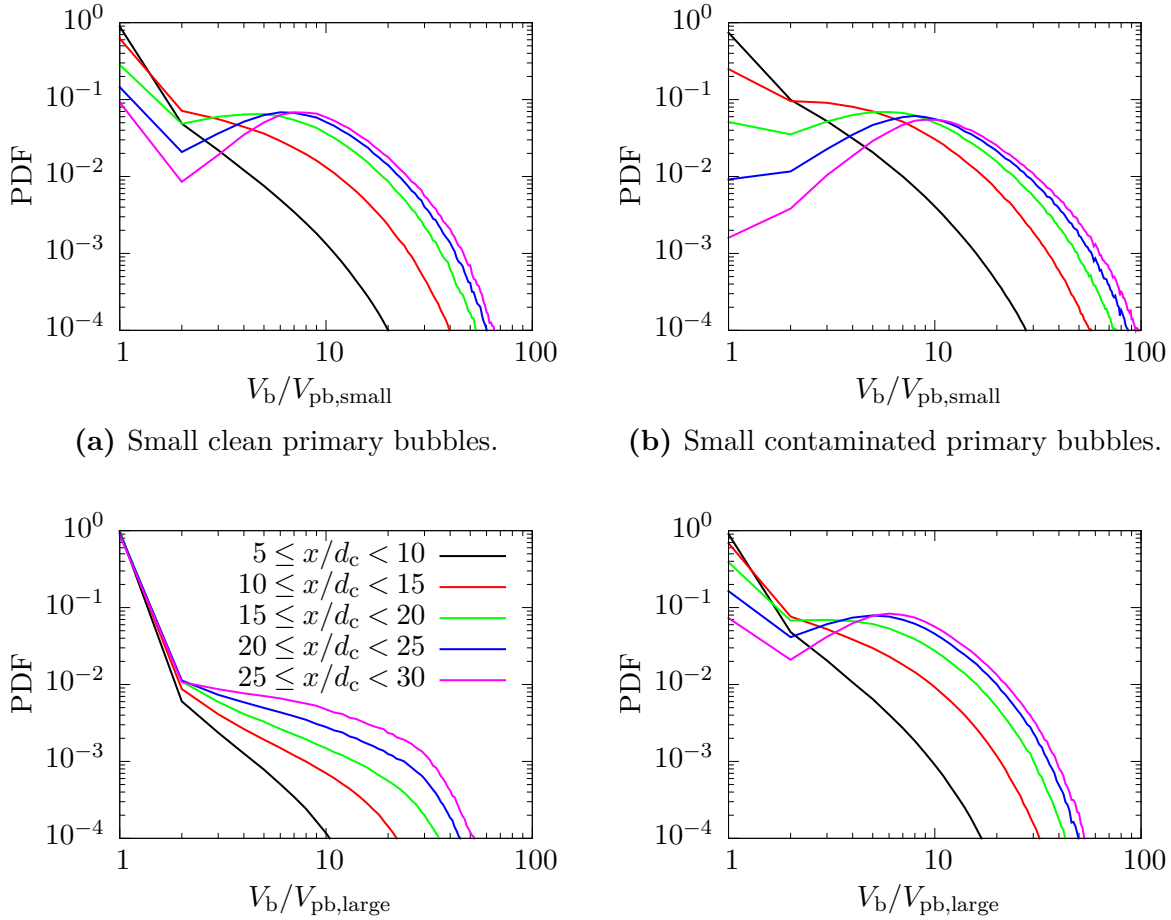

(a) Small clean primary bubbles.

(b) Small contaminated primary bubbles.

(c) Large clean primary bubbles.

(d) Large contaminated primary bubbles.

Fig. 11.24. Average bubble size distribution in different sections of the bubble column (see Fig. 10.1 in Section 10.4) for small and large primary bubbles with both clean and contaminated surface conditions. Based on Hoppe and Breuer (2018).

smaller by at least two orders of magnitude for larger bubbles of $V_b/V_{pb,large} \geq 2$ meaning that all sections of the bubble column are mostly populated by primary bubbles with only a few larger bubbles present. This complies with Fig. 11.21, where the majority of the visible bubbles are primary bubbles. Here, it is important not to confuse the evolution of the probability density function with the evolution of the bubble number density. Naturally, the latter quantity decreases for an increasing distance to the bottom of the column (compare Figs. 11.21(a) and (c)) due to coalescence processes. On the other hand, a PDF indicates what portion of the total number of bubbles have a volume within a certain range. Hence, despite the decreasing number of bubbles in Fig. 11.21(c) compared with Fig. 11.21(a), the ratio of the number of primary bubbles to the total number of bubbles remains nearly unchanged in the different sections. If large contaminated bubbles are considered, the probability density functions of bubbles of sizes of about $V_b/V_{pb,large} = 10$ increases by one to two orders of magnitude in the upper regions of the column compared

with the clean case. At the same time the probability density of the primary bubbles decreases, see Fig. 11.22 where this has been observed as well.

In order to investigate the reasons behind the different evolution of the bubble phase in the considered cases, the cumulative number of all collision and coalescence processes, $N_{\mathrm{coll}}^{\mathrm{cumul}}$ and $N_{\mathrm{coal}}^{\mathrm{cumul}}$, occurring in the entire bubble column are shown in Fig. 11.25. Additionally, the resulting total coalescence rate $N_{\mathrm{coal}}^{\mathrm{cumul}}/N_{\mathrm{coll}}^{\mathrm{cumul}}$ is shown. The figures compare the results of the small and the large bubbles for both clean and contaminated surface conditions. Firstly, since the cumulative numbers of collision and coalescence processes shown in Figs. 11.25(a) and (b) linearly increase with time, it is obvious that in all cases the bubble column has reached a statistical steady-state. Furthermore, it can be seen from Fig. 11.25(a) that in the case of small primary bubbles the cumulative number of collisions is larger than in the case of large primary bubbles. This result is expected, since the volume flux of the bubbles is set to $\dot{Q}_{\mathrm{b}}^{*} = 1.89 \times 10^{-4}$ in all cases. Hence, the number of small primary bubbles released per time step is higher by a factor of $n_{\mathrm{pb,small}}/n_{\mathrm{pb,large}} = 11/6 \approx 1.83$ compared with the case of large primary bubbles. According to the kinetic theory of gases (Pauli, 1973), the collision frequency Z is proportional to the square of the number density n and the diameter of the (spherical) bubbles:

$$Z \sim (n\, d_{\mathrm{b}})^2 . \tag{11.1}$$

Assuming a uniform distribution the number density of the small and large bubbles can be approximated by the corresponding number of released bubbles, i.e., $n_{\mathrm{pb,small}}$ and $n_{\mathrm{pb,large}}$, respectively. Hence, one can estimate the increase of the collision frequency in the case of the small compared with the large primary bubbles to be:

$$\frac{Z_{\mathrm{small}}}{Z_{\mathrm{large}}} = \left(\frac{d_{\mathrm{pb,small}}}{d_{\mathrm{pb,large}}}\right)^2 \left(\frac{n_{\mathrm{pb,small}}}{n_{\mathrm{pb,large}}}\right)^2 \approx 2.16, \tag{11.2}$$

where the respective diameters of the released primary bubbles have been inserted. It is apparent from Fig. 11.25(a) that a factor of about two is a good approximation for the difference between the cumulative number of collision processes of small and large bubbles for both clean and contaminated bubbles.

For both primary bubble sizes the cumulative number of collisions is augmented by the contamination of the bubbles. In case of the small primary bubbles the number of collisions is about 63.3% higher for the contaminated bubbles, while the increase amounts to 87.5% in case of the large primary bubbles. Interestingly, for both primary bubble sizes the cumulative number of coalescence processes of clean and contaminated bubbles is approximately equal, see Fig. 11.25(b). The coalescence rate $N_{\mathrm{coal}}^{\mathrm{cumul}}/N_{\mathrm{coll}}^{\mathrm{cumul}}$ shown in Fig. 11.25(c) reveals that in the present case clean bubbles always coalesce regardless of their size, i.e., the coalescence for both small and large clean primary bubbles is equal to unity. For the contaminated case the total coalescence rate is about 64% for small primary bubbles and 56% for large primary bubbles. From these results one may conclude that all bubbles that have collided once would eventually coalesce. For clean bubbles the coalescence process would directly occur at the first contact. In case of

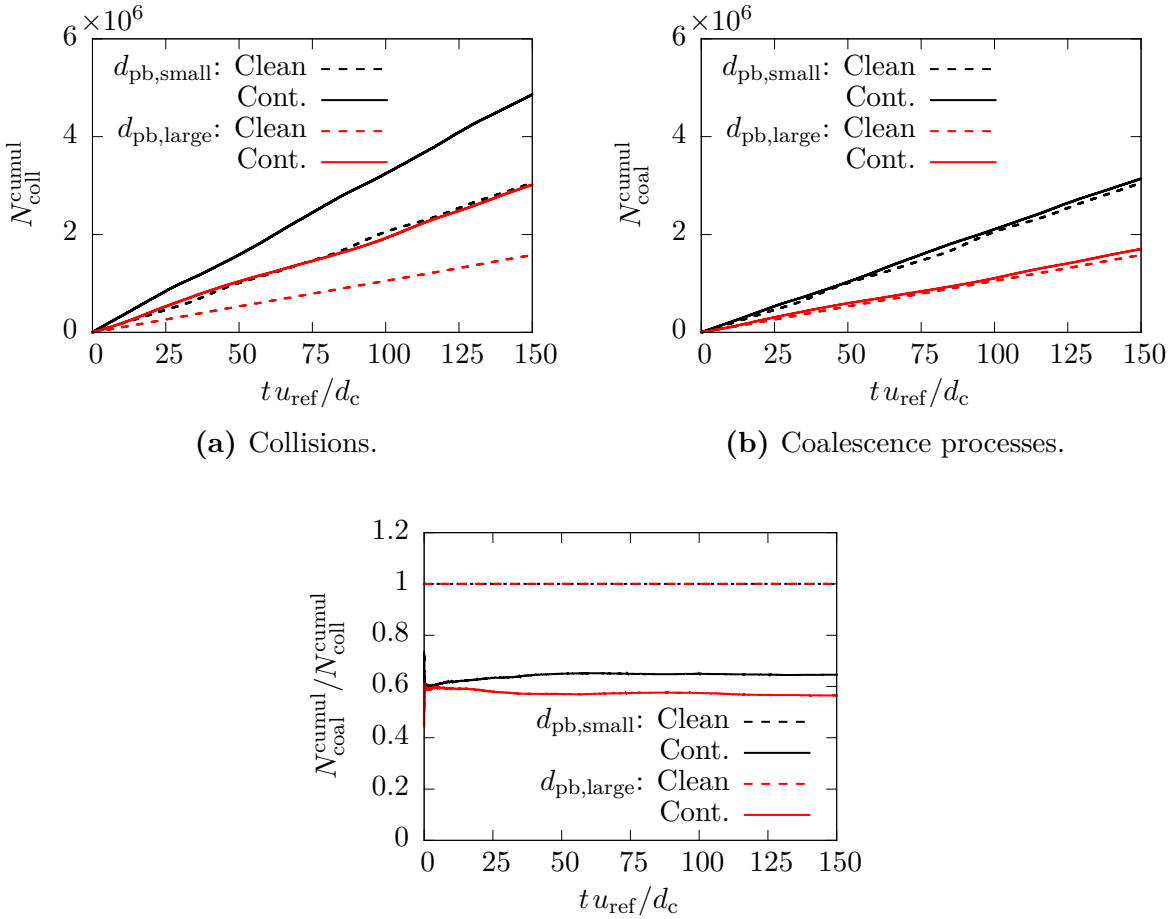

(a) Collisions.

(b) Coalescence processes.

(c) Coalescence rate.

Fig. 11.25. Temporal evolution of (a) the cumulative number of collision processes $N_{\mathrm{coll}}^{\mathrm{cumul}}$, (b) the cumulative number of coalescence processes $N_{\mathrm{coal}}^{\mathrm{cumul}}$ and (c) the total coalescence rate $N_{\mathrm{coal}}^{\mathrm{cumul}}/N_{\mathrm{coll}}^{\mathrm{cumul}}$. Based on Hoppe and Breuer (2018).

contaminated bubbles, which initially rebound from each other, the separation after the collision might not be sufficiently far. Consequently, the contaminated bubbles could re-approach each other with a lower collision velocity, i.e., repeated collisions occur until the coalescence condition is fulfilled at some point. Kuerten and Vreman (2016) observed a similar mechanism of repeated collisions of solid particles in a turbulent channel flow. The results of rising bubbles coalescing with a free surface presented in Section 11.3.1 already revealed that a decreasing collision velocity significantly improves the chance of a successful coalescence process due to the reduced deformation of the colliding bubbles, which leads to a smaller amount of liquid being trapped between the bubbles. Naturally, a smaller amount of liquid can be drained faster during the contact time leading to a stronger reduction of the thickness of the liquid film trapped between the bubbles. Hence, a coalescence process is more likely.

It is possible that the aforementioned effect of repeated collisions is indeed partly responsible for the temporal evolution of the cumulative numbers of coalescence processes

observed in Fig. 11.25(b). However, this mechanism would require that the distribution of the averaged number of coalescence processes per time step along the height x/d_c of the column is nearly the same for clean and contaminated bubbles of the same primary bubble size. Only the distribution of the number of collisions per time step would have to be higher for contaminated bubbles. However, Fig. 11.26 demonstrates that the distributions of the average number of coalescence processes per time step differs for clean and contaminated bubbles of both primary bubble sizes. For example, it can be seen in Fig. 11.26 that in the vicinity of the region, where the primary bubbles are released, N_{coal} per time step is higher for contaminated bubbles compared with the case of clean bubbles. For small primary bubbles this is the case up to a height of $x/d_c \approx 7$, while the region extends to $x/d_c \approx 12$ for large primary bubbles. At larger heights of the column the number of coalescence processes per time step is actually larger for the case of clean bubbles. This effect is more pronounced for the case of large primary bubbles, compare Figs. 11.26(c) and (d). Hence, it is apparent that the mechanism of repeated collisions described by Kuerten and Vreman (2016) is not dominant in the present case.

In order to explain the previous results, a different mechanism is required. Coming back to the explanation that turbulent structures in the fluid induced by the bubbles are responsible for the differences in the distribution of the bubbles observed in the snapshots (Figs. 11.19 to 11.22), the averaged turbulent kinetic energy of the fluid $\langle k^f_{turb} \rangle = \langle u'_{f,i}\, u'_{f,i} \rangle / 2$ is displayed in Fig. 11.27. Note that the averaged one-dimensional profile along the height x/d_c is obtained by averaging in time and in the radial and circumferential directions of the column. Firstly, it is apparent from Fig. 11.27 that the turbulent kinetic energy is higher for contaminated bubbles than for clean bubbles. This is true for both primary bubble sizes. However, the effect is especially pronounced for the case of large primary bubbles. Secondly, one can see from Fig. 11.27 that for both clean and contaminated bubbles the turbulent kinetic energy of the fluid is larger for small primary bubbles than for large ones. For contaminated bubbles the maximum of the turbulent kinetic energy of the fluid is larger for small primary bubbles, i.e., the dimensionless maxima are 12.8×10^{-3} and 11.6×10^{-3} for small and large contaminated primary bubbles, respectively. Again, this effect is especially visible for clean bubbles, where $\langle k^f_{turb} \rangle$ is much larger for the case of small primary bubbles compared with the large primary bubbles. Note that a possible explanation for this behavior is provided below.

Due to the augmented fluid turbulence, the velocity fluctuations of the bubbles are larger for the case of contaminated primary bubbles (both sizes) and small clean primary bubbles. Consequently, a higher number of bubble-bubble collisions is found for these cases compared with the case of large clean primary bubbles. Note that Breuer and Hoppe (2017) found a similar effect for the case of solid particles, see Sections 11.2.2 and 11.2.3. In this case the additional velocity fluctuations of the fluid at the position of the particles due to the application of an enhanced subgrid-scale model lead to an increased number of inter-particle collisions.

The physical mechanism responsible for these results is probably the drag force, which varies for the four cases considered. By inspecting Eqs. (4.8) and (4.12) defining the drag coefficient for clean and contaminated bubbles, it is obvious that the drag coefficient depends on the surface condition as well as on the bubble Reynolds number Re_b, which is

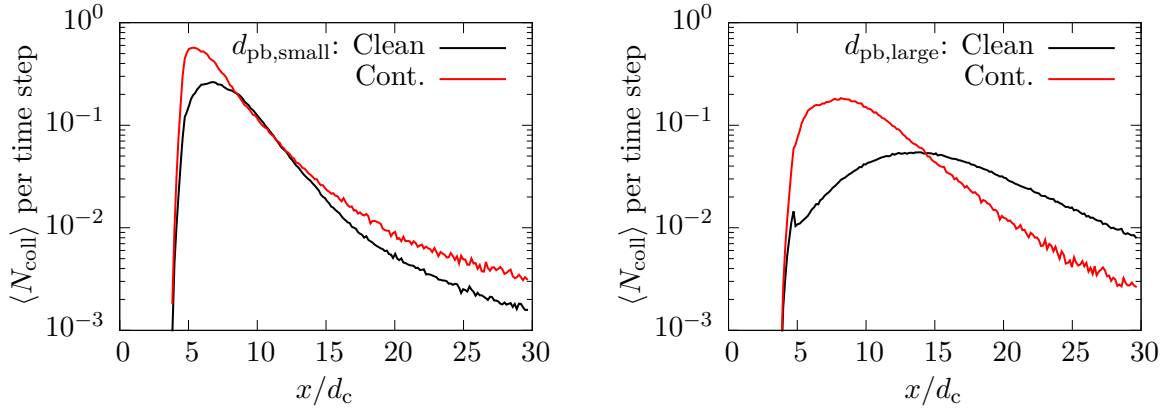

(a) Small primary bubbles. **(b)** Large primary bubbles.

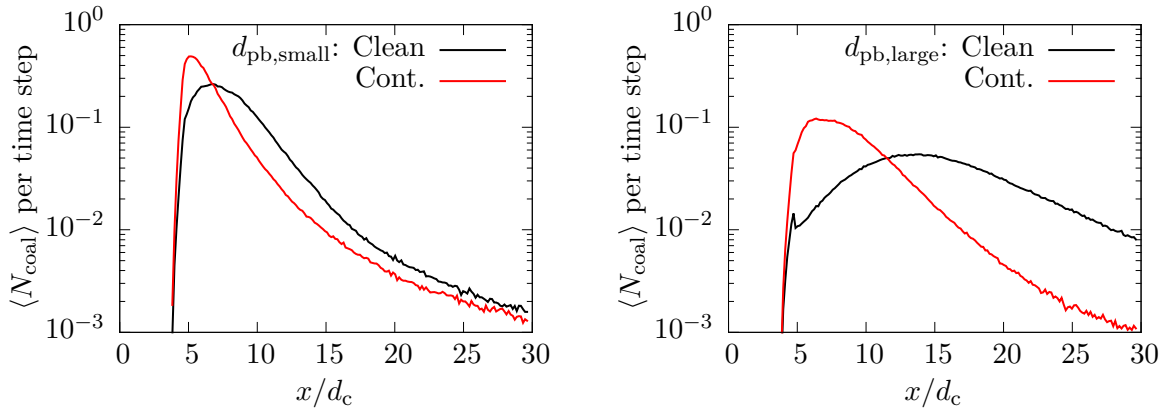

(c) Small primary bubbles. **(d)** Large primary bubbles.

Fig. 11.26. Spatial variation along the height of the bubble column of the averaged number of collisions per time step for the case of (a) the small and (b) the large primary bubbles and the corresponding number of coalescence processes per time step for the case of (c) the small and (d) the large primary bubbles. Based on Hoppe and Breuer (2018).

influenced by the bubble size as well as its velocity. Note that the velocity of the bubbles is given by the equation of motion (4.1), which, in turn, depends on the drag force.

Firstly, the effect of the contamination of the bubbles is considered. Dividing Eq. (4.12) by Eq. (4.8) it is obvious that for a bubble Reynolds number tending to zero the drag coefficient of a contaminated bubble is by a factor of at least $C_{\mathrm{D,cont.}}/C_{\mathrm{D,clean}} \approx 24/16 = 1.5$ larger than the one applied for a clean bubble. This ratio increases further for an increasing $\mathrm{Re_b}$. Consequently, the momentum transferred to the fluid by the bubbles is larger for contaminated bubbles compared with clean bubbles. This explains the augmented turbulent kinetic energy of the fluid seen in Fig. 11.27 for contaminated bubbles.

Another mechanism playing an important role in the present cases is the influence of the actual sizes of the bubbles present in the flow. As already explained above, the drag force also depends on the bubble properties in form of $\mathrm{Re_b}$. Thus, both an increased size and an

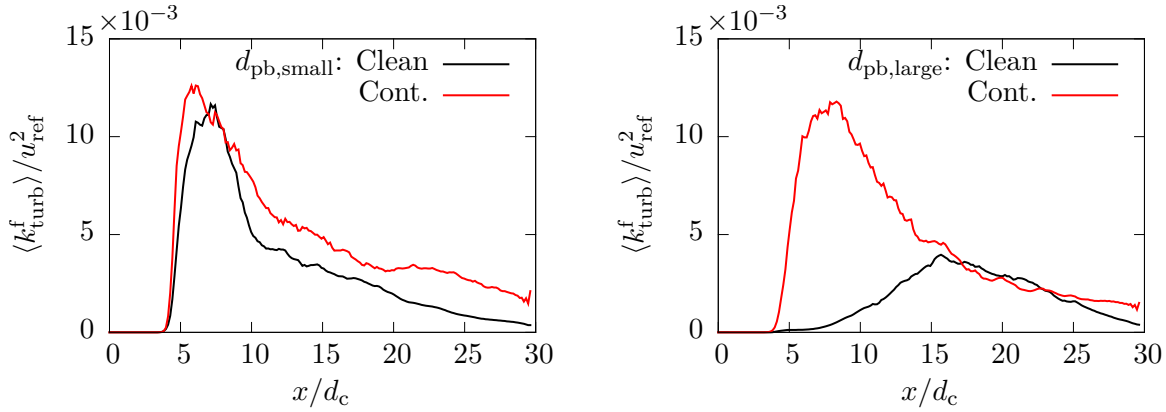

(a) Small primary bubbles. **(b)** Large primary bubbles.

Fig. 11.27. Spatial variation of the averaged dimensionless turbulent kinetic energy of the fluid along the height of the bubble column. Based on Hoppe and Breuer (2018).

increased velocity augments the momentum coupling back to the fluid. Hence, if for some reason large coalesced bubbles containing several primary bubbles are present in the flow, these large bubbles transfer an increased amount of momentum to the fluid. Furthermore, the source of momentum is concentrated at one location within a certain volume of fluid, whereas the corresponding primary bubbles would transfer their momentum distributed within the considered volume. Due to the more concentrated momentum source, larger fluid velocity fluctuations can be excited. Note again that a quantitative discussion is difficult, since the strength of the momentum sources are dependent on the actual properties of the bubbles.

Comparing the cases of small and large clean primary bubbles, the number density of bubbles is much larger for the small primary bubbles, since a larger number (11 compared with 6) is released into the fluid at each time step. It was already argued above that the increased bubble density leads to an increased frequency of collisions between the bubbles. Consequently, more coalesced bubbles of a larger size are present in the fluid, which can induce more turbulence. Subsequently, the induced turbulent fluctuations of the fluid lead to more bubble-bubble collision and coalescence processes generating even more large bubbles. Hence, a self-fortifying feedback loop is obtained, where the formation of larger bubbles leads to more turbulence yielding even more large bubbles. Note that this mechanism is reinforced by the contamination of the bubbles. Due to the increased momentum transfer by contaminated bubbles, the formation of large bubbles is augmented, which improves the momentum transfer.

Summarizing, the augmented momentum transfer to the fluid is responsible for the present observations. The physical mechanisms behind the momentum transfer are a larger drag coefficient in case of contaminated compared with clean bubbles or an improved formation of large turbulence-inducing bubbles. Both mechanisms reinforce each other leading to a complex non-linear self-fortifying response of the system to variations of the properties of the primary bubbles. Hence, for the case of large clean primary bubbles the induced turbulence is small, since the drag coefficient is smaller compared with con-

taminated bubbles and the collision frequency of the bubbles is reduced compared with the case of small primary bubbles hindering the formation of larger bubbles in the first place. Consequently, only turbulence of a comparably small magnitude can be induced (Fig. 11.27(b)), which further prevents coalescence. In contrast, considering large contaminated bubbles allows for an improved momentum transfer to the fluid by the different surface condition. Subsequently, larger bubbles are present due to augmented coalescence, which again leads to an increase of the turbulent velocity fluctuations. Similarly, for the case of small clean bubbles the increased bubble collision frequency caused by the larger number density of the bubbles leads to the presence of large turbulence-inducing bubbles. Lastly, for the case of small contaminated bubbles both effects are combined, i.e., both a high collision frequency and the augmented momentum transfer due to the bubble contamination play a role for this case.

Note that the pronounced deviation of the turbulent kinetic energy of the fluid for clean large primary bubbles (Fig. 11.27(b)) to the other cases agrees with the large differences observed in the snapshots of the clean and contaminated bubbles in Figs. 11.19 to 11.22 and, consequently, between the corresponding bubble size distributions shown in Fig. 11.24. For the case of small primary bubbles the turbulent kinetic energy is only marginally larger for contaminated bubbles than for clean bubbles. Consequently, both the snapshots (Figs. 11.19 and 11.20) and the bubble size distributions (Figs. 11.24(a) and (b)) are very similar to each other. As argued above, the most pronounced difference between the two cases is that the number of primary bubbles is more strongly reduced for contaminated bubbles, which can be explained by the larger values of $\langle k^{\mathrm{f}}_{\mathrm{turb}} \rangle$. Similarly, by comparing Figs. 11.27(a) and (b) it is apparent that in the case of large contaminated primary bubbles the turbulent kinetic energy of the fluid is on approximately the same level as for the small bubbles resulting in similar appearances of the corresponding snapshots and size distributions. In contrast, if large clean primary bubbles are considered, the bubbles are not able to induce sufficiently strong velocity fluctuations in the horizontal plane of the column. Hence, the occurrence of bubble-bubble collisions and coalescence processes is suppressed, which in turn hinders the formation of coalesced bubbles. Additionally, the reduced number of bubbles of varying size due to fewer coalescences restricts the range of the rise velocity of the bubbles leading to a further impairment of collision and coalescence processes.

In order to demonstrate the mechanism explained above more clearly, the magnitude of the momentum sources $\langle S_{\mathrm{b}} \rangle = \sqrt{\langle S_{\mathrm{y}} \rangle^2 + \langle S_{\mathrm{z}} \rangle^2}$ of the bubbles (Eq. (5.3)) averaged in time and along the (vertical) axial direction of the column between $5 \leq x/d_{\mathrm{c}} \leq 10$ is shown in Fig. 11.28 in its dimensionless form, i.e., $\langle S^*_{\mathrm{b}} \rangle = \langle S_{\mathrm{b}} \rangle / (\rho_{\mathrm{f}}\, u_{\mathrm{ref}}\, d_{\mathrm{c}}^3)$. In Figs. 11.28(a) and (b) the dimensionless strength of the momentum sources for small clean and contaminated primary bubbles are depicted, while Figs. 11.28(c) and (d) show the case of large primary bubbles. It is apparent that the cases of small primary bubbles are very similar to the case of large contaminated bubbles (Fig. 11.28(d)), i.e., the amount of momentum transferred from the bubbles to the fluid is comparable (see below for more details). However, comparing Fig. 11.28(c) with the remaining cases, it is obvious that the momentum transferred to the fluid by the bubbles is about one order of magnitude smaller for the case of large clean primary bubbles. Further averaging the dimensionless strength $\langle S^*_{\mathrm{b}} \rangle$

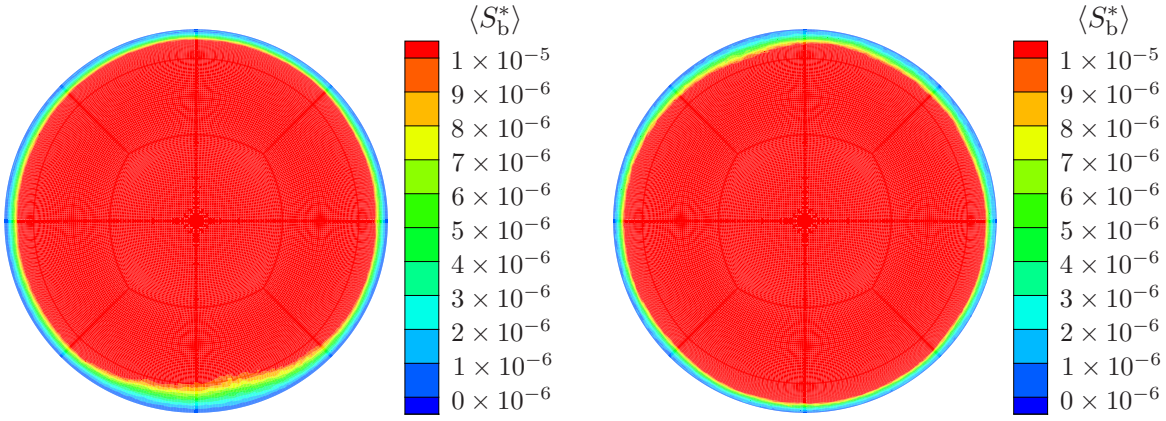

(a) Small clean primary bubbles.

(b) Small contaminated primary bubbles.

(c) Large clean primary bubbles.

(d) Large contaminated primary bubbles.

Fig. 11.28. Dimensionless strength of the momentum sources averaged temporally and spatially between $5 \leq x/d_c < 10$. Based on Hoppe and Breuer (2018).

of the momentum sources in the radial and the circumferential direction yields the total magnitude of the momentum sources $\langle S^*_{b,tot} \rangle$ in the lowermost section ($5 \leq x/d_c \leq 10$) of the column. The resulting values are summarized in Table 11.4. The visual impression that within the lowermost section of the column the bubbles in the case of small clean and contaminated primary bubbles as well as in the case of large contaminated primary bubbles on average transfer a comparable amount of dimensionless momentum to the fluid is confirmed. Furthermore, the strength of the momentum sources is indeed more than one order of magnitude smaller in the case of large clean primary bubbles.

In Fig. 11.29 the averaged relative collision velocity based on the results of the present simulation is shown for both primary bubble sizes (solid lines). Additionally, an estimation

Tab. 11.4. Comparison of the total magnitude of the bubble momentum sources $\langle S^*_{\mathrm{b,tot}} \rangle$ averaged in time and in space within $5 \leq x/d_\mathrm{c} \leq 10$.

$\langle S^*_{\mathrm{b,tot}} \rangle$			
Small primary bubbles		Large primary bubbles	
Clean	Cont.	Clean	Cont.
1.72×10^{-5}	1.93×10^{-5}	1.26×10^{-6}	1.60×10^{-5}

by Liao et al. (2015) described below is included in the figures (symbols). It is apparent that again large differences in the behavior of contaminated and clean bubbles exist. For contaminated bubbles of both primary bubble sizes the relative collision velocities quickly approach a constant value along the x-axis, which is approximately equal for both cases. In contrast, clean bubbles collide with a higher relative velocity. For the case of small clean bubbles $\langle u_\mathrm{rel} \rangle$ reaches a constant value, which is roughly twice as large as the corresponding relative velocity of the small contaminated bubbles. On the other hand, for large clean bubbles the relative collision velocity does not approach a constant value, but $\langle u_\mathrm{rel} \rangle$ increases along the height of the column. Furthermore, for all x/d_c the collision velocity is significantly larger than for contaminated bubbles, i.e., the relative collision velocity obtained for clean bubbles is larger by a factor of up to four. Again, the drag force plays an important role for these observations, since the ratio of the drag coefficients of clean bubbles to contaminated bubbles is $C_{\mathrm{D,clean}}/C_{\mathrm{D,cont.}} \approx 16/24 = 2/3$. Hence, clean bubbles are usually faster compared with contaminated bubbles of the same size.

Reconsidering the lower turbulent kinetic energy of the fluid induced by the (large) clean bubbles (Fig. 11.27), it seems to be plausible that clean and contaminated bubbles collide in a different manner. Note that this appears to be especially the case for the large clean bubbles, which are not able to induce significant turbulent fluctuations. According to the reviews by Liao and Lucas (2010) and Liao et al. (2015) several collision mechanisms can be distinguished. In the present case the collisions of contaminated bubbles are driven by turbulence. Hence, these collisions are denoted as *turbulence induced* (Liao and Lucas, 2010; Liao et al., 2015). For this mechanism the bubbles are assumed to vertically rise upwards side by side, with turbulent velocity fluctuations causing collisions. Due to this mechanism, the small and rather uniform relative collision velocity of $\langle u_\mathrm{rel} \rangle / u_\mathrm{ref} = 0.15$ for both the small and the large contaminated bubbles is observed in Fig. 11.29. According to Liao et al. (2015) in case of turbulence-induced collisions the relative collision velocity depends on the relative turbulent velocities $\langle u^\mathrm{b}_\mathrm{t} \rangle$ of the bubbles, which in turn can be determined by the velocity fluctuations $\langle u'_{\mathrm{b},i}\, u'_{\mathrm{b},i} \rangle$ of the bubbles. Hence, the relative collision velocity due to turbulence can be estimated by (Liao et al., 2015):

$$\langle u_\mathrm{t,rel} \rangle = \left(2 \langle u^\mathrm{b}_\mathrm{t} \rangle^2 \right)^{\frac{1}{2}} \qquad \text{with} \qquad \langle u^\mathrm{b}_\mathrm{t} \rangle = \left(\frac{1}{3} \langle u'_{\mathrm{b},i}\, u'_{\mathrm{b},i} \rangle \right)^{\frac{1}{2}} . \tag{11.3}$$

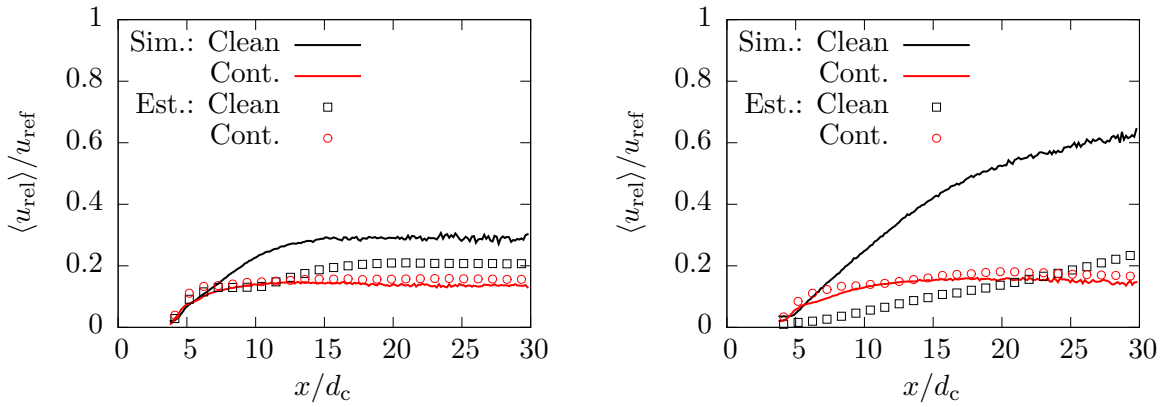

(a) Small primary bubbles. **(b)** Large primary bubbles.

Fig. 11.29. Averaged relative collision velocity observed in the simulations (solid lines) and estimated by Eq. (11.3) (symbols) along the bubble column. Based on Hoppe and Breuer (2018).

For all cases considered the relative collision velocity estimated by Eq. (11.3) are included in Fig. 11.29. It can be seen that for the contaminated bubbles Fig. 11.29 yields collision velocities of $\langle u_{\mathrm{t,rel}} \rangle / u_{\mathrm{ref}} \approx 0.15$ for $x/d_{\mathrm{c}} \gtrsim 10$, which agrees well with the relative collision velocities found in the simulations. Hence, the idea that contaminated bubbles collide due to turbulent velocity fluctuations is further confirmed. Since the turbulent velocity fluctuations affect all bubbles regardless of their size, bubbles of all diameters collide with each other leading to the appearance of the snapshots in Figs. 11.20 and 11.22 and the corresponding shift of the bubble size distributions of contaminated bubbles at the averaging section further away from the bottom of the column observed in Fig. 11.24.

The rise velocity of clean bubbles is higher due to the smaller drag coefficient, but the path they follow is more rectilinear. Consequently, the total number of collisions is reduced. Larger bubbles are able to catch up with smaller bubbles rising in front of them, due to the larger buoyancy force acting on the large bubbles. Hence, the large bubbles collect more and more small bubbles growing larger with increased distance from the bottom of the column. On the other hand, the primary bubbles rarely collide, since the turbulent velocity fluctuations are small. Note again that this is especially the case for the large clean primary bubbles, whereas the small clean primary bubbles are able to induce turbulence of a sufficient magnitude. Due to the fact that in case of the large clean bubbles the collisions are mainly driven by the buoyancy force, the collisions are denoted as *buoyancy induced* (Liao and Lucas, 2010; Liao et al., 2015). This mechanism explains the increase of the average collision velocity of clean bubbles with x/d_{c} observed in Fig. 11.29(b). Since the larger already coalesced bubbles rise faster than the remaining primary bubbles, the relative collision velocity of the large clean bubbles increases. Furthermore, the form of the snapshots (Fig. 11.21) and the bubble size distributions (Fig. 11.24(c)) agrees with the above explanation. According to Liao et al. (2015), the relative velocity of buoyancy-induced collisions $u_{\mathrm{r,rel}}$ is given by the difference of the rise velocities of the colliding

bubbles. In order to further validate the statement that (large) clean bubbles collide due to the buoyancy effect, the relative collision velocity is approximated by:

$$\langle u_{\mathrm{r,rel}} \rangle = \langle u_{\mathrm{b},x} \rangle_{(\geq 2)} - \langle u_{\mathrm{b},x} \rangle_{(1)} \,, \tag{11.4}$$

where $\langle u_{\mathrm{b},x} \rangle_{(1)}$ and $\langle u_{\mathrm{b},x} \rangle_{(\geq 2)}$ denote the rise velocities averaged over all primary bubbles ($V_\mathrm{b}/V_\mathrm{pb} = 1$) and all coalesced bubbles ($V_\mathrm{b}/V_\mathrm{pb} \geq 2$) present in the bubble column at an arbitrary instant in time, respectively. Note that this estimation was not given in Hoppe and Breuer (2018), since the authors realized this later. For the case of large clean primary bubbles estimation (11.4) yields a relative collision velocity of $\langle u_{\mathrm{r,rel}} \rangle / u_\mathrm{ref} \approx 0.80 - 0.24 = 0.56$. This value agrees well with the range of the collision velocity of the large clean bubbles shown in Fig. 11.29(b), especially considering the fact that Eq. (11.4) only provides a coarse approximation. For the case of small clean primary bubbles a collision velocity of $\langle u_{\mathrm{r,rel}} \rangle / u_\mathrm{ref} \approx 0.52 - 0.19 = 0.33$ is obtained, which is somewhat larger than the value of approximately 0.28 observed by the simulation for $x/d_\mathrm{c} \geq 15$. Since the estimation (11.3) of the collision velocity for the turbulence-induced case yields values of roughly 0.22, it is apparent that in the case of small clean primary bubbles both turbulence and buoyancy play a role. Considering the evolution of the bubble sizes with the height x/d_c (Figs. 11.19 and 11.24(a)) and the significant amount of turbulent kinetic energy (Fig. 11.27(a)) induced by the momentum transferred to the fluid (Fig. 11.28(a) and Table 11.4) by the small clean bubbles, it seems plausible that turbulence-induced collisions are somewhat more important. Similar results are obtained for contaminated bubbles. Applying Eq. (11.4) in the case of small contaminated primary bubbles yields a relative collision velocity of $\langle u_{\mathrm{r,rel}} \rangle / u_\mathrm{ref} \approx 0.33 - 0.13 = 0.20$, while for large contaminated bubbles $\langle u_{\mathrm{r,rel}} \rangle / u_\mathrm{ref} \approx 0.43 - 0.18 = 0.25$ is obtained. Comparing these values with the actual dimensionless collision velocities of about 0.15 observed for $x/d_\mathrm{c} \gtrsim 10$ in Fig. 11.29 for the contaminated bubbles of both sizes, it is apparent that buoyancy-driven collisions play only a minor role for these cases.

11.3.2.2 Influence of the Added-Mass Coefficient

As already mentioned, the results presented in Section 11.3.2.1 have been obtained by an added-mass coefficient variably adjusted in the range $C'_\mathrm{m} = 0.2$ to 0.8 according to Eq. (7.7), whereas for the originally published results by Hoppe and Breuer (2018) a constant added-mass coefficient of $C'_\mathrm{m} = 0.8$ (Eq. (7.6)) has been assumed. Hence, the influence of the different formulations on the coalescence behavior of the bubbles in the column has to be investigated by comparing the results of the previous section with the results by Hoppe and Breuer (2018). Note again that the added-mass coefficient mostly affects the contact time given by Eq. (7.14), i.e., a larger C'_m as used for the constant value leads to a larger contact time t_c.

In Fig. 11.30 the total coalescence rate $N_\mathrm{coal}^\mathrm{cumul}/N_\mathrm{coll}^\mathrm{cumul}$ is depicted for a variable and a constant added-mass coefficient. Again, the four cases of small and large primary bubbles with clean and contaminated surface conditions are considered. It is apparent that the total coalescence rate of clean bubbles is unity regardless of the contact time. The physical

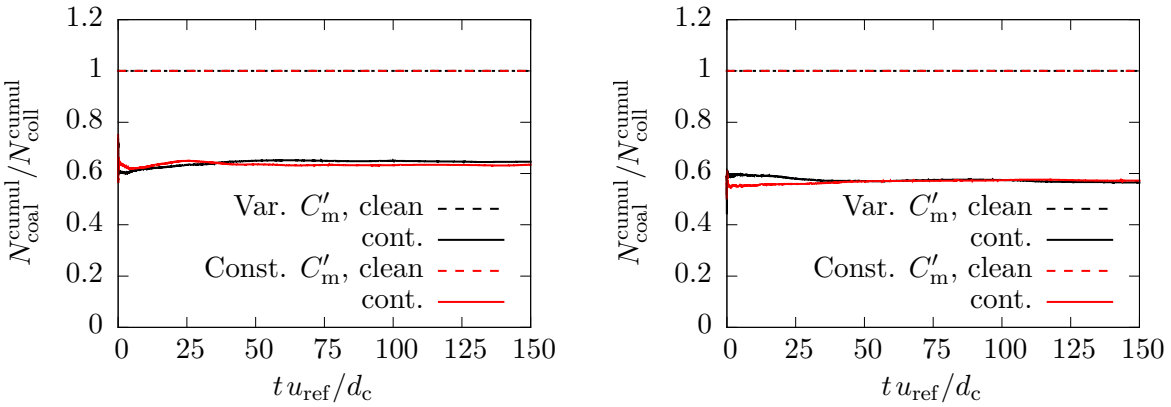

(a) Small contaminated primary bubbles. **(b)** Large contaminated primary bubbles.

Fig. 11.30. Comparison of the total coalescence rate $N_{\mathrm{coal}}^{\mathrm{cumul}}/N_{\mathrm{coll}}^{\mathrm{cumul}}$ for a variable and a constant added-mass coefficient. Results partly taken from Hoppe and Breuer (2018).

reason behind this result is that the liquid trapped between the colliding bubbles is drained so fast in the inertia-controlled case of clean bubbles that an increased contact time does not have any influence on the outcome of bubble-bubble collisions. Consequently, for the remainder of this section only the case of contaminated small and large primary bubbles is considered, since the results for clean bubbles shown in the previous section are not affected by the added-mass coefficient. Figure 11.30 shows that in case of contaminated bubbles the total coalescence rate is also nearly unaffected by the form of the estimation of t_{c}. Only for the small contaminated bubbles a marginally smaller coalescence rate is obtained, if the added-mass coefficient is chosen to be constant. In case of large contaminated bubbles the total coalescence rate is equal for both a variable and a constant C'_{m}.

The impression that the added-mass coefficient does not significantly affect the coalescence in a bubble column is further confirmed by Fig. 11.31 depicting the evolution of the bubble size distribution over the distance from the bottom of the column for the case of contaminated bubbles. Note that in contrast to Fig. 11.24 only the results of two averaging sections ($15 \leq x/d_{\mathrm{c}} < 20$ and $25 \leq x/d_{\mathrm{c}} < 30$) are shown for the sake of brevity. The only visible difference between the two estimations of C'_{m} is found for the size distribution of the small contaminated bubbles in the upper section of the column. Here, the number of remaining primary bubbles is reduced more strongly, if the added-mass coefficient is variably adjusted by Eq. (7.7). For the case of large contaminated bubbles no deviation between the bubble size distributions can be seen. In the other regions of the bubble column not shown in Fig. 11.31, similar results are obtained.

The fact that the coalescence of contaminated bubbles is not affected by the added-mass coefficient may appear surprising at first, since the value of C'_{m} directly influences the contact time of the colliding bubbles. As argued before, a longer contact time usually improves the likelihood of a successful coalescence process, since the liquid film trapped between the bubbles can be drained for a longer period of time. Remembering that estimating the added-mass coefficient by Eq. (7.7) yields an added-mass coefficient varying in the range $0.2 \leq C'_{\mathrm{m}} \leq 0.8$ in comparison to the constant value of $C'_{\mathrm{m}} = 0.8$ given by

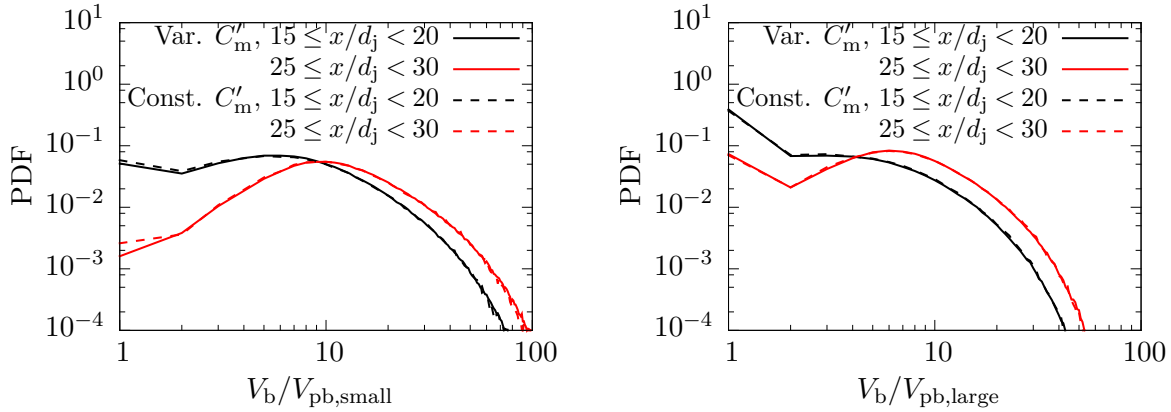

(a) Small contaminated primary bubbles. **(b)** Large contaminated primary bubbles.

Fig. 11.31. Comparison of the bubble size distribution for a variable and a constant added-mass coefficient at two sections of the column. Results partly taken from Hoppe and Breuer (2018).

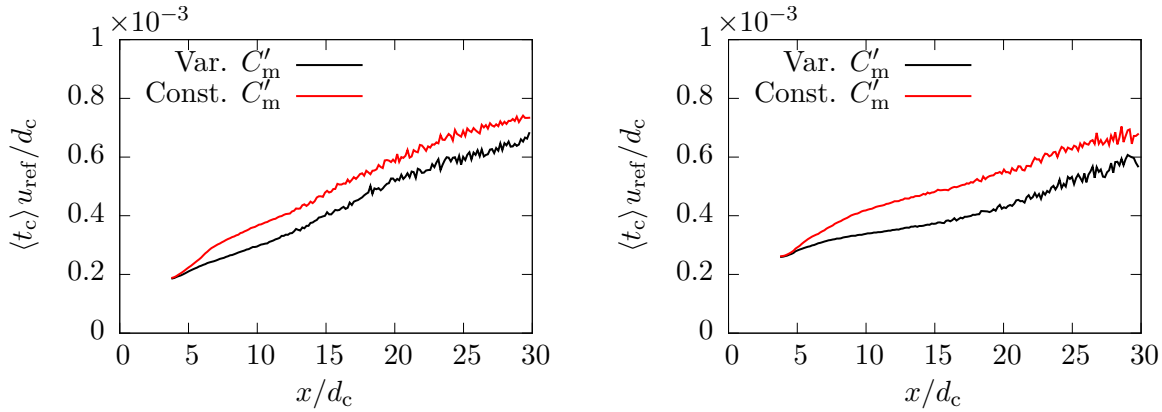

(a) Small contaminated primary bubbles. **(b)** Large contaminated primary bubbles.

Fig. 11.32. Comparison of the axial variation of the dimensionless contact time t_c for a variable and a constant added-mass coefficient. Results partly taken from Hoppe and Breuer (2018).

Eq. (7.6), the contact time should be smaller for the estimation of the variable added-mass coefficient. Figure 11.32 confirms this statement for both small and large contaminated primary bubbles, i.e., the dimensionless contact time is larger throughout the whole bubble column for a constant C'_m.

In order to understand why coalescence is not augmented due to the increased contact time by assuming a constant added-mass coefficient, the relative transition time t_j/t_c is shown in Fig. 11.33. As explained in Chapter 7, for contaminated bubbles the liquid outflow is initially inertia-controlled during a time period of t_j. Afterwards, the viscous-controlled drainage takes place. During the inertial drainage the reduction of the film thickness is substantial, since the drainage mechanism is very fast, see Eq. (7.22). On

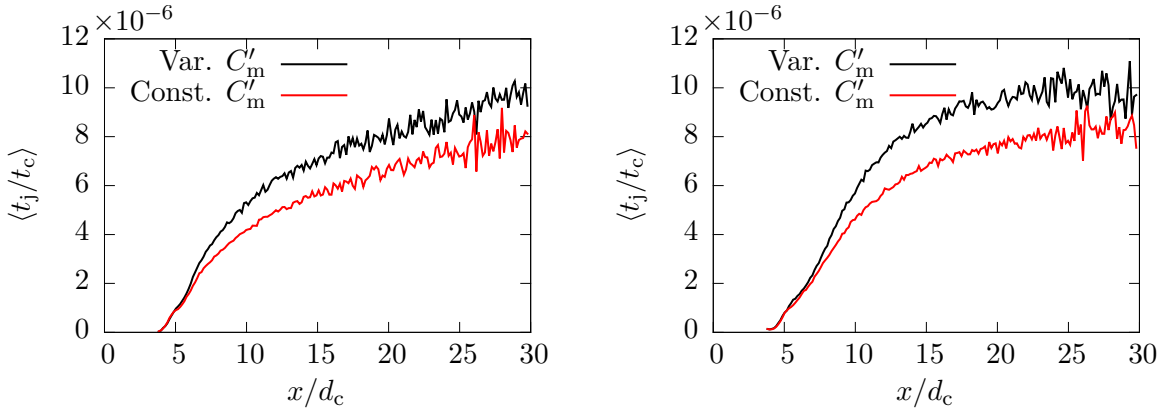

(a) Small contaminated primary bubbles. **(b)** Large contaminated primary bubbles.

Fig. 11.33. Comparison of the axial variation of the relative transition time t_j/t_c for a variable and a constant added-mass coefficient. Results partly taken from Hoppe and Breuer (2018).

the other hand, viscous drainage is comparably slow (Eq. (7.23)). Figure 11.33 reveals that the relative transition time is larger for the case of a variable added-mass coefficient compared with a constant value throughout the whole bubble column. The reason for this observation is that the relative transition time t_j/t_c depends on the inverse of the contact time t_c, while the transition time t_j is nearly unaffected by the added-mass coefficient, see the conditional equation (7.29). Consequently, while the overall contact time is shorter for a variable C'_m, the effect on bubble coalescence is balanced by an extended relative time period t_j/t_c of inertia-controlled drainage during which the film thickness is reduced more strongly compared to the case of a constant C'_m, see Section 7.3.2 where the increase of t_j/t_c with a decrease of C'_m has been demonstrated.

11.3.2.3 Summary of the Results

A bubble column is considered in order to assess the extended coalescence model in a setup containing a large number (up to 600,000) of bubbles. The coalescence model was found to be highly efficient, i.e., despite the frequent occurrence of collisions only 1 to 2% of the total CPU-time is required for the evaluation of the coalescence processes. Especially for the case of contaminated bubbles this demonstrates that the a-priori estimation of the relative transition time t_j/t_c based on the two-step procedure described in Section 7.3 yields a significant improvement to the speed of the calculations.

Furthermore, the test case allowed to examine the evolution of the bubbles within the bubble column and the effects of varying bubble properties. It was shown that the appearance of the bubbles visibly changes, if the size of the primary bubbles released at the bottom of the column as well as the contamination of the bubbles with surfactants is varied. The case of large clean primary bubbles especially deviates considerably from the other cases. This qualitative impression is quantitatively confirmed by the evolution of the bubble size distribution with increasing distance to the injection plane. While in

the case of small clean and contaminated bubbles and large contaminated bubbles the probability density functions are strongly shifted towards bubbles of larger size, this is not the case for large clean primary bubbles, where the probability density of primary bubbles is only marginally decreased with an increasing distance from the bottom of the column. It was demonstrated that the contamination of the bubbles leads to a shift of the size distributions towards larger bubbles for regions further away from the bottom, while the probability density of primary bubbles is reduced. In other words, the number of small bubbles decreases along the axial direction of the column leading to an increased number of large coalesced bubbles. A decreasing size of the primary bubbles also leads to a shift of the probability density functions towards larger bubble size, which is accompanied by a decrease of the probability density of the primary bubbles.

By analyzing the turbulent kinetic energy of the fluid induced by the presence of the bubbles, it was revealed that the observed differences are caused by the ability of the bubbles to induce turbulent velocity fluctuations. Two physical mechanisms have been identified. On the one hand, the increased number density associated with small primary bubbles compared with the case of large primary bubbles leads to more frequent bubble collisions. The number density of the small bubbles is larger, since the same volume flux was assumed for the bubbles. Consequently, an enlarged number of coalesced bubbles is present in the flow, which are able to induce more turbulence. Note that the ratio of the collision frequencies of small and large primary bubbles was in accordance with an estimation based on the kinetic theory of gases. On the other hand, the contamination of the bubbles causes more turbulence due to the larger drag coefficient. The increased turbulent velocity fluctuations of the fluid lead to more bubble-bubble collisions, which form larger bubbles able to induce more turbulence. Hence, a self-exciting feedback loop is obtained.

Applying these assumptions to the present cases, one can explain why the case of large clean primary bubbles behaves differently compared with the other cases. Neither the bubble number density nor the surface condition of the bubbles allows for a sufficient induction of turbulence, which by collisions and coalescence processes can then lead to the formation of larger turbulence-inducing bubbles. For the other cases (small clean and large contaminated primary bubbles) one mechanism or both mechanisms (small contaminated primary bubbles) provide enough momentum to induce significant turbulent fluctuations, which then reinforce the whole process. The averaged magnitude of the momentum sources of the bubbles confirm this speculation, i.e., the averaged momentum transferred to the fluid by the bubbles is significantly larger for small clean and small/large contaminated bubbles than for large clean primary bubbles.

To further confirm these findings, the collision velocities of the bubbles were investigated in the four considered cases. It was shown that contaminated bubbles of both primary bubble sizes collide due to turbulent velocity fluctuations. On the other hand, the collisions of clean bubbles are buoyancy induced in the case of large primary bubbles. For small clean primary bubbles the turbulence-induced and to a minor extent the buoyancy-induced collision mechanism seem to play a role. The aforementioned results were backed up by a comparison of the averaged relative collision velocities observed in the simulations with estimates provided by Liao et al. (2015).

Lastly, the influence of the added-mass coefficient C'_{m} has been analyzed, since the originally published results by Hoppe and Breuer (2018) assumed a constant added-mass coefficient of $C'_{\mathrm{m}} = 0.8$, whereas the results presented in this thesis applied a variable coefficient adjusted in the range $C'_{\mathrm{m}} = 0.2$ to 0.8 based on the properties of the colliding bubbles. The different assumptions mostly affect the contact time t_{c}, which decreases for a smaller C'_{m}. It was demonstrated that the averaged contact time is indeed larger for a constant added-mass coefficient in all regions of the column. However, the impact on the bubble size distribution was found to be marginal. The reason behind this result is that relative transition time $t_{\mathrm{j}}/t_{\mathrm{c}}$ during which inertia-dominated liquid drainage takes place increases with a decreasing contact time. Consequently, the overall lower contact time of the bubbles is balanced by an extended relative time period of inertia-controlled drainage, which substantially decreases the film thickness.

11.4 Breakup in a Turbulent Jet Flow

Lastly, the results obtained by applying the breakup model described in Chapter 8 to the case of bubbles injected into a fully developed, self-similar turbulent jet flow are discussed. The setup, which is based on the experiments by Martínez-Bazán et al. (1999a,b), is described in detail in Section 10.5. As previously explained, bubbles are assumed to break up due to the interaction with the turbulent structures of the flow, which have a size comparable to the diameter of the bubbles. Hence, before the breakup of the bubbles can be investigated, the properties of the fluid flow in the simulations have to be compared with experimental results in order ensure a correctly predicted flow field. This is done in Section 11.4.1. Afterwards, in Section 11.4.2 the evolution of the bubble sizes with an increasing downstream position observed in the simulation is compared with the experimental results by Martínez-Bazán et al. (1999a). In the following sections the influence of various parameters on the breakup of the bubbles in the jet flow is investigated. In Section 11.4.3 the influence of the time lag Δt_{idle} is considered by varying the proportionality constant C_{break} described in Section 8.2.4. Furthermore, the results of this section serve as a confirmation of the choice of $\Delta t_{\mathrm{break,etf}}$ (Eq. (8.32)) for the estimation of the time lag yielding the best agreement with the experiments by Martínez-Bazán et al. (1999a). Next, in Section 11.4.4 simulation results obtained by neglecting bubble coalescence are compared with the results[2] taking coalescence into account. Lastly, the effect of the surface tension on the breakup behavior of the bubbles is investigated in Section 11.4.5. Note that similar to the remainder of Chapter 11 most of the following results have recently been published in Hoppe and Breuer (2020).

11.4.1 Continuous Flow Field

Before the breakup of the bubbles can be investigated, the properties of the fluid flow are compared with experimental results by Hussein et al. (1994) and Zaman and Hussain (1980) in order to ensure a correctly predicted flow field. In both experiments jet flows

[2] All other results presented in Section 11.4 account for coalescence.

at Reynolds numbers of 32,000 (Zaman and Hussain, 1980) and 95,500 (Hussein et al., 1994) based on the nozzle diameter and the exit velocity of the jet are considered. Hence, the Reynolds numbers are comparable to the Reynolds number of 38,250 of the present test case, see Section 10.5. Note that $\mathcal{LESOCC}$ predicts the velocity components in the Cartesian frame of reference. However, since a jet flow is rotationally symmetric around the centerline, the usage of cylindrical coordinates is more suitable for the following presentation of the results. The transformation of Cartesian velocities to the cylindrical[3] frame of reference is explained in Appendix A.

In Fig. 11.34 the temporally and circumferentially averaged streamwise fluid velocity is shown along the centerline (Fig. 11.34(a)) and in radial direction (Fig. 11.34(b)) at various downstream positions. It is apparent from Fig. 11.34(a) that the agreement between the predicted mean streamwise velocity along the jet centerline with the experimental results by Zaman and Hussain (1980) is good. Note that the depicted velocity component is normalized by the inflow velocity u_{jc} of the jet. Furthermore, it can be seen that shortly downstream of the inlet at around $x/d_{\mathrm{j}} = 10$ the centerline velocity starts to decrease inversely proportional to the distance x/d_{j}. This is a typical behavior of fully developed, self-similar jet flows (Hussein et al., 1994; Zaman and Hussain, 1980). According to Hussein et al. (1994) and Panchapakesan and Lumley (1993), it is possible to describe the centerline velocity of the fluid in that region of the jet by:

$$\frac{\langle u_{\mathrm{f,x,c}} \rangle}{u_{\mathrm{jc}}} = B_u \left(\frac{x}{d_{\mathrm{j}}} - \frac{x_0}{d_{\mathrm{j}}} \right)^{-1}, \tag{11.5}$$

where B_u and x_0 are constants, which have to be specified by fitting Eq. (11.5) to the observed centerline fluid velocity of an experiment or a simulation. For example, Hussein et al. (1994) determined values of $B_u = 5.8$ and $x_0/d_{\mathrm{j}} = 4.0$ based on their experimental results. Other authors found somewhat different values of $B_u = 5.7$ and $x_0/d_{\mathrm{j}} = 3.0$ (Wygnanski and Fiedler, 1969) or $B_u = 6.06$ and $x_0/d_{\mathrm{j}} = 0$ (Panchapakesan and Lumley, 1993). Based on the present simulation constants of about $B_u = 4.8$ and $x_0/d_{\mathrm{j}} = 1.1$ are obtained. Hence, the present results are in reasonable agreement with the available values of the reference literature, especially, if the large scatter of the data found therein is considered.

Figure 11.34(b) shows the averaged streamwise velocity $\langle u_{\mathrm{f,x}} \rangle$ in the radial direction at four downstream positions of $x/d_{\mathrm{j}} = 20$, 25, 30 and 35 normalized by the corresponding centerline velocities $\langle u_{\mathrm{f,x,c}} \rangle$ at those positions. The radial distributions are shown as a function of $r/(x - x_0)$. This style of plotting allows to depict the mean streamwise velocity such that the profiles ideally overlap at all downstream positions. It is obvious from Fig. 11.34(b) that the present predictions of the jet flow fulfill this condition of a fully developed self-similar jet flow. Additionally, the radial distributions of the averaged streamwise velocity agree well with the experimental results by Hussein et al. (1994).

In Fig. 11.35 the temporally and circumferentially averaged radial distributions of the velocity fluctuations are depicted at four downstream positions. Note that all profiles are

[3] Note that in the present case the x-direction (streamwise direction) denotes the vertical component of the cylindrical coordinates and not the commonly used z-direction.

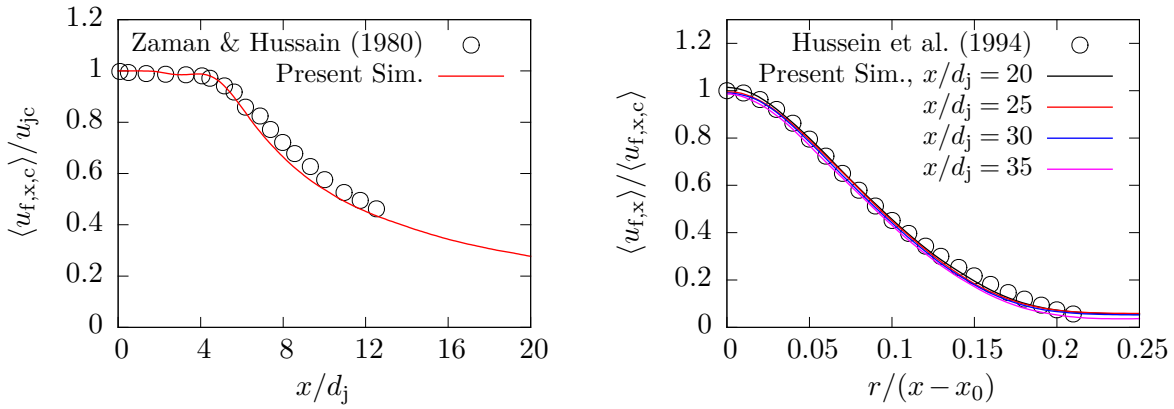

(a) Along the centerline **(b)** Radial direction

Fig. 11.34. Temporally and circumferentially averaged streamwise fluid velocity. Taken from Hoppe and Breuer (2020).

normalized by the square of the averaged centerline fluid velocity $\langle u_{\mathrm{f,x,c}} \rangle^2$ at the corresponding downstream position. The depicted fluctuations in streamwise (Fig. 11.35(a)), radial (Fig. 11.35(b)) and circumferential (Fig. 11.35(c)) direction as well as the only non-zero Reynolds shear stress component (Fig. 11.35(d)) are again compared with the experimental results by Hussein et al. (1994). Similar to the radial profiles of the mean streamwise velocity (Fig. 11.34(b)), the curves shown in Fig. 11.35 should ideally overlap in the fully developed self-similar part of a jet flow. The small deviations among each other and to the results by Hussein et al. (1994) are probably caused by the application of the weak co-flow in the simulations. However, the overall good agreement with the reference data demonstrates that $\mathcal{LESOCC}$ is capable of reliably predicting a jet flow and its turbulent structures, which is required for a proper comparison of the breakup model with the experiment by Martínez-Bazán et al. (1999a,b).

Lastly, Fig. 11.36 depicts two-dimensional contour plots of several fluid quantities of the predicted jet flow: the instantaneous streamwise fluid velocity $u_{\mathrm{f,x}}$ (Fig. 11.36(a)), the mean streamwise fluid velocity $\langle u_{\mathrm{f,x}} \rangle$, the resolved turbulent kinetic energy $\langle k_{\mathrm{turb}} \rangle = 0.5 \, \langle u'_{\mathrm{f},i} \, u'_{\mathrm{f},i} \rangle$ (Fig. 11.36(c)) and the resolved Reynolds shear stress component $\langle u'_{\mathrm{f,x}} \, u'_{\mathrm{f,r}} \rangle$ (Fig. 11.35(d)). The instantaneous streamwise velocity at an arbitrary instant in time is shown in Fig. 11.36(a) in order to give an impression of the jet and to illustrate the turbulent structures of the actual flow field. The spreading of the mean jet flow and the corresponding decrease of the averaged fluid velocity with an increasing distance from the inlet of the jet is visible in Fig. 11.36(b). It is obvious from Figs. 11.36(c) and (d) that the resolved turbulent fluctuations are largest in the shear layer of the jet, which is the expected behavior of such a flow configuration. Furthermore, Fig. 11.36 clearly demonstrates that at the release position of the bubbles ($x/d_{\mathrm{j}} = 16.1$) the (mean) streamwise fluid velocity has already halved compared with the exit velocity of the jet at the inlet, while the normal Reynolds stress components and the Reynolds shear stress component are attenuated compared to the shear layer region.

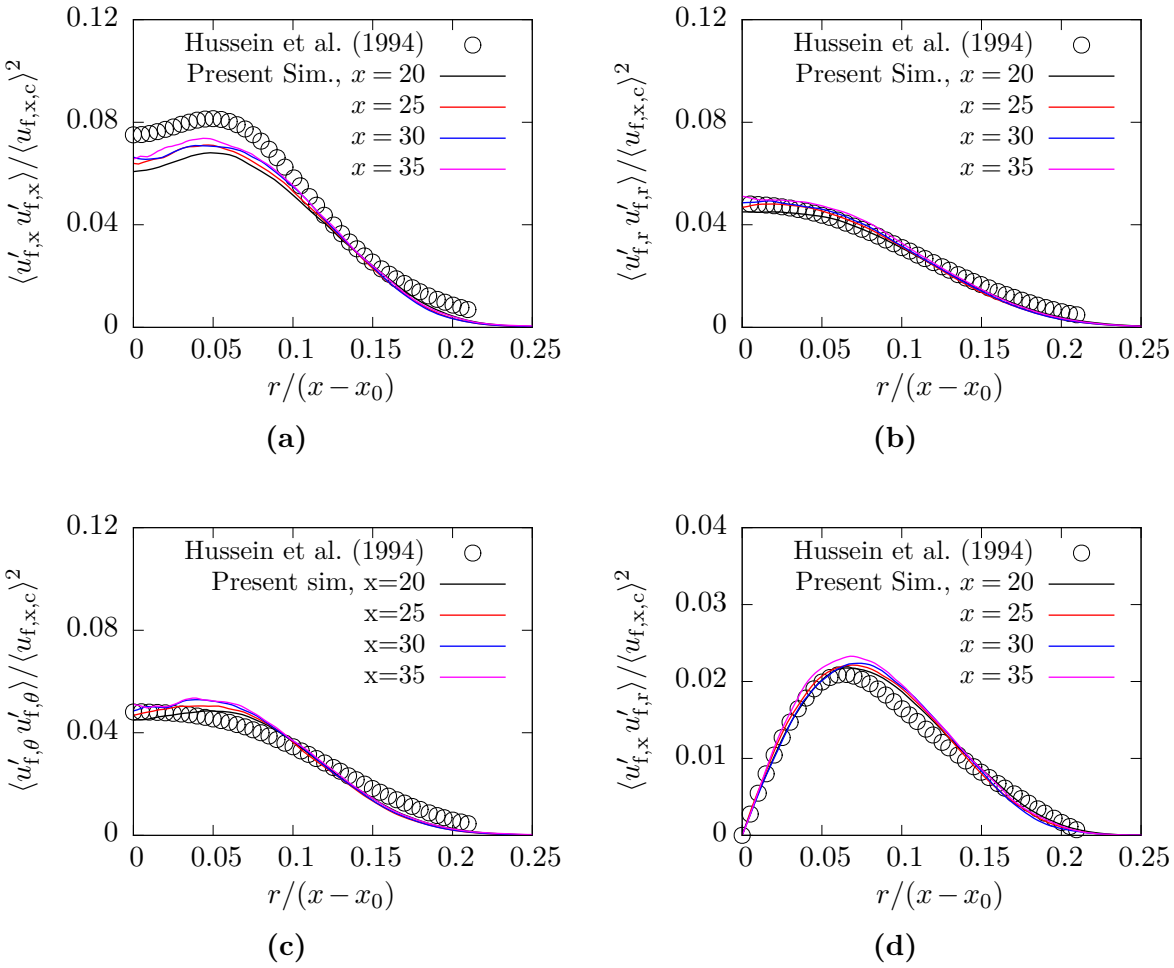

Fig. 11.35. Temporally and circumferentially averaged radial distributions of the normal Reynolds stress components in (a) the streamwise, (b) the radial and (c) the circumferential direction as well as (d) the relevant Reynolds shear stress component. The data are normalized with the square of the averaged centerline velocity. Taken from Hoppe and Breuer (2020).

11.4.2 Comparison with the Experimental Results by Martínez-Bazán et al. (1999a,b)

After the present simulations of the turbulent jet flow (continuous phase) have been validated in the previous section, the bubble statistics obtained by applying the extended breakup model can be compared with the experimental results by Martínez-Bazán et al. (1999a). Firstly, Fig. 11.37 is supposed to give an impression of the distribution of the bubbles inside the jet flow. The depicted snapshot is taken at an instant in time of $\Delta T^* = 6000$ after the release of the bubbles. For the sake of an improved visibility, the color of the bubbles is chosen according to their size, i.e., small bubbles are colored blue, while large bubbles are red. At the shown instant in time a total number of 100 bubbles is present in the computational domain. It is apparent that the bubbles released

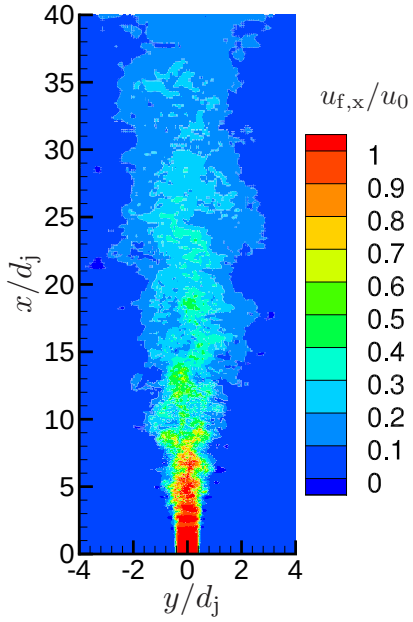

(a) Instantaneous streamwise velocity.

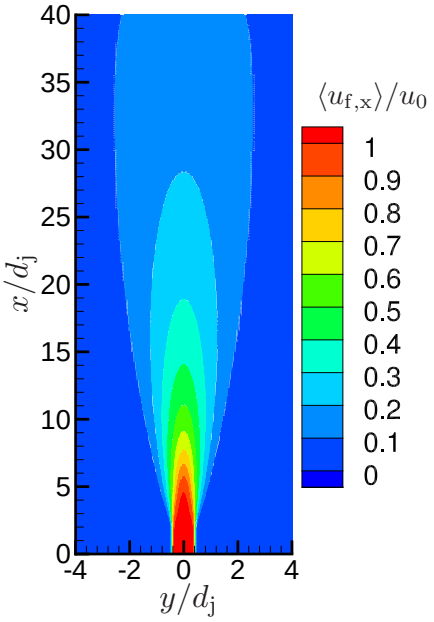

(b) Mean streamwise velocity.

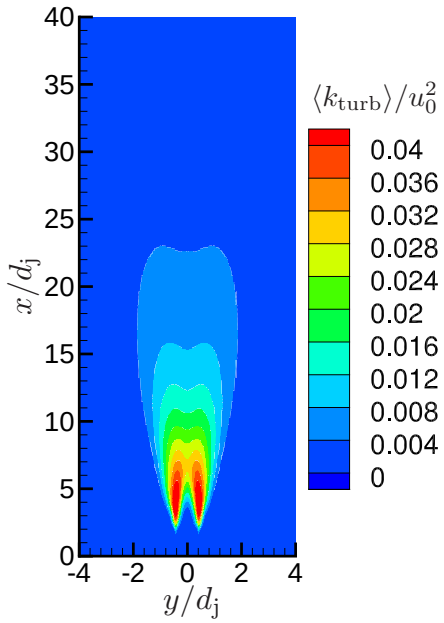

(c) Turbulent kinetic energy.

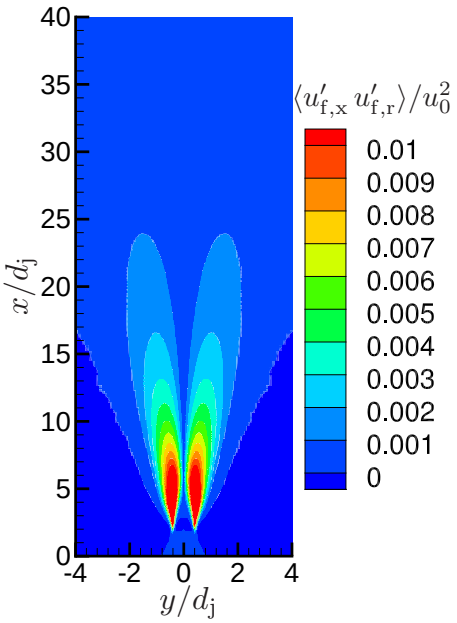

(d) Reynolds shear stress.

Fig. 11.36. (a) Contour plot of the instantaneous streamwise fluid velocity. Contour plots of temporally and circumferentially averaged fluid results: (b) mean streamwise velocity, (c) resolved turbulent kinetic energy and (d) resolved Reynolds shear stress. Taken from Hoppe and Breuer (2020).

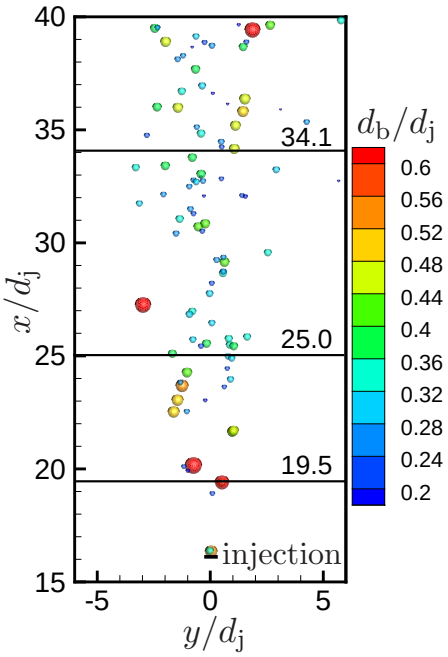

Fig. 11.37. Snapshot of the bubbles at a dimensionless instant in time of $\Delta T^* = 6000$ after the release of the bubbles. The bubble color is chosen according to their size. Taken from Hoppe and Breuer (2020).

at the injection point ($x/d_j = 16.1$) are mainly carried downstream by the flow, while the migration in the radial direction is only a minor effect. Due to the interaction with the turbulent velocity fluctuations of the fluid, the bubbles can break up leading to the various bubble sizes observable in Fig. 11.37. Additionally, the three downstream positions ($x/d_j = 19.5$, 25.0 and 34.1) at which the bubble size distributions are compared (see below) with the results of Martínez-Bazán et al. (1999a) are sketched in Fig. 11.37.

The evolution of the bubble sizes along the streamwise direction of the jet can be seen in Fig. 11.38 depicting the volumetric probability density function at the aforementioned three downstream positions. Note that the bubbles are inserted at a downstream position of $x/d_j = 16.1$. The bubble diameters are randomly chosen following the size distribution given by Martínez-Bazán et al. (1999a), see Fig. 10.3. Since at the injection position the probability density functions of the bubble diameter observed in the present simulations and by Martínez-Bazán et al. (1999a) coincide, they are not shown in Fig. 11.38.

It can be seen from Fig. 11.38(a) that the bubble size distribution in the simulation is slightly shifted towards smaller bubble diameters compared with the experiment at the first downstream position, i.e., the peak of the bubble size distribution is located at $d_b/d_j \approx 0.3$. In the experiments by Martínez-Bazán et al. (1999a) the peak is observed at about $d_b/d_j = 0.4$. Hence, in the experiments more bubbles with a dimensionless diameter of $d_b/d_j > 0.3$ are present at $x/d_j = 19.5$ compared with the simulation, where too many small bubbles are found. It can be concluded from this result that the breakup into small bubbles is

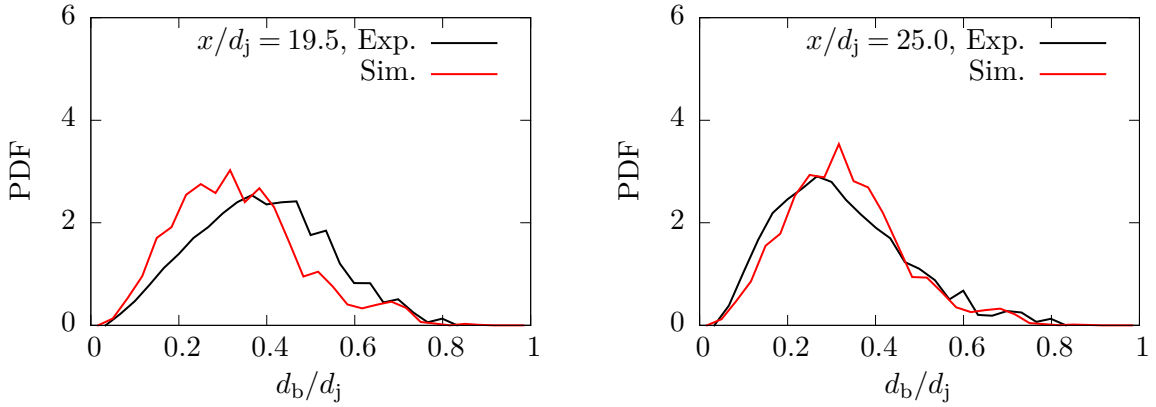

(a) $x/d_j = 19.5$.

(b) $x/d_j = 25.0$.

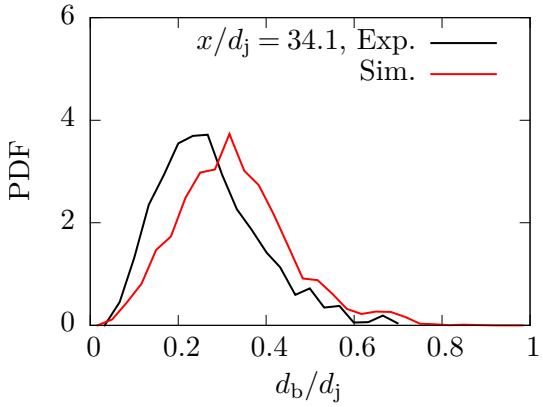

(c) $x/d_j = 34.1$.

Fig. 11.38. Comparison of the volumetric probability density functions of the bubble diameter of the present simulation with the experimental results by Martínez-Bazán et al. (1999a) at three downstream positions. Taken from Hoppe and Breuer (2020).

somewhat overestimated by the present breakup model after the release of the bubbles, i.e., in the region between $x/d_j = 16.1$ and 19.5. At the next downstream position ($x/d_j = 25.0$) at which Martínez-Bazán et al. (1999a) provided a bubble size distribution, the present simulation agrees well with the experimental results. The probability density functions of the experiment and the simulation shown in Fig. 11.38(b) are nearly identical, except for a more pronounced peak of the predicted size distribution found at a dimensionless diameter of $d_b/d_j \approx 0.3$. Lastly, at $x/d_j = 34.1$ the peak of the bubble size distribution remains at $d_b/d_j = 0.3$ in the present simulation. Martínez-Bazán et al. (1999a) observed that the probability density function is shifted towards smaller diameters of about $d_b/d_j = 0.22$ at this downstream position. This means that in the experiments bubbles further break up into small daughters in the region between $x/d_j = 25.0$ and 34.1. Hence, the results of the present simulations indicate that the breakup model somewhat underestimates the breakup into small daughter bubbles in the region downstream of $x/d_j \approx 20$, which leads to the small differences of the predicted size distributions visible in Figs. 11.38(b) and (c).

To further validate the present results, a comparison of the bubble number flux of the simulation with the number flux observed in the experiment is shown in Fig. 11.39. In order to determine the bubble number flux in the simulation, every bubble passing through a certain downstream plane (x/d_j = 15 to 40) is counted during the averaging period of time ($\Delta T^* = 6000$) resulting in the axial distribution of the total number of bubbles passing through each plane. Afterwards, the total numbers of bubbles are normalized by the number of bubbles released during the averaging time period, i.e., by $N_\mathrm{b,tot}^\mathrm{sim} = 883$. In the experiments the total number of bubbles present at various downstream positions is counted during a certain time interval. Unfortunately, the exact length of this time period is not provided by Martínez-Bazán et al. (1999a). Hence, in order to normalize the bubble number flux given by Martínez-Bazán et al. (1999a) and to make it comparable to the normalized number flux obtained by the simulation, the experimentally observed total number of bubbles ($N_\mathrm{b,tot}^\mathrm{exp} = 5785$) at the first downstream position ($x/d_\mathrm{j} = 16.1$) is used for the normalization. Hence, the total number of bubbles counted by Martínez-Bazán et al. (1999a) at the various downstream positions are divided by $N_\mathrm{b,tot}^\mathrm{exp}$ resulting in the normalized distribution of the bubble number flux shown in Fig. 11.39.

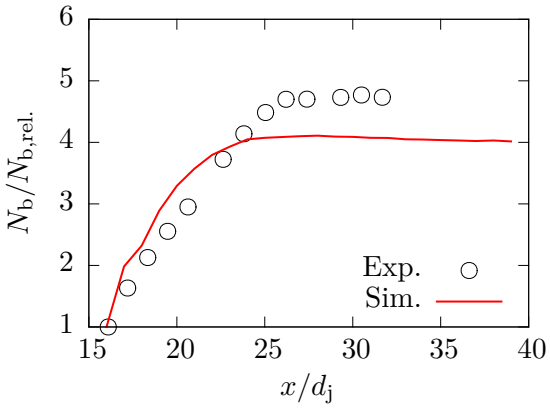

Fig. 11.39. Number of bubbles passing through certain downstream planes within a dimensionless time period of $\Delta T^* = 6000$ normalized by the number of released bubbles. Comparison with the experiments by Martínez-Bazán et al. (1999a). Taken from Hoppe and Breuer (2020).

The comparison between the experimental results and the results of the simulation shows that in the region directly after the bubble injection ($x/d_\mathrm{j} = 16.1$ to about 23) the normalized bubble number flux of the simulation is slightly larger than the corresponding quantity of the experiments. This result reflects the overestimated breakup into small daughter bubbles predicted by the present breakup model in the region directly behind the release. Consequently, in the simulation too many small bubbles are present in the region shortly after the bubble injection. Further downstream of $x/d_\mathrm{j} \approx 23$ a plateau of the bubble number flux is reached in the simulation, i.e., $N_\mathrm{b}/N_\mathrm{b,rel}$ does not increase anymore. The reason behind this observation is that the breakup criterion (8.4) is only rarely fulfilled downstream of $x/d_\mathrm{j} \approx 23$ leading to the absence of breakup processes and, therefore, a stagnating number of bubbles. A similar behavior was observed by

Martínez-Bazán et al. (1999a). However, in the experiments the plateau was reached slightly further downstream at $x/d_\mathrm{j} \approx 26$. Additionally, Martínez-Bazán et al. (1999a) obtained a maximum value of the normalized bubble number flux of about $N_\mathrm{b}/N_\mathrm{b,rel} = 4.7$, while in the simulations a slightly lower maximum value of the bubble number flux of $N_\mathrm{b}/N_\mathrm{b,rel} \approx 4.1$ is observed. Again, this is a consequence of the underestimated breakup into bubbles with diameters smaller than $d_\mathrm{b}/d_\mathrm{j} = 0.3$ mentioned above. Hence, in the experiment the downstream region is populated by a larger number of smaller bubbles compared with the simulation. Consequently, a smaller number of larger bubbles is present at $x/d_\mathrm{j} \gtrsim 23$ in the experiment.

Summarizing the previous results, Figs. 11.38 and 11.39 demonstrate that the extended breakup model by Hoppe and Breuer (2020) described in Chapter 8 yields a reasonable agreement with the reference data by Martínez-Bazán et al. (1999a,b).

11.4.3 Influence of the Time Lag

In Section 8.2.4 a time lag Δt_idle is introduced, which defines a minimum period of time during which the daughter bubbles formed by a breakup process cannot break up. Furthermore, it is shown in Section 8.2.4 that the time lag can be described by three different estimates, which are all based on a turbulent breakup time. These turbulent breakup times are denoted $\Delta t_\mathrm{break,AA}$, $\Delta t_\mathrm{break,etk}$ and $\Delta t_\mathrm{break,etf}$ and are given by Eq. (8.28), (8.31) and (8.32), respectively. The functional dependency on the diameter $d_\mathrm{b,p}$ of the parent bubble and the local dissipation rate ϵ at the position of the bubble is the same for all three formulations. However, the proportionality constants vary for the estimates. Consequently, for the same parameters different idle times are obtained. For example, the time lag $\Delta t_\mathrm{break,etk}$ given by Eq. (8.31) is by a factor of $\sqrt{2} \approx 1.41$ larger than $\Delta t_\mathrm{break,etf}$ estimated by Eq. (8.32). If estimation (8.28) is applied under the assumption that $C_\mathrm{AA} = 1/2$ and $\beta \approx 7.81$, one obtains a time lag $\Delta t_\mathrm{break,AA}$ that is by a factor of $C_\mathrm{AA}\,\beta^{3/2}/2 \approx 5.46$ larger than the estimate by Eq. (8.32), i.e., $\Delta t_\mathrm{break,AA} > \Delta t_\mathrm{break,etk} > \Delta t_\mathrm{break,etf}$. Thus, the purpose of this section is to investigate the influence of the different formulations of the time lag on the bubble breakup in the jet flow. Furthermore, the choice of $\Delta t_\mathrm{break,etf}$ as the standard idle time in Section 8.2.4 is supposed to be reassured by the following results. Note that all other results presented in this chapter are obtained by applying this standard formulation (Eq. (8.32)).

In Fig. 11.40 the downstream evolution of the bubble size distribution for the three different estimations of the time lag is shown. The volumetric probability density functions at three different downstream positions ($x/d_\mathrm{j} = 19.5$, 25.0 and 34.1) are compared with each other. Additionally, the experimental results by Martínez-Bazán et al. (1999a) are depicted as a reference. Firstly, one can see from Fig. 11.40 that the results obtained by Eqs. (8.31) and (8.32) are very similar to each other, which is expected based on the small difference between the idle times $\Delta t_\mathrm{break,etk}$ and $\Delta t_\mathrm{break,etf}$. The most noticeable difference between the two results is that for $\Delta t_\mathrm{break,etk}$ the peak of the bubble size distribution is found for bubble diameters of about $d_\mathrm{b}/d_\mathrm{j} = 0.35$ at $x/d_\mathrm{j} = 34.0$ (Fig. 11.40(c)), whereas the peak value of the probability density function for $\Delta t_\mathrm{break,etf}$ is at $d_\mathrm{b}/d_\mathrm{j} = 0.30$. Consequently, the increased idle time $\Delta t_\mathrm{break,etk}$ leads to a slightly worse agreement with the

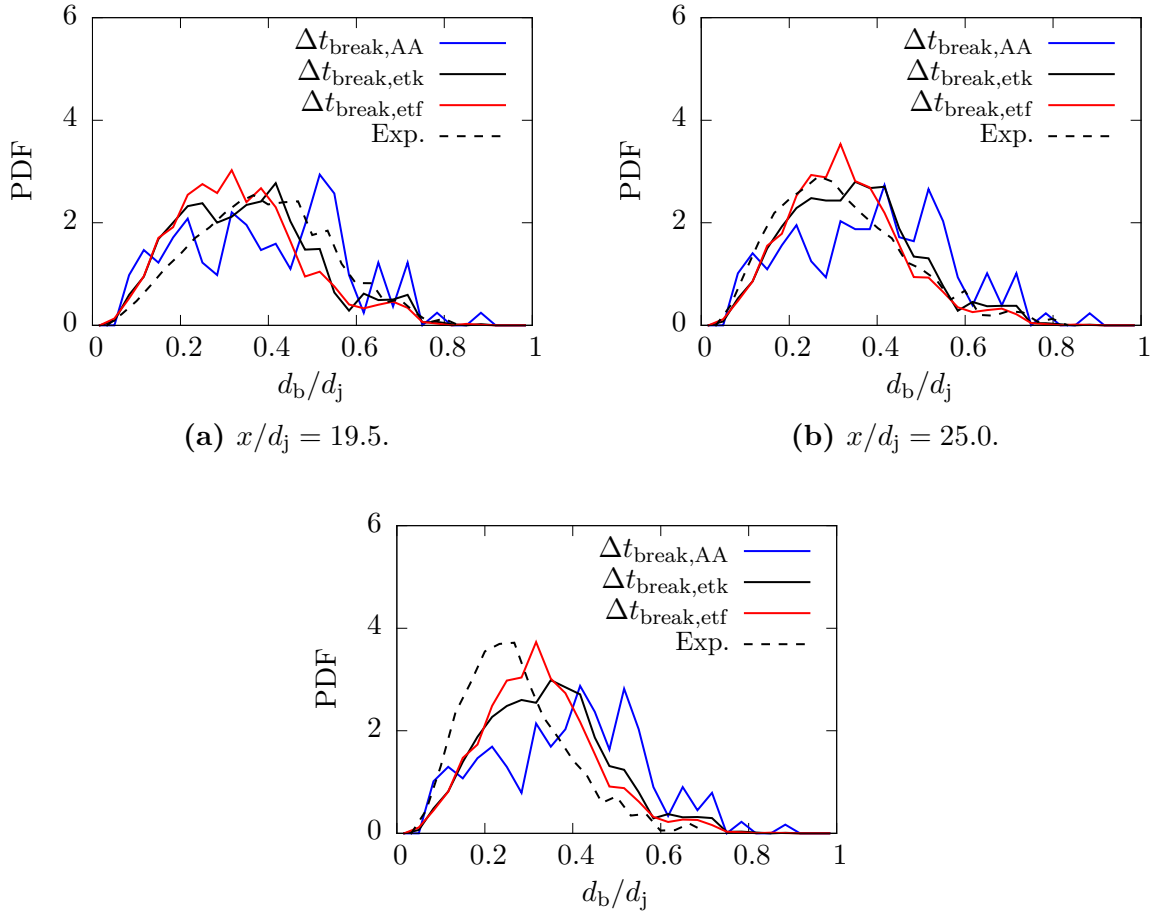

(a) $x/d_j = 19.5$. **(b)** $x/d_j = 25.0$.

(c) $x/d_j = 34.1$.

Fig. 11.40. Comparison of the evolution of the volumetric probability density functions of the bubble diameter of the present simulations with different estimations of the idle time $\Delta t_{idle} = \Delta t_{break}$ at three downstream positions. The experimental results by Martínez-Bazán et al. (1999a) are included as a reference.

experimental results by Martínez-Bazán et al. (1999a). This observation can be explained by the larger time lag during which the daughter bubbles cannot further break up in case of an estimation by Eq. (8.31) resulting in somewhat larger bubbles. It is obvious from Fig. 11.40 that applying $\Delta t_{break,AA}$ (relation (8.28)) proposed by Andersson and Andersson (2006a) leads to an even more pronounced shift of the bubble size distribution towards large bubble diameters. The explanation given above for the deviations between the results obtained by $\Delta t_{break,etf}$ and $\Delta t_{break,etk}$ is valid for this case as well. Hence, the larger bubbles observed for $\Delta t_{break,AA}$ are caused by the even larger idle time.

The comparison of the normalized bubble number flux obtained for the estimation of the idle time by $\Delta t_{break,etf}$, $\Delta t_{break,etk}$ and $\Delta t_{break,AA}$ in Fig. 11.41 confirms the observation that an increasing time lag suppresses the occurrence of breakup processes. It is apparent that the normalized bubble number flux is reduced by a larger time lag. Note that the number of released bubbles used for the normalization of the counted number of bubbles at

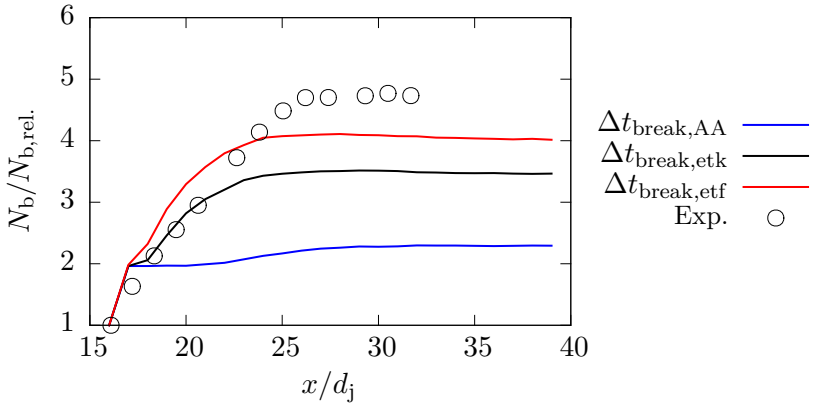

Fig. 11.41. Comparison of the bubble number fluxes obtained in the simulations for the different estimations of the idle time $\Delta t_{idle} = \Delta t_{break}$. The experimental results by Martínez-Bazán et al. (1999a) are included as reference.

the various downstream positions in the simulations is equal in all cases, i.e., $N_{b,rel.} = 883$. As expected, the difference between $N_b/N_{b,rel.}$ obtained for $\Delta t_{break,etf}$ and $\Delta t_{break,etk}$ is relatively small. Note that the agreement of the predicted bubble number flux using $\Delta t_{break,etk}$ with the experiments by Martínez-Bazán et al. (1999a) is slightly better in the region directly downstream of the bubble injection ($x/d_j = 16.1$ to about 20). As described above, in the region close to the bubble injection the present breakup model has the tendency to overpredict the breakup into somewhat too small bubbles leading to a too large number of small bubbles in case of the standard choice for the idle time, i.e., for $\Delta t_{break,etf}$. This tendency appears to be balanced by the larger time lag, if the estimation by $\Delta t_{break,etk}$ is used instead. However, the increased idle time of the daughter bubbles after a breakup event leads to a smaller maximum bubble number flux for $\Delta t_{break,etk}$, i.e., the number flux approaches a constant magnitude of about $N_b/N_{b,rel.} = 3.5$ compared with approximately 4.1 in the case of $\Delta t_{break,etf}$ or 4.7 observed in the experiment. Hence, in the downstream region of the jet flow the agreement with the experiment becomes worse. Note that for $\Delta t_{break,etk}$ the plateau of the bubble number flux is reached slightly further downstream at a position of approximately $x/d_j = 25$ compared with $x/d_j = 23$ in the case of $\Delta t_{break,etf}$. This can be explained by the on average slightly larger size of the bubbles at this downstream region for the former case, see Fig. 11.40. These larger bubbles can fulfill the breakup criterion (Eq. (8.4)) more easily, i.e., breakup still occurs slightly further downstream.

The deviation of the normalized bubble number flux obtained for $\Delta t_{break,AA}$ from the experimental results is even larger, due to the idle time being approximately five times larger than in the case of an estimation by $\Delta t_{break,etf}$. Based on the sudden increase of the bubble number flux to a value of roughly two, one can see from Fig. 11.41 that in the case of $\Delta t_{break,AA}$ most of the bubbles break up shortly after their injection ($x/d_j = 16.1$ to 17) into the flow. Due to the long idle time of the daughter bubbles, the bubbles are transported far downstream by the jet flow without any further breakups. By averaging the breakup times Δt_{break} of all breakup processes taking place during the averaging time period

($\Delta T^* = 6000$), one obtains a dimensionless idle time of about $\langle \Delta t^*_{\mathrm{break,AA}} \rangle = 40.68$ for relation (8.28). In contrast, Eqs. (8.31) and (8.32) yield much lower average dimensionless idle times of approximately $\langle \Delta t^*_{\mathrm{break,etk}} \rangle = 9.65$ and $\langle \Delta t^*_{\mathrm{break,etf}} \rangle = 6.70$, respectively. Note that $\langle \Delta t^*_{\mathrm{break,AA}} \rangle / \langle \Delta t^*_{\mathrm{break,etf}} \rangle \approx 6.07$ and $\langle \Delta t^*_{\mathrm{break,etk}} \rangle / \langle \Delta t^*_{\mathrm{break,etf}} \rangle \approx 1.44$. Hence, after the idle period of time $\Delta t_{\mathrm{break,AA}}$, after which breakup is possible again, the bubbles are located in a region with significantly attenuated turbulence, see Fig. 11.36. Consequently, the magnitude of the turbulent velocity fluctuations is not sufficient to further break up the bubbles explaining the marginal increase of bubble number flux observed for $\Delta t_{\mathrm{break,AA}}$ in Fig. 11.41.

In conclusion, the results shown in Figs. 11.40 and 11.41 demonstrate that the best agreement with the experimental results by Martínez-Bazán et al. (1999a) is indeed obtained for an estimation of the idle time by $\Delta t_{\mathrm{break,etf}}$ defined by Eq. (8.32).

11.4.4 Influence of Bubble Coalescence

The results presented in the previous sections are obtained by accounting for the enhanced coalescence model described in Chapter 7. In order to assess the influence of bubble coalescence on the evolution of the bubbles in the turbulent jet flow, simulations have been performed without taking the coalescence of bubbles into account, i.e., the bubble-bubble interaction is limited to collisions and rebounds. For this purpose, the extended coalescence model is deactivated, while the remaining bubble properties are unchanged.

The results of the simulations with and without coalescence taken into account are shown in Fig. 11.42. Again, the experimental results by Martínez-Bazán et al. (1999a) are included as a reference. It can be seen from Fig. 11.42(a) that the results obtained with and without the coalescence model only marginally deviate from each other at the first downstream position of $x/d_{\mathrm{j}} = 19.5$. Consequently, coalescence is of minor importance in the region directly after the bubble injection. At the next downstream position ($x/d_{\mathrm{j}} = 25.0$) depicted in Fig. 11.42(b) the bubble size distribution of the bubbles is slightly shifted towards smaller bubble diameters in the case without coalescence. For this case the probability density function is larger at about $d_{\mathrm{b}}/d_{\mathrm{j}} = 0.25$ compared with the case with coalescence. On the other hand, the probability density of bubbles with diameters larger than $d_{\mathrm{b}}/d_{\mathrm{j}} = 0.45$ is decreased, if coalescence is neglected. Hence, in the simulations taking coalescence into account, the small shift towards larger bubbles is due to the coalescence of bubbles. Lastly, the position furthest downstream ($x/d_{\mathrm{j}} = 34.0$) is shown in Fig. 11.42(c). Similar to the previous location shown in Fig. 11.42(b) the size distribution of the bubbles is slightly shifted towards smaller bubble diameters due to the absence of coalescence processes generating larger bubbles. Note that this shift leads to a slightly better agreement of the simulation results with the experiments by Martínez-Bazán et al. (1999a). One can conclude from Fig. 11.42 that the overall influence of bubble coalescence on the evolution of the dispersed bubble phase is small in the present case. This result agrees with the results by Martínez-Bazán et al. (1999a), who made the same observation. Note that the influence of bubble coalescence is not further investigated considering, for example, the normalized bubble number flux, since the small differences between the cases with and without coalescence are represented in this quantity as well.

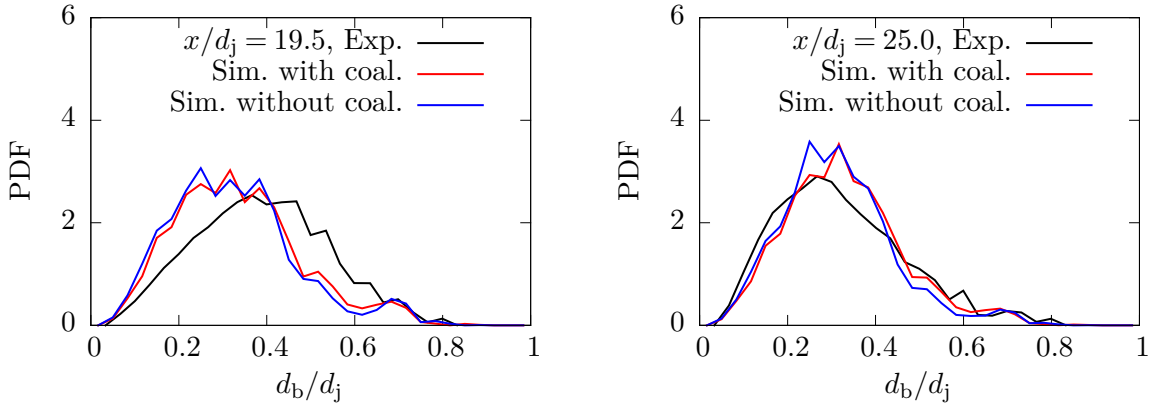

(a) $x/d_j = 19.5$. **(b)** $x/d_j = 25.0$.

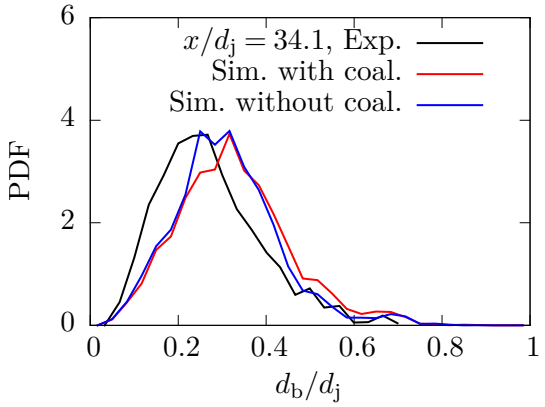

(c) $x/d_j = 34.1$.

Fig. 11.42. Comparison of the evolution of the volumetric probability density functions of the bubble diameter of the present simulations with and without coalescence taken into account. The experimental results by Martínez-Bazán et al. (1999a) are included as a reference. Taken from Hoppe and Breuer (2020).

11.4.5 Influence of the Surface Tension

Lastly, the influence of the bubble properties on breakup is analyzed by varying the surface tension of the bubbles. All of the results shown so far have been obtained by applying the typical surface tension value of an air-water interface ($\sigma = 72.86 \times 10^{-3}\,\mathrm{N/m}$ according to (Pallas and Harrison, 1990)) corresponding to $\sigma^* = 1.49 \times 10^{-4}$. In this section, additional cases with a 30 percent smaller surface tension of $\sigma = 51.0 \times 10^{-3}\,\mathrm{N/m}$ and a 70 percent larger value of $\sigma = 123.86 \times 10^{-3}\,\mathrm{N/m}$ are considered. These additional values correspond to dimensionless surface tensions of $\sigma^* = 1.05 \times 10^{-4}$ and 2.54×10^{-4}, respectively.

The evolution of the bubble size distributions obtained for the three different surface tensions is depicted in Fig. 11.43. Again, the volumetric probability density functions of the simulations are shown at three downstream positions of $x/d_j = 19.5$, 25.0 and 34.1 together with the experimental results by Martínez-Bazán et al. (1999a). It is apparent

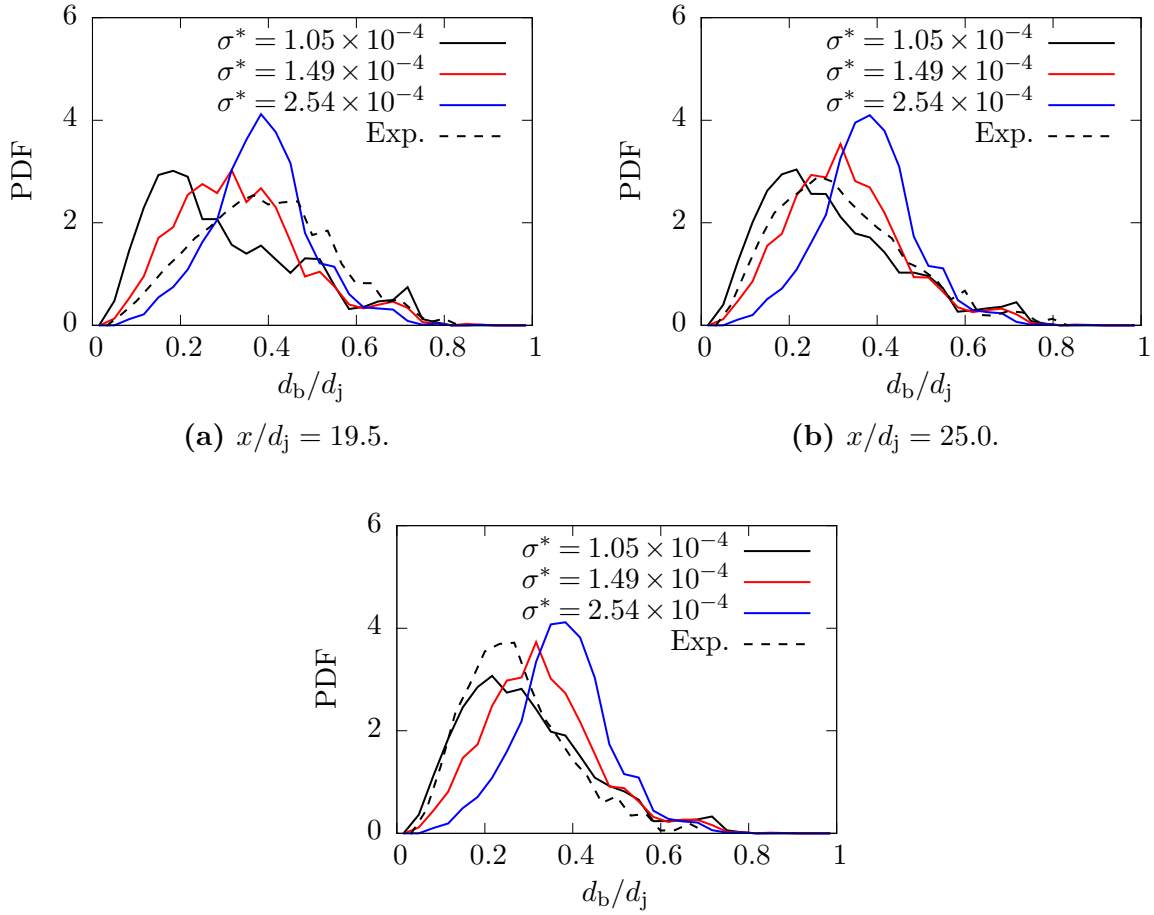

(a) $x/d_j = 19.5$. **(b)** $x/d_j = 25.0$.

(c) $x/d_j = 34.1$.

Fig. 11.43. Comparison of the volumetric probability density functions of the bubble diameter for three different surface tensions at three downstream positions. The experimental results by Martínez-Bazán et al. (1999a) are included as a reference. Taken from Hoppe and Breuer (2020).

from the results shown in Fig. 11.43 that a reduction of the surface tension leads to a shift of the bubble size distribution towards smaller diameters. At the first downstream position of $x/d_j = 19.5$ the peak value of the probability density function is found at $d_b/d_j \approx 0.18$ for $\sigma^* = 1.05 \times 10^{-4}$. For the usual case corresponding to $\sigma^* = 1.49 \times 10^{-4}$ the peak is located at about $d_b/d_j = 0.3$ at this downstream position. The same trend is obtained for the other two downstream positions of $x/d_j = 25.0$ and 34.1, i.e., the bubble size distribution is visibly shifted towards smaller bubble diameters for $\sigma^* = 1.05 \times 10^{-4}$ compared with $\sigma^* = 1.49 \times 10^{-4}$. Increasing the surface tension to $\sigma^* = 2.54 \times 10^{-4}$ has the opposite effect on the probability density function. In this case the bubble size distribution is moved towards larger bubble diameters, e.g., the peak of the PDF is found at about $d_b/d_j = 0.4$ at all downstream positions considered.

The results shown in Fig. 11.43 can be readily explained by the influence of the surface tension on the dimensionless Weber number. According to the definition of the Weber

number, the surface tension appears in the denominator of Eq. (8.5). Hence, for the same diameter of the parent bubble $d_{\mathrm{b,p}}$ and the same strength of the turbulent fluctuations $\langle u_i' \, u_i' \rangle_{d_{\mathrm{b,p}}}$, a larger Weber number is obtained for a decreasing surface tension, while increasing σ leads to a smaller Weber number. Considering that the breakup criterion defined by Eq. (8.4) requires a minimum value of the Weber number of $\mathrm{We}_{\mathrm{min}} \approx 15.12$ (Eq. (8.6)) for breakup to occur, it is obvious that criterion (8.4) can be fulfilled more easily, if the dimensionless surface tension is decreased to $\sigma^* = 1.05 \times 10^{-4}$. In other words, less intense turbulent fluctuations are required to break up bubbles compared to the case of $\sigma^* = 1.49 \times 10^{-4}$. Consequently, the shift of the bubble size distribution towards smaller bubble diameters observed in Fig. 11.43 for $\sigma^* = 1.05 \times 10^{-4}$ is caused by the augmented breakup into smaller daughter bubbles.

Due to the presence of more but smaller bubbles, a second consequence of a decreased surface tension is an enhanced bubble number flux. The corresponding normalized quantity is shown in Fig. 11.44 together with the results obtained for the larger surface tensions. Note that the plateau of the bubble number flux is not only quantitatively larger for $\sigma^* = 1.05 \times 10^{-4}$ but is also reached further downstream ($x/d_{\mathrm{j}} \approx 28$) compared with the standard case of $\sigma^* = 1.49 \times 10^{-4}$ ($x/d_{\mathrm{j}} \approx 23$). This finding is also caused by the fact that less intense turbulent fluctuations are sufficient for breakup to occur. On the other hand, increasing σ^* to a value of 2.54×10^{-4} renders the fulfillment of criterion (8.4) more difficult, since the strength of the turbulent fluctuations has to be larger in order to fulfill the breakup criterion. Consequently, as seen in Fig. 11.43 the bubble size distribution is shifted towards larger bubble diameters leading to a decreased bubble number flux with the nearly constant plateau already reached at about $x/d_{\mathrm{j}} = 21$, see Fig. 11.44.

The results shown in Figs. 11.43 and 11.44 are meaningful from a physical point of view. Bubbles of a small surface tension tend to deform more easily. Thus, the probability of a successful breakup into smaller daughter bubbles is larger than for a bubble with a larger surface tension, which prevents the bubble to be deformed by turbulent structures impacting on their surface. Consequently, the bubbles are less likely to break up.

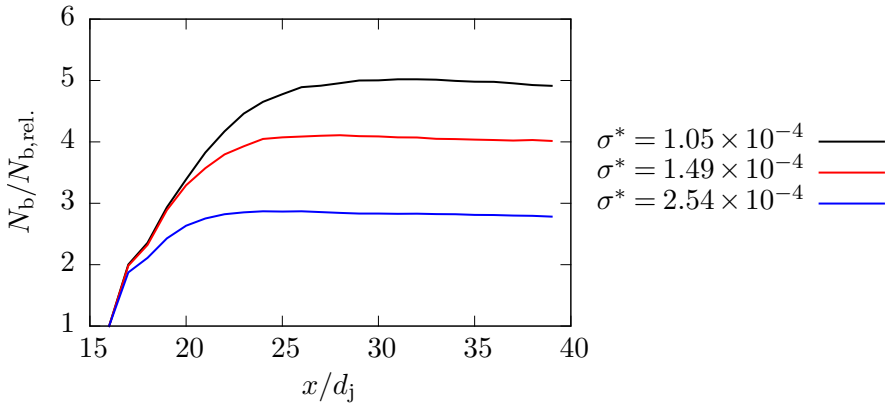

Fig. 11.44. Comparison of the normalized bubble number flux for the three surface tensions considered.

11.4.6 Summary of the Results

The present breakup model described in Chapter 8 is validated by using the experiments by Martínez-Bazán et al. (1999a,b) as a reference case. Martínez-Bazán et al. (1999a,b) examined the breakup of bubbles injected into a fully developed turbulent jet flow. In the corresponding simulations the experimental setup described in Section 10.5 is mimicked by tracking bubbles through a jet flow at a Reynolds number of $\mathrm{Re_j} = 38,250$. The bubbles are inserted into the fluid at $x/d_\mathrm{j} = 16.1$ with the diameter of the bubbles inversely sampled based on the bubble size distribution (Fig. 10.3) given by Martínez-Bazán et al. (1999a) at the same downstream position. Afterwards, the turbulence-induced breakup of the bubbles being carried downstream by the flow is investigated.

Firstly, the correct prediction of the fluid flow is validated by comparing the results of the simulations with experimental data by Hussein et al. (1994) and Zaman and Hussain (1980). It is shown that the predicted distribution of the mean streamwise velocity along the centerline of the jet and in the radial direction agrees very well with the experiments. The radial profiles of the normal Reynolds stress components in the streamwise, the radial and the circumferential direction as well as the only non-vanishing Reynolds shear stress component are also in accordance with the experimental results.

Afterwards, the probability density functions of the bubble diameter obtained by the simulation are compared with the experimental results by Martínez-Bazán et al. (1999a) at three downstream positions ($x/d_\mathrm{j} = 19.5$, 25.0 and 34.1). It is observed that at the first downstream position the bubble size distribution of the simulation is slightly shifted towards too small bubble diameters compared with the results of the experiments. Further downstream the opposite is true, i.e., the predicted bubble sizes are slightly too large. From these results it can be concluded that the present breakup model slightly overpredicts breakup into small bubbles in the region directly after the bubble injection, but then underpredicts it further downstream. This result is also reflected in the normalized number flux of the bubbles. Compared with the experiment, the number flux is slightly too large directly after the bubble injection, i.e., too many small bubbles are present in the flow. Downstream of $x/d_\mathrm{j} \approx 23$ the predicted number flux reaches a plateau, which is somewhat too small in magnitude compared with the experiment. Despite these small deviations, the overall agreement of the predicted bubble size distributions with the experimental results is good. Hence, the breakup model is able to reliably predict breakup.

In order to further analyze the present breakup model, the influence of the idle time $\Delta t_\mathrm{idle} = \Delta t_\mathrm{break}$ estimated by the approaches described in Section 8.2.4 is investigated. The idle time prevents the breakup of daughter bubbles during a certain time period after their generation. Note again that $\Delta t_\mathrm{break,etf}$ given by Eq. (8.32) is used as the standard time lag in the other cases presented above, while for this study additional simulations are performed applying $\Delta t_\mathrm{break,AA}$ and $\Delta t_\mathrm{break,etk}$ described by Eqs. (8.28) and (8.31), respectively. It is apparent from the obtained results that the longer idle times for $\Delta t_\mathrm{break,AA}$ and $\Delta t_\mathrm{break,etfk}$ result in a shift of the bubble size distributions to larger bubble diameters. This can be explained by the extended periods of time during which the daughter bubbles cannot break up resulting in larger bubble diameters. Correspondingly, the bubble number flux decreases for an increasing duration of the idle time. The overall

agreement with the experimental results by Martínez-Bazán et al. (1999a) is worse for the cases estimating $\Delta t_{\mathrm{break}}$ by Eqs. (8.28) and (8.31). Consequently, the choice of $\Delta t_{\mathrm{break,etf}}$ described by Eq. (8.32) as standard is affirmed.

Afterwards, the influence of bubble coalescence on the evolution of the bubbles is investigated. It is revealed that the results of simulations with and without coalescence only marginally deviate from each other. Consequently, it is found that in the present case coalescence does not play an important role, which agrees with the results by Martínez-Bazán et al. (1999a).

Lastly, the present breakup model is used to analyze the influence of the bubble properties on the breakup, i.e., the surface tension of the bubbles is varied. It is shown that decreasing the surface tension moves the probability density function of the bubble diameter towards smaller bubble sizes, while increasing the surface tension has the opposite effect. This result can be readily explained by the fact that bubbles of a smaller surface tension can be deformed more easily allowing for breakup due to less intense turbulent velocity fluctuations. On the other hand, for a larger surface tension stronger turbulent fluctuations are required for deformations sufficient for breakup. Again, the shifts of the size distributions to on average smaller or larger bubble diameters is reflected in the bubble number flux.

In summary, a reliable and an efficient model to describe breakup of bubbles in the Euler–Lagrange framework using LES to predict the turbulent flow is obtained.

12 Conclusions and Outlook

The objective of this thesis was the numerical description of turbulent flows containing a possibly huge number of dispersed bubbles including important phenomena such as bubble coalescence and breakup. For this purpose, the in-house CFD code $\mathcal{LESOCC}$ developed at PfS was chosen as a framework. The code relies on Euler–Lagrange predictions, where the turbulent fluid flow is resolved by large-eddy simulations. Prior to this thesis, $\mathcal{LESOCC}$ was already able to efficiently track a huge number of particles or droplets, while incorporating mechanisms to realistically predict inter-particle collisions and collisions of the particulate phase with smooth or rough walls, agglomeration and breakup of solid particles and coalescence of droplets (Alletto and Breuer, 2012, 2013a,b, 2015; Almohammed and Breuer, 2016a,b, 2019; Breuer and Alletto, 2011, 2012; Breuer et al., 2012; Breuer and Almohammed, 2015; Breuer and Khalifa, 2019a,b). The results of the extensions were published before in Breuer and Hoppe (2017, 2018) and Hoppe and Breuer (2017, 2018, 2020).

The first step towards the prediction of bubble-laden flows was the extension of the existing **Lagrangian tracking** methodology. This involved an adaption of the drag and the lift forces allowing to account for clean or contaminated bubbles. The drag relation also takes deviations from a spherical shape into account. Additionally, the added-mass force and the pressure gradient force were included in the force balance. The Lagrangian bubble tracking and the associated two-way coupling describing the feedback of the bubbles on the fluid have been tested by a comparison with the results of a DNS of a bubble-laden channel flow (Molin et al., 2012). An overall satisfactory agreement with the available reference data could be achieved. Minor deviations could be traced back to the fact that Molin et al. (2012) applied a pseudo-spectral solver for the estimation of the fluid flow, which yielded an improved accuracy compared with the more flexible large-eddy framework applied in the present thesis. Hence, the entire simulation methodology (particle tracking and two-way coupling) reliably predicts the motion of bubbles within a turbulent flow.

Aside from the adaption of the bubble tracking scheme, three major topics have been the focus of this thesis:

I. The estimation of the **unresolved scales** at the position of the bubbles (or particles) by a particle subgrid-scale model.

II. The physically meaningful modeling of the **bubble coalescence** process.

III. The reliable prediction of the **bubble breakup** process and the formulation of suitable post-breakup conditions.

For all topics suitable modeling approaches have been chosen based on reviews of the available literature. Afterwards, the selected models were extended in various ways in order to improve their accuracy and to enhance the efficiency of the associated computations.

For the modeling of the **unresolved scales** seen by the particles or bubbles, the Langevin subgrid-scale model by Pozorski and Apte (2009) was chosen as a starting point (Breuer and Hoppe, 2017). This choice was motivated by the fact that the model accounts for the temporal correlation of the subgrid scales, the crossing-trajectory effect and the continuity effect and its numerical effort is low. An arbitrarily orientated particle motion was taken into account by extending the model towards a matrix formulation proposed by Minier et al. (2004, 2014). Furthermore, an unconditionally stable integration-based solution method (Minier et al., 2003; Peirano et al., 2006) was derived, which is of special importance for LES of wall-bounded flows.

The extended Langevin model was applied to two different downward channel flow setups considering gas bubbles ($\mathrm{Re}_\tau = 150$) and solid particles of three different Stokes numbers ($\mathrm{Re}_\tau = 644$). The results for the case of bubbles were:

- Neither the trivial nor the extended Langevin model yielded a noticeable deviation from the results obtained without any subgrid-scale model for the unresolved scales seen by the bubbles. This was attributed to the small subgrid-scale velocities estimated by the models.
- The Langevin model correctly estimates the level of the turbulent kinetic energy of the subgrid scales $k_{\mathrm{SGS}}^{\mathrm{seen}}$ seen by the dispersed phase (bubbles and particles).
- Due to the preferential accumulation of the bubbles in regions of high fluid velocity fluctuations, the averaged values of $\langle k_{\mathrm{SGS}}^{\mathrm{seen}} \rangle$ slightly deviated from $\langle k_{\mathrm{SGS}} \rangle$.

For solid particles the following results were obtained:

- Due to the higher Reynolds number, the influence of the Langevin subgrid-scale model increased.
- The averaged turbulent kinetic energy of the subgrid scales seen by the particles $\langle k_{\mathrm{SGS}}^{\mathrm{seen}} \rangle$ was found to be approximately equal to the turbulent kinetic energy of the unresolved scales $\langle k_{\mathrm{SGS}} \rangle$. This could be explained by the higher inertia of the particles preventing a preferential accumulation.
- The extended Langevin subgrid-scale model led to a significant increase of the averaged particle volume fraction in the vicinity of solid walls. This agrees with results by Marchioli et al. (2008).
- An enlarged number of particle-particle collisions was observed for the simulations with the Langevin subgrid-scale model compared with the case without any model, which had a significant impact on the particle agglomeration (Almohammed, 2018). Similar effects were observed for particle-wall collisions and deposition processes.
- A variation of the particle Stokes number St^+ revealed that the effect of the Langevin model on the particle statistics is affected by the Stokes number.

Consequently, it could be concluded that the overall influence of the extended Langevin model devised by Breuer and Hoppe (2017) is mainly restricted to quantities such as the volume fraction in the vicinity of the walls and associated effects, i.e., inter-particle or particle-wall collisions. Furthermore, an increasing Reynolds number of the flow increases the influence of the subgrid-scale model. It has to remarked again that the numerical effort associated with the extended Langevin model is reasonable. For the particle-laden channel flow the average computational time required for the complete simulation is increased by about 15% by the extended Langevin model. For comparison, the much simpler trivial model increases the overall CPU-time by 8% without significantly influencing the averaged properties of the dispersed phase.

Bubble coalescence is modeled by the approach by Jeelani and Hartland (1991) in the present thesis. It possesses the advantage to consider the temporally evolving contact surface and the ability to describe the coalescence of clean and contaminated bubbles. Furthermore, the transition time between inertia-dominated and viscous-controlled drainage is taken into account for contaminated bubbles. Additionally, the contact time of the colliding bubbles is estimated by the model. In the present thesis the physical mechanism responsible for the liquid drainage was improved by assuming a radial pressure gradient in the liquid trapped between the colliding bubbles for the derivation of the drainage equations. Furthermore, the necessity to numerically determine the transition time for each collision of contaminated bubbles was circumvented by relying on a regression function determined once at the beginning of the simulation using a non-linear least-squares fit for a pre-defined set of bubble diameters and relative collision velocities (Hoppe and Breuer, 2018). Thus, an efficient methodology results, which allows to apply the coalescence model to flows containing a huge number of bubbles. The coalescence model was further improved within this thesis by a variably adjusted added-mass coefficient C'_{m} of the bubbles.

The model was assessed in two distinctive test cases. In the first case, the results were compared with the experiments by Kosior et al. (2014) and Zawala and Malysa (2011) for single clean and contaminated bubbles coalescing with a free surface. The results can be summarized as follows:

- For both a constant and a variable added-mass coefficient the results agreed well with the reference data. For clean bubbles coalescence was predicted at velocities agreeing reasonably well with the experiment, while the absence of coalescence of contaminated bubbles was correctly reproduced by the extended coalescence model.

- In both cases of a constant and a variable added-mass coefficient C'_{m}, the results predicted by the extended coalescence model were significantly improved compared with the results of simpler coalescence models, which require an additional model for the contact time.

- For a constant added-mass coefficient the results showed some deviations to the experimental data, especially regarding the contact times. Accounting for a variable adjustment of C'_{m} yielded a better agreement with the experiments.

The second case was a bubble column allowing for an evaluation of the coalescence model for flows containing a large number of bubbles. The obtained results were:

- The evolution of the bubble size with an increasing distance to the injection visibly changed by a variation of the primary bubble size and the contamination with surfactants, which was reflected in the probability density functions of the bubble size at various heights within the column. In general, the size distribution of the bubbles was shifted towards larger bubbles by considering contaminated bubbles and smaller primary bubbles.
- Analyzing the bubble-induced turbulent kinetic energy of the fluid revealed that the observed differences are caused by the ability of the bubbles to induce turbulence. Two mechanisms were identified:
  - The higher bubble number density for the case of small primary bubbles led to more frequent collisions and coalescence processes, where the resulting larger bubbles were able to transfer more momentum to the fluid.
  - Contaminated bubbles were able to transfer more momentum to the fluid due to the generally larger drag coefficient. Consequently, the magnitude of the turbulent fluid fluctuations was increased.
- Due to the bubble-induced turbulence, the frequency of bubble collisions was augmented leading to larger bubbles inducing more turbulent fluid velocity fluctuations. Hence, a self-exciting feedback loop was obtained.
- For large clean primary bubbles neither of the two mechanisms was sufficiently strong to induce significant fluctuations preventing further coalescence events. For all other cases one or both mechanisms provided enough momentum to induce turbulence.
- A comparison of the collision velocities showed that contaminated bubbles of both sizes and small clean bubbles collided due to turbulent velocity fluctuations, while for large clean bubbles the collisions were buoyancy driven. The averaged collision velocities agreed with estimations by Liao et al. (2015).
- The bubble size distributions were only marginally affected by the determination of the (constant or variable) added-mass coefficient, despite the contact time being lower for a variable C'_{m}. This result was explained by a prolonged relative transition time during which the substantially faster inertia-controlled drainage was active.

In summary, the extended coalescence model reliably predicts coalescence of both clean and contaminated bubbles. Due to the use of a regression function, the numerical effort required for the prediction of the coalescence of contaminated bubbles could be successfully reduced. Despite the up to $600,000$ bubbles simultaneously present in the column, the coalescence model required only about 1 to 2% of the total CPU-time demonstrating the cost-effectiveness of the extended coalescence model.

Bubble breakup has been described by transferring the breakup model by Hagesaether et al. (2002) from the Euler–Euler to the Euler–Lagrange framework. The model was

chosen due to its physically realistic breakup mechanism and the possibility to deterministically estimate the size of the resulting daughter bubbles. Inevitable definitions of suitable post-breakup conditions for the Euler–Lagrange framework involved the separation axis and the separation velocity of the daughter bubbles. Neither of these quantities has been considered in previous studies relying on the Euler–Euler framework. Additionally, a breakup time during which daughter bubbles cannot further break up after their formation was estimated in order to prevent an unphysical dependency of the breakup frequency on the numerical time-step size. All these quantities were derived purely based on physical arguments (Hoppe and Breuer, 2020).

In order to validate the breakup model, the breakup of bubbles dispersed in a turbulent fully developed jet flow was investigated. The case was based on the experimental study by Martínez-Bazán et al. (1999a,b). The following conclusions could be drawn:

- The comparison of the bubble size distributions at three different downstream locations with experimental results by Martínez-Bazán et al. (1999a) showed an overall good agreement of the predicted results with the reference data.

- The present breakup model slightly overpredicts breakup into somewhat too small daughter bubbles shortly downstream of the bubble injection, while further downstream the breakup into smaller daughter bubbles is underestimated.

- The estimation of the time lag by $\Delta t_{\mathrm{break,etf}}$ according to Eq. (8.32) yielded the best agreement with the experimental data affirming the choice as the standard idle time. In general, a prolonged idle time led to a shift of the bubble size distributions towards larger bubbles.

- Bubble coalescence only marginally affected the results, which agrees with observations by Martínez-Bazán et al. (1999a).

- While a decrease of the surface tension resulted in an augmented breakup into small daughter bubbles, the opposite effect was achieved by increasing the surface tension. This observation can be explained by physical arguments, i.e., bubbles of a lower surface tension are deformed more easily, while bubbles with a high surface tension resist the deformation by turbulent velocity fluctuations.

Consequently, the breakup criterion by Hagesaether et al. (2002) was successfully transfered from the Euler–Euler to the Euler–Lagrange framework with a fully deterministic prediction of the post-breakup conditions of the daughter bubbles allowing a reliable description of turbulence-induced bubble breakup. Again, the methodology (Hoppe and Breuer, 2020) derived during this thesis is highly efficient. On average, only 1.8% of the total CPU-time is required for the estimation of bubble breakup.

Summarizing the results of this thesis, the LES-based Euler–Lagrange framework $\mathcal{LESOCC}$ was successfully extended towards the description of turbulent bubble-laden flows including important physical mechanisms such as bubble coalescence and breakup.

In the future, further extensions of the **Lagrangian tracking** should consider partially contaminated bubbles (Tomiyama et al., 1998), where the boundary condition on some parts of the bubble surface is of a no-slip type, while on the remaining parts a free-slip condition is valid. Additionally, if flows laden with larger bubbles are supposed to be considered in the future, the influence of surface deformations have to be accounted for (Sommerfeld et al., 2018). These larger bubbles also pose a difficulty for the two-way coupling methodology, since the bubbles may span several control volumes. Hence, a modification of the coupling mechanism should be considered, e.g., by the approach proposed by Hu and Celik (2008). Another reasonable option for the description of large bubbles would be the coupling of an Euler–Lagrange approach for the small bubbles with an Euler–Euler ansatz for the prediction of the large bubbles.

The extended Langevin **subgrid-scale model** should be investigated in flows of even higher Reynolds numbers, in order to further assess how the extended model affects the dispersed phase, if a larger part of the turbulent spectrum has to be modeled. Furthermore, for an improved modeling of the unresolved scales effects such as inhomogeneous and non-isotropic turbulence should be taken into account. Presently neglected terms preventing spurious drift effects should also be incorporated in the model. Additionally, the effects of a spatial correlation of the unresolved scales seen by particles in close vicinity to each other should be taken into account (Mazzitelli et al., 2014). Lastly, it may be worthwhile to combine the approximate deconvolution method and the Langevin-based modeling of the subgrid scales as proposed by Adams (2011) and Michałek et al. (2013) in order to obtain the beneficial properties of both approaches.

The **bubble coalescence** should be further assessed by analyzing the self-exciting feedback loop of bubble-induced turbulence. Especially, the onset of this mechanism should be quantified. Possible future advancements of the coalescence model itself should involve an improved description of the physical mechanism, e.g., the assumption of a flat contact surface between the colliding bubbles is known to be a rather harsh simplification (Chan et al., 2011; Chesters and Hofman, 1982; Manica et al., 2016). Furthermore, the coalescence model could be extended towards the description of the coalescence of bubbles with a partially immobile surface (Chesters, 1991). Lastly, considering the importance of bubble-induced turbulence for the bubble column setup, the excitation of fluid fluctuations by the rapid bubble coalescence occurring after the rupture of the liquid film should be investigated.

Regarding **bubble breakup**, future extensions of the model should involve the inclusion of the entire spectrum of turbulence for the estimation of the turbulent velocity fluctuations as proposed by Castellano et al. (2019), Karimi and Andersson (2019) and Solsvik and Jakobsen (2016a,b). Furthermore, despite the fact that non-binary breakups are uncommon, the possibility of such an event should at least be considered by the breakup model. Additionally, the breakup due to the resonance mechanism observed by Risso and Fabre (1998) should be taken into account. Another improvement of the present model would be to actually set the positions of the daughter bubbles along the axis of separation with a certain distance such that the daughters do not touch each other after the breakup event.

A Transformation to a Cylindrical Coordinate System

In this chapter the transformation of a velocity vector (u, v, w) in Cartesian coordinates to a velocity vector (u_x, u_r, u_θ) in cylindrical coordinates is explained. This measure is necessary, since $\mathcal{LESOCC}$ works with Cartesian coordinates, while in the test case described in Section 10.5 a cylindrical coordinate system makes more sense in order to improve the statistical averages. Note that here the x-axis describes the vertical direction. Hence, the radius r and the angle θ are determined by the y- and z-components of the Cartesian coordinate system according to the relations:

$$r = \left(y^2 + z^2\right)^{\frac{1}{2}}, \tag{A.1a}$$

$$\theta = \arctan\left(\frac{z}{y}\right). \tag{A.1b}$$

For the sake of simplicity it is assumed in Eq. (A.1b) that θ is within 0 and $\pi/2$, i.e., that $y > 0$ and $z \geq 0$. Hence, one can readily see that the components of the velocity vector $\mathrm{d}\boldsymbol{r}/\mathrm{d}t = (u_x, u_r, u_\theta)$ in cylindrical coordinates are determined by:

$$u_x = \frac{\mathrm{d}x}{\mathrm{d}t} = u, \tag{A.2a}$$

$$u_r = \frac{\mathrm{d}r}{\mathrm{d}t} = \frac{y\,v + z\,w}{(y^2 + z^2)^{\frac{1}{2}}} = \frac{y}{r}\,v + \frac{z}{r}\,w, \tag{A.2b}$$

$$u_\theta = r\,\frac{\mathrm{d}\theta}{\mathrm{d}t} = \frac{y\,w - z\,v}{(y^2 + z^2)^{\frac{1}{2}}} = \frac{y}{r}\,w - \frac{z}{r}\,v. \tag{A.2c}$$

Note that the transformation by Eq. (A.2) is valid regardless of the quadrant of the angle θ. Consequently, if one has averaged velocity components $\langle u\rangle, \langle v\rangle, \langle w\rangle$ in a Cartesian frame of reference, the corresponding averaged velocities in cylindrical coordinates can be readily determined by:

$$\langle u_x\rangle = \langle u\rangle, \tag{A.3a}$$

$$\langle u_r\rangle = \frac{y}{r}\,\langle v\rangle + \frac{z}{r}\,\langle w\rangle, \tag{A.3b}$$

$$\langle u_\theta\rangle = \frac{y}{r}\,\langle w\rangle - \frac{z}{r}\,\langle v\rangle. \tag{A.3c}$$

Similarly, the fluctuations can be calculated using the definition:

$$u'_x = u - \langle u \rangle = u', \tag{A.4a}$$

$$u'_r = \frac{y}{r}\,(v - \langle v \rangle) + \frac{z}{r}\,(w - \langle w \rangle) = \frac{y}{r}\,v' + \frac{z}{r}\,w', \tag{A.4b}$$

$$u'_\theta = \frac{y}{r}\,(w - \langle w \rangle) - \frac{z}{r}\,(v - \langle v \rangle) = \frac{y}{r}\,w' - \frac{z}{r}\,v'. \tag{A.4c}$$

Consequently, the velocity fluctuations in a cylindrical coordinate system are:

$$\langle u'_x\,u'_x \rangle = \langle u'\,u' \rangle, \tag{A.5a}$$

$$\langle u'_r\,u'_r \rangle = \frac{y^2}{r^2}\,\langle v'\,v' \rangle + \frac{z^2}{r^2}\,\langle w'\,w' \rangle + 2\,\frac{y\,z}{r^2}\,\langle v'\,w' \rangle, \tag{A.5b}$$

$$\langle u'_\theta\,u'_\theta \rangle = \frac{y^2}{r^2}\,\langle w'\,w' \rangle + \frac{z^2}{r^2}\,\langle v'\,v' \rangle - 2\,\frac{y\,z}{r^2}\,\langle v'\,w' \rangle, \tag{A.5c}$$

$$\langle u'_x\,u'_r \rangle = \frac{y}{r}\,\langle u'\,v' \rangle + \frac{z}{r}\,\langle u'\,w' \rangle, \tag{A.5d}$$

$$\langle u'_x\,u'_\theta \rangle = \frac{y}{r}\,\langle u'\,w' \rangle - \frac{z}{r}\,\langle u'\,v' \rangle, \tag{A.5e}$$

$$\langle u'_r\,u'_\theta \rangle = \frac{y^2}{r^2}\,\langle v'\,w' \rangle - \frac{z^2}{r^2}\,\langle v'\,w' \rangle - \frac{y\,z}{r^2}\,(\langle v'\,v' \rangle - \langle w'\,w' \rangle)\,. \tag{A.5f}$$

Based on these values an additional averaging in circumferential direction is possible. In case of the results shown in Section 11.4.1 the circumferential averaging is done by utilizing the post-processing tool "Tecplot 360". First, a pre-defined number of slices N_{slices} containing the temporally averaged fluid statistics given by Eqs. (A.3) and (A.5) is extracted based on a linear interpolation of the data stored in the eight cell centers closest to a certain position (x, r, θ) on a given slice. The slices pass through the centerline axis of the jet, but each slice is rotated by an angle of $2\,\pi/N_{\text{slices}}$. Afterwards, all values located at a certain position (x, r) on the different slices are averaged up by Eqs. (9.56) and (9.59).

Bibliography

Abid, S. and A. K. Chesters (1994). The drainage and rupture of partially-mobile films between colliding drops at constant approach velocity. *International Journal of Multiphase Flow* 20 (3), 613–629.

Adams, N. A. (2011). A stochastic extension of the approximate deconvolution model. *Physics of Fluids* 23 (5), 055103.

Albert, C., H. Raach and D. Bothe (2012). Influence of surface tension models on the hydrodynamics of wavy laminar falling films in Volume of Fluid-simulations. *International Journal of Multiphase Flow* 43, 66–71.

Alletto, M. (2014). Numerical investigation of the influence of particle-particle and particle-wall collisions in turbulent wall-bounded flows at high mass loadings. PhD thesis. Department of Fluid Mechanics, Helmut-Schmidt-University, Hamburg, Germany.

Alletto, M. and M. Breuer (2012). One-way, two-way and four-way coupled LES predictions of a particle-laden turbulent flow at high mass loading downstream of a confined bluff body. *International Journal of Multiphase Flow* 45, 70–90.

Alletto, M. and M. Breuer (2013a). Large-eddy simulation of the particle-laden turbulent flow in a cyclone separator. In: *High Performance Computing in Science and Engineering '13*. Ed. by W. E. Nagel, D. H. Kröner and M. M. Resch. Springer International Publishing, 377–391.

Alletto, M. and M. Breuer (2013b). Prediction of turbulent particle-laden flow in horizontal smooth and rough pipes inducing secondary flow. *International Journal of Multiphase Flow* 55, 80–98.

Alletto, M. and M. Breuer (2015). Four-way coupled LES predictions of dense particle-laden flows in horizontal smooth and rough pipes. In: *Direct and Large-Eddy Simulation IX*. Ed. by J. Fröhlich, H. Kuerten, B. J. Geurts and V. Armenio. Springer International Publishing, 605–612.

Almohammed, N. (2018). Modeling and Simulation of Particle Agglomeration, Droplet Coalescence and Particle-Wall Adhesion in Turbulent Multiphase Flows. PhD thesis. Department of Fluid Mechanics, Helmut-Schmidt-University, Hamburg, Germany.

Almohammed, N. and M. Breuer (2016a). Modeling and simulation of agglomeration in turbulent particle-laden flows: A comparison between energy-based and momentum-based agglomeration models. *Powder Technology* 294, 373–402.

Almohammed, N. and M. Breuer (2016b). Modeling and simulation of particle–wall adhesion of aerosol particles in particle-laden turbulent flows. *International Journal of Multiphase Flow* 85, 142–156.

Almohammed, N. and M. Breuer (2019). Towards a deterministic composite collision outcome model for surface-tension dominated droplets. *International Journal of Multiphase Flow* 110, 1–17.

Anderson, T. B. and R. Jackson (1967). Fluid mechanical description of fluidized beds. Equations of motion. *Industrial & Engineering Chemistry Fundamentals* 6 (4), 527–539.

Andersson, R. and B. Andersson (2006a). On the breakup of fluid particles in turbulent flows. *AIChE Journal* 52 (6), 2020–2030.

Andersson, R. and B. Andersson (2006b). Modeling the breakup of fluid particles in turbulent flows. *AIChE Journal* 52 (6), 2031–2038.

Anguelova, M. D. and P. Huq (2012). Characteristics of bubble clouds at various wind speeds. *Journal of Geophysical Research: Oceans* 117 (C3), 1–22.

Antia, H. M. (2012). *Numerical Methods for Scientists and Engineers*. 3rd ed. Hindustan Book Agency.

Apte, S. V., K. Mahesh, P. Moin and J. C. Oefelein (2003). Large-eddy simulation of swirling particle-laden flows in a coaxial-jet combustor. *International Journal of Multiphase Flow* 29 (8), 1311–1331.

Armenio, V. and V. Fiorotto (2001). The importance of the forces acting on particles in turbulent flows. *Physics of Fluids* 13, 2437–2440.

Armenio, V., U. Piomelli and V. Fiorotto (1999). Effect of the subgrid scales on particle motion. *Physics of Fluids* 11 (10), 3030–3042.

Auton, T. R. (1987). The lift force on a spherical body in a rotational flow. *Journal of Fluid Mechanics* 183, 199–218.

Auton, T. R., J. C. R. Hunt and M. Prud'Homme (1988). The force exerted on a body in inviscid unsteady non-uniform rotational flow. *Journal of Fluid Mechanics* 197, 241–257.

Aybers, N. M. and A. Tapucu (1969). The motion of gas bubbles rising through stagnant liquid. *Wärme- und Stoffübertragung* 2 (2), 118–128.

Baggett, J. S., J. Jiménez and A. G. Kravchenko (1997). Resolution requirements in large-eddy simulations of shear flows. In: *Annual Research Briefs*. Center for Turbulence Research, 51–66.

Balachandar, S. and J. K. Eaton (2010). Turbulent dispersed multiphase flow. *Annual Review of Fluid Mechanics* 42 (1), 111–133.

Bandara, U. C. and P. D. Yapa (2011). Bubble sizes, breakup, and coalescence in deepwater gas/oil plumes. *Journal of Hydraulic Engineering* 137 (7), 729–738.

Bardina, J., J. H. Ferziger and W. C. Reynolds (1980). Improved subgrid-scale models for large-eddy simulation. *AIAA Paper* 80 (1357), 80–1357.

Basset, A. B. (1888). *A Treatise On Hydrodynamics, Vol. 2.* 2nd ed. Deighton, Bell and Co.

Batchelor, G. K. (1953). *The Theory of Homogeneous Turbulence.* Cambridge University Press. ISBN: 0521041171.

Benocci, C. and A. Pinelli (1990). The role of the forcing term in the large eddy simulation of equilibrium channel flow. In: *Engineering Turbulence Modeling and Experiments.* Ed. by W. Rodi and E. N. Ganić, 287–296.

Berrouk, A. S., D. Laurence, J. J. Riley and D. E. Stock (2007). Stochastic modelling of inertial particle dispersion by subgrid motion for LES of high Reynolds number pipe flow. *Journal of Turbulence* 8 (50), 1–20.

Berrouk, A. S., D. E. Stock, D. Laurence and J. J. Riley (2008). Heavy particle dispersion from a point source in turbulent pipe flow. *International Journal of Multiphase Flow* 34, 916–923.

Bhavaraju, S. M., T. W. F. Russell and H. W. Blanch (1978). The design of gas sparged devices for viscous liquid systems. *AIChE Journal* 24 (3), 454–466.

Bianco, F., S. Chibbaro, C. Marchioli, M. V. Salvetti and A. Soldati (2012). Intrinsic filtering errors of Lagrangian particle tracking in LES flow fields. *Physics of Fluids* 24 (4), 045103.

Binninger, B. (1989). Untersuchung von Modellströmungen in Zylindern von Kolbenmotoren. PhD thesis. Aerodynamisches Institut, RWTH Aachen, Aachen, Germany.

Bird, G. A. (1976). *Molecular Gas Dynamics.* 1st ed. Claredon.

Bogey, C. and C. Bailly (2006). Large eddy simulations of transitional round jets: Influence of the Reynolds number on flow development and energy dissipation. *Physics of Fluids* 18 (6), 065101.

Bogey, C. and C. Bailly (2010). Influence of nozzle-exit boundary-layer conditions on the flow and acoustic fields of initially laminar jets. *Journal of Fluid Mechanics* 663, 507–538.

Bombardelli, F. A., A. E. González and Y. I. Niño (2008). Computation of the particle Basset force with a fractional-derivative approach. *Journal of Hydraulic Engineering* 134 (10), 1513–1520.

Boussinesq, J. V. (1878). Essai sur la théorie des eaux courantes. *Journal de Mathématiques Pures et Appliquées* 4, 335–376.

Brennen, C. E. (1982). *A Review of Added Mass and Fluid Inertial Forces.* Tech. rep. Department of the Navy, Naval Civil Engineering Laboratory. Port Hueneme, CA, USA.

Brennen, C. E. (2005). *Fundamentals of Multiphase Flows*. Cambridge University Press.

Breuer, M. (1998a). Large-eddy simulation of the sub-critical flow past a circular cylinder: Numerical and modeling aspects. *International Journal of Numerical Methods in Fluids* 28 (9), 1281–1302.

Breuer, M. (1998b). Numerical and modeling influences on large-eddy simulations for the flow past a circular cylinder. *International Journal of Heat and Fluid Flow* 19 (5), 512–521.

Breuer, M. (2000). A challenging test case for large-eddy simulation: High Reynolds number circular cylinder flow. *International Journal of Heat and Fluid Flow* 21 (5), 648–654.

Breuer, M. (2002). *Direkte Numerische Simulation und Large–Eddy Simulation turbulenter Strömungen auf Hochleistungsrechnern*. Habilitationsschrift, Universität Erlangen–Nürnberg, Berichte aus der Strömungstechnik, Shaker Verlag, Aachen.

Breuer, M. (2013). *Numerische Strömungsmechanik*. Lecture Notes. Department of Fluid Mechanics, Helmut-Schmidt-University, Hamburg.

Breuer, M. and M. Alletto (2011). Two–phase flow predictions of the turbulent flow in a combustion chamber including particle–particle interactions. *Journal of Physics: Conference Series* 318 (5), 052002.

Breuer, M. and M. Alletto (2012). Efficient simulation of particle-laden turbulent flows with high mass loadings using LES. *International Journal of Heat and Fluid Flow* 35, 2–12.

Breuer, M., M. Alletto and F. Langfeldt (2012). Sandgrain roughness model for rough walls within Eulerian–Lagrangian predictions of turbulent flows. *International Journal of Multiphase Flow* 43, 157–175.

Breuer, M. and N. Almohammed (2015). Modeling and simulation of particle agglomeration in turbulent flows using a hard-sphere model with deterministic collision detection and enhanced structure models. *International Journal of Multiphase Flow* 73, 171–206.

Breuer, M., H. T. Baytekin and E. A. Matida (2006a). Prediction of aerosol deposition in 90° bends using LES and an efficient Lagrangian tracking method. *Journal of Aerosol Science* 37 (11), 1407–1428.

Breuer, M. and F. Hoppe (2017). Influence of a cost-efficient Langevin subgrid-scale model on the dispersed phase of large-eddy simulations of turbulent bubble-laden and particle-laden flows. *International Journal of Multiphase Flow* 89, 23–44.

Breuer, M. and F. Hoppe (2018). A Langevin subgrid-scale model for the prediction of turbulent disperse multiphase flows. In: *ERCOFTAC Bulletin*. Vol. 116. European Research Community on Flow, Turbulence and Combustion (ERCOFTAC), 38–43.

Breuer, M. and A. Khalifa (2019a). Revisiting and improving models for the breakup of compact dry powder agglomerates in turbulent flows within Eulerian–Lagrangian simulations. *Powder Technology* 348, 105–125.

Breuer, M. and A. Khalifa (2019b). Refinement of breakup models for compact powder agglomerates exposed to turbulent flows considering relevant time scales. *Computers & Fluids*. accepted for publication.

Breuer, M., B. Kniazev and M. Abel (2006b). Development of wall models for LES of separated flows. In: *Direct and Large-Eddy Simulation VI*, 373–380.

Breuer, M., E. A. Matida and A. Delgado (2007). Prediction of aerosol drug deposition using an Eulerian-Lagrangian method based on LES. In: *International Conference on Multiphase Flow*. ICMF 2007, July 9–13, 2007, Leipzig, Germany.

Carrà, S. and M. Morbidelli (1987). Gas-Liquid Reactors. In: *Chemical Reaction and Reactor Engineering*. Ed. by J. J. Carberry and A. Varma. Marcel Dekker.

Castellano, S., L. Carrillo, N. Sheibat-Othman, D. Marchisio, A. Buffo and S. Charton (2019). Using the full turbulence spectrum for describing droplet coalescence and breakage in industrial liquid-liquid systems: Experiments and modeling. *Chemical Engineering Journal* 374, 1420–1432.

Cernick, M. J., S. W. Tullis and M. F. Lightstone (2015). Particle subgrid scale modelling in large-eddy simulations of particle-laden turbulence. *Journal of Turbulence* 16 (2), 101–135.

Chan, D. Y. C., E. Klaseboer and R. Manica (2011). Film drainage and coalescence between deformable drops and bubbles. *Soft Matter* 7 (6), 2235–2264.

Chan, T. F., G. H. Golub and R. J. Leveque (1983). Algorithms for computing the sample variance: Analysis and recommendations. *The American Statistician* 37 (3), 242–247.

Chang, I.-S. and S. J. Judd (2002). Air sparging of a submerged MBR for municipal wastewater treatment. *Process Biochemistry* 37 (8), 915–920.

Chen, M., K. Kontomaris and J. McLaughlin (1999). Direct numerical simulation of droplet collisions in a turbulent channel flow. Part I: Collision algorithm. *International Journal of Multiphase Flow* 24 (7), 1079–1103.

Chen, P., M. P. Duduković and J. Sanyal (2005). Three-dimensional simulation of bubble column flows with bubble coalescence and breakup. *AIChE Journal* 51 (3), 696–712.

Cheng, L., G. Ribatski and J. R. Thome (2008). Two-phase flow patterns and flow-pattern maps: Fundamentals and applications. *Applied Mechanics Reviews* 61 (5), 050802.

Chesters, A. K. (1975). The applicability of dynamic-similarity criteria to isothermal, liquid-gas, two-phase flows without mass transfer. *International Journal of Multiphase Flow* 2 (2), 191–212.

Chesters, A. K. (1991). Modelling of coalescence processes in fluid-liquid dispersions: A review of current understanding. *Chemical Engineering Research and Design* 69 (4), 259–227.

Chesters, A. K. and G. Hofman (1982). Bubble coalescence in pure liquids. *Applied Scientific Research* 38 (1), 353–361.

Clift, R., J. R. Grace and M. E. Weber (1978). *Bubbles, Drops, and Particles*. Academic Press.

Colombo, M. and M. Fairweather (2016). RANS simulation of bubble coalescence and break-up in bubbly two-phase flows. *Chemical Engineering Science* 146, 207–225.

Coulaloglou, C. A. and L. L. Tavlarides (1977). Description of interaction processes in agitated liquid-liquid dispersions. *Chemical Engineering Science* 32 (11), 1289–1297.

Crowe, C. T., M. P. Sharma and D. E. Stock (1977). The Particle-Source-In-Cell (PSI-CELL) model for gas-droplet flows. *Journal of Fluids Engineering* 99, 325–332.

Crowe, C. T., M. Sommerfeld and Y. Tsuji (1998). *Multiphase Flows with Droplets and Particles*. CRC Press.

Csanady, G. T. (1963). Turbulent diffusion of heavy particles in the atmosphere. *Journal of the Atmospheric Sciences* 20, 201–208.

Dabiri, S., J. Lu and G. Tryggvason (2013). Transition between regimes of a vertical channel bubbly upflow due to bubble deformability. *Physics of Fluids* 25 (10), 102110.

Daitche, A. (2015). On the role of the history force for inertial particles in turbulence. *Journal of Fluid Mechanics* 782, 567–593.

Darmana, D., N. G. Deen and J. A. M. Kuipers (2006). Parallelization of an Euler–Lagrange model using mixed domain decomposition and a mirror domain technique: Application to dispersed gas-liquid two-phase flow. *Journal of Computational Physics* 220 (1), 216–248.

Deckwer, W.-D. and A. Schumpe (1993). Improved tools for bubble column reactor design and scale-up. *Chemical Engineering Science* 48 (5), 889–911.

Deen, N. G., T. Solberg and B. H. Hjertager (2001). Large eddy simulation of the gas–liquid flow in a square cross-sectioned bubble column. *Chemical Engineering Science* 56 (21), 6341–6349.

Degaleesan, S., M. Dudukovic and Y. Pan (2001). Experimental study of gas-induced liquid-flow structures in bubble columns. *AIChE Journal* 47 (9), 1913–1931.

Deike, L., L. Lenain and W. K. Melville (2017). Air entrainment by breaking waves. *Geophysical Research Letters* 44 (8), 3779–3787.

Deju, L., S. C. P. Cheung, G. H. Yeoh and J. Y. Tu (2013). Capturing coalescence and break-up processes in vertical gas-liquid flows: Assessment of population balance methods. *Applied Mathematical Modelling* 37 (18), 8557–8577.

Dennis, J., D. Gay and R. Walsh (1981a). An adaptive nonlinear least-squares algorithm. *ACM Transactions on Mathematical Software* 7 (3), 348–368.

Dennis, J., D. Gay and R. Walsh (1981b). Algorithm 573: NL2SOL – An adaptive nonlinear least-squares algorithm. *ACM Transactions on Mathematical Software* 7 (3), 369–383.

Devroye, L. (1986). *Non-Uniform Random Variate Generation*. 1st ed. Springer.

Dijkhuizen, W., I. Roghair, M. van Sint Annaland and J. A. M. Kuipers (2010). DNS of gas bubbles behaviour using an improved 3D front tracking model - Drag force on isolated bubbles and comparison with experiments. *Chemical Engineering Science* 65 (4), 1415–1426.

Domaradzki, J. A. and K.-C. Loh (1999). The subgrid-scale estimation model in the physical space representation. *Physics of Fluids* 11 (8), 2330–2342.

Dorgan, A. J. and E. Loth (2007). Efficient calculation of the history force at finite Reynolds numbers. *International Journal of Multiphase Flow* 33 (8), 833–848.

Doubliez, L. (1991). The drainage and rupture of a non-foaming liquid film formed upon bubble impact with a free surface. *International Journal of Multiphase Flow* 17 (6), 783–803.

Douteau, L. (2016). Implementation and evaluation of the influence of the Basset history force. Master thesis. Department of Fluid Mechanics, Helmut-Schmidt-University/University of the German Federal Armed Forces, Hamburg, Germany.

Duineveld, P. C. (1995). The rise velocity and shape of bubbles in pure water at high Reynolds number. *Journal of Fluid Mechanics* 292, 325–332.

Elghannay, H. A. and D. K. Tafti (2016). Development and validation of a reduced order history force model. *International Journal of Multiphase Flow* 85, 284–297.

Elghobashi, S. (1991). Particle-laden turbulent flows: Direct simulation and closure models. *Applied Scientific Research* 48 (3), 301–314.

Elghobashi, S. (1994). On predicting particle-laden turbulent flows. *Applied Scientific Research* 52 (4), 309–329.

Farrell, K. J. (2003). Eulerian/Lagrangian analysis for the prediction of cavitation inception. *Journal of Fluids Engineering* 125 (1), 46–52.

Fede, P., O. Simonin, P. Villedieu and K. D. Squires (2006). Stochastic modeling of the turbulent subgrid fluid velocity along inertial particle trajectories. In: *Proceedings of the 2006 CTR Summer Program*, 247–258.

Fernandes, R. C., R. Semiat and A. E. Dukler (1983). Hydrodynamic model for gas-liquid slug flow in vertical tubes. *AIChE Journal* 29 (6), 981–989.

Ferziger, J. H. and M. Perić (2002). *Computational Methods for Fluid Mechanics*. 3rd ed. Springer.

Gao, N., J. Niu, Q. He, T. Zhu and J. Wu (2012). Using RANS turbulence models and Lagrangian approach to predict particle deposition in turbulent channel flows. *Building and Environment* 48, 206–214.

Gardiner, C. (2003). *Handbook of Stochastic Methods*. 3rd ed. Springer. ISBN: 978-3-540-70712-7.

Garg, R., C. Narayanan, D. Lakehal and S. Subramaniam (2007). Accurate numerical estimation of interphase momentum transfer in Lagrangian–Eulerian simulations of dispersed two-phase flows. *International Journal of Multiphase Flow* 33, 1337–1364.

Garg, R., C. Narayanan and S. Subramaniam (2009). A numerically convergent Lagrangian–Eulerian simulation method for dispersed two-phase flows. *International Journal of Multiphase Flow* 35, 376–388.

Garnier, E., N. Adams and P. Sagaut (2009). *Large Eddy Simulation for Compressible Flows*. 1st ed. Springer.

Gatignol, R. (1983). The Faxén formulae for a rigid particle in an unsteady non-uniform Stokes flow. *Journal de Mécanique théorique et appliquée* 1 (2), 143–160.

Germano, M., U. Piomelli, P. Moin and W. H. Cabot (1991). A dynamic subgrid-scale eddy viscosity model. *Physics of Fluids A: Fluid Dynamics* 3 (7), 1760–1765.

Geurts, B. J. (1997). Inverse modeling for large-eddy simulation. *Physics of Fluids* 9 (12), 3585–3587.

Gibou, F., R. Fedkiw and S. Osher (2018). A review of level-set methods and some recent applications. *Journal of Computational Physics* 353, 82–109.

Giusti, A., F. Lucci and A. Soldati (2005). Influence of the lift force in direct numerical simulation of upward/downward turbulent channel flow laden with surfactant contaminated microbubbles. *Chemical Engineering Science* 60 (22), 6176–6187.

Gohil, T. B., A. K. Saha and K. Muralidhar (2011). Direct numerical simulation of naturally evolving free circular jet. *Journal of Fluids Engineering* 133 (11), 111203.

Gohil, T. B., A. K. Saha and K. Muralidhar (2014). Large eddy simulation of a free circular jet. *Journal of Fluids Engineering* 136 (5), 051205.

Golovin, A. M. and M. F. Ivanov (1971). Motion of a bubble in a viscous liquid. *Journal of Applied Mechanics and Technical Physics* 12 (1), 91–94.

Gresch, M., M. Armbruster, D. Braun and W. Gujer (2011). Effects of aeration patterns on the flow field in wastewater aeration tanks. *Water Research* 45 (2), 810–818.

Grima, E. M., Y. Chisti and M. Moo-Young (1997). Characterization of shear rates in airlift bioreactors for animal cell culture. *Journal of Biotechnology* 54 (3), 195–210.

Gruber, M. C., S. Radl and J. G. Khinast (2015). Rigorous modeling of CO2 absorption and chemisorption: The influence of bubble coalescence and breakage. *Chemical Engineering Science* 137, 188–204.

Gupta, A. and S. Roy (2013). Euler–Euler simulation of bubbly flow in a rectangular bubble column: Experimental validation with Radioactive Particle Tracking. *Chemical Engineering Journal* 225, 818–836. ISSN: 1385-8947.

Hagesaether, L., H. A. Jakobsen and H. F. Svendsen (2002). A model for turbulent binary breakup of dispersed fluid particles. *Chemical Engineering Science* 57, 3251–3267.

Hamaker, H. C. (1937). The London–van der Waals attraction between spherical particles. *Physica* 4 (10), 1058–1072.

Hartland, S. (1967). The approach of a liquid drop to a flat plate. *Chemical Engineering Science* 22 (12), 1675–1687.

Hartland, S., S. A. K. Jeelani and A. Suter (1989). Inertial effects in thin film drainage. *Chemical Engineering Science* 44 (2), 387–391.

Hashizume, K. (1983). Flow pattern and void fraction of refrigerant two-phase flow in a horizontal pipe. *Bulletin of JSME* 26 (219), 1597–1602.

Hesketh, R. P., A. W. Etchells and T. W. F. Russell (1991a). Bubble breakage in pipeline flow. *Chemical Engineering Science* 46 (1), 1–9.

Hesketh, R. P., A. W. Etchells and T. W. F. Russell (1991b). Experimental observations of bubble breakage in turbulent flow. *Industrial and Engineering Chemistry Research* 30 (5), 835–841.

Hewitt, G. F. and D. N. Roberts (1969). *Studies of two-phase flow patterns by simultaneous X-ray and flash photography*. Tech. rep. Atomic Energy Research Establishment.

Hiemenz, P. C. (1986). *Principles of Colloid and Surface Chemistry*. 2nd ed. Marcel Dekker.

Hinze, J. O. (1955). Fundamentals of the hydrodynamic mechanism of splitting in dispersion processes. *AIChE Journal* 1 (3), 289–295.

Hinze, J. O. (1975). *Turbulence*. 2nd ed. McGraw–Hill.

Hirt, C. W. and B. D. Nichols (1981). Volume of fluid (VOF) method for the dynamics of free boundaries. *Journal of Computational Physics* 39 (1), 201–225.

Hlawitschka, M. W., P. Kováts, K. Zähringer and H.-J. Bart (2017). Simulation and experimental validation of reactive bubble column reactors. *Chemical Engineering Science* 170, 306–319.

Hopkins, M. A. and M. Y. Louge (1991). Inelastic microstructure in rapid granular flows of smooth disks. *Physics of Fluids A: Fluid Dynamics* 3 (1), 47–57.

Hoppe, F. and M. Breuer (2017). Euler–Lagrange simulations of turbulent two-phase flows with an advanced deterministic bubble coalescence model. *Proceedings in Applied Mathematics and Mechanics* 17 (1), 655–656.

Hoppe, F. and M. Breuer (2018). A deterministic and viable coalescence model for Euler–Lagrange simulations of turbulent microbubble-laden flows. *International Journal of Multiphase Flow* 99, 213–230.

Hoppe, F. and M. Breuer (2020). A deterministic breakup model for Euler–Lagrange simulations of turbulent microbubble-laden flows. *International Journal of Multiphase Flow* 123, 103119.

Horwitz, J. A. K. and A. Mani (2016). Accurate calculation of Stokes drag for point–particle tracking in two-way coupled flows. *Journal of Computational Physics* 318, 85–109.

Hu, G. and I. Celik (2008). Eulerian–Lagrangian based large-eddy simulation of a partially aerated flat bubble column. *Chemical Engineering Science* 63 (1), 253–271.

Huber, M. M. et al. (2005). Oxidation of pharmaceuticals during ozonation of municipal wastewater effluents: A pilot study. *Environmental Science & Technology* 39 (11), 4290–4299.

Hussein, H. J., S. P. Capp and W. K. George (1994). Velocity measurements in a high-Reynolds-number, momentum-conserving, axisymmetric, turbulent jet. *Journal of Fluid Mechanics* 258, 31–75.

Israelachvili, J. N. (2011). *Intermolecular and Surface Forces*. 3rd ed. Academic Press.

Jain, D., J. A. M. Kuipers and N. G. Deen (2014). Numerical study of coalescence and breakup in a bubble column using a hybrid volume of fluid and discrete bubble model approach. *Chemical Engineering Science* 119, 134–146.

Jeelani, S. A. K. and S. Hartland (1991). Effect of approach velocity on binary and interfacial coalescence. *Chemical Engineering Research and Design* 69 (A4), 271–281.

Jeffreys, G. V. and G. A. Davis (1971). Coalescence of liquid droplets and liquid dispersion. In: *Recent Advances in Liquid-Liquid Extraction*. Ed. by C. Hanson. Pergamon Press, 495–584.

Kamp, A. M., A. K. Chesters, C. Colin and J. Fabre (2001). Bubble coalescence in turbulent flows: A mechanistic model for turbulence-induced coalescence applied to microgravity bubbly pipe flow. *International Journal of Multiphase Flow* 27 (8), 1363–1396.

Kantarci, N., F. Borak and K. O. Ulgen (2005). Bubble column reactors. *Process Biochemistry* 40 (7), 2263–2283.

Karimi, M. and R. Andersson (2019). Dual mechanism model for fluid particle breakup in the entire turbulent spectrum. *AIChE Journal* 65 (8), 1–15.

Kaufmann, A., M. Moreau, O. Simonin and J. Helie (2008). Comparison between Lagrangian and mesoscopic Eulerian modelling approaches for inertial particles suspended in decaying isotropic turbulence. *Journal of Computational Physics* 227 (13), 6448–6472.

Kelessidis, V. C. and A. E. Dukler (1989). Modeling flow pattern transitions for upward gas-liquid flow in vertical concentric and eccentric annuli. *International Journal of Multiphase Flow* 15 (2), 173–191.

Kempe, T. and J. Fröhlich (2012). An improved immersed boundary method with direct forcing for the simulation of particle laden flows. *Journal of Computational Physics* 231 (9), 3663–3684.

Kim, J., P. Moin and R. Moser (1987). Turbulence statistics in fully developed channel flow at low Reynolds number. *Journal of Fluid Mechanics* 177, 133–166.

Kim, J. W. and W. K. Lee (1987). Coalescence behavior of two bubbles in stagnant liquids. *Journal of Chemical Engineering of Japan* 20 (5), 448–453.

Kirkpatrick, R. D. and M. Lockett (1974). The influence of approach velocity on bubble coalescence. *Chemical Engineering Science* 29 (12), 2363–2373.

Klein, M., A. Sadiki and J. Janicka (2003). A digital filter based generation of inflow data for spatially developing direct numerical or large eddy simulations. *Journal of Computational Physics* 186 (2), 652–665.

Kloeden, P. E. and E. Platen (1995). *Numerical Solution of Stochastic Differential Equations*. 2nd ed. Springer. ISBN: 3-540-54062-8.

Koenig, B., K. Schügerl and C. Seewald (1981). Penicillin production in a bubble column air lift loop reactor. In: *Scientific and Engineering Principles*. Ed. by M. Moo-Young, C. W. Robinson and C. Vezina. Pergamon, 573–579.

Konsowa, A. H. (2003). Decolorization of wastewater containing direct dye by ozonation in a batch bubble column reactor. *Desalination* 158 (1), 233–240.

Kosior, D., J. Zawala, R. Todorov, D. Exerowa and K. Malysa (2014). Bubble bouncing and stability of liquid films formed under dynamic and static conditions from n-octanol solutions. *Colloids and Surfaces A: Physiochemical and Engineering Aspects* 460, 391–400.

Krepper, E. and R. Rzehak (2011). CFD for subcooled flow boiling: Simulation of DEBORA experiments. *Nuclear Engineering and Design* 241 (9), 3851–3866.

Krishna, R., J. M. van Baten, M. I. Urseanu and J. Ellenberger (2001). Design and scale up of a bubble column slurry reactor for Fischer–Tropsch synthesis. *Chemical Engineering Science* 56 (2), 537–545.

Kuerten, J. G. M. (2006). Subgrid modeling in particle-laden channel flow. *Physics of Fluids* 18 (2), 025108.

Kuerten, J. G. M., B. J. Geurts, A. W. Vreman and M. Germano (1999). Dynamic inverse modeling and its testing in large-eddy simulations of the mixing layer. *Physics of Fluids* 11 (12), 3778–3785.

Kuerten, J. G. M. and A. W. Vreman (2005). Can turbophoresis be predicted by large-eddy simulation? *Physics of Fluids* 17 (1), 011701.

Kuerten, J. G. M. and A. W. Vreman (2016). Collision frequency and radial distribution function in particle-laden turbulent channel flow. *International Journal of Multiphase Flow* 87, 66–79.

Kurose, R. and S. Komori (1999). Drag and lift forces on a rotating sphere in a linear shear flow. *Journal of Fluid Mechanics* 384, 183–206.

Lamb, H. (1932). *Hydrodynamics*. 6th ed. Cambridge University Press.

Landau, L. D. and E. M. Lifshitz (1966). *Fluid Mechanics*. 3rd ed. Pergamon Press.

Langevin, P. (1908). Sur la théorie du mouvement brownien. *Comptes rendus de l'Académie des Sciences* 146, 530–533.

Lau, Y. M., K. Thiruvalluvan Sujatha, M. Gaeini, N. G. Deen and J. A. M. Kuipers (2013). Experimental study of the bubble size distribution in a pseudo-2D bubble column. *Chemical Engineering Science* 98, 203–211.

Lau, Y. M., W. Bai, N. G. Deen and J. A. M. Kuipers (2014). Numerical study of bubble break-up in bubbly flows using a deterministic Euler–Lagrange framework. *Chemical Engineering Science* 108, 9–22.

Legendre, D. and J. Magnaudet (1998). The lift force on a spherical bubble in a viscous linear shear flow. *Journal of Fluid Mechanics* 368, 81–126.

Lehr, F., M. Millies and D. Mewes (2002). Bubble-size distributions and flow fields in bubble columns. *AIChE Journal* 48 (11), 2426–2443.

Leslie, D. C. and G. L. Quarini (1979). The application of turbulence theory to the formulation of subgrid modelling procedures. *Journal of Fluid Mechanics* 91 (1), 65–91.

Letzel, H. M., J. C. Schouten, R. Krishna and C. M. van den Bleek (1999). Gas holdup and mass transfer in bubble column reactors operated at elevated pressure. *Chemical Engineering Science* 54 (13), 2237–2246.

Liang, J.-H., J. C. McWilliams, P. P. Sullivan and B. Baschek (2011). Modeling bubbles and dissolved gases in the ocean. *Journal of Geophysical Research: Oceans* 116 (C3), 1–17.

Liang, J.-H., C. Deutsch, J. C. McWilliams, B. Baschek, P. P. Sullivan and D. Chiba (2013). Parameterizing bubble-mediated air-sea gas exchange and its effect on ocean ventilation. *Global Biogeochemical Cycles* 27 (3), 894–905.

Liao, Y. and D. Lucas (2009). A literature review of theoretical models for drop and bubble breakup in turbulent dispersions. *Chemical Engineering Science* 64 (15), 3389–3406.

Liao, Y. and D. Lucas (2010). A literature review on mechanisms and models for the coalescence process of fluid particles. *Chemical Engineering Science* 65 (10), 2851–2864.

Liao, Y., R. Rzehak, D. Lucas and E. Krepper (2015). Baseline closure model for dispersed bubbly flow: Bubble coalescence and breakup. *Chemical Engineering Science* 122, 336–349.

Lilly, D. K. (1992). A proposed modification of the Germano subgrid-scale closure method. *Physics of Fluids A: Fluid Dynamics* 4 (3), 633–635.

Liu, Z. and B. Li (2018). Scale-adaptive analysis of Euler–Euler large eddy simulation for laboratory scale dispersed bubbly flows. *Chemical Engineering Journal* 338, 465–477.

Loh, K.-C. and J. A. Domaradzki (1999). The subgrid-scale estimation model on nonuniform grids. *Physics of Fluids* 11 (12), 3786–3792.

Lu, J., A. Fernández and G. Tryggvason (2005). The effect of bubbles on the wall drag in a turbulent channel flow. *Physics of Fluids* 17 (9), 095102.

Lu, J. and G. Tryggvason (2006). Numerical study of turbulent bubbly downflows in a vertical channel. *Physics of Fluids* 18 (10), 103302.

Lu, J. and G. Tryggvason (2007). Effect of bubble size in turbulent bubbly downflow in a vertical channel. *Chemical Engineering Science* 62 (11), 3008–3018.

Lu, J. and G. Tryggvason (2008). Effect of bubble deformability in turbulent bubbly upflow in a vertical channel. *Physics of Fluids* 20 (4), 040701.

Lu, J. and G. Tryggvason (2013). Dynamics of nearly spherical bubbles in a turbulent channel upflow. *Journal of Fluid Mechanics* 732, 166–189.

Luo, H. and H. F. Svendsen (1996). Theoretical model for drop and bubble breakup in turbulent dispersions. *AIChE Journal* 42 (5), 1225–1233.

Ma, T., T. Ziegenhein, D. Lucas, E. Krepper and J. Fröhlich (2015). Euler–Euler large eddy simulations for dispersed turbulent bubbly flows. *International Journal of Heat and Fluid Flow* 56, 51–59.

Magnaudet, J. and I. Eames (2000). The motion of high-Reynolds number bubbles in inhomogeneous flows. *Annual Review of Fluid Mechanics* 32 (1), 659–708.

Majumder, S. K., G. Kundu and D. Mukherjee (2006). Bubble size distribution and gas-liquid interfacial area in a modified downflow bubble column. *Chemical Engineering Journal* 122 (1–2), 1–10.

Manica, R., E. Klaseboer and D. Y. C. Chan (2016). The impact and bounce of air bubbles at a flat fluid interface. *Soft Matter* 12 (13), 3271–3282.

Marchioli, C., V. Armenio and A. Soldati (2007). Simple and accurate scheme for fluid velocity interpolation for Eulerian–Lagrangian computation of dispersed flows in 3D curvilinear grids. *Computers and Fluids* 36 (7), 1187–1198.

Marchioli, C., M. V. Salvetti and A. Soldati (2008). Some issues concerning large-eddy simulation of inertial particle dispersion in turbulent bounded flows. *Physics of Fluids* 20 (4), 040603.

Marrucci, G. (1969). A theory of coalescence. *Chemical Engineering Science* 24 (6), 975–985.

Martínez-Bazán, C. (2018). Private Communication.

Martínez-Bazán, C., J. L. Montañes and J. C. Lasheras (1999a). On the breakup of an air bubble injected into a fully developed turbulent flow. Part 1. Breakup frequency. *Journal of Fluid Mechanics* 401, 157–182.

Martínez-Bazán, C., J. L. Montañes and J. C. Lasheras (1999b). On the breakup of an air bubble injected into a fully developed turbulent flow. Part 2. Size PDF of the resulting daughter bubbles. *Journal of Fluid Mechanics* 401, 183–207.

Martínez-Bazán, C., J. Rodríguez-Rodríguez, G. B. Deane, J. L. Montañes and J. C. Lasheras (2010). Considerations on bubble fragmentation models. *Journal of Fluid Mechanics* 661, 159–177.

Maxey, M. R. and J. J. Riley (1983). Equation of motion for a small rigid sphere in a nonuniform flow. *Physics of Fluids* 26 (4), 883–889.

Mazzitelli, I. M. (2003). Turbulent Bubbly Flow. PhD thesis. University of Twente, Enschede, the Netherlands.

Mazzitelli, I. M., F. Toschi and A. S. Lanotte (2014). An accurate and efficient Lagrangian sub-grid model. *Physics of Fluids* 26 (9), 095101.

McLaughlin, J. B. (1991). Inertial migration of a small sphere in linear shear flows. *Journal of Fluid Mechanics* 224, 261–274.

Medwin, H. and N. D. Breitz (1989). Ambient and transient bubble spectral densities in quiescent seas and under spilling breakers. *Journal of Geophysical Research: Oceans* 94 (C9), 12751–12759.

Mei, R. (1993). History force on a sphere due to a step change in the free-stream velocity. *International Journal of Multiphase Flow* 19 (3), 509–525.

Mei, R. (1994). Flow due to an oscillating sphere and an expression for unsteady drag on the sphere at finite Reynolds number. *Journal of Fluid Mechanics* 270, 133–174.

Mei, R. and R. J. Adrian (1992). Flow past a sphere with an oscillation in the free-stream velocity and unsteady drag at finite Reynolds number. *Journal of Fluid Mechanics* 237, 323–341.

Mei, R. and J. F. Klausner (1992). Unsteady force on a spherical bubble at finite Reynolds number with small fluctuations in the free-stream velocity. *Physics of Fluids A: Fluid Dynamics* 4 (1), 63–70.

Mei, R., J. F. Klausner and C. J. Lawrence (1994). A note on the history force on a spherical bubble at finite Reynolds number. *Physics of Fluids* 6 (1), 418–420.

Melville, W. K. (1996). The role of surface-wave breaking in air-sea interaction. *Annual Review of Fluid Mechanics* 28 (1), 279–321.

Michaelides, E. E. (1992). A novel way of computing the Basset term in unsteady multiphase flow computations. *Physics of Fluids A: Fluid Dynamics* 4 (7), 1579–1582.

Michałek, W. R., J. G. M. Kuerten, J. C. H. Zeegers, R. Liew, J. Pozorski and B. J. Geurts (2013). A hybrid stochastic-deconvolution model for large-eddy simulation of particle-laden flow. *Physics of Fluids* 25 (12), 123302.

Michalke, A. (1984). Survey on jet instability theory. *Progress in Aerospace Sciences* 21, 159–199.

Minier, J.-P., E. Peirano and S. Chibbaro (2003). Weak first- and second-order numerical schemes for stochastic differential equations appearing in Lagrangian two-phase flow modeling. *Monte Carlo Methods and Applications* 9, 93–133.

Minier, J.-P., E. Peirano and S. Chibbaro (2004). PDF model based on Langevin equation for polydispersed two-phase flows applied to a bluff-body gas-solid flow. *Physics of Fluids* 16 (7), 2419–2431.

Minier, J.-P., S. Chibbaro and S. B. Pope (2014). Guidelines for the formulation of Lagrangian stochastic models for particle simulations of single-phase and dispersed two-phase turbulent flows. *Physics of Fluids* 26 (11), 113303.

Minier, J.-P. and E. Peirano (2001). The pdf approach to turbulent polydispersed two-phase flows. *Physics Reports* 352 (1-3), 1–214.

Mirón, A. S., M. C. García, A. C. Gómez, F. G. Camacho, E. M. Grima and Y. Chisti (2003). Shear stress tolerance and biochemical characterization of Phaeodactylum tricornutum in quasi steady-state continuous culture in outdoor photobioreactors. *Biochemical Engineering Journal* 16 (3), 287–297.

Mitchell, I. M. (2008). The flexible, extensible and efficient toolbox of level set methods. *Journal of Scientific Computing* 35 (2), 300–329.

Molin, D., C. Marchioli and A. Soldati (2012). Turbulence modulation and microbubble dynamics in vertical channel flow. *International Journal of Multiphase Flow* 42, 80–95.

Moore, D. W. (1963). The boundary layer on a spherical gas bubble. *Journal of Fluid Mechanics* 16 (2), 161–176.

Morbidelli, M., R. Paludetto and S. Carra (1986). Gas-liquid autoxidation reactors. *Chemical Engineering Science* 41 (9), 2299–2307.

Morel, C. (2015). *Mathematical Modeling of Disperse Two-Phase Flows*. Springer International Publishing.

Morris, P. J. (1976). The spatial viscous instability of axisymmetric jets. *Journal of Fluid Mechanics* 77 (3), 511–529.

Müller-Fischer, N., P. Tobler, M. Dressler, P. Fischer and E. J. Windhab (2008). Single bubble deformation and breakup in simple shear flow. *Experiments in Fluids* 45 (5), 917–926.

Oeters, F., W. Pluschkell, E. Steinmetz and H. Wilhelmi (1988). Fluid flow and mixing in secondary metallurgy. *Steel Research* 59 (5), 192–201.

Okong'o, N. and J. Bellan (2000). A priori subgrid analysis of temporal mixing layers with evaporating droplets. *Physics of Fluids* 12 (6), 1573–1591.

Olivieri, S., F. Picano, G. Sardina, D. Iudicone and L. Brandt (2014). The effect of the Basset history force on particle clustering in homogeneous and isotropic turbulence. *Physics of Fluids* 26 (4), 041704.

Olmos, E., C. Gentric, C. Vial, G. Wild and N. Midoux (2001). Numerical simulation of multiphase flow in bubble column reactors. Influence of bubble coalescence and break-up. *Chemical Engineering Science* 56 (21), 6359–6365.

Oolman, T. O. and H. W. Blanch (1986). Bubble coalescence in stagnant liquids. *Chemical Engineering Communications* 43 (4-6), 237–261.

Osher, S. and R. P. Fedkiw (2001). Level set methods: An overview and some recent results. *Journal of Computational Physics* 169 (2), 463–502.

Osher, S. and J. A. Sethian (1988). Fronts propagating with curvature-dependent speed: Algorithms based on Hamilton-Jacobi formulations. *Journal of Computational Physics* 79 (1), 12–49.

Pallas, N. R. and Y. Harrison (1990). An automated drop shape apparatus and the surface tension of pure water. *Colloids and Surfaces* 43 (2), 169–194.

Panchapakesan, N. R. and J. L. Lumley (1993). Turbulence measurements in axisymmetric jets of air and helium. Part 1. Air jet. *Journal of Fluid Mechanics* 246, 197–223.

Pang, M. and J. Wei (2014). A mechanism on liquid-phase turbulence modulation by microbubbles. *Advances in Mechanical Engineering* 6, 405864.

Patel, D., A. Chaudhari, A. Laari, M. Heiliö, J. Hämäläinen and K. Agrawal (2006). Numerical simulation of bubble coalescence and break-up in multinozzle jet ejector. *Journal of Applied Mathematics* 2016, 1–19.

Pauli, W. (1973). *Thermodynamics and the Kinetic Theory of Gases*. Dover Publications.

Peirano, E., S. Chibbaro, J. Pozorski and J.-P. Minier (2006). Mean-field PDF numerical approach for polydispersed turbulent two-phase flows. *Progress in Energy and Combustion Science* 32, 315–371.

Peskin, C. S. (1972). Flow patterns around heart valves: A numerical method. *Journal of Computational Physics* 10 (2), 252–271.

Peskin, C. S. (1977). Numerical analysis of blood flow in the heart. *Journal of Computational Physics* 25 (3), 220–252.

Peskin, C. S. (2002). The immersed boundary method. *Acta Numerica* 11, 479–517.

Pilliod, J. E. and E. G. Puckett (2004). Second-order accurate volume-of-fluid algorithms for tracking material interfaces. *Journal of Computational Physics* 199 (2), 465–502.

Piomelli, U. and J. R. Chasnov (1996). Large-Eddy Simulations: Theory and Applications. In: *Turbulence and Transition Modelling*. Ed. by M. Hallbäck, D. S. Henningson, A. V. Johansson and P. H. Alfredsson. Springer, 269–336.

Piomelli, U. (2008). Wall-layer models for large-eddy simulations. *Progress in Aerospace Sciences* 44 (6), 437–446.

Piomelli, U. and E. Balaras (2002). Wall-layer models for large-eddy simulations. *Annual Review of Fluid Mechanics* 34 (1), 349–374.

Piomelli, U., J. Ferziger, P. Moin and J. Kim (1989). New approximate boundary conditions for large eddy simulations of wall-bounded flows. *Physics of Fluids A: Fluid Dynamics* 1 (6), 1061–1068.

Pope, S. B. (1994). Lagrangian PDF methods for turbulent flows. *Annual Review of Fluid Mech.* 26, 23–63.

Pope, S. B. (2000). *Turbulent Flows*. Cambridge University Press.

Pozorski, J. and S. V. Apte (2009). Filtered particle tracking in isotropic turbulence and stochastic modeling of subgrid–scale dispersion. *International Journal of Multiphase Flow* 35, 118–128.

Press, W. H., S. A. Teukolsky, W. T. Vetterling and B. P. Flannery (2007). *Numerical Recipes: The Art of Scientific Computing*. 3rd ed. Cambridge University Press.

Prince, M. J. and H. W. Blanch (1990). Bubble coalescence and break-up in air-sparged bubble columns. *AIChE Journal* 36 (10), 1485–1499.

Prosperetti, A. and G. Tryggvason (2007). *Computational Methods for Multiphase Flow*. Cambridge University Press.

Qian, D., J. B. McLaughlin, K. Sankaranarayanan, S. Sundaresan and K. Kontomaris (2006). Simulation of bubble breakup dynamics in homogeneous turbulence. *Chemical Engineering Communications* 193 (8), 1038–1063.

Reeks, M. W. (1983). The transport of discrete particles in inhomogeneous turbulence. *Journal of Aerosol Science* 14 (6), 729–739.

Rhie, C. M. and W. L. Chow (1983). Numerical study of the turbulent flow past an airfoil with trailing edge separation. *AIAA Journal* 21 (11), 1525–1532.

Ridders, C. J. F. (1979). A new algorithm for computing a single root of a real continuous function. *IEEE Transactions on Circuits and Systems* 26 (11), 979–980.

Risso, F. and J. Fabre (1998). Oscillations and breakup of a bubble immersed in a turbulent field. *Journal of Fluid Mechanics* 372, 323–355.

Rosso, D., L. E. Larson and M. K. Stenstrom (2008). Aeration of large-scale municipal wastewater treatment plants: State of the art. *Water Science and Technology* 57 (7), 973–978.

Sadeghi, H., P. Lavoie and A. Pollard (2018). Effects of finite hot-wire spatial resolution on turbulence statistics and velocity spectra in a round turbulent free jet. *Experiments in Fluids* 59 (40), 1–10.

Sagaut, P. (2006). *Large Eddy Simulation for Incompressible Flows*. 3rd ed. Springer.

Sagert, N. H. and M. J. Quinn (1976). The coalescence of H_2S and CO_2 bubbles in water. *Canadian Journal of Chemical Engineering* 54, 392–398.

Saha, D. (2013). Experimental analysis of aggregate breakup in flows observed by three-dimensional particle tracking velocimetry. PhD thesis. ETH Zürich, Zürich, Switzerland.

Sassi, G., B. Ruggeri, V. Specchia and A. Gianetto (1991). Citric acid production by A. niger with banana extract. *Bioresource Technology* 37 (3), 259–269.

Sato, Y., M. Sadatomi and K. Sekoguchi (1981a). Momentum and heat transfer in two-phase bubble flow—I. Theory. *International Journal of Multiphase Flow* 7 (2), 167–177.

Sato, Y., M. Sadatomi and K. Sekoguchi (1981b). Momentum and heat transfer in two-phase bubble flow—II. A comparison between experimental data and theoretical calculations. *International Journal of Multiphase Flow* 7 (2), 179–190.

Scardovelli, R. and S. Zaleski (1999). Direct numerical simulation of free-surface and interfacial flow. *Annual Review of Fluid Mechanics* 31 (1), 567–603.

Schäfer, F. and M. Breuer (2002). Comparison of c-space and p-space particle tracing schemes on high-performance computers: Accuracy and performance. *International Journal for Numerical Methods in Fluids* 39 (4), 277–299.

Schäfer, M. (2006). *Computational Engineering*. 1st ed. Springer.

Schiller, L. and A. Naumann (1933). A drag coefficient correlation. *VDI Zeitschrift* 77, 318–320.

Schmidt, S. and M. Breuer (2015). Extended synthetic turbulence inflow generator within a hybrid LES–URANS methodology for the prediction of non-equilibrium wall-bounded flows. *Flow, Turbulence and Combustion* 95 (4), 669–707.

Schumann, U. (1975). Subgrid scale model for finite difference simulations of turbulent flows in plane channels and annuli. *Journal of Computational Physics* 18 (4), 376–404.

Schwarz, S., T. Kempe and J. Fröhlich (2016). An immersed boundary method for the simulation of bubbles with varying shape. *Journal of Computational Physics* 315, 124–149.

Seitz, R. (2011). Bright water: hydrosols, water conservation and climate change. *Climatic Change* 105 (3), 365–381.

Shah, Y. T., B. G. Kelkar, S. P. Godbole and W.-D. Deckwer (1982). Design parameters estimations for bubble column reactors. *AIChE Journal* 28 (3), 353–379.

Shaikh, A. and M. Al-Dahhan (2013). Scale-up of bubble column reactors: A review of current state-of-the-art. *Industrial & Engineering Chemistry Research* 52 (24), 8091–8108.

Sharp, D. H. (1984). An overview of Rayleigh–Taylor instability. *Physica D* 12 (1–3), 3–10.

Sheng, Y. Y. and G. A. Irons (1995). The impact of bubble dynamics on the flow in plumes of ladle water models. *Metallurgical and Materials Transactions B* 26 (3), 625–635.

Shi, P. and R. Rzehak (2018). Bubbly flow in stirred tanks: Euler-Euler/RANS modeling. *Chemical Engineering Science* 190, 419–435.

Shotorban, B. and F. Mashayek (2005). Modeling subgrid-scale effects on particles by approximate deconvolution. *Physics of Fluids* 17 (8), 081701.

Singh, R. N. and S. Sharma (2012). Development of suitable photobioreactor for algae production – A review. *Renewable and Sustainable Energy Reviews* 16 (4), 2347–2353.

Situ, R., T. Hibiki, M. Ishii and M. Mori (2005). Bubble lift-off size in forced convective subcooled boiling flow. *International Journal of Heat and Mass Transfer* 48 (25), 5536–5548.

Smagorinsky, J. (1963). General circulation experiments with the primitive equations: I. The basic experiment. *Monthly Weather Review* 91, 99–165.

Solsvik, J. and H. A. Jakobsen (2014). Bubble coalescence modeling in the population balance framework. *Journal of Dispersion Science and Technology* 35 (11), 1626–1642.

Solsvik, J. and H. A. Jakobsen (2015). Single air bubble breakup experiments in stirred water tank. *International Journal of Chemical Reactor Engineering* 13 (4), 477–491.

Solsvik, J. and H. A. Jakobsen (2016a). A review of the statistical turbulence theory required extending the population balance closure models to the entire spectrum of turbulence. *AIChE Journal* 62 (5), 1795–1820.

Solsvik, J. and H. A. Jakobsen (2016b). Development of fluid particle breakup and coalescence closure models for the complete energy spectrum of isotropic turbulence. *Industrial & Engineering Chemistry Research* 55 (5), 1449–1460.

Solsvik, J., S. Maaß and H. A. Jakobsen (2016). Definition of the single drop breakup event. *Industrial & Engineering Chemistry Research* 55 (10), 2872–2882.

Solsvik, J., V. T. Skjervold and H. A. Jakobsen (2017). A bubble breakage model for finite Reynolds number flows. *Journal of Dispersion Science and Technology* 38 (7), 973–978.

Solsvik, J., S. Tangen and H. A. Jakobsen (2013). On the constitutive equations for fluid particle breakage. *Reviews in Chemical Engineering* 29 (5), 241–356.

Sommerfeld, M., E. Bourloutski and D. Bröder (2003). Euler/Lagrange calculations of bubbly flows with consideration of bubble coalescence. *Canadian Journal of Chemical Engineering* 81, 508–518.

Sommerfeld, M., M. Muniz and T. Reichardt (2018). On the importance of modelling bubble dynamics for point-mass numerical calculations of bubble columns. *Journal of Chemical Engineering of Japan* 51 (4), 301–317.

Sommerfeld, M., B. van Wachem and R. Oliemans (2008). *Best Practice Guidelines for Computational Fluid Dynamics of Dispersed Multiphase Flows*. Version 1. European Research Community On Flow, Turbulence and Combustion. ISBN: 978-91-633-3564-8.

Sovová, H. (1981). Breakage and coalescence of drops in a batch stirred vessel – II Comparison of model and experiments. *Chemical Engineering Science* 36 (9), 1567–1573.

Sreenivasan, K. R. (1995). On the universality of the Kolmogorov constant. *Physics of Fluids* 7 (11), 2778–2784.

Sridhar, G. and J. Katz (1999). Effect of entrained bubbles on the structure of vortex rings. *Journal of Fluid Mechanics* 397, 171–202.

Stewart, C. W. (1995). Bubble interaction in low-viscosity liquids. *International Journal of Multiphase Flow* 21 (6), 1037–1046.

Stolz, S. and N. A. Adams (1999). An approximate deconvolution procedure for large-eddy simulation. *Physics of Fluids* 11 (7), 1699–1701.

Stolz, S., N. A. Adams and L. Kleiser (2001). An approximate deconvolution model for large-eddy simulation with application to incompressible wall-bounded flows. *Physics of Fluids* 13 (4), 997–.1015.

Stone, H. (1968). Iterative solution of implicit approximations of multidimensional partial differential equations. *SIAM Journal on Numerical Analysis* 5 (3), 530–558.

Sungkorn, R., J. J. Derksen and J. G. Khinast (2012). Euler–Lagrange modeling of a gas-liquid stirred reactor with consideration of bubble breakage and coalescence. *AIChE Journal* 58 (5), 1356–1370.

Taitel, Y., D. Bornea and A. E. Dukler (1980). Modelling flow pattern transitions for steady upward gas-liquid flow in vertical tubes. *AIChE Journal* 26 (3), 345–354.

Taitel, Y. and A. E. Dukler (1976). A model for predicting flow regime transitions in horizontal and near horizontal gas-liquid flow. *AIChE Journal* 22 (1), 47–55.

Takemura, F. and J. Magnaudet (2003). The transverse force on clean and contaminated bubbles rising near a vertical wall at moderate Reynolds number. *Journal of Fluid Mechanics* 495, 235–253.

Tanaka, T. and Y. Tsuji (1991). Numerical simulation of gas-solid two-phase flow in a vertical pipe: On the effect of inter-particle collision. In: *Gas-Solid Flows*. Ed. by D. E. Stock, Y. Tsuji, J. T. Jurewicz, M. W. Reeks and M. Gautam, 123–128.

Taniére, A. and B. Arcen (2014). Prediction of a particle-laden turbulent channel flow: Examination of two classes of stochastic dispersion models. *International Journal of Multiphase Flow* 60, 1–10.

Tans, P. P., I. Y. Fung and T. Takahashi (1990). Observational constraints on the global atmospheric CO_2 budget. *Science* 247 (4949), 1431–1438.

Tennekes, H. and J. L. Lumley (1972). *A First Course in Turbulence*. The MIT Press.

Terrill, E. J., W. K. Melville and D. Stramski (2001). Bubble entrainment by breaking waves and their influence on optical scattering in the upper ocean. *Journal of Geophysical Research: Oceans* 106 (C8), 16815–16823.

Tisnadjaja, D., N. A. Gutierrez and I. S. Maddox (1996). Citric acid production in a bubble-column reactor using cells of the yeast Candida guilliermondii immobilized by adsorption onto sawdust. *Enzyme and Microbial Technology* 19 (5), 343–347.

Tomiyama, A., H. Tamai, I. Zun and S. Hosokawa (2002). Transverse migration of single bubbles in simple shear flows. *Chemical Engineering Science* 57 (11), 1849–1858.

Tomiyama, A., I. Zun and T. Sakaguchi (1998). Drag coefficients of single bubbles under normal and micro gravity conditions. *The Japanese Society of Mechanical Engineers, International Journal Series B* 41 (2), 472–479.

Tripathi, M. K., K. C. Sahu and R. Govindarajan (2015). Dynamics of an initially spherical bubble rising in quiescent liquid. *Nature Communication* 6, 1–9.

Tsao, H. and D. L. Koch (1997). Observations of high Reynolds number bubbles interacting with a rigid wall. *Physics of Fluids* 9 (1), 44–56.

Tsouris, C. and L. L. Tavlarides (1994). Breakage and coalescence models for drops in turbulent dispersions. *AIChE Journal* 40 (3), 395–406.

Uhlmann, M. (2005). An immersed boundary method with direct forcing for the simulation of particulate flows. *Journal of Computational Physics* 209 (2), 448–476.

Ünal, H. C. (1976). Maximum bubble diameter, maximum bubble-growth time and bubble-growth rate during the subcooled nucleate flow boiling of water up to 17.7 MN/m2. *International Journal of Heat and Mass Transfer* 19 (6), 643–649.

Vagle, S., C. McNeil and N. Steiner (2010). Upper ocean bubble measurements from the NE Pacific and estimates of their role in air-sea gas transfer of the weakly soluble gases nitrogen and oxygen. *Journal of Geophysical Research: Oceans* 115 (C12), 1–16.

Van Driest, E. R. (1956). On turbulent flow near a wall. *Journal of Aeronautical Sciences* 23, 1007–1011.

Van Hinsberg, M. A. T., J. H. M. ten Thije Boonkkamp and H. J. H. Clercx (2011). An efficient, second-order method for the approximation of the Basset history force. *Journal of Computational Physics* 230 (4), 1465–1478.

Viccione, G., V. Bovolin and E. P. Carratelli (2008). Defining and optimizing algorithms for neighbouring particle identification in SPH fluid simulations. *International Journal for Numerical Methods in Fluids* 58 (6), 625–638.

Wachi, S. and H. Morikawa (1987). Chlorination of ethylene in a boiling bubble column reactor. *Journal of Chemical Engineering of Japan* 20 (3), 238–245.

Walter, J. F. and H. W. Blanch (1986). Bubble break-up in gas-liquid bioreactors: Break-up in turbulent flows. *The Chemical Engineering Journal* 32 (1), B7–B17.

Wang, L.-P. and D. E. Stock (1993). Dispersion of heavy particles by turbulent motion. *Journal of the Atmospheric Sciences* 50 (13), 1897–1913.

Wang, Q. and K. D. Squires (1996). Large eddy simulation of particle-laden turbulent channel flow. *Physics of Fluids* 8 (5), 1207–1223.

Wang, T., J. Wang and Y. Jin (2003). A novel theoretical breakup kernel function for bubbles/droplets in a turbulent flow. *Chemical Engineering Science* 58 (20), 4629–4637.

Wang, Z. and B. Sun (2009). Annular multiphase flow behavior during deep water drilling and the effect of hydrate phase transition. *Petroleum Science* 6 (1), 57–63.

Wei, Y. K., Y. Qian and H. Xu (2012). Lattice Boltzmann simulations of single bubble deformation and breakup in a shear flow. *Journal of Computational Multiphase Flows* 4 (1), 111–117.

Werner, H. and H. Wengle (1993). Large-eddy simulation of turbulent flow over and around a cube in a plate channel. In: *Turbulent Shear Flows 8*. Ed. by F. Durst, R. Friedrich, B. E. Launder, F. W. Schmidt, U. Schumann and J. H. Whitelaw. Springer, 155–168.

Wilkinson, P. M., H. Haringa and L. L. Van Dierendonck (1994). Mass transfer and bubble size in a bubble column under pressure. *Chemical Engineering Science* 49 (9), 1417–1427.

Wilkinson, P. M., A. P. Spek and L. L. van Dierendonck (1992). Design parameters estimation for scale-up of high-pressure bubble columns. *AIChE Journal* 38 (4), 544–554.

Wilkinson, P. M. and L. L. van Dierendonck (1990). Pressure and gas density effects on bubble break-up and gas hold-up in bubble columns. *Chemical Engineering Science* 45 (8), 2309–2315.

Wilkinson, P. M., A. van Schayk, J. P. M. Spronken and L. van Dierendonck (1993). The influence of gas density and liquid properties on bubble breakup. *Chemical Engineering Science* 48 (7), 1213–1226.

Winterbottom, J. M., H. Marwan, E. H. Stitt and R. Natividad (2003). The palladium catalysed hydrogenation of 2-butyne-1,4-diol in a monolith bubble column reactor. *Catalysis Today* 79-80, 391–399.

Woolf, D. K. (1993). Bubbles and the air-sea transfer velocity of gases. 31 (4), 517–540.

Wunsch, D., P. Fede and O. Simonin (2008). Development and validation of a binary collision detection algorithm for a polydispersed particle mixture. In: *Proceedings of the ASME 2008 Fluids Engineering Division Summer Meeting*.

Wygnanski, I. and H. Fiedler (1969). Some measurements in the self-preserving jet. *Journal of Fluid Mechanics* 38 (3), 577–612.

Yamamoto, Y., M. Potthoff, T. Tanaka, T. Kajishima and Y. Tsuji (2001). Large-eddy simulation of turbulent gas-particle flow in a vertical channel: Effect of considering inter-particle collisions. *Journal of Fluid Mechanics* 442, 303–334.

Yang, M., K. Uesugi and H. Myoga (1999). Ammonia removal in bubble column by ozonation in the presence of bromide. *Water Research* 33 (8), 1911–1917.

Yang, S.-M. and L. G. Leal (1991). A note on memory-integral contributions to the force on an accelerating spherical drop at low Reynolds number. *Physics of Fluids A: Fluid Dynamics* 3 (7), 1822–1824.

Young, J. and A. Leeming (1997). A theory of particle deposition in turbulent pipe flow. *Journal of Fluid Mechanics* 340, 129–159.

Youngs, E. A. and E. M. Cramer (1971). Some results relevant to choice of sum and sum-of-product algorithms. *Technometrics* 13 (3), 657–665.

Zahid, A. A., S. R. ur Rehman, S. Rushd, A. Hasan and M. A. Rahman (2018). Experimental investigation of multiphase flow behavior in drilling annuli using high speed visualization technique. *Frontiers in Energy*, 1–9.

Zaman, K. B. M. Q. and A. K. M. F. Hussain (1980). Vortex pairing in a circular jet under controlled excitation. Part 1. General jet response. *Journal of Fluid Mechanics* 101 (3), 449–491.

Zawala, J., M. Krasowska, T. Dabros and K. Malysa (2007). Influence of bubble kinetic energy on its bouncing during collisions with various interfaces. *Canadian Journal of Chemical Engineering* 85 (5), 669–678.

Zawala, J., S. Dorbolo, N. Vandewalle and K. Malysa (2013). Bubble bouncing at a clean water surface. *Physical Chemistry Chemical Physics* 15 (40), 17324–17332.

Zawala, J. and T. Dabros (2013). Analysis of energy balance during collision of an air bubble with a solid wall. *Physics of Fluids* 25 (12), 123101.

Zawala, J. and K. Malysa (2011). Influence of the impact velocity and size of the film formed on bubble coalescence time at water surface. *Langmuir* 27 (6), 2250–2257.

Zenit, R. and D. Legendre (2009). The coefficient of restitution for air bubbles colliding against solid walls in viscous liquids. *Physics of Fluids* 21 (8), 083306.

Zhang, C., S. Eckert and G. Gerbeth (2007). The flow structure of a bubble-driven liquid-metal jet in a horizontal magnetic field. *Journal of Fluid Mechanics* 575, 57–82.

Zhang, X., M. Lewis and B. Johnson (1998). Influence of bubbles on scattering of light in the ocean. *Applied Optics* 37 (27), 6525–6536.

Zhang, X., M. Lewis, M. Lee, B. Johnson and G. Korotaev (2002). The volume scattering function of natural bubble populations. *Limnology and Oceanography* 47 (5), 1273–1282.

Zieminski, S. A. and R. C. Whittemore (1971). Behavior of gas bubbles in aqueous electrolyte solutions. *Chemical Engineering Science* 26 (4), 509–520.

Curriculum Vitae

Felix Hoppe, geboren am 19.12.1989 in München

02/2014	-	heute	**Wissenschaftlicher Angestellter** Helmut Schmidt Universität / Universität der Bundeswehr Hamburg, Fakultät für Maschinenbau, Professur für Strömungsmechanik
10/2011	-	10/2013	**Master-Studium** Ludwig Maximilians Universität München
10/2008	-	10/2011	**Bachelor-Studium** Ludwig Maximilians Universität München
1999	-	2008	**Schulbildung** Josef-Hofmiller-Gymnasium, Freising